

TECHNICAL PAPERS

- Architecture and Sequence Stratigraphy of Late Triassic Fluvial System, Abu Shaybah formation, NW Libya
G. Mayouf 1
- Assessment of Formation Damage of Sandstone Reservoirs Impact of Fines Migration and Solids Plugging on Sandstones' Reservoir Quality, Sarir
Faraj M. Elkhatri 21
- Remote Sensing Techniques in Update Geologic and Geomorphologic Mapping of Seif Al Uwaynat, Southeastern Libya
Eddawi Ali Elhatmi 29
- The Effect of Wettability on Archie Saturation Exponent for Libyan Nubian Sandstone Reservoirs
H. Sbiga 37
- Evaluation of Empirical PVT Correlations and Eos Tuning to Model Libyan Crude Oil Properties Using PVTi Software
Wahid R. Shtewi, Msc 45
- The Effects of Changes in Overburden Pressure on Klikenberg Permeability Measurements for Sirt Basin
Rashid Toumi, Adel Grera, Ahmed Naami 51
- Libyan Gass Composition Analysis and Prediction
Omar Hussein El Ayadi Esra A. Swedan 55
- Bacterial Corrosion Induced by Aerobic and Anaerobic and Microorganism
I.El Musrati and B.Gammudi 67
- Optimisation of Biostimulation by Using Different Nutrient Ratios to Improve Bioremediation of Petroleum Contaminated
Althalb Hakima 77
- An Electrochemical Behavior of CO₂ Corrosion of Static Carbon Steel Electrode in Presence of Acetic Acid, Acetate and Metal Inhibitor (Zn⁺², Ca⁺²) Using AC and DC Electrochemical Techniques
H. A. Mahfud 89
- Accurate Age Range Prediction System of Individuals from Facial Images
Tariq Khalifa, Kamal Solaiman, Tarik Idbeaa and Samar Husain 99
- Oxidation of Sodium Sulfide in Industrial Wastewater and Spent Caustic by Hydrochlorite Ion Solution
Youssef Ahmed Al Mestiri 109

VOLUME 23 - (2018)

**Libyan Petroleum Institute
P.O. Box 6431, Tripoli
State of Libya**

Chairman

DR. MANSOUR EMTIR

Editor-in-Chief

MAHMOUD T. ELBAKAI

Co-ordinator

ABDULMAGID A. ELMRYED

TECHNICAL PAPERS

Architecture and Sequence Stratigraphy of Late Triassic Fluvial System, Abu Shaybah formation, NW Libya	1
Assessment of Formation Damage of Sandstone Reservoirs Impact of Fines Migration and Solids Plugging on Sandstones' Reservoir Quality, Sarir	21
Remote Sensing Techniques in Update Geologic and Geomorphologic Mapping of Seif Al Uwaynat, Southeastern Libya	29
The Effect of Wettability on Archie Saturation Exponent for Libyan Nubian Sandstone Reservoirs	37
Evaluation of Empirical PVT Correlations and Eos Tuning to Model Libyan Crude Oil Properties Using PVTi Software	45
The Effects of Changes in Overburden Pressure on Klikenberg Permeability Measurements for Sirt Basin	51
Libyan Gass Composition Analysis And Prediction	55
Bacterial Corrosion Induced by Aerobic and Anaerobic and Microorganism	67
Optimisation of Biostimulation by Using Different Nutrient Ratios to Improve Bioremediation of Petroleum Contaminated	77
An Electrochemical Behavior of CO ₂ Corrosion of Static Carbon Steel Electrode in Presence of Acetic Acid, Acetate and Metal Inhibitor (Zn ⁺² , Ca ⁺²) Using AC and DC Electrochemical Techniques	89
Accurate Age Range Prediction System of Individuals from Facial Images	99
Oxidation of Sodium Sulfide in Industrial Wastewater and Spent Caustic by Hydrochlorite Ion Solution	109

Copyright © 2018 by Libyan Petroleum Institute (LPI)
Published by the Libyan Petroleum Institute (LPI), Tripoli, Libya

All rights Reserved

No part of this publication may be reproduced or transmitted in any form or by any means, electronically or mechanically including photocopying, recording or any information storage or retrieval system, without prior permission from the copyright holders.

Printed by Gutenberg Press Limited - Malta

Table 2 reacted and non reacted hypochlorite and sulfide ions.

Exp. No.	mg reacted OCl ⁻¹	mg non reacted OCl ⁻¹	mg reacted S ⁻²	mg non reacted S ⁻²
1	11.03	*	2.50	0.90
2	4.34	*	1.74	0.32
3	6.50	*	2.32	0.42
4	0.76	*	0.43	2.07
5	1.14	*	0.80	1.70
6	4.96	*	1.26	1.50
7	15.60	6.45	3.40	*
8	6.73	4.11	2.06	*
9	8.70	18.40	2.74	*
10	17.90	9.20	5.48	*
11	11.30	6.40	2.76	*
12	7.15	10.55	2.20	*
13	4.84	12.86	1.38	*
14	7.86	1.67	2.00	*
15	5.03	4.50	1.25	*
S1	7.20	8.75	7.35	*
S2	8.96	4.93	5.30	*
S3	5.26	4.00	1.28	*
S4	5.86	3.40	1.24	*
S5	22.15	1.00	4.27	*
S6	21.95	1.20	4.50	*
S7	19.93	3.22	4.64	*

ACKNOWLEDGMENT

Much grateful to all that support and facilitate my work to finish this study.

REFERENCES

Allison, Joe D., *et al* (2010) Processes and Oxidizing Agents for Oxidizing Sulfide Ion to Innocuous, Soluble Sulfur Species December, 1987-4710305. [WWW Document], <http://www.freepatentsonline.com/4710305.html>.

- Kubicek, D. H. (2010). Conversion of Hydrogen Sulfide to Sulfur by Direct Oxidation, [WWW Document] <http://www.freepatentsonline.com/4412981.html>.
- Saikat. M. and Naveed, A. (2010). Removal of Sodium Sulfide from Waste Water by Oxidation Process in the Presence of Nano Ferric Oxide Catalyst, [WWW Document], <http://www.icms.com.au/chemeca2009/abstract/63.asp>
- Saikat, M., Naveed, A.; Binay, K. D. and Farooq, A. (2010). Remediation of Sulfidic Wastewater by Catalytic Oxidation with Hydrogen Peroxide, [WWW Document] http://d.wanfangdata.com.cn/Periodical_jes-e200912017.aspx
- Standard Methods for the Examination of Water and Wastewater (1985). Publisher Public Health Association, USA, *16th edition*: 464-477.
- Sulfide Treatment (2010). [WWW Document], <http://www.westgeneral.com/outofthebox/compounds/s.html>
- UOP Sulfide Oxidation Process for Treating Spent Caustic (2010) [WWW Document], <http://www.uop.com/objects/5%20Sulfide%20Oxidation.pdf>
US Patent References. E-mail: info@uop.com.
- Vogel, A. I. (1972). A Text Book of Quantitative Inorganic Chemical Analysis, Longman, Inc., New York, *3rd edition* (1962), New Impression: 363-365.
- Wanner, M., Anderson, R. and Wilson, T. P. (2010). Reduction of Hydrogen Sulfide in Water Treatment Systems or Other Systems that Collect and Transmit Bi-Phasic Fluids, [WWW Document] <http://www.faqs.org/patents/app/20080197085>.
- Ueno, Y., Williams, A. & Murray, F. E. (1979). A New Method for Sodium Sulfide Removal from an Aqueous Solution and Application to Industrial Wastewater and Sludge, Water, Air and Soil Pollution, *V. II(4)*: 23-42,

FOREWORD

On behalf of the Libyan Petroleum Institute, I have the pleasure to introduce the 23d issue of the Petroleum Research Journal to the scientific community which had many interesting scientific papers. The publication of this Journal is intended to enhance existing knowledge and to promote available means of exchanging scientific information of interest on both national and international levels.

I would like to thank the members of the editorial committee for their successful efforts in getting this issue in the present form. I, also, take this opportunity to invite local and outside researchers to contribute in the development of this Journal. I hope they will find their contributions in future issues of this Journal encouraging and professionally rewarding.

Dr. Mansour Emtir
LPI, Chairman of Management Committee

EDITORIAL

Editors would like to express their thanks to all staff members of the Libyan Petroleum Institute for their unlimited support and encouragements.

Our thanks are also extended to all researchers who showed interesting to the P R Journal and contributed by sending their subjects idea for publications. The papers printed herein were edited but not reviewed and, therefore, the ideas expressed by authors are of course their own.

We shall not forget to express our gratitude and high appreciation to the managements of the Libyan Petroleum Institute (LPI) and National Oil Corporation (NOC) for giving permission and financial support to publish this volume.

Our goal is to continue stressing higher standards for P R Journal while improving upon both clarity of communication and timeliness of information.

The Editors

PETROLEUM RESEARCH JOURNAL

Editorial Policies

The Petroleum Research Journal (Petroleum Res. J.) is a multi-disciplinary scientific technical journal published periodically by the Libyan Petroleum Institute. The aim of the journal is to publish articles classified as original papers, short communications and reviews of both practical and theoretical interests, which deal with scientific and technical advances in the fields of geology, geophysics, geochemistry, chemistry, petroleum and chemical engineering. Subject matter should be relevant to hydrocarbon exploration, evaluation and industry. The opinions and views expressed by the authors in their contributions are solely their responsibility.

- Ideas of the preliminary results of investigation, that have not advanced yet to the point at which they warrant publication as a full paper, may be submitted for publication as short communications. Other types of contributions such as discussions, book reviews and conference reports may also be submitted.
- Manuscripts may be submitted in Arabic or in English. Manuscripts in Arabic require English abstract.
- Manuscripts are accepted with the understanding that they have not been published elsewhere, and are not currently under consideration by another journal nor will be submitted to another journal. Manuscripts accepted for publication are the copy right of the journal.
- Manuscripts are processed by the Editor-in-Chief. Three copies of each submitted manuscript are sent to the appropriate Associate Editor for technical review. The Associated Editor will seek evaluation from three reviewers

qualified to judge value of the paper, collect the reviews received, synthesize their contents and make a recommendation to the Editor-in-Chief concerning the acceptability of the manuscript. The final decision on a paper's disposition is then made by the Editorial Committee and communicated to the author(s) by the Editor-in-Chief.

- Twenty five free reprints of each published paper will be supplied to the author.

Instructions to Authors

Conformity to the following instructions is a prerequisite for consideration:

1. Manuscripts should be submitted with a letter stating (1) that the contents have not been published elsewhere; and (2) that the paper is not being submitted elsewhere.
2. Manuscripts should be submitted in electronic format in Microsoft Word (.doc) on CD-ROM, which must be checked with up-to-date virus scanner. Manuscripts may also be submitted via e-mail.
3. Alternatively, an original copy for each manuscript can be sent to the Editor-in-Chief of the Journal. However, the final revised version of the accepted manuscript must be submitted in electronic format as described above.
4. A title page should accompany the text, which includes: (a) paper title which should be informative and brief; (b) all authors' full names; (c) all affiliations clearly indicated; (d) key words (up to six) characterizing the subject material; and (e) the name, post and e-mail addresses, and telephone and FAX numbers of the corresponding author.

5. Computer illustration, including photographs (which must be kept to a minimum), charts and diagrams, must be submitted in high resolution format, and must be at least 300 dpi. Submit each illustration as separate file and indicate its location within the manuscript. Non-computer illustrations should be submitted in 21x28cm format. They should accompany the manuscript but should not be inserted in the text.

6. Illustrations are to be referred to as "Figures" and should be numbered consecutively in the order in which they are referred to in the text. They should be designed to go across a single or double column width of the journal page. Brief captions should be provided to make the figures as informative as possible.

7. All hand line drawings should be made with black drawing on white paper (preferably tracing paper). The authors' last name should be written in the margins (or on back) for identifications.

8. Non-computer photographs should be glossy prints. The authors last name and identification, as to which is the top of the photo, is to be written in pencil on the back.

9. A list of figures and table captions are to be typed on a separate page and attached to the end of the manuscript. List the figure number in the form "Fig. 1".

10. In the manuscript, principal headings should be typed at the centre of the page in capital letters. Headings of the text, first lower rank should be typed in small letters (first letters of the headings and proper nouns are to be capitalized). The following text should begin on the next line. For headings of second lower rank, underline and place a dash after the headings, and follow with text on the same line.

11. All references should be grouped at the end of the paper, under the heading REFERENCES, either alphabetically or numbered in the order they appear in the text. For a given author referred to more than once, use chronological listings with a suffix (a, b, etc.) to distinguish references of the same year. In the list of references, the following order and punctuation should be observed:

For references to a paper from journals:

- author(s) name (last name first, initials),
- year of publication,

- title (capitalize first word):
- journal name (abbreviate conforming to world list of scientific periodicals), volume number should be in bold; journal name and/or book title in italics.
- Page number (followed by beginning and ending page numbers).

Example:

Lagha, S. (1997). Petrography of the Triassic Phosphorites in the Gharyan Area, N.W. Libya. *Petroleum Res. J.*, **9**, 45-50.

For reference books:

- author(s) name (as above).
- year of publication
- title (capitalize all words of the title).
- publisher (firm name).

Example:

Tucker, M.E. (1981). *Sedimentary Petrology: An Introduction*. Blackwell Scientific, 251 p.

For references to a paper within a book:

- author(s) name
- Year of publication,
- Title of paper/(followed by)
- Editor(s) name(s)
- Title (of book):
- Page range,
- Publisher.

Example:

El-Bakai, M.T. (1996). Diagenesis and diagenetic History of the Lidam Formation, N.W. Sirt Basin In: M.J. Salem, A.S. El-Hawat and A.M. Sbeta (eds.) *The Geology of Sirt Basin*, **I**, 83-97. Elsevier, Amsterdam.

12. All correspondence should be addressed to:

Editor-in-Chief

Petroleum Journal

Libyan Petroleum Institute P.O. Box: 6431

Tripoli

State of Libya

Tel: 4830022/27 – 4836821/24

Fax: (21) 4830031

e-mail address: m.elbakai@lpilibya.com

Web-site: www.lpilibya.com

ARCHITECTURE AND SEQUENCE STRATIGRAPHY OF LATE TRIASSIC FLUVIAL SYSTEM, ABU SHAYBAH FORMATION, NW LIBYA

G. Mayouf*

Abstract: The Abu Shaybah Formation (ASF) ranges in age from Carnian to Norian (Late Triassic), and is exposed from the foothill slopes of the Tarhuna-Gharyan scarp stretching west wards to Ar Rabitah and Al Khums to the eastward along the Jabal Nafusah. The Lower boundary is sharp and unconformable with the Al Aziziyah Formation, (marine deposits) and the upper is locally unconformable with the Abu Ghaylan Formation (marine deposits). Seven sections have been measured in the study area and the maximum thickness of Abu Shaybah Formation is about 254m was observed in the Wadi Ghan area. It consists of gravely sandstone, coarse sandstone, silty clay and mainly mudstone facies. Whereas, in Abu Ghaylan road section it is about 21m of mainly mudstone facies. Series of sandstone bodies, fining up ward cycles, from 8 to 12m thick of cycles in fluvial meandering and 20 to 25m thickness of fluvial braided cycles. Four main facies association can be characterized in ASF; Facies Association 1: Fluvial braided, channel deposits (CH). It exhibits extensive sandstone coarse to very coarse grained, pebbly scattered and characterised by graded trough cross stratification, up to 15m thick of channels with no clay content. Facies Association 2: Fluvial meandering, its sandstone is medium to coarse grained highly argillaceous, trough cross stratification point bar deposits overlain by 3 to 5m thick of shale (over bank and crevasse splay deposits), and isolated sand bodies lateral accretion. Facies Association 3: Flood plain and over bank sediments consist of red to green silty shale commonly mottled and content rootlet, upto 30m thick in Wadi Ghan section. Facies Association 4: It seems to be as marine transitional zone. These sediments of ASF deposited under two strongly controlled forces (climate and tectonic), with large subaerial accommodation space rather than increases in subsidence rate in the study area. Sequence stratigraphic theory can be applied to these continental deposits, by defining base level and accommodation space, within the context of genetically related, coherent depositional sequences. Amalgamated multi-storey sand bodies are typical of low stand conditions, isolated ribbon sand bodies typify transgressive conditions (subdivided into early and late stages), and isolated multi-lateral sand bodies characterize high stand conditions.

Keywords: Abu Shaybah Formation (ASF), Triassic, Fluvial deposits, Jabal Nafusah.

OUTLINE OF TRIASSIC RESEARCH

The Triassic in a worldwide stage has long been recognised as an important geological period due to the predominance of fluvial red beds and their potential to act as petroleum reservoirs and aquifers. Exploration in Libya has some what neglected the Triassic unlike neighboring North Africa countries (e.g. Algeria TAG-I). However, in recent years there has been going awareness of the important Triassic in the Ghadames Basin, and potential

findings in the Sirt and Al Kufrah basins. Much of the Triassic succession in Libya is only found in the subsurface and most previous knowledge is based on seismic and well logged sections. The Abu Shaybah Formation (ASF) of the Jabal Nafusah area produces one of the few well exposed sections of Late Triassic fluvial succession (Fig.1). This study will focus upon the architectural elemental analyses recognized and well defined geometries and bounding surfaces using the methodology of Miall (1996). Fluvial strata provides an objective method for determining the three dimensional geometry of ancient river systems (Allen, 1983; Hirst, 1991; Miall, 1993, 1994). There are, however, relatively few examples from detailed field observations of

*Libyan Petroleum Institute, Km7 Gergarish road, P.O.Box 6431, Tripoli, Libya E-mail: gmayouf@yahoo.com

the three-dimensional geometry of an entire braided to meandering fluvial system along the escarpment of Jabal Nafusah. The ASF offers ideal conditions for a detailed architectural study of a braided and meandering fluvial system. The excellent outcrops, the large size and well-established geology allows for detailed analysis of the architecture in the context of structural control and along-strike sediment supply variations. This study focuses on the Late Triassic sediments ASF which was deposited over Hercynian Orogeny in incised valley systems and filled by a thick sequence of stacked amalgamated fluvial channel sandstones, meandering and flood plain deposits. This incised valley was formed by both erosional and tectonic forces and changes lateral to evaporites of the Bir El Ghanam Formation (Late Triassic-Early Jurassic) in the west of Gharyan (Fig. 1). These sediments provide a good example for understanding controlled climatically dry, wet and humid seasonal variations during the deposition.

GEOLOGICAL SETTING

Northwestern part of Libya is comprised of two major physiographic units; the Jifarah Basin which is bounded to the north by the Mediterranean Sea and, the escarpment of Jabal Nafusah which forms a prominent escarpment bounding the plain to the south. In broad terms the plain is formed of Pleistocene and Holocene sands and gravels underlain by Miocene and Mesozoic rocks which are exposed in the escarpment (Anketell & Ghellali, 1991 and Fig. 1). Over 1.5km thickness of siliciclastic, carbonate and evaporites sequences are exposed along a 400km's long horseshoe shaped escarpment extending from the town of Al Khums, NW Libya westward to Gabes in Tunisia. Jabal Nafusah elevation ranges from few meters in the east to over 800m in the centre south of Gharyan and descends into 200m in Gabes. The escarpment is a retreating fault scarp, its shape and extension is controlled by the E-W trending Al-Aziziyah fault zone and the Jifarah Arch. The Abu Shaybah Formation (ASF) of Late Triassic (Carnian to Norian), forms the foothill slopes of the Tarhuna-Gharyan scarp stretching west wards to Ar Rabitah and Al Khums to the eastward along the Jabal Nafusah. The lower boundary is sharp and unconformable with the Al Aziziyah Formation, and the upper is locally unconformable with the Abu Ghaylan Formation. The maximum thickness

of Abu Shaybah Formation is about 254 m located in Wadi Ghan (Fig. 2).

SEDIMENTOLOGY

The sediments of the ASF are dominated by gravelly coarse-grained sandstones, medium to coarse grained sandstones, fine grained sandstones, siltstones and mudstone and some poorly developed palaeosols. For purpose of this study the sediments have been subdivided into different lithofacies and then later grouped to form architectural elements Table 1 and 2, (Allen, 1983; Miall, 1983, 1988). The data for this study were primarily collected by means of outcrop. Facies analysis performed in six main sections located within the confines of the ASF (Fig. 1). The results of this work, as well as the interpretation of the data, are illustrated in Tables 1 & 2. Previous research has interpreted the Abu Shaybah Formation as a fluvial system (Rubino *et al.*, 2002). However, even casual observation of the sections the fluvial system can be subdivided into braided and meandering stream deposits. Using lithofacies and facies associations this study documents the regional alluvial architecture of the ASF and relates it to the long-term discharge history occurs in the escarpment. The ASF was divided into nine lithofacies (Table 1) which were adapted from Miall (1978). The nine lithofacies were grouped into four facies associations. Each association is described and interpreted utilizing two and three dimensional architecture found in both vertical and lateral profiles. The studied sections show a dominantly clastic succession with lithologies ranging from claystone and shale to sandstones and conglomerate lag deposits. Numerous iron-rich palaeosols horizons occur and assist inter regional climate interpretations for the Triassic. The dominance of a particular lithofacies or group of lithofacies, in different parts of the formation allows the definition of four main facies associations, as outlined below (Table 1).

FACIES ASSOCIATION

Detailed analyses of the sedimentology (i.e. grain size, sedimentary structures body and trace fossils) have allowed four main facies association to be identified within the study area (Fig. 1). These were deposited within four main depositional environments; they are fluvial braided, fluvial meandering, flood plain and transitional marine.

Table 1. Facies associations for the Abu Shaybah Formation, (ASF). Facies code adapted from Mail (1978, 1985, and 1996).




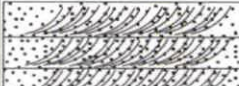
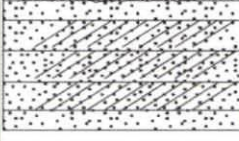
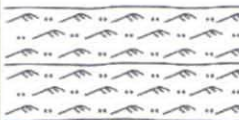

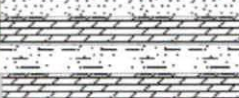
No.	Type of Facies	Description	Sedimentary structures	Interpretation	Thickness (m)
1	Facies 1a. Conglomerate channel (Gsh)	Horizontally cross stratification gravels, laterally, and mud intraclast up to .5cm in diameters, scour surfaces (Se).		Channel deposit (CH, Se)	0.1 - 2m
	Facies 1b. Planner cross strati. (Gsp)	Coarse to very coarse grained sandstone, normal graded planner cross stratification.		Channel deposit (CH, Se)	0.1 -1.5m
	Facies 1c. Trough cross strati. (Gst)	Coarse to very coarse grained sandstone, normal graded trough cross stratification.			
2	Facies 2a. Trough cross strati. (St)	Sandstone, medium to coarse grained, pebbly scattered, trough cross stratification (St).		Crevasse Spaly deposit	0.1 -0.5m
	Facies 2b. Planner cross strati. (Sp)	Sandstone, medium to coarse grained, pebbly scattered, planner cross stratification (Sp).		Point bar and/or channel deposit (SS)	0.1 -1.5m
	Facies 2c. Ripple cross strati. (Sr)	Sandstone, fine to medium grained, horizontal cross stratification, and current ripples.		Point bar and/or channel deposit (SS).	0.1 -1.5m
3	Facies 3a. Siltstone - mudstone (SI)	Clay to silt in size, and sand scattered. Stratification .		Over bank and flood plain.	0.1 -25m
	Facies 3b. Mudstone (Fsc)				
4	Facies 4a. Wavy ripples (Sr)	Sandstone, very fine grained intercalation with clay and dolomite beds, wavy ripples abundant by H. Burrows		Transitional zone	20m

Table 2. Summary of facies association and main characterization of each lithofacies in Abu Shaybah Formation (ASF), Wadi Ghan section.

No	Intervals	Lithofacies code	Lithofacies description	Grain size	Thick.
5	(154.5 - 221.5m)	Sand sheet (SS), Over bank (OF) Se, St	Ss with clay intervals, -fining upward cycles, -coarsening in small scale moderately to good sorting, trough and planner Xstrata.	Clay, M-C Ss	Total thickness is 67m (clay thick about 45m, sandstone thickness about 22m)
4	(132.5 -154.5m)	Channel - fill complex (CH) Se, Gsp, Gst, St, Sr and Se	Ss, small and large scale of trough cross stratifications, climbing ripples, convolute structures and at the base of channel abundant clasts.	Gravel, Coarse Ss	Total thickness is 22m (Single channel 2 -2.5 m thick.) No clay in this interval
3	(52 - 132.5m)	Sand sheet (SS) Over bank (OF) Se, St, Sr	Ss with clay intervals, -fining upward cycles, -coarsening in small scale moderately to good sorting, trough and planner x.start. and overturned (convolute structure).	Clay, M-C Ss Clay- is reddish colour.	Total thickness is 78m (Single channel 0.5 -1.5 m thick.) Clay thick about 53.5m Sandstone thickness about 22.5m Mix clay inter sand about 2m
2	(34 - 52m)	Channel - fill complex (CH) Se, Gsp, Gst, St and Se	Ss, ferruginous, very poorly sorting, graded trough and planner x. strata., Clasts up 10-15cm in diameters at the base of channel	Gravel, C-VC Ss	Total thickness is 18m (Single channel 0.5 -2.5 m thick.) No clay in this interval.
1	(0 - 34m)	Flood plain Fl	Mudstone, vary coloured, calcareous.	Mud, vary coloured.	Total thickness is 34m

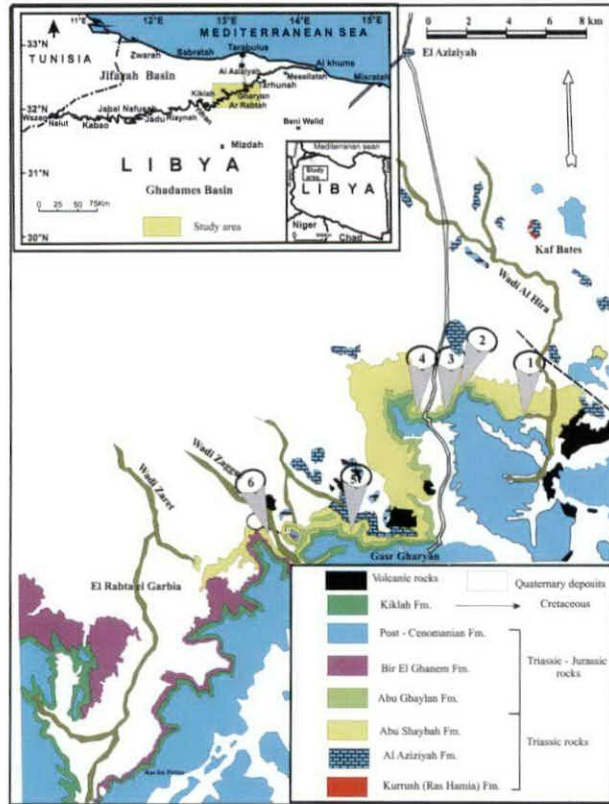


Fig. 1. Geological sketch of study area and location of measured sections, (1) Wadi Ghan section, (2, 3 and 4) Abu Ghaylan Road sections, (5) Gharyan dome section and (6) Abu Rashada road section (Modified from Desio *et al.*, 1963).

Facies Association 1: Fluvial braided (FB) (Fig. 2 & Fig. 3)

This facies association comprises sandstone, coarse grained and gravel or conglomerate facies that were deposited within a fluvial braided system.

The facies is formed from approximately 70% sandstone, 30% conglomerate.

Facies 1a. Conglomerate channel (Gh).

Description: This facies is interbedded with lithofacies 1b and 1c and represents less than 30% of thickness (about 3m thick and limited in lateral extension about 25m). This facies is predominantly composed of coarse to very coarse grained sandstone, cross bedded, as single sets, or more often in multi-storey associations (Figs. 3A-F). Multi-storey, cross-bedded, sandstones of lithofacies are often continuous for several hundred meters. However, some examples are laterally truncated or grade into other facies over distances of a few tens of meters. Sharp boundaries between individual cross bed sets and cosets are often marked by thin but persistent siltstone partings (Fig. 3D). Facies 1a, typically grades laterally and vertically into smaller-scale bed packages of facies 1b or 1c and rare siltstone and mudstone found as mud matrix in this facies. Trough cross bed sets is generally 0.3-0.5m thick (rarely up to 1 m) but multi-storey suites reach up to 10m in thickness. Set widths are upto 5m. Grain size are generally bimodal within this facies although a pebble layer is sometimes present at the base of cross-bed sets and a slight reduction in grain size to medium-grained sandstone normal graded cross stratification. Also containing intraclast at the base upto 10-20cm in diameters, are relatively common near the base of multi-storey size, decreases upwards within up section in diameter. Soft-sediment deformation is common in the form of large-scale convoluted bedding (Fig. 3C).

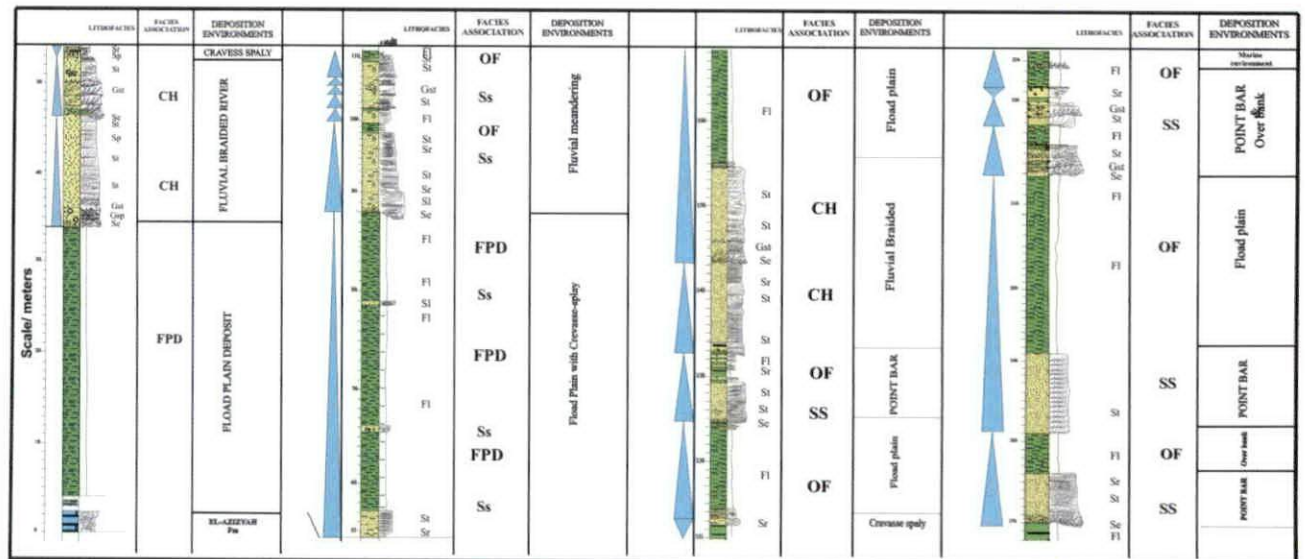


Fig. 2. Detailed logged of Abu Shaybah Formation (ASF) using architectural elements in fluvial systems.

Interpretation: Facies 1a is essentially identical to the massive to horizontal cross stratification, trough and planner cross sets of Miall (1977, 1996) although bedforms reach slightly greater dimensions in the ASF in individual cross bed sets may occasionally reach 1m thick and cosets may reach thicknesses of up to 10m. The predominance of gravel and trough cross bedding in facies 1a suggests deposition within major channels as large migrating dunes (megaripples of Singh & Kumar, 1974). The small size of extraformational clasts and relative frequency of siltstone intraclast above scour surfaces suggests that deposition occurred at a considerable distance from the chief sediment source area. These sediments have been largely reworked from older, mature, sandstone-dominated sedimentary sequences. Paleocurrent for facies 1a chiefly reflects east-west directed sediments transport of fluvial braided unit 1.

Facies 1b. Planner cross stratification gravel-sandstone, (Gp).

Description: This facies consists of coarse to very coarse pebbly and scattered grained sandstone.

Planner (Gp) cross-bed sets are generally 0.5-1.5m thick but multi-storey suites reach 10-13m in thickness. Set widths are up to 20m. Grain sizes are generally relatively uniform within this facies although a pebble scattered from quartz grains, white colour, silica, carbonate and ferruginous cemented. (Figs. 3E & F). These sets occasionally occur in multi-story packages up to 3m thick. Sp facies suites are sheet-like, ribbon-like or broadly lenticular and extend laterally for several tens of meters. They lens out laterally or are truncated by low-angle erosion surfaces into wedge-shaped terminations. This facies Gp packages generally rest sharply on other association sandstone facies. Paleocurrent orientations commonly show the flow toward the west direction of cross stratification measurements' Sr, St and Sp (Fig. 4).

Interpretation: Facies 1b corresponds to Miall's (1977) planner cross-bedded sands facies (Facies Sp) and Rust's (1978) low-angle cross-stratified sand facies (facies Sl). Medium to large scale bedforms producing planner cross bedding in modern sandy braided rivers include both linguoide and straight-crested transverse bars



Fig. 4 Graphic logs of the Fluvial meandering, and flood plain deposits in Abu Shaybah Formation (Localities 2, 3 and 4 in Fig. 1).

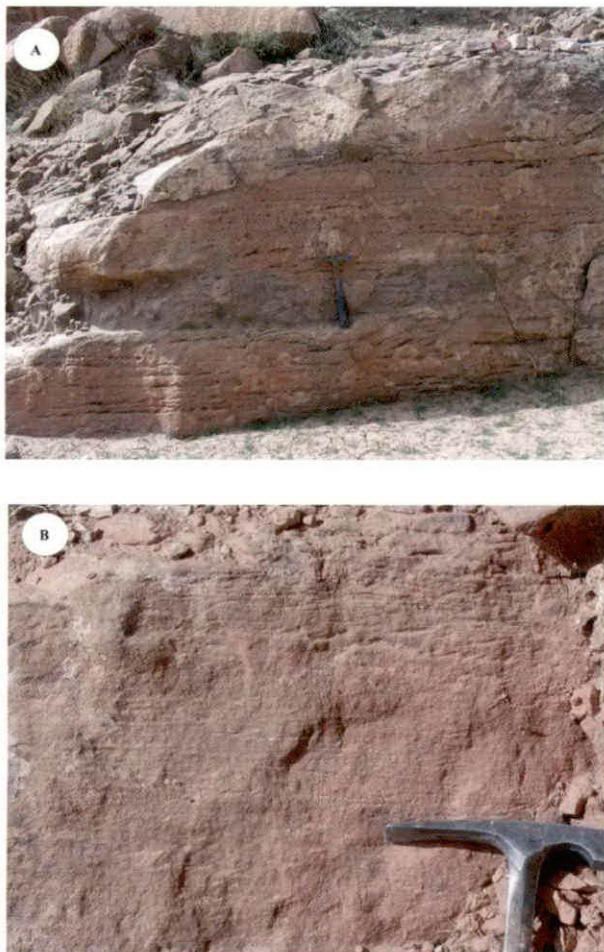


Fig. 5. Facies association 1: fluvial meandering (FM), Photo (A) climbing and photo (B) current ripples in Facies 2c .

(Smith, 1971, 1972). Low angle cross beds may represent deposition under high energy conditions or in special channel location such as the base of longitudinal bars at the intersections of channels.

Facies 1c. Trough crosses stratification gravel-sandstone (Gt).

Description: This facies consists of mostly coarse to very coarse-grained, cross bedded, sandstone and granulestone as single sets, or more often in multi-storey associations. Trough cross bed sets is generally 0.3-0.5m thick rarely up to 1.2m, but multi-storey suites reach 2m in thickness. Set widths are up to 200m. Grain sizes are generally relatively uniform within this facies although a pebble layer is sometimes present at the base of cross-bed sets. Slight reduction in grain size to medium-grained sandstone is sometimes evident at siltstone intraclasts, up to 10-15cm in diameter, are relatively common at the base of multi-storey sandstones suites. Soft sediment deformation is present in the

form of large scale convoluted bedding. (Figs. 3 A & C)

Interpretation Facies 1c is essentially identical to the trough cross-bedded sand facies (Facies St) of Miall (1977) although bedforms reach slightly greater dimensions in the ASF (individual cross bed sets may occasionally reach 1.5m thick and cosets may reach thicknesses of up to 5m. The predominance of festoon trough cross bedding in (CH) Facies suggests deposition within major channels as a large migrating dunes (megaripples of Singh & Kumar, 1974). The scarcity and small size of extraformational clasts and relative frequency of siltstone intraclasts above scour surfaces suggest that deposition occurred at a considerable distance from the chief sediment source area or that the sediments have been largely reworked from older, mature, sandstone dominated sedimentary sequences.

Facies Association 2: Fluvial Meandering (FM) Facies 2a. Trough cross stratification sandstone (St) (Fig. 4)

Description: This facies comprises troughs (St) developed by the migration of 3-D dunes, its content medium to coarse grained sand. Pebbles present in this lithofacies (St), clean quartzitic, well sorted sand and there is commonly a lag of poorly sorted sand with large intraclast at the base of the trough cross stratification consists of curved sets. This channel ranges between 1.5-2m in thickness and extended several ten meters laterally and the paleocurrent direction related to cross bedding is to north.

Interpretation: Facies 2a (St) is troughs developed by the migration of 3-D dunes (Miall 1977, 1996). Bedforms reach slightly greater dimension in the ASF (individual cross bed sets may occasionally reach 1.5m thick and cosets may reach thicknesses of up to 3m in small scale). The predominance of festoon trough cross-bedding in Facies 2a suggests deposition within major channels as large migrating dunes (megaripples of Singh & Kumar, 1974).

Facies 2b. Planner cross stratification sandstone (Sp).

Description: This facies consists of mostly coarse to very coarse-grained, cross bedded, sandstone and granulestone as single sets, or more often in multi-storey associations. Trough cross bed sets is generally 0.3-0.5m thick rarely up to 1.2m, but multi-storey suites reach 2m in thickness. Set widths

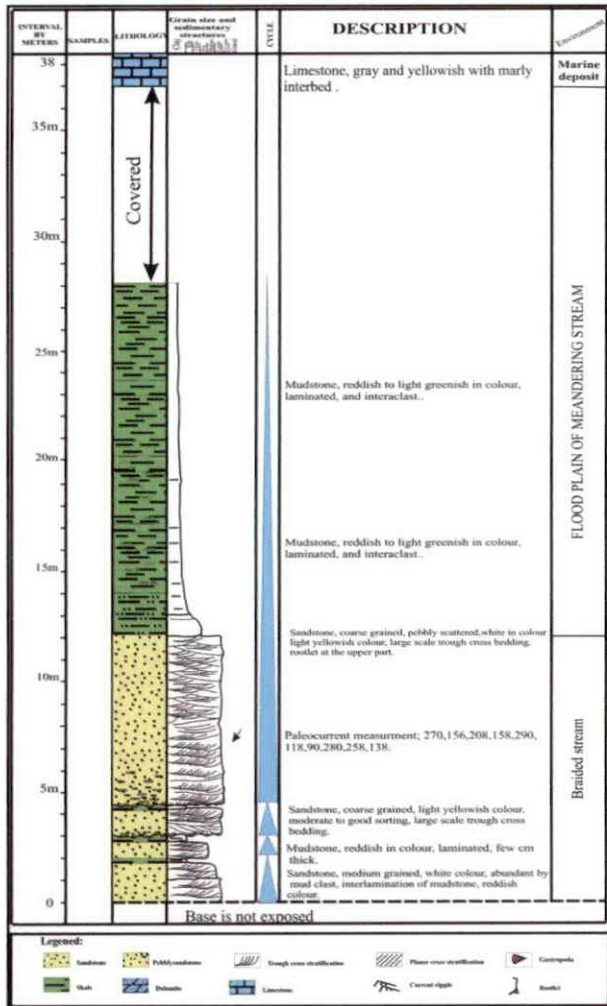


Fig. 6 Outcrop logged section of floodplain facies (FP).

are up to 200m. Grain sizes are generally relatively uniform within this facies although a pebble layer is sometimes present at the base of cross-bed sets. Slight reduction (In grain size to medium-grained sandstone) is sometimes evident at siltstone intraclast, up to 10-15cm in diameter, are relatively common at the base of multi-storey sandstones suites. Soft sediment deformation is present in the form of large scale convoluted bedding.

Interpretation: This facies was formed by the migration of 2-D dunes (Miall, 1996). Sand was transported up the flank of the bedforms by traction and intermittent suspension (commonly forming a carpet of small-scale current ripples), and deposited at the crest, where bed-shear stress drops at the point of flow separation. Cross bedding's angle of this facies is typically 25°-30° (Fig. 3F), with sharp, angular, upper and lower bounding surfaces. They are typically flat, with little evidence of scour surfaces. Sand in this facies is typically sorted by

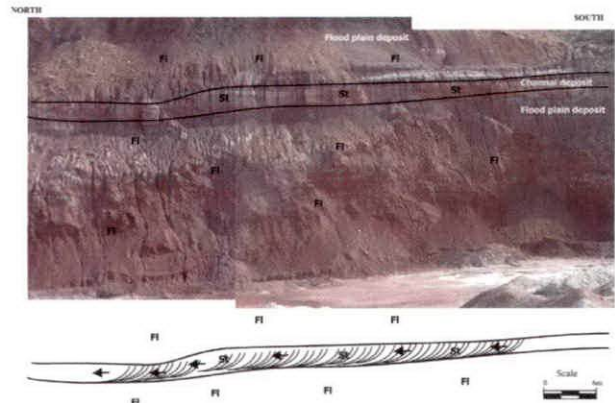


Fig. 7 Facies association 3; Flood plain (FP), facies 3b

the process of ripple migration up the stoss side of the dune, resulting in foresets in which the modal sand grain size may differ by several size classes (Miall, 1996).

Facies 2c. Ripple cross stratification (Sr).

Description: This facies is composed of fine to medium grained sandstones, trough cross bedded and large scale, climbing ripple (Fig. 5), cross laminated sandstones in multi-storey. Individual cross-bed sets and cross laminated beds is typically 5-20cm thick and generally is about 1.5m thickness (Fig. 5). A wide variety of internal structures may be generated from ripple migration, depending on flow velocity and the rate of sediment supply (Jopling and Walker 1968; Allen 1984).

Interpretation: Ripples developed at low flow speeds (< 1 m / s), and are very sensitive to changes in flow conditions (Miall 1996).

Facies Association 3: Flood plain deposit (FP)

Facies Association 3 sediments are composed of stacked fining up cycles of clean sand, friable, trough cross bedded sandstones grading into variegated claystone and siltstones representing meandering stream deposits. These grade from the lower sets of medium to coarse grained sandstones highly cross planar and trough stratification (Sp & St) deposited by a braided stream (Fig. 6).

Facies 3a. Siltstone-mudstone-Fine grain facies, (SI)

Description: This facies consists of thin to moderately 30-50cm thickness of claystone interbedded with fine to medium grained sandstones, reddish to yellowish in colour, massive and laminated and ripples, mud intraclast, calcareous silt and mud. Vertical and horizontal bioturbation are common in

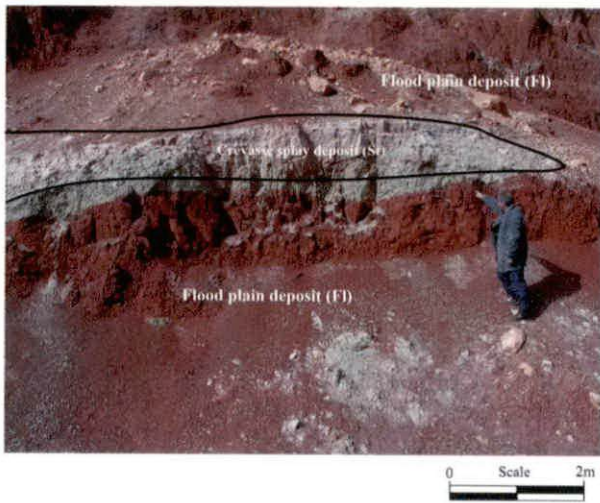
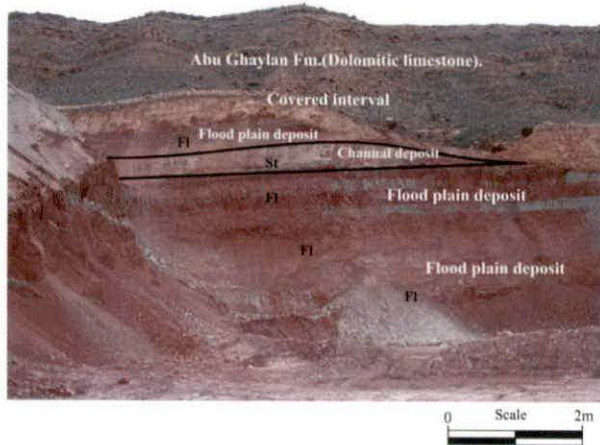


Fig. 8 Facies association 3: Flood plain (FP), facies 3A General view, 3B Close view of Crevasse splay.

this facies (facies Fm and Fl) of Miall (1977) and Rust (1978). They differ from each other in their content of carbonaceous material (Figs. 7 & 8). **Interpretation:** This facies is interpreted as crevasse splay deposits occur throughout sequence of ASF at Wadi Ghan section, and are interpreted to have been deposited in lobes adjacent to channel bodies. They are typically well sorted, fine to very fine grain laminated sandstones. These are locally rich in claystone and bioturbation. Sandstones display ripples cross laminations and syn-sedimentary deformation. Crevasse splay deposits typically range in thickness from 0.2m to 1m.

Facies 3b. Mudstone facies (Fsc) (Fig. 7 & Fig. 8)

Description: This facies (Fsc) consists of massive, reddish mudstone up to 10m thickness and up to 200m extended in Wadi Ghan section (Figs. 7 & 8). That was the main features of this facies which distinguishes it from Fl,

Interpretation: This facies is interpreted as floodplain deposit somewhat more distal relative to clastic sources such as nearby fluvial channels.

Facies Association 4: Transitional zone (marine to continental)

This facies is located in Abu Rashada road in the west of Gharyan Dome (Fig. 1). It exhibits interlayer's dolomitic limestone and fine sandstone with claystone common horizontal burrow (Upper Al Aziziyah Formation and base of ASF) about 21m thick (Fig. 9).

Facies 4a. Wavy ripples (Sr) (Fig. 3.10)

Description: This facies consists of interlaminations of mud, silt, and very fine grained sand. The thickness of particular sharp-based bodies varies from 0.1m to more than 1m. They pass upward into fine grained, wavy ripple bedded sandstone, and interlaminated by dolomite (Fig. 10).

Interpretation: Sediments of this facies were deposited mainly as fine grained, intercalation clay with silt, horizontal burrows and wavy ripples. The most probably represent a transitional zone from marine to continental.

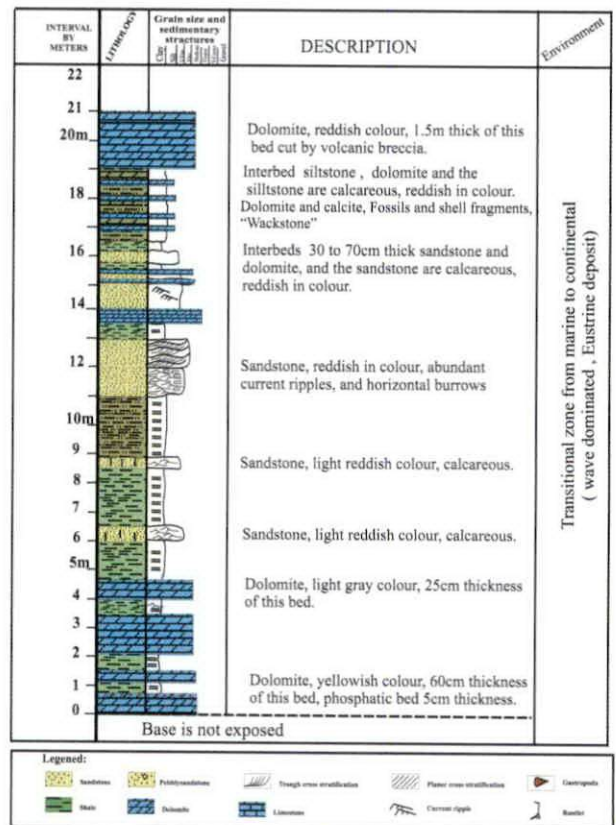


Fig. 9 Logging of Abu Rashada section showing the transitional zone.

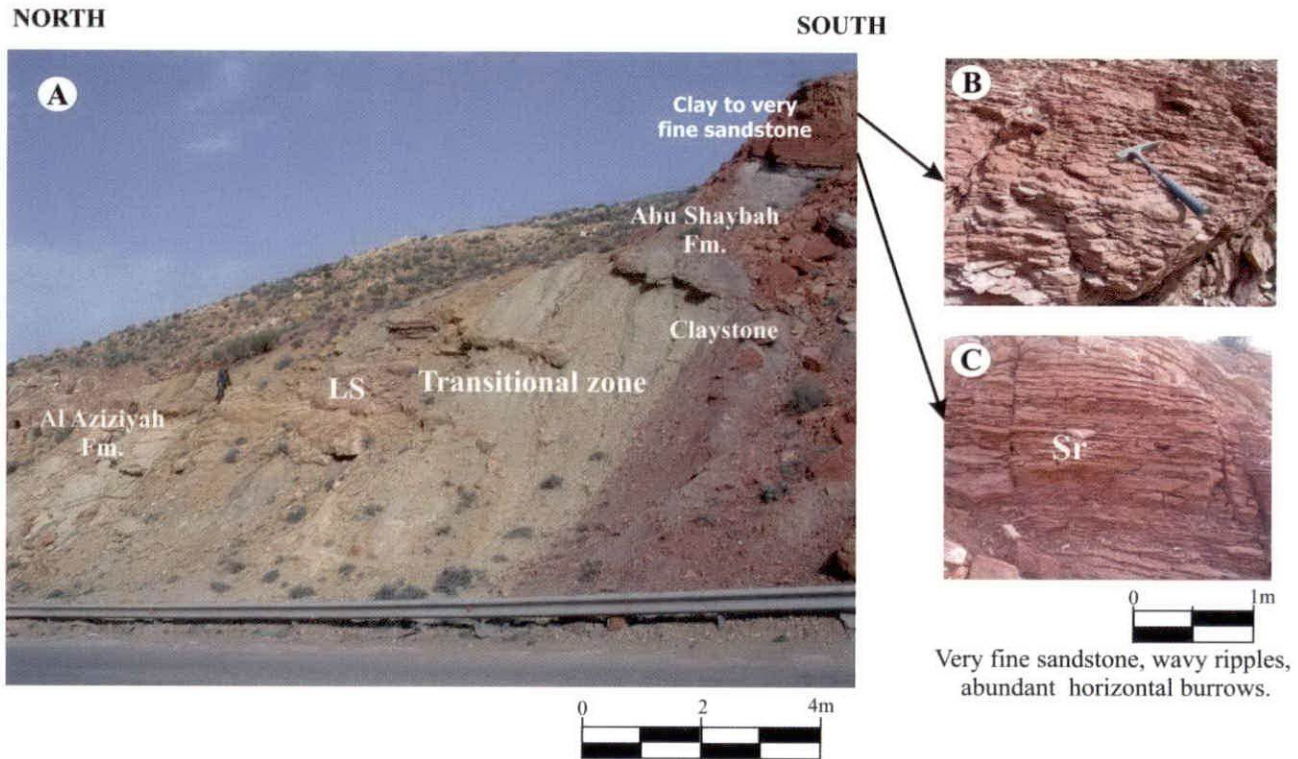


Fig. 10 Facies association 4: (A) Showing transitional marine top of Al Aziziyah and base of Abu Shaybah Formations. light greenish to reddish colour mudstone, (B and C) wavy ripples.

FACIES MODEL OF THE DEPOSITINAL SYSTEM

Wadi Ghan zone area is one of the most spectacular in the region, largely since many of its component faults crop out in the Jabal around Wadi Ghan. The component faults display two dominant trends, NW-SE and WNW-ESE and commonly about against each other to produce a rhomboidal to anastomosing framework NE-SW faults. This zone is approximately 25km wide and can be followed from the southeast, where it appears from under a cover of Tertiary lava flows, for a distance of 50km to northwest towards Al-Aziziyah south of merges with Al Aziziyah Fault zone (Anketell & Ghellali, 1991 and Anketell, 1996). In this region, several major NW trending faults of the Wadi Ghan zone about one against the other, defining a highly characteristic rhomboid pattern. Fig. 11 illustrates the importance for not only analysing the vertical succession, but also the lateral extent of the individual architectural elements. Deposition occurred in a range of fluvial subenvironments. The basal facies is conglomerate, gravely sandstone (Facies 1a-1c) were deposited in fluvial braided system that changed vertically and laterally to facies from massive to horizontal cross

stratification (Facies 1a) and associated channelized conglomerate (Facies 1b and 1c) occurred in a fluvial braided, abundant gravely and normal trough and planar cross bedding interpreted as major channels with large migration dune. Depositional of facies association 2a-2c are characterised by broad channel complexes, sand sheets and numerous mid-channel bars with accretionary fore sets (Fig. 11). The increases in grain size, deeper channels and number of macro forms in this middle and upper part profile suggest that the fluvial system had a greater stream power and an increased sediment supply. Trough and small scale planar cross bedding is interpreted as dune fields migrating downstream, which are commonly overlain by clearly defined laterally extensive sheet sands. The large-scale lateral and downstream accretionary foresets are the result of marginal and mid-channel bars. The overbank fine grained sandstones and siltstones are interpreted as having been deposited during flood stages and the immediate following waning stage, for each of the facies association units. Depositional of facies association 3 are characterised by mudstone and siltstone deposited in flood plain. This facies is important in subsurface reservoirs for correlation of well logs.

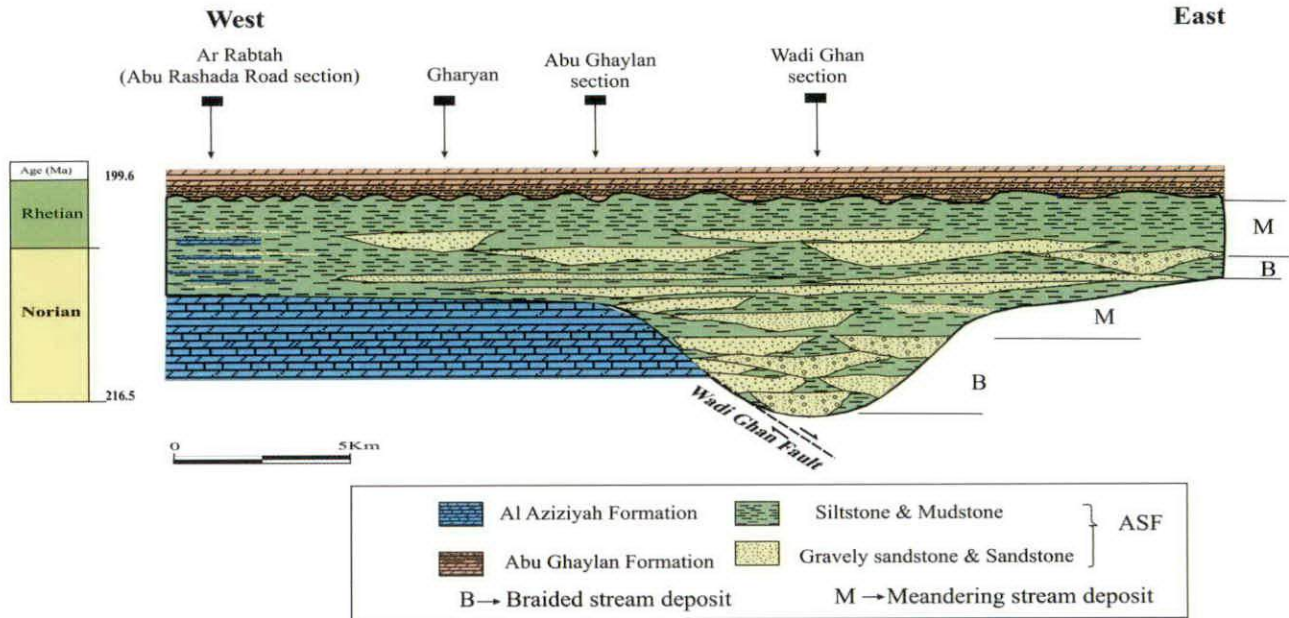


Fig. 11 Depositional model lateral and vertical variation of ASF along Jabal Nafusah, NW Libya.

Four phases interpretation of Early–Late Triassic (249.7 -199.6 Ma)

The boundary between Al Aziziyah Limestone (shallow marine) to continental of Abu Shaybah is unconformity and characterised by deep fluvial erosion, with the development of an incised valley system (Rubino *et al.*, 2002). The upper Al Aziziyah Formation in Wadi Ghan section consists of several meters thick shallowing-upward cycles showing storm and wave dominated features.

First stage, Early Triassic-Middle Triassic (Marine to Non Marine). The first stage of deposition of ASF in Wadi Ghan section in incised valley began after end of marine sequence or surface erosion top of Al Aziziyah Formation, Late Triassic (Carnian 228 -216.5 Ma). The lithostratigraphic formation boundary between the Al Aziziyah and Abu Shaybah formations is marked by a major unconformity and hence it is also a chronostratigraphic boundary. This simplify the communication, although it must be kept in mind that formations are rock units and are normally time-transgressive. The fluvial braided consists of conglomerate sandstone and scattered intraclast at the base of trough and planner cross bedding.

Second stage, Middle-Late Triassic (from braided to meandering system). The second stage started by deposition of the extensive sheets of sandstone complex channel of braided river (CH) (facies association 1a, b and c) in the incised valley. This channel showed that braided system deposits consist

of blocky sand units made up of superimposed 1 to 10m thick megariipples deposited by low stand system tract. It changes gradually to meandering system defined by thinning and decreases in grain size and climbing ripples (Facies association 2a, b and c). The channels in this system are clear lateral accretion by trough and planner cross stratification (St, Sp and Sr), intercalation by 0.5-5m thickness of mudstone and siltstone (Floodplain and crevasse splay deposits) facies association 3. This phase is braided river sit on major unconformity and characterized by fluvial erosion, with the development of an incised valley fill system.

Third stage, Middle-Late Triassic (from meandering to braided system). A change from meandering to braided river patterns can be triggered by a number of causes. At a given discharge, braided channels occur on steeper slopes than do meandering channels. On the basis of this relation, a change from meandering to braided morphology can be inferred to reflect an increased channel slope and increases in clastic sediments sandstone body as thick channels of trough cross stratification 3-5m. The vertical evolution of the fluvial system in a single sequence records a strong decreases of the slope angle of the fluvial profile. The sequence is though to record the composite effected by tectonic and climate.

Fourth stage, Late Triassic–Early Jurassic (Continental to marine). This stage is transitional phase from continental (meandering stream deposits)

to marine deposits of Abu Ghaylan Formation, 20cm thickness of limestone with algal mat at the contact of Wadi Ghan section and abundant marine fauna, and contorted interbeds of carbonate and marl. Ripple marks, mud cracks, solution collapse breccias and tepee structures are also observed. The contorted bedding has been related to syn-sedimentary tectonic influences (Hammuda *et al.*, 2000).

SEQUENCE ARCHITECTURE AND STREAM EQUILIBRIUM PROFILE FLUCTUATION IN THE ASF

Figures 12 and 13 show alluvial extensive unconformity surfaces, and their correlative conformities. Deposition of the alluvial suite commences with amalgamation of channel sand bodies due to a lack of accommodation space causing local lateral migration or avulsion of the channel units, floodplain reworking, abandonment and preservation of channel sands before lateral avulsion or migration of the channel system re-

occurs. Sequence boundaries in the non-marine realm are caused by a lowering of the alluvial systems Stream Equilibrium Profile (SEP) with respect to the actual stream profile. The extent to which the SEP is lowered relative to the actual stream profile, and the lag time until a response occurs governs whether a confined or unconfined sequence will develop. As in coastal and marine sequence stratigraphic, two types of sequence boundary can be differentiated (Fig. 14). The “confined amalgamated channel unit” is the geomorphologic equivalent of the incised valley system and Type I sequence boundary of Van Wagoner *et al.*, (1988). The “unconfined amalgamated channel unit” is the geomorphologic equivalent of the Type II sequence boundary. The terms Type I and type II sequence boundaries are not used here in this model of continental sequence stratigraphy as they imply a dominant relative sea-level control on the depositional system. Similar types of strata bounding surfaces occur within sequences in hinterland regions (Mitchum, 1977). Confined continental sequences are bounded below by an erosional valley surface (caused by SEP Low) and above by a confined

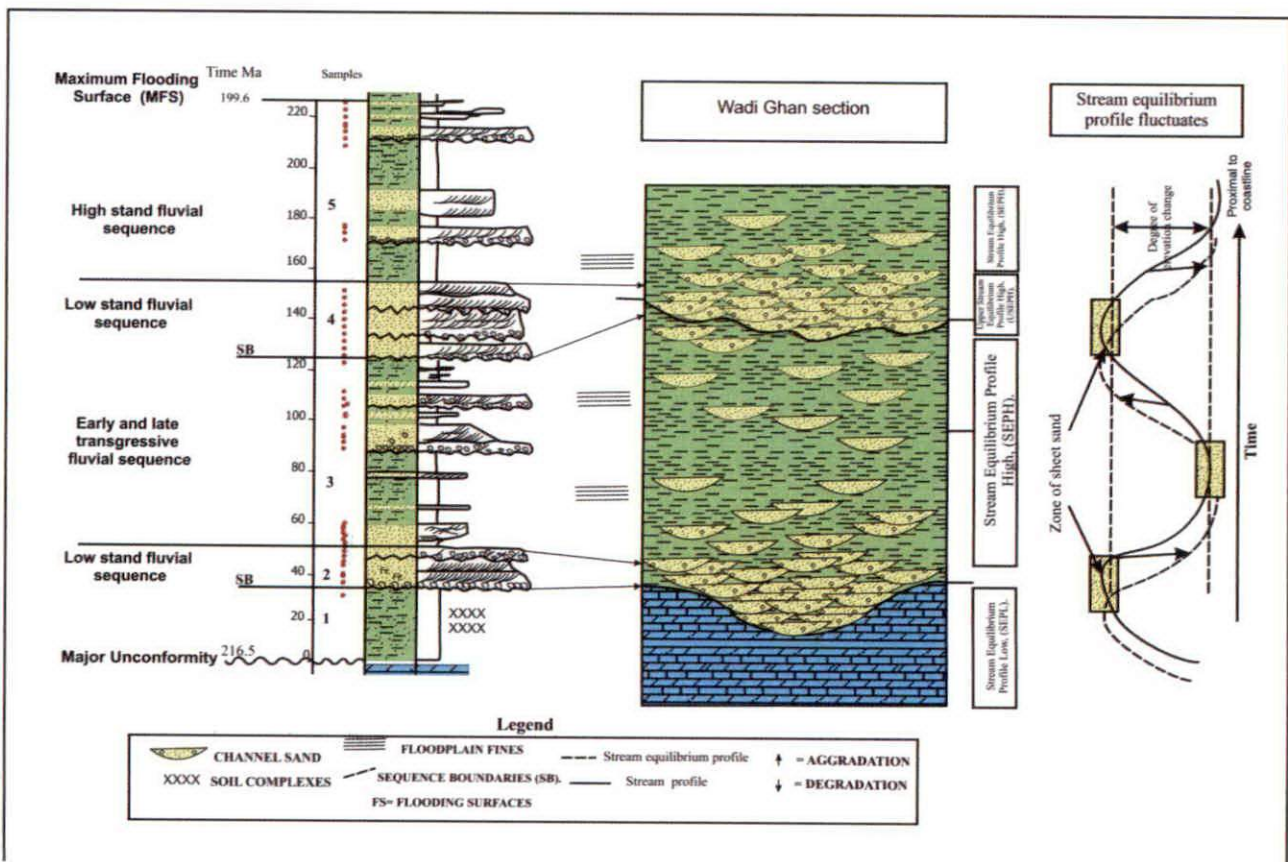


Fig. 12. Illustration of gross sequence architecture and continental systems tracts of Abu Shaybah Formation, (ASF) in Wadi Ghan section, which develop with stream equilibrium profile elevation fluctuation, resulting from alteration of allocyclic controlling mechanisms.

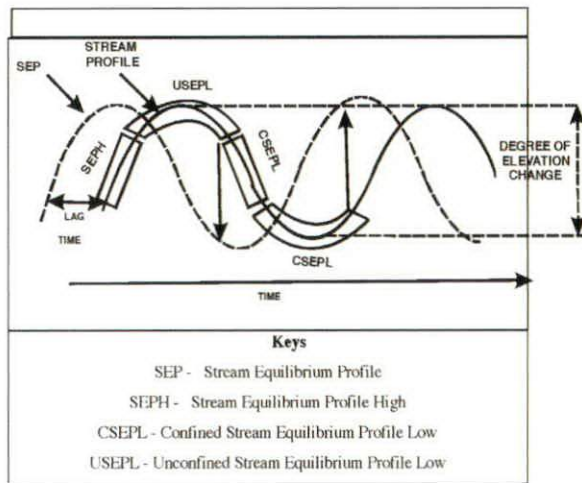


Fig. 13 Continental system tracts and their time of elevation with respect of fluctuation of The stream profile and the stream equilibrium profile.

or unconfined sequence boundary. Unconfined continental sequences are bounded below by an erosional surface (again caused by SEP Low) which follows the bases of the lowermost erosive channel sand units which constitute the amalgamated channel sand sheet resulting from a stream equilibrium profile relative lowstand. An unconfined sequence is bounded above by either a confined or unconfined continental sequence boundary. Unless a confining incised valley can be demonstrated, amalgamated channel sands should be described as being unconfined, SEP Lows can occur without the development of incised valleys. Wright and Marriott (1993) and Shanley and McCabe (1991, 1994) have subdivided continental sequences into lowstand (LST), transgressive (TST), and highstand (HST) systems tract to temporally equate environments. However, use of terminology such as transgressive systems tract in environments where influence of relative transgression on the coastal plain

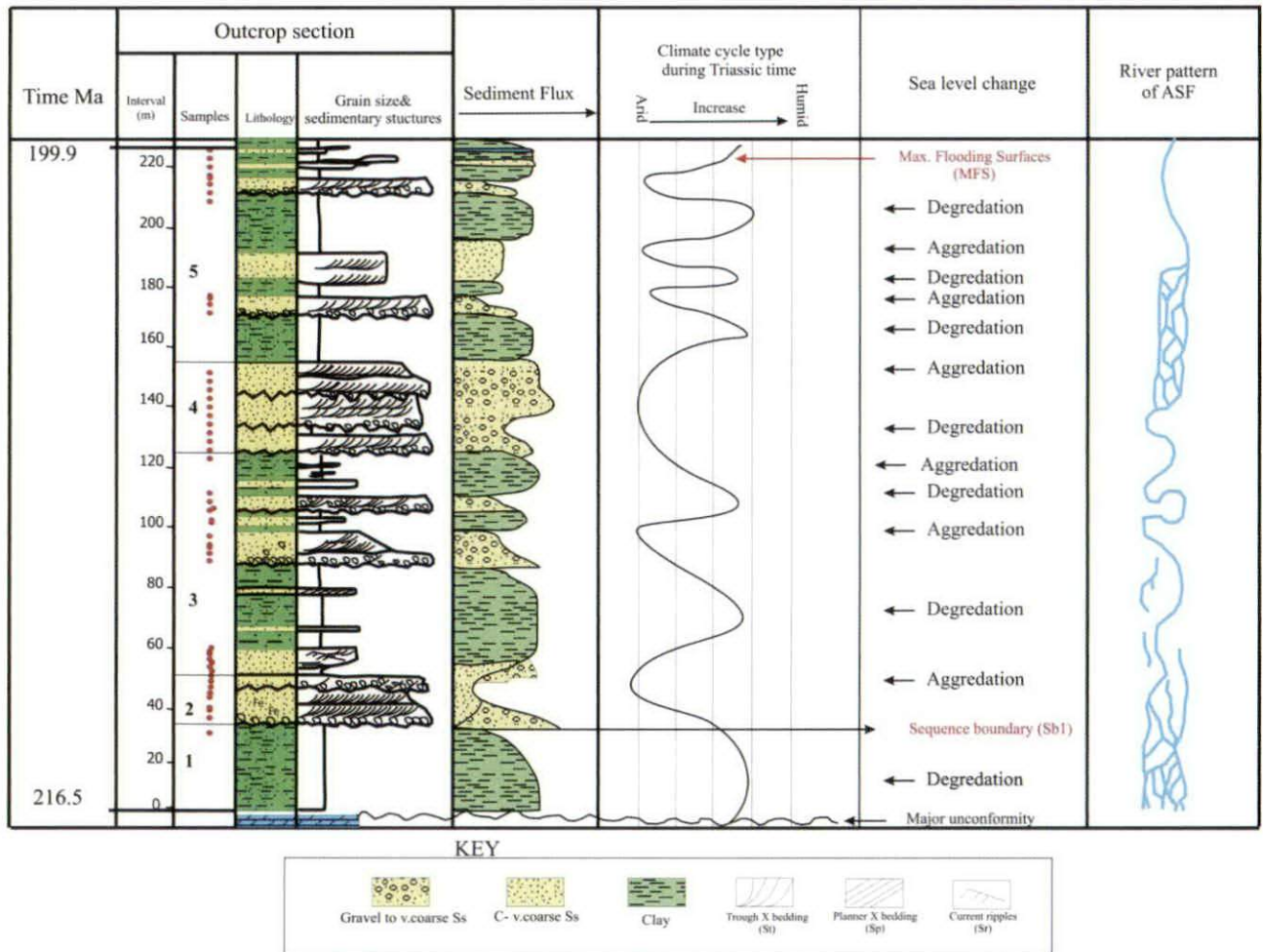


Fig. 14 Relationship between climatically mediated stream discharge and sediment flux under a range of climatic regime during Late Triassic for the Wadi Ghan section, NW Libya (concept adapted from Demko *et al.*, 2002; Meadows, 2006).

has a low probability of being physically expressed further upstream. (i.e., over most of the alluvial plain), can create confusion in correlation of strata surfaces (e.g., the coastal type I; Van Wagoner *et al*, 1988) and regional erosional surfaces that develop entirely within the subaerial realm. Due to the differing importances of allocyclic controls in different reaches of the fluvial system, a sequence boundary developed as a result of a relative sea level fall at the coast. However, the two different sequence boundaries may tie together at some point in the subaerial depositional basin, even though they are not chronostratigraphically equivalent. Figure 14 illustrates the continental phases of deposition and erosion which generate the subaerial equivalent of systems tracts, developing as a result of fluctuation of the stream equilibrium profile. The amalgamated channel sands within an incised valley constitute the initial deposits of the Confined Stream Equilibrium Profile Low (CSEPL) of Fig. 14. The fine grained sediments of this unit have poor preservation potential due to lateral switching of, reworking by, and preservation of channel sands. A CSEPL, essentially generates a continental sequence boundary, or incised valley surface. On the alluvial plain it is unlikely that this will be caused by a drop in relative sea level. Soil horizons may develop (Bown and Kraus, 1987; Wright and Marriott, 1993) on well drained river terraces produced by a low stand event, and these could represent some of the correlative conformities corresponding to the hiatal sequence boundary. The sediments of the CSEPL are comprised mainly of amalgamated channel sand bodies deposited within the confining incised valley system. These sandy units are frequently exploited for mineral and hydrocarbon resources. As aggradation continues, so the incised valley fills. As the stream equilibrium profile fluctuation cycle moves on into the Stream Equilibrium Profile High (SEPH) the rate of aggradation increases, causing channel sand bodies to become more isolated within better preserved fine grained sediments of the floodplain (Figs. 13 & 14). Very early and very late SEPH floodplain deposits, where rates of sedimentation (aggradation) are quite low, may be dominated by soil development. However, when aggradation rates increase, development of thick mature soil horizons will be inhibited, and floodplain fines will be preserved without significant pedification. Posamentier and Vail (1988a & b), Shanley and McCabe 1994 and the present conceptual model all suggest that alluvial flooding surfaces reflect rapidly aggradation. Alluvial flooding surfaces are regionally extensive

subaqueously deposited complexes of fine grained floodplain deposits, which exhibit a higher degree of preservation of original sedimentary structure (i.e., have a low degree of pedification). This contradicts the model of Wright and Marriott (1993, Figure 1) which suggests that amalgamated channel sheet sands are generated by a Stream Equilibrium Profile High. Unconfined Stream Equilibrium Profile Lows will develop upon lowering of the rate of aggradation after the relative SEPH, causing a higher degree of channel amalgamation and reworking of any floodplain fines or soil complexes that have developed. Given enough times a regionally extensive amalgamated channel sheet sand will develop due to low rates of elevation change. If the stream profile remains above the stream equilibrium profile then the system will continue to degrade, incising into its previous deposits, possibly generating the deposits of the Confined Stream Equilibrium Profile Low as previously discussed.

DISCUSSION

Climatic controls on fluvial sedimentation

Regional climatic variations arise as a function of plate positions and how they change through time. Climate directly controls aridity, humidity and rainfall patterns and as a direct result perhaps the fluvial environment is one of the most sensitive indicators of climate change in the rock record (Frostick & Jones 2002; Jones & Frostick 2008). Climate has a direct impact on erosion, drainage patterns and deposition within a sedimentary basin. Any changes in climate can have a marked and devastating change for the whole of a river system (Blum & Tornqvist 2000; Hartshorn *et al*, 2002). Studies of climate change controlling fluvial deposition in the Pre-Quaternary are rather sparse in the geological literature compared to the vast array of literature on sea-level and base level changes following the introduction of sequence stratigraphic concepts. However, by far the most widely used climate indicator are palaeosols in floodplain successions as outlined by several workers over recent years (e.g. Retallack, 2001; Kraus, 1999; Wright and Marriott, 1993). Instead, the discussion below focuses firstly on where workers have specifically interpreted depositional sequences in response to climate change and secondly how climate variations can be determined in the fluvial packages of the Late Triassic Abu Shaybah Formation (ASF) in this study. Many workers have inferred climate change through the use of a variety of proxies or transition from fluvial to other strata. These are highlighted

below: 1-Changing from braid plain environments then to a meandering stream dominated setting that pass laterally environments, were attributed to shifts towards from arid and then more humid conditions.

A number of studies also interpret transitions between fluvial and other strata due to climate changes over time (Cojan's 1993; Yang & Nio's, 1993; Olsen & Larsen, 1993; Clemmensen *et al*, 1994; Dubiel *et al*, 1996). 2-Different thickness of floodplain and channels, Olsen (1990, 1994) identified two scales of cyclicity in the thickness of channel sand bodies. 3-Different in sediment supply stages (aggradation and degradation), Smith (1994) suggested that changes in channel sandbody geometry, sand-to-mud ratios, sediment accumulation rates and types of palaeosols in Arizona (USA) occurred during a tectonically quiescent period and might instead reflect climate changes. 4-The relationship between stream discharge and sediment flux under a range of climate regimes (Lane 1955; Bull 1991; Demko *et al.*, 2002; Meadows 2006; Jones & Frostick, 2008), in which net fluvial aggradation or degradation is strongly influenced by the relationship between bedload and stream discharge. It is very easy in this study to ascribe the practise as outlined above in 1 to 3 as not only is the ASF located between two marine successions, but also the ASF changed gradually from a braided river as part of an incised valley fill to a meandering stream with isolated channel sandstones enclosed by siltstone and mudstone of floodplain deposits. Such a sequence is similar to that predicted by Shanley and McCabe (1994). It is obvious that climate has played a role in the behaviour of the ASF fluvial systems at a sequence scale, but more important is how climatic changes can be recognised at the outcrop and used in correlation of fluvial facies over 10's kms.

Meadows 2006; Demko *et al*, 2002 have modelled the effects of climatic change on patterns of fluvial discharge and sediment flux under a range of differing climatic regimes. In considering climate change, Demko *et al* (2002) looked at a range of climatic regimes from wet and tropical monsoonal climates through to dry seasonal and desert climates, the types of vegetation associated with these and the relative proportions of chemical and mechanical weathering. In doing so it was concluded that the greatest sediment flux is associated with wet and tropical monsoonal climates, but that the vast majority of this comprises clay-and silt grade material liberated through chemical weathering. With progressively drier climates the equilibrium sediment flux decreases but becomes increasingly dominated

by sand-and gravel-grade material liberated by mechanical erosion. If such a methodology is applied to the ASF then it can clearly be demonstrated that a cyclicity exists within the fluvial succession from being wet seasonal through dry seasonal to relatively dry and with an increasing proportion of sand grade material the finer-grained sediment becomes less abundant. The climate change model therefore provides a means by which the maximum sediment flux and the maximum stream discharge are not equilibrium. Rather, there are episodes during which the sediment flux increases dramatically, generating conditions favourable for rapid net deposition and aggradation, and episodes during which discharge increases without a concomitant increase in bedload (Fig. 15). At such times, the river would be likely to undergo net degradation, reworking previously deposited sediment and incising its floodplain. Demko *et al*, (2002) proposed an idealized strata architecture resulting from this imbalance that illustrates the effect of alternating phases dominated by degradation and then aggradation. Interestingly, this also generates incised valley systems filled with stacked amalgamated fluvial channel deposits (Facies association 1-braided stream) overlain by isolated fluvial channel sandstones enclosed within floodplain deposits (Facies association 2 & 3-meandering and flood plain). In this case, it can be inferred that incision occurs during the most pluvial part of the climatic cycle, that sediment flux and discharge become effectively balanced as the climate becomes arid and, presumably, during this phase the river remains trapped within the previously incised valley system. As the climate begins to become wetter, and stream discharge increases, the sediment pulse is released and the river aggrades rapidly, infilling the incised valley until it breaks out onto the wider floodplain. At this stage both the increase area of the floodplain and the declining sediment flux, especially the coarser-grained bedload component, increase the preservation potential of floodplain facies (Facies association 3) and therefore render it more likely to generate isolated channels encased within those deposits. The main climate control on drainage development is through discharge variability. It is to be expected that lithofacies heterogeneities will increase with increasing seasonal or long-term variability in discharge, and that the frequency of the minor bounding surface will increase (i.e. second and third order surfaces; Miall, 1996). The lithofacies and change in fluvial style in the ASF during Triassic undoubtedly can be explained by

changes in discharge sediment ratios (or sediment flux) and correspondingly discharge from waning flood events. The succession of facies described here is known to span the time of gradual continental break-up of Pangaea and a change from icehouse to greenhouse conditions with a trend towards more temperature-humid conditions. The gradual change in climate coincides with changes in character of the fluvial systems from dominantly alluvial fans and coarse-grained braided rivers to meandering streams. However, rivers react to a number of stimuli, and it is difficult to determine whether a given change in character reflects tectonic or climatic influences, or both (Frostick & Reid, 1989; Frostick & Jones, 2002). The evidence the ASF is affected by climate control is contained in the hot red beds are typical for semi arid regions and many form through the release of iron from mafic minerals during early burial and its precipitation around grains as a hydrated iron oxide, which ages to haematite (Tucker, 2001). The climate change model therefore provides a means by which the maximum sediment flux and the maximum stream discharge are not coincident. Rather, there are episodes during which the sediment flux increases dramatically, generating conditions favourable for rapid net deposition and aggradations, and episodes during which dis-degradation, increases without a concomitant increase in bedload. At such times, the river would be likely to undergo net degradation, reworking previously deposited sediment and incising its floodplain (Demko *et al.*, 2002; Meadows 2006). The architecture resulting from this imbalance that, illustrates the effect of alternating phases dominated by degradation and then aggradations. Interestingly, this also generates incised valley systems filled with stacked amalgamated fluvial channel deposits overlain by isolated fluvial channel sandstones enclosed within floodplain deposits Demko *et al.* (2002). In ASF section, it can be inferred that incision occurs during the most fluvial part of the climatic cycle, the sediment flux and discharge become effectively balanced as the climate becomes drier and, presumably, during this phase the river remains trapped within the previously incised valley system. As the climate begins to become humidity, and stream discharge increases, the sediment plus is released and the river aggrades rapidly, infilling the incised valley until it breaks out onto the wider floodplain. At this stage, both the increased area of the floodplain and the declining sediment flux. When interpreting fluvial successions climate alone cannot reliably be used due to the complex interactions and feedback

loops associated with tectonism (e.g. Frostick, 1993; Frostick & Jones 2002).

Tectonic control on fluvial successions

Background

Rivers are sensitive indicators of tectonic subsidence, uplift and tilting. In tectonically active areas, and especially during synrift phases of basin evolution, tectonics can be recognised as an important control on gradients, water supply, stream power, shear stress, long profiles, terrace patterns and channel sinuosity (e.g. Seeber & Gortniz, 1983; Ouchi, 1985; Rasanen *et al.*, 1987; Jones 2002; Frostick & Jones 2002). Frequently in the literature tectonics is ascribed as one of the main controls on fluvial architecture, geometry of channel sand bodies, spatial distribution of fluvial systems and direct control on sediment flux routing into sedimentary basins (e.g. Gawthorpe & Leeder, 2000). However, process-based models of alluvial stratigraphy have been developed that consider the effects of compaction, tectonic tilting of the floodplain and variation in the aggradation rate with distance from channel belt (Bridge & Leeder, 1979; Mackey & Bridge, 1995). Such predictive process-based models are widely used in understanding fluvial systems and routinely incorporated into reservoir models for petroleum exploration. Mackey and Bridge (1995, p. 28) identified that even with advances in the models several components are still lacking for a complete understanding of ancient fluvial behaviour (e.g. sediment flux, channel diversion occurrence, fluid flow, creation of levees, lakes and crevasse splays). There have been several attempts at developing physical based three-dimensional models of fluvial deposition (reviewed by Kolterman & Gorelick, 1996; North, 1996; Paola, 2000). However, none of these approaches has been able to successfully simulate three-dimensional fluvial architecture to a satisfactory level of detail.

The Jifarah Basin and the ASF

The Jifarah region has previously been discussed by Anketell & Ghellali 1991, but the importance of the tectonics of the region is further emphasised here. Uplift in the southern Jifarah region during the late Triassic accounts for the unconformity at the base of the Abu Shaybah Formation and the onset of continental conditions of sedimentation at this time. Both the NW-SE and E-W structural grains associated with the Caledonian and Hercynian structures in the

Jifarah basin are of importance in their influence on later structural events (Mikbel, 1977; Goudarzi, 1980; Anketell & Ghellali, 1991). Faults within the region display a characteristics *en echelon* arrangement that are interpreted in terms of long-lived reidel shears and imbricate fan splays related to strike-slip fault movements on deep seated basement fractures (Anketell & Ghellali, 1991).

Due to the tectonic activity of the research area and many of the outcrops located near important strike-slip faults along the Jabal Nafusah escarpment (e.g. Coastal zone, the Al Aziziyah zone in the west and central Jifarah, the Tiji zone in the foothills of the Jabal Nafusah and, the Nalut zone exposed at the top of the escarpment), it is tempting to speculate that the fluvial systems of the ASF were strongly controlled by tectonic activity and perhaps many of the coarse beds represent tectonically induced erosion and sediment flux from the hinterland catchments (e.g. Blair and McPherson 1994; Mack and Leeder, 1999; Viseras *et al*, 2003). However, from field observations and geological mapping it is evident that the Late Triassic fault activity is important in controlling the gross geometry of the fluvial succession and hence their drainage patterns for the ASF. Recent studies have highlighted the importance of tectonic grain and changes in fault orientations in controlling drainage patterns and hence outlet spacing into a depositional basin (e.g. Hovius, 1996; Jones, *et al*, 2001; Jones, 2004). Furthermore, the physiographic changes to the landscape, induced by fault activity are likely to have far-reaching implications on fluvial style and flow directions.

The incised valleys fills of ASF are most likely to have formed through a combination of both erosional and tectonic forces (e.g. Stanley, 1994). This is reflected in the basal erosional sequence boundary of the ASF (Fig. 13). The amalgamated fluvial deposits that are confined within the incised valley were further controlled by localized faulted margins. Through the Late Triassic (c. 15.9 Myrs) the fluvial systems changed character and became less influenced by tectonism reflecting fewer multistory/amalgamated fluvial deposits and more isolated channel networks. Any changes in the river behaviour can be attributed to regional gradient changes of the basin floor or minor diversion by reactivation of basement strike slip faults.

Although it has been widely recognised that fault movement, fault geometries and subsidence create a topography control fluvial patterns and deposition, it is climate that exerts a more discrete control

on sedimentation of fluvial sequences and their architecture. This is perhaps too easily overlooked in ancient basin settings, but as recognised in this study, climate is a more important control on fluvial sequences once a drainage pattern has been created. This study has demonstrated that although tectonism can induce and control fluvial system development, it is climate that exerts a strong influence upon the nature of the fluvial sequences and how they interrelate to associated facies and can be correlated. This is easily overlooked in the need to identify tectonic events and interpret ancient basin history. Furthermore it is parameters related to climate (e.g. rainfall, stream power) that need to be further understood in ancient successions to improve process based models of fluvial deposition.

CONCLUSION

Lateral and vertical variations in the facies architecture of the fluvial strata of the ASF along Jabal Nafusah, NW Libya can be explained by consideration of allocyclic controls on sedimentation. Tectonism in the source area was probably important in determining the timing and location of the alluvial wedge. Differential subsidence in the depositional basins influenced the location of braided rivers and determined the degree of interconnectedness of sandstone bodies. A gradual climatic change produced change in the style of rivers and the geometry of their resulting facies. Changes in stratigraphic base level resulted from shrinkage and expansion of lacustrine systems downstream from the study area. These changes in base level are interpreted to have caused variations in the rate of creation of accommodation which resulted in a sharp base to the formation and an upward change from thin, highly amalgamated, sheet sandstone bodies to thick, isolated, sheet sandstone bodies. The causes of the fluctuations in lake size are beyond the scope of this study, but it is possible that they were related to climatic shifts or, because of their position on a broad coastal plain, to changes in sea level in the seaway to the north. This study emphasizes the importance of taking a holistic approach to understanding controls on fluvial sedimentation. The role of both upstream and downstream controls on sedimentation needs to be considered in addition to subsidence and climate at the site of deposition. The climate change model therefore provides a means by which the maximum sediment flux and the maximum stream discharge are not coincident. Rather, there are episodes during which

the sediment flux increases dramatically, generating conditions favourable for rapid net deposition and aggradations, and episodes during which discharge increases without a concomitant increase in bedload. At such times, the river would be likely to undergo net degradation, reworking previously deposited sediment and incising its floodplain. Demko *et al* (2002) proposed an idealized strata architecture resulting from this imbalance that illustrates the effect of alternating phases dominated by degradation and than aggradations. Interestingly, this also generates incised valley systems filled with stacked amalgamated fluvial channel deposits overlain by isolated fluvial channel sandstones enclosed within floodplain deposits. In this case, it can be inferred that incision occurs during the most pluvial part of the climatic cycle, that sediment flux and discharge become effectively balanced as the climate becomes drier and, presumably, during this phase the river remains trapped within the previously incised valley system. As the climate begins to become wetter, and stream discharge increases, the sediment pulse is released and the river aggrades rapidly, infilling the incised valley until it breaks out onto the wider floodplain. At this stage, both the increased area of the floodplain and the declining sediment flux, especially the coarse grained bedload component, increase the preservation potential of floodplain facies (sandflats in the case of the ASF) and therefore render it more likely to generate isolated channels encased within those deposits. Several important conclusions can be drawn from the architectural study of the ASF that has implications for the development of drainage networks in the Jifarah Basin.

1. The depositional model comprises of fluvial system by low sinuosity braided and then meandering stream deposited.
2. The architecture of the braided fluvial deposits are dominated by channel –fill complexes (GST & GSp), sands sheet, and associated simple and more complex bar types. The meandering stream sediments record several fining –up successions interpreted as point bars.
3. The braided system was deposited under a more humid climate with high rates of reworking base level is interpreted to have fallen markedly and meandering system was deposited under semi arid climatic conditions, stable fluvial activity and floodplain storage.
4. The geometry and architecture of the two sequences can be described simply as sequence

(1) of braided system, stacked multi-storey sand bodies, with a sheet like geometry procuring an amalgamate high net / gross (80%) sand body complex. Sequence

(2) of meandering system, isolated channel-fill sand bodies with multi-storey / multi – lateral component, producing low net to gross (20%) sandstone ribbons, with a low connection potential.

5. Channel (CH). Consists of gravel bars and bed forms (GSp and GST). Gravel bar and bed form thicknesses are upto 3-5 in most cases and widths are 50m to 150m.
6. Sand bed forms (SB) consist of St, Sp, Sr and SL with sharp base. SB has sheet-like geometry and is often eroded channels. SB is usually about 1.5-2m thick. Widths vary between 150 and 200m. The average width/thickness ration of 15:1 within the whole studied area.
7. Paleocurrent indicators from the ASF show the flow to ward the west direction of cross stratification measurements' Sr, St and Sp
8. The two main fluvial systems contrast markedly, meandering stream was deposited under semi arid climate conditions, stable fluvial activity and flood plain. And braided stream was deposited under a more humid climate with high rates of reworking base level.
9. Based on the work of Demko *et al.*, 2002 and Meadows 2006 for alternating episodes of incision and aggradation through climatic mediation of the relationship between fluvial discharge and sediment flux controlled by a changing climate. This is supported by recorded changes in thickness of floodplain facies association 2 & 3 in which the humid parts while the channel of sandstones facies association I in arid part.

REFERENCES

- Allen, J. R. L. (1983). Studies in Fluvial Sedimentation: Bars, Bar Complexes and Sandstone Sheets (Low-Sinuosity Braided Stream) in the Brownstones (L. Devonian) Welsh Borders. *Sedimentary Geology* 33: 237-293.
- Allen, J. R. L. (1984). Parallel Lamination Developed from Upper Stage Plane Beds a Model Based on the Larger Coherent Structures of the Turbulent Boundary Layer. *Sed. Geol.*, 39: 227-42
- Anketell, J. M. and Ghellali, S. M. (1991). A Paleogeographic Map of the Pre-Tertiary Surface in the Region of the Jifarah Plain and its

- Implications to the Structural History of Northern Libya. *Third Symposium on the Geology of Libya*. eds. M.J. Salem, A.M. Sbeta and M.R. Bakbak. Elsevier, Amsterdam, 6: 2381-2406.
- Blair, T. C. and McPherson, J. G. (1994). Alluvial Fans and their Natural Distribution from Rivers Based on Morphology, Hydraulic Processes, Sedimentary Processes, and Facies Assemblages. *J. Sediment Res*, A64: 450 – 489.
- Blum, M. D. and Tornqvist, T. (2000). Fluvial Responses to Climate and Sea-Level Change: A Review and Look Forward. *Sedimentology*, 47: 2-48.
- Bown, T. M. and Kraus, M. J. (1987). Integration of Channel and Floodplain Suites. I Developmental Sequence and Lateral Relations of Alluvial Paleosols: *Journal of Sedimentary Petrology*, 57: 587 -601.
- Bridge, J. S. and Leeder, M. R. (1979). A simulation Model of Alluvial Stratigraphy. *Sedimentology*, 26: 617–644.
- Bridge, J. S. (1995). Paleochannel Patterns Inferred from Alluvial Deposits: A Critical Evolution. *J. Sed. Pet.*, 55: 579-89.
- Bull, W. B. (1991). *Geomorphic Responses to Climate Change*. Oxford University Press, New York.
- Clemmensen L. B., Oxnevadiei and De Boer P.L. (1994). Climatic Controls on Ancient Sedimentation: Some Late Palaeozoic and Mesozoic Examples from NW Europe and the Western Interior of the USA. In: *Orbital Forcing and Cyclic Sequences* (Ed. By P. L. de Boer and D. G. Smith), *Spec. Publ. Int. Assoc. Sediment.*, 19: 439 -457.
- Cojan, I. (1993). Alternating Fluvial and Lacustrine Sedimentation: Tectonic and Climatic Controls (Provence Basin, S. France, Upper Cretaceous/Palaeocene), In: *Alluvial Sedimentation* (Ed. By M. Marzo and C. Puigdefabregas), *Spec. Publ. Int. Assoc. Sediment.*, 17: 425 -438.
- Demko, T. M., Drzewiecki, P. A., Feldman, H. R., Geslin, J. K., Hasiotis, S. T., Mc Crimmon, G. G., Van Wagoner, J. C. and Wellner M R. W. (2002). The Influence of Climatically Mediated Stream Discharge and Sediment Flux on the Sedimentary Record of Landscape Evolution: Implications for the Sequence Stratigraphy of Continental Strata. *AAPG Annual Meeting, Houston, Abstracts vol. A41*.
- Desio, C. R. Ronchetti, R. Pozzi, F. Clerici, G. Invernizzi, C. Pisoni and Vigano, P. (1963). Startigraphic Studies in the Tripolitanian Jebel (Libya). *Rev. Ital. Paleont. Strata. Mem. IX*: 126pp
- Dubieli, R. F., Huntoon, J. E., Condon, S. M. and Stanesco, J. D. (1996). Permian Deposystems, Palaeogeography and Palaeoclimate of the Paradox Basin and Vicinity. In: *Palaeozoic Systems of the Rocky Mountain Region* (Ed. By M. W. Longman and M. D. Sonnenfeld). *SEPM* 427-444. Rocky Mountain Section.
- Frostick and Reid, (1989). Climatic Versus Tectonic Controls of Fan Sequences. Lessons from the Dead Sea, Israel. *J. Geol. Soc. Lond.* 146: (527-538).
- Frostick, L. E. and Jones, S. J. (2002). Impact of Periodicity on Sediment Flux in Alluvial Systems: Grain to Basin Scale. In: JONES, S. J. FROSTICK, L. E. (eds) *Sediment Flux to Basins: Causes, Controls and Consequences*, Geological Society, London, *Special Publication*, 191: 81-95.
- Gawthorpe, R. L. and Leeder, M. R. (2000). Tectonic-Sedimentary Evolution of Active Extensional Basins. *Basin Research*, 12, 195-218.
- Goudarzi, G. H. (1980). Structure–Libya. *Second Symposium on the geology of Libya*. (eds. M. J. Salem and M. T. Busrewil). Academic Press, London. 3: (879-892).
- Hammuda O. S., Sbeta A. M. and Worsley, D. (2000). *Field guide to the Mesozoic Succession of Jabal Nefusah, NW Libya*: 1-50.
- Hartshorn, K., Hovius, N., Wade, W. B.; and Slingerland, R. L. (2002). Climate-Driven Bedrock Incision in an Active Mountain Belt. *Science*, 297: 2036–2038.
- Hirst, J. P. P. (1983). Oligo-Miocene Alluvial Systems in the Northern Ebro Basin, Huesca Province, Spain: University of Cambridge, England, *Unpublished Ph.D. dissertation*: 247p.
- Hovius, N. (1996). Regular Spacing of Drainage Outlets from Linear Mountain Belts. *Basin Research*, 8: 28-44.
- Jopling, A. V. and Walker, R. G. (1968). Morphology and Origin of Ripple-Drift Cross-Lamination, with Examples from the Pleistocene of Massachusetts, *J. Sediment. Petrol*, 38: 971–984.
- Jones S. J. Frostick L.E. and Astin T.R., (2001), Braided Stream and Flood Plain Architecture: the Rio Vero Formation, Spanish Pyrenees. *Sedimentary Geology* 139: 229-260.

- Jones S. J. (2002). Transverse Rivers Draining the Spanish Pyrenees: Large Scale Patterns of Sediment Erosion and Deposition. In: Jones, S.J., Frostick, L.E., (eds.), *Sediment Flux to Basins: Causes, Controls and Consequences. Geological Society, London, Special Publication, 191*: 171 – 185.
- Jones, S. J. (2004). Tectonic Controls on Drainage Evolution and Development of Terminal Alluvial Fans, Southern Pyrenees. *Spain Terra Nova, 16*: 121-127.
- Jones S. J. and Frostick L. E. (2008). Inferring Bedload Transport from Stratigraphic Successions: Examples from Tertiary and Pleistocene Rivers, South Central Pyrenees, Spain. In: Gallagher, K., Jones, S.J. & Wainwright, J. (Eds) *The Earth's Dynamic Surface, Geological Society, London, Special Publication, In Press*.
- Kraus, M. J. (1999). Paleosols in Clastic Sedimentary Rocks: Their Geologic Applications. *Earth-Science Reviews 47*: 41-70.
- Koltermann, C. E. and Gorelik, S. M. (1996). Heterogeneity in Sedimentary Deposits: A Review of Structure-Imitating and Descriptive Approaches. *Water Resources Research, 32, 9*: 2617-2658.
- Lane, E. W. (1955). The Importance of Fluvial Morphology in Hydraulic Engineering. *Am. Soc. Civil Eng. Proc., 81 (745)*: 1-17.
- Mackey, S. D. and Bridge, J. S. (1995). Three Dimensional Model of Alluvial Stratigraphy: Theory and Application. *J. Sediment. Res., B65*: 7-31.
- Mack, G. H. and Leeder, M. R. (1999). Climatic and Tectonic Controls on Alluvial Fan and Axial Fluvial Sedimentation in the Plio-Pleistocene Palomas Half Graben, Southern Rio Grande Rift. *Journal of Sedimentary Research, 69*: 635-652.
- Meadows, N. S. (2006). The Correlation and Sequence Architecture of the Ormskirk Sandstone Formation in the Triassic Sherwood Sandstone Group of the East Irish Sea Basin, NW England. *Geol. J. 41*: 93-122.
- Miall, A. D. (1977). A Review of Braided River Depositional Environments. *Earth Sci. Rev. 13*: 1-62.
- Miall, A. D. (1978a). Fluvial Sedimentology. *Can. Soc. Petrol. Geol. Mem., 5*.
- Miall, A. D. (1978b). Fluvial Sedimentology. An Historical Review. In: Miall AD (ed) *Fluvial Sedimentology. Can. Soc. Petrol. Geol. Mem., 5*: 1-47.
- Miall, A. D. (1983). Basin Analysis of Fluvial Sediments. Modern and Ancient Fluvial Systems, Collinson, J. D., Lewin, J. (Eds.). *Spec. Publ. Int. Assoc. Sedimentology. 6*: 279-286.
- Miall, A. D. (1985). Architectural Element Analysis: a New Method of Facies Analysis Applied to Fluvial Deposits. *Earth Sci. Rev. 22*: 261-308.
- Miall, A. D. (1988a). Facies Architecture in Clastic Sedimentary Basins Analysis. *Springer: New York. 67-81*.
- Miall, A. D. (1993). The Architecture of Fluvio-Deltaic Sequences in the Upper Mesaverde Group (Upper Cretaceous), Book Cliffs, Utah. Braided Rivers, Best, J. L., Bristow, C.S. (Eds). *Geol. Soc. Lond., Spec. Publ., 75*: 305-332.
- Miall, A. D. (1994). Reconstructing Fluvial Macroform Architecture from Two-Dimensional Outcrops: Examples from the Castlegate Sandstone, Book Cliffs, Utah, *J. Sediment Res., B64*: 146-158.
- Miall, A. D. (1996). The Geology of Fluvial Deposits. Sedimentary Facies, Basin Analysis, and Petroleum Geology, Springer-Verlag, Berlin Heidelberg.
- Mikbel, S. R. (1977). Basement Configuration and Structure of West Libya. *Libyan Jour. Sci., 7A*: 19-34.
- Mitchum, Jr., R. M., Vail, P. R., and Thompson III, S. (1977). Seismic Stratigraphy and Global Changes of Sea-Level, Part 2: the Depositional Sequence as a Basic Unit for Stratigraphic Analysis, in Payton, C. E. ed., *Seismic Stratigraphy-Applications to Hydrocarbon Exploration: Tulsa. American Association of Petroleum Geologist Memoir; 26*: 53-62.
- North, C. P. (1996). The Prediction and Modelling of Subsurface Fluvial Stratigraphy. In: Carling, P., Dawson, M. (Eds.): *Advances in Fluvial Dynamics and Stratigraphy. Wiley, Chichester*: 395-508.
- Olsen, H. (1990). Astronomical Forcing of Meandering River Behaviour: Milankovitch Cycles in Devonian of East Greenland. *Palaeogeog, Palaeoclimatol, Palaeoecol., 79*: 99-115.
- Olsen, H. (1994). Orbital Forcing on Continental Depositional Systems—Lacustrine and Fluvial Cyclicality in the Devonian of East Greenland. In: de Boer, P. L., & Smith D. G. (eds), *Orbital Forcing and Cyclic Sequences. Int. Assoc. Sediment. Spec. Pub., 19*: 429-38.

- Olsen, H. and Larsen, P. H. (1993). Structural and Climatic Controls on Fluvial Depositional Systems: Devonian of East Greenland. In: Alluvial Sedimentation (Ed. By M. Marzo and C. Puigdefabrigas), *Spec. Publ. Int. Assoc. Sedim.*, **17**: 401-423.
- Ouchi, S. (1985). Response of Alluvial Rivers to Show Active Tectonic Movement. *Geological Society of America Bulletin*, **96**: 504-515.
- Paola, C. (2000). Quantitative Models of Sedimentary Basin Filling. *Sedimentology*, **47**: 121-178.
- Posamentier, H. W. and Vaill, P. R. (1988a). Eustatic Controls on Clastic Deposition I-Continental Framework. In: Wilgus *et al.*, (eds.): Sea Level Changes: An Integrated Approach, *SEPM Spec. Publ.* **42**: 109-124.
- Posamentier, H. W. and Vaill, P. R. (1988b). Eustatic Controls on Clastic Deposition II-Sequence and System Tract Models. In: Wilgus, C. K., Hastings, B. S., Kendall, C. G. St. C., Posamentier, W., Ross, C. A. and Van Wagoner, J. C., (eds.), Sea Level Changes: An Integrated Approach: Tulsa, *Society of Economic Paleontologists and Mineralogists Special Publication*, **42**: 125-154.
- Rasanen, M.; Salo, J. and Kalliola, R. J. (1987). Fluvial Perturbance in the Western Amazon Basin: Regulation by Long-Term Sub-Andean Tectonics. *Science*, **238**: 1398-1401.
- Retallack, G. J. (2001). Soils of the Past: An Introduction to Paleopedology, 2nd edn. Blackwell, Oxford.
- Reynolds, A. J. (1965). Waves on the Credible Bed of an Open Channel. *J. Fluid Mech.*, **22**: 113-33.
- Rubino, J.; Galeazzi S. and Sbeta A. (2000). Depositional Facies and Sequence Stratigraphy of the Triassic Series of the Libyan-Tunisian Jabal Nafusah: A Preliminary Report (Abstract only). Second Symposium on the Sedimentary Basins of Libya, Geol. of Northwest Libya, *Book of Abstracts*: 79.
- Rust, B. R. (1978). Depositional Models for Braided Alluvium. In Fluvial Sedimentology (Ed. A. D. Miall): *Canadian Society of Petroleum Geologists Memoir*, **5**: 605-625.
- Seeber, L. and Gortniz, V. (1983). River Profiles Along Himalayan Arc as Indicators of Active Tectonics. *Tectonophysics*, **92**: 335-367.
- Shanley, K. and McCabe, P. (1991). Predicting Facies Architecture Through Sequence Stratigraphy an Example from the Kaiparowits Plateau. *Utah: Geology*, **19**: 742-745.
- Shanley, K. and McCabe P. (1994). Perspectives on the Sequence Stratigraphy of Continental Strata. *A. A. P. G. Bulletin*, **78**: 544-658.
- Singh, I. B. and Kumar, S. (1974). Mega-and Giant Ripples in the Ganga, Yamuna and Son Rivers. Uttar Pradesh, India. *Sedimentary Geology*, **12**: 53-66.
- Smith, N. D. (1971). Transverse Bars and Braiding in the Lower Plate River, Nebraska. *Geological Society of America, Bulletin*, **82**: 3407-20.
- Smith, N. D. (1972). Some Sedimentological Aspects of Planar Cross-Stratification in a Sandy Braided River. *Journal of Sedimentary Petrology*, **42**: 624-34.
- Stanley, S. M. (1994). Global Change and the Origin of the Human Genus. (Ibid.): 233-243.
- Tucker, M. (2001). Sedimentary Petrology. *Third edition*: 261pp.
- Van Wagoner, J.; Posamentier, H.; Mitchum, R.; Vail, P., Sarg, J.; Louttt, T. and Herdenbol, J. (1988). An Overview of the Fundamental of Sequence Stratigraphy: In Wilgus, C. K.; Hastings, B. S.; Kendall, C. G. St. C.; Posamentier, H. W.; Ross, C. A. and Van Wagoner, J. C. (eds.): Sea-Level Changes: An Integrated Approach: Tulsa. *Society of Economic Paleontologists and Mineralogists Special Publ.*, **42**: 39-45.
- Viseras, C.; Calvache, M. L.; Soria, J. M. and Fernandez, J. (2003). Differential Features of Alluvial Fans Controlled by Tectonic or Eustatic Accommodation Space. Examples from the Betic Cordillera, Spain. *Geomorphology*, **50**: 181-202.
- Wright, V. P. and Marriott S. (1993). The Sequence Stratigraphy of Fluvial Depositional Systems: the role of Floodplain Sediment Storage. *Sedimentary Geology*, **86**: 203-210.
- Yang, C. S. and Nio, S. D. (1993). Application of High Resolution Sequence Stratigraphy to the Upper Rotliegend in the Offshore. In: Siliciclastic Sequence Stratigraphy (Ed. by: P. Weimer and H. W. Posamentier), *Am. Assoc. Petrol. Geol., Mem.*, **58**: 285-316.

ASSESSMENT OF FORMATION DAMAGE OF SANDSTONE RESERVOIRS IMPACT OF FINES MIGRATION AND SOLIDS PLUGGING ON SANDSTONES' RESERVOIR QUALITY, SARIR

Faraj M. Elkhatri*

Abstract: Fundamental controls on formation damage and reservoir quality of Sarir Formation Sirt Basin Libya are authigenic clay mineral types and their distributions. However, petrologies investigation obtained from the study area in five wells and concentrated on main rock components and the parameters that may have impacts on reservoirs. The petrographic observation shows the main authigenic clay minerals are kaolinite and dickite, these investigations have confirmed by X.R.D analysis. Clay fraction, mainly kaolinite and dickite were extensively presented in all wells as high amounts. As well as traces of detrital semictite and less amounts of illitized mud-matrix can be seen using SEM. Thin layers of clay is also present as clay-grain coatings in local depth interpreted as remains of dissolved clay matrix which is partly transformed into kaolinite adjacent and towards pore throat. This also may have impacts on most of the pore throats of this sandstone which are open and relatively clean with some of fine material have been formed within these pores. This material is identified by EDS analysis to be collections of not only kaolinite booklets but also small disaggregated kaolinite platelets derived from the disaggregation of larger kaolinite booklets. These patches of kaolinite not only fill these pores, but also coat some of the surrounding framework grains. Quartz grains often enlarged by authigenic quartz overgrowths partially occlude and reduce porosity. Scanning Electron Microscopy (SEM) with Energy Dispersive Spectroscopy (EDS) was conducted on the post-test samples to examine any mud filtrate particles that may be in the pore throats. Semi-qualitative elemental data on selected minerals observed during the SEM study were obtained through the use of an Energy Dispersive Spectroscopy (EDS) unit. The samples showed mostly clean open pore throats, with limited occlusion by kaolinite. The EDS analysis confirmed the identification of the fine grained disaggregated material as mainly kaolinite, though sample from well VV6-65 (8912.70 feet) did show some other very fine-grained elemental combinations (Si/Al/Na/Cl, Si/Al Ca/Cl/Ti, and Qtz/Ti).

Keywords: Pore throat, fines migration, formation damage, quartz overgrowths, porosity loss, Sarir Formation.

INTRODUCTION

This research has gathered three stages of study including sedimentology, petrology, and advanced core analysis and Mud Lake Off test to explicate the importance of studying the diagenetic clay menials alteration; and thus what is their impact reservoir quality. Sedimentology and petrology study both are always taking the first place in this study considering the variation in sediment's lithology reflects the different mineralogy. Sandstone reservoirs of five oil

wells in Sarir Formation, Sirt Basin Libya have been strongly affected by fine kaolinite migration and less impact of solids plugging. The main diagenetic mineral of studied sandones is kaolinite which presented as kaolinite fines booklet like. Normally, transport of kaolinite fines in the siliclastic reservoirs at low temperatures is dependent on both hydrodynamic and colloidal forces. Colloidal forces dominate except near the wellbore where fluid velocities are the highest. Mobilization of kaolinite fines controlling by the water chemistry and is favored by high Ph and low salt concentration, whereas hydrodynamic kaolinite migration can be occur during oil production.

*Libyan Petroleum Institute, Km7 Gergarish road, P.O.Box 6431, Tripoli, Libya

METHODOLOGY

Sedimentology study: Five well cores representing the subjected reservoirs have been sedimentologically described and defined the fluvial sandstone sediments. 25 sandstone samples were collected based on variation porosity and permeability in studied wells for petrographical and geochemical analyses. Petrographic analyses were performed on thin-sectioned samples, which were prepared subsequent to impregnation with Blue Dyed Epoxy under a vacuum. The modal compositions of the sandstones were obtained by counting 300 points per thin section. The investigation of textural habits and diagenetic alterations was performed on ten sandstone samples using a Scanning Electron Microscope (SEM) equipped with a digital imaging system. The samples were coated with a thin layer of gold and examined under an acceleration voltage of 20kV. Chemical analysis of the clay diffraction using XRD was performed on 15 samples.

Advanced core analysis study: Sample was loaded into the CMS-300TM for determination of permeability and porosity. Net confining pressures were applied. The sample was placed into a rubber sleeve between stainless steel end pieces and confining pressure applied. Helium was injected into the sample from reference cells of known volume and pressure. A direct pore volume was determined using Boyle's Law of gas expansion, then pressure was vented at a known rate and unsteady-state Klinkenberg permeability was determined by pressure decay. Porosity was calculated for the sample as the pore volume fraction of the summation (grain volume + pore volume) bulk volume.

Mud Lake off test : Four (4) samples were submitted for regain permeability to oil after oil-based or water-based mud circulation and mud lake off. The core plugs were injected with kerosene (in the production direction) at the temperature of 230°F and permeability to oil was measured. Oil-based mud was circulated across the face of samples 3 (8869.60 feet) and 5 (8912.70 feet) for 4 hours at 300 psi overbalance and water-based mud was circulated across the face of samples 4 (8726.30 feet) and 8 (8806.30 feet) for 4 hours at 300 psi overbalance (Table 1). The samples were then locked in for 16 hours. Each sample showed an immediate drop in permeability after mud circulation and lock-in, with slight increases in the permeability observed in the

test results as kerosene injection continued (increases did not reach initial permeability levels).

RESULTS OF PETROGRAPHIC STUDY

Rock Texture: From the petrographic observation the sandstone seems to be fine to medium grained with medium-grained dominance. Grains are characterised by sub-rounded to less common rounded and sub-angular; they are contacted as point contact to concave-convex mud supporting grains in local depths.

Framework Composition: Sarir Formation in studied area presented by sandstones which are very fine-to medium grained quartz arenite with an average modal composition of Q100,F00, L00 (Fig.1A) in VV4 and VV5 wells. Quartz grains (69-80 vol.%, av. 74.22%); (Table 2) are dominantly monocrystalline (av. 65%) and less commonly polycrystalline (av. 4%); however, sandstones in wells VV1 and VV2 are argillaceous as mud rich and calcified as quartz wacky (Fig.1B) where mud to sand ratio is up to (20-vol. 50%) (Table 2). Mica mainly muscovite (0-1 vol. %,

Table 1 Shows results of Mud Lake off test for one of samples and permeability change at mud or water injection.

Fluid Injected	Cumulative Fluid Injected, pore		Apparent Permeability to Liquid,	Permeability/ Permeability Initial
	Fluid	Total		
Treated Kerosene	1.68	1.68	293.	1.00
<i>Permeability before mud injection</i>	4.67	4.61	289.	0.988
	5.81	5.73	293.	1.00
4 hour mud injection at 300psi overbalanced. Then sample was locked in for 16 Hours				
	0.047	5.78	4.48	0.0153
	0.142	5.87	4.97	0.0170
Treated Kerosene	0.236	5	6.83	0.0233
	0.330	6	8.79	0.0300
<i>Permeability after mud injection</i>	0.425	6	17	0.0597
	0.519	6.25	18	0.0646
	0.614	6	22	0.0759
	0.708	6.44	27	0.0933
	1.27	7	39	0.136
	1.84	7	46	0.158
	2.41	8	56.4	0.192
	2.97	8	56	0.192
	3.54	9	57.2	0.195
	4.11	9	57	0.195
	4.6	10.4	57	0.195
	5.24	11.0	57	0.195
	5.81	11.5	57	0.195
	6.94	12.7	57	0.195
	8.07	13.8	57	0.197
	9.20	14.9	57	0.197
	9.77	15.5	58	0.200
	10.3	16.1	58	0.200
	11.5	17.2	58	0.199
	12.0	17.8	58	0.200
	13.2	18.9	58	0.200
	13.7	19.5	59	0.202
	14.3	20.0	59	0.204
	15.4	21.2	55	0.188
	16.0	21.7	57	0.198
	17.1	22.9	59	0.204
	18.3	24.0	59	0.204
	19.4	25.1	59	0.204
	20.5	26.3	59.6	0.204

Fig.(1A) Classification of quartz arenite of sandstone samples after Pettijohn. (1987)

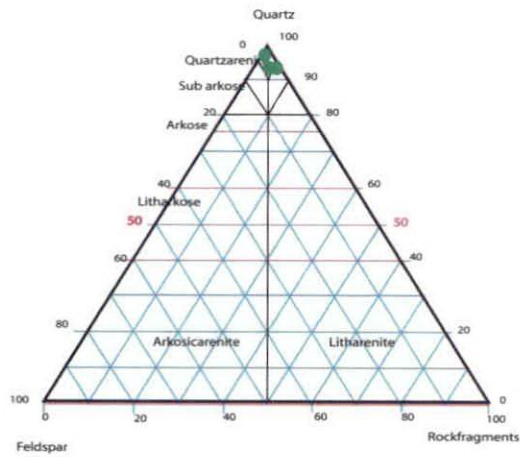


Fig.(1B) Classification of quartz wacky of sandstone samples after Pettijohn. (1987)

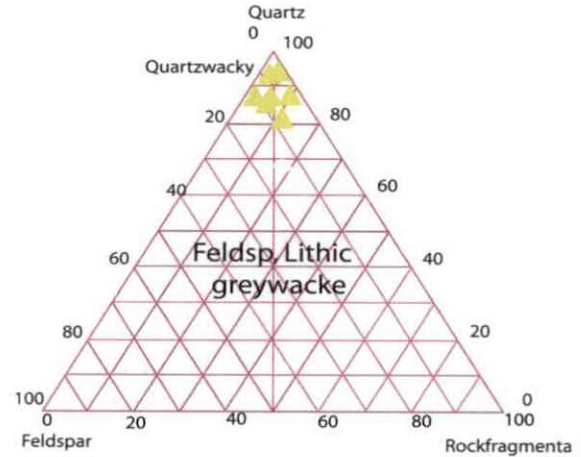


Fig.1(A and B) Detrital composition of selected sandstone samples from the Sarir Formation in VV-65 area, plotted on a Pettijohn. (1987) triangular classification diagram.

av. 0.11%) is more abundant within the matrix. Mud matrix is presented by different amounts that made up to (0-20% vol. av.7.22%), clay matrix where dominated in certain interval that shows very low to nil porosity. Clay matrix partly to completely altered into kaolinite and in rare cases replaced by dolomite (Fig. 5B). Remains of dissolved clay appears coating quartz grains which replaced by kaolinite. (Fig. 4B). Matrix not only muddy or silt, however, occasionally displays a few amounts of very fine martial appears plugging pore throats (Morales and De Ros, 1990). EDS signature identifies not only kaolinite ($\text{Al}_2\text{Si}_2\text{O}_5(\text{OH})_4$), but also very fine-grained zones. For example, various elemental combinations of silicon, aluminum, calcium, sodium, titanium, oxygen, and chlorine are detected by EDS. (Fig. 2A & B) as well as traces of anhydrite also present (Fig. 3B). The EDS tool has a spatial resolution of about $2\mu\text{m}$ and so can record X-ray photons from nearby material when focused on very fine-grained material ($<2\mu\text{m}$) such as seen in one of the pores from the sample at depth 8912.70 feet (Plate 4).

DISCUSSION

Petrographical and geochemical analyses of the studied Sarir Formation samples show that the sandstones have various maturity classification as facies controlled and classified to quartz arenite and quartz wacky (Pettijohn *et al*, 1981); and have undergone various stages of diagenetic alterations (Morad *et al*, 1994).

Authogenic Components

Kaolinite

Kaolinite and less common dickite are very common in this area that made up (vol. 0-20%; av.6% with SD. 5.1). Kaolinite formation is the most common diagenetic mineral that mainly replacing mud matrix, feldspars, and less common mud clasts (Fig. 4C). Kaolinite is engulfed by; and thus predated quartz cementation (Fig 2A). Vermicular kaolinite-like is filled number of pore throats (Fig.4B) and also smaller particles whose morphologies appear to be individual platelets of kaolinite derived from the disaggregation of larger kaolinite booklets (Fig. 2A). This visual is confirmed by Energy Dispersive Spectroscopy analysis. EDS analysis identifies the fine-grained disaggregated material as kaolinite.

Dolomite

Dolomite in studied sandstone with variation in habits and types (trace-2 vol.%, av.0.1%; Table 3). It is occurred as cement with microcrystalline quartz habit (5-50 μm across); and occurs as scattered patches that have replaced, pervasively to nearly completely, mud matrix, and in less common micas and feldspars (Fig. 3A). Dolomite in certain depth occurred as saddle dolomite in late diagenetic stage that extensively replacing mud matrix (Radke and Mathis, 1980). Dolomite engulfs; and thus post-dating, quartz over growth; and completely replaced mud matrix and partly quartz grains (Fig 5B) and kaolinite (Fig. 3A). Dolomite is closely

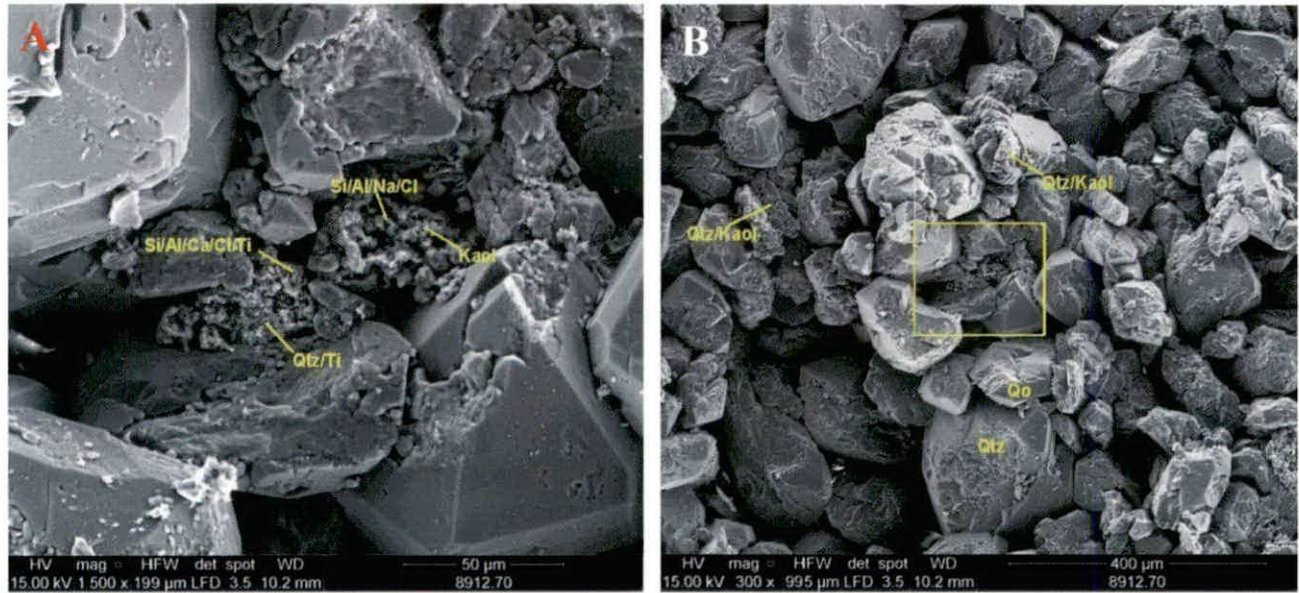


Fig. 2 SEM: photo (A) depicts a sample that contains mostly clean, unconcluded pores. Quartz grains (Qtz) and quartz overgrowths (Qo) are visible. few grains appear coated with small platelets of kaolinite, although EDS analyses of these areas produce a mixed signature of quartz and kaolinite (Qtz/Kaol) because of the intimate association of the two materials. In the higher magnification of Photo B, the material in the pore is featured. Using the EDS tool, not only is kaolinite (Kaol) identified, but also very fine-grained material that produces variously elemental signatures of Si/Al/Na/Cl, Si/Al Ca/Cl/Ti, and a combination of quartz and titanium (Qtz/Ti) less than $2\mu\text{m}$ in size.

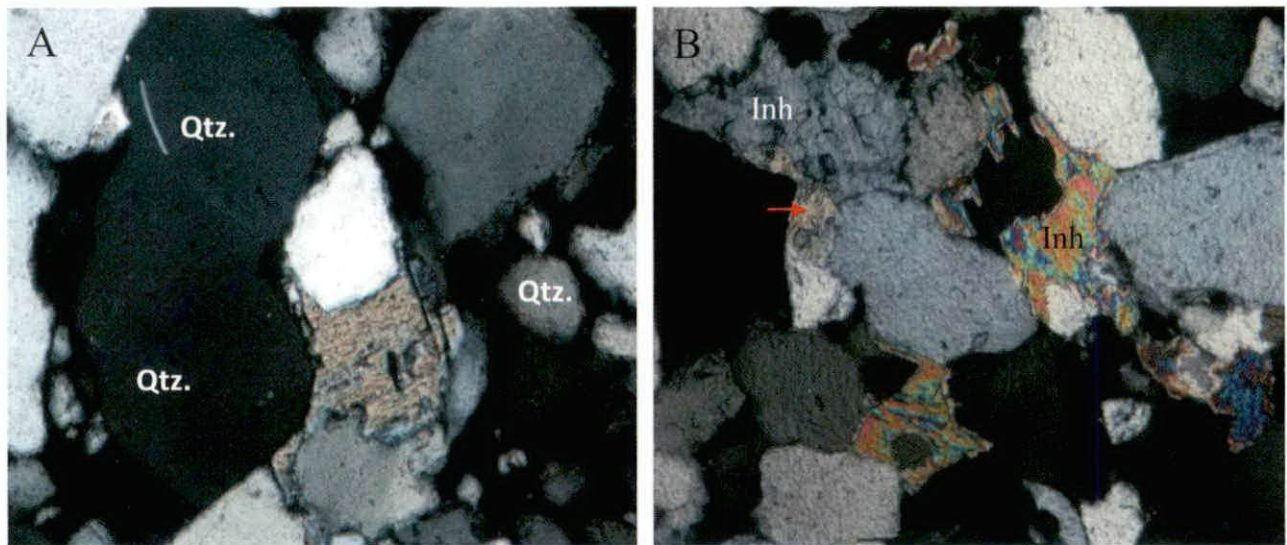


Fig.3. Both are polarized microscopic image (A) poorly sorted sandstone note that quartz grains has wide size range (Qtz); the brownish grains in center is originally feldspar mostly replaced by dolomite, partly grain dissolution porosity (the blue). (B) in this sample trace amount of anhydrite (Inh.) is taken place that formed as cement; its engulfed by and thus predate dolomite (red arrow).

associated with kaolinite; thin kaolinite crystals have been displaced by dolomite which has formed in intercrystalline spaces. Optical micrographs (x-nicols) imaging may suggest that kaolinite is replaced by dolomite (Fig. 4D). In some cases dolomite crystals are arranged perpendicular to framework grains; this siderite may partly fill mouldic porosity formed by dissolution and/or kaolinitization of framework grains (Fig. 4E).

Quartz Cement

Quartz cement (0-9.7vol. %, av. 4.8%; Table 3) occurs mainly as euhedral syntaxial overgrowths ($30\mu\text{m}$ thick) around detrital quartz grains. Overgrowths are highly discontinuous or absent when the quartz grains are coated by thick layers of clay minerals (Fig. 4D); whereas, quartz overgrowths are extensive to complete when quartz grain surfaces are clean (Worden and Morad,

Table 2 Data summary of petrography study shows average, maximum, and minimum of studied sandstone composition

Distributions of the main detrital and authigenic components of five studied wells															
VV65 AREA	VV1-65 Well			VV2-65 Well			VV3-65 Well			VV4-65 Well			VV5-65 Well		
	AV.	MAX	MIN.	AV.	MAX	MIN.	AV.	MIN	MAX	AV.	MAX	MIN.	AV.	MAX	MIN.
Main detrital components															
Quartz	74	80	69	71.5	85	50	74	78	72	76	78	73	82	80	79
Feldspar	0	0	0	0	0	0	0	0	0	0	0	0	0	0	0
Mica	0	1	0	0	0	0	0	0	0	0	0	0	0	0	0
Rock frag.	0	0	0	0	1	0	0	0	0	0	0	0	0	0	0
Clay mat.	7	20	0	7.7	50	0	0	1	0	1	3	0	3	3	2
Mud clas.	0	0	0	0	0	0	0	0	0	0	0	0	0	0	0
Heavy. M.	0	0	0	0	0	0	0	0	0	0	0	0	0	0	0
Authigenic components															
Kaolinite	6	20	1	4.5	9	0	2	5	0	1	3	0	3	3	2
Semictite	2	8	0	0	1	0	3	1	0	1	4	0	4	3	3
Q.OV	2	6	0	3	5	0	5	6	2	6	7	4	10	9	8
Dolomite	0	0	0	0.4	2	0	0	0	0	0	0	0	0	0	0
Calcite	0	0	0	0.5	3	0	0	0	0	0	0	0	0	0	0
Anhydrite	0	0	0	0.7	7	0	3	11	0	0	0	0	0	0	0
Types of porosity															
Integrin.	3	7	0	5	7	0	6	7	5	6	7	5	8	8	7
Grain dis.	5	10	0	6.1	9	0	8	9	7	9	11	7	13	12	11
Micro frac.	0	1	0	0	0	0	0	0	0	0	0	0	0	0	0

2000). Quartz overgrowths may fill intergranular pores (Fig. 5A) which have resulted from partial to extensive dissolution of feldspars. In a few cases, quartz can occur as outgrowths which fill partly to extensively adjacent pores. In addition to syntaxial quartz overgrowths quartz cement occurs as small (< 15µm) discrete crystals that are randomly-orientated or aligned parallel to each other, and which cover quartz grain surfaces. These crystals developed on quartz grains coated by micro-quartz, which are in turn frequently coated by clay. Quartz overgrowths are typically engulfs; and thus postdating kainite, and engulfed by and thus predating dolomite (Fig 5C).

RESERVOIR QUALITY AND ZONATION

Porosity in thin-section of the studied Sarir Formation sandstones varies from (zero to 22%; av. 15,3%; Table 3). It is more abundant in wells VV4 and VV5 (18-20% vol.%, av. 18%) respectively than in VV1 and VV2 wells (0-17 vol.%, av. 8%, Table 2). Thin section porosity types are intergranular,

grain dissolution and micro fracture pores and includes both micro(< 10µm) and macro-sized pore spaces. Intergranular porosity (trace -8%vol; av. 7% with SD.2.4) is more common than molodic dissolution porosity (trace – 13 vol. %, av. 8.2% with SD. 3.8). However, micro fracture porosity is less abundant (trace – 1 vol.%, av. 0.1% with SD.0.2). (Table 3). Grain dissolution porosity is the most common abundant in well VV5 (11-13%, av. 12%) (Table 2). This is due to partially dissolution of mud matrix; and partially or completely dissolution of feldspars and less common mud interclasts. Lack correlation between porosity and permeability in some reservoirs intervals (Fig. 6) is attributed to abundance of grain dissolution porosity as well as micro porosity distribution due to formation of kaolinite and dissolution; whereas, nil or lack of intergranular porosity is due to abundance of mud matrix particularly in well VV2 which is depositional controlling (El-Ghali, *et al*; 2006). The extent of framework grain dissolution was greater in the coarser-grained of studied samples than in finer-grained.

FORMATION DAMAGE CONTROLLING

In the majority of these oil sands reservoirs, the most abundant clay mineral present is kaolinite. Kaolinite has two different types of formation damage, both leading to permeability change, at low temperatures, kaolinite contributes to fines migration or transport; at the high temperatures accompanying steam

Table 3 Shows average, maximum, minimum, and SD. of framework grains, diagenetic grains and pore types distributed of all studied area

VV65 AREA	AV.	MAX	MINA	SD
Framework components				
Quartz	70.0	85.0	0.0	8.0
Feldspar				
Mica	0.1	1.0	0.0	0.2
Rock fragments				
Clay matrix	6.1	50.0	0.0	13.1
Mud clasts				
Heavy minerals	0.0	0.0	0.0	0.0
Diagenetic components				
Kaolinite	3.7	20.0	0.0	5.1
Semictite				
Q.OV	4.8	9.7	0.0	2.8
Dolomite				
Calcite	0.2	3.0	0.0	0.8
Anhydrite				
intergranular	5.3	8.0	0.0	2.4
Grain dissolution				
micro - fracture	0.1	1.0	0.0	0.2

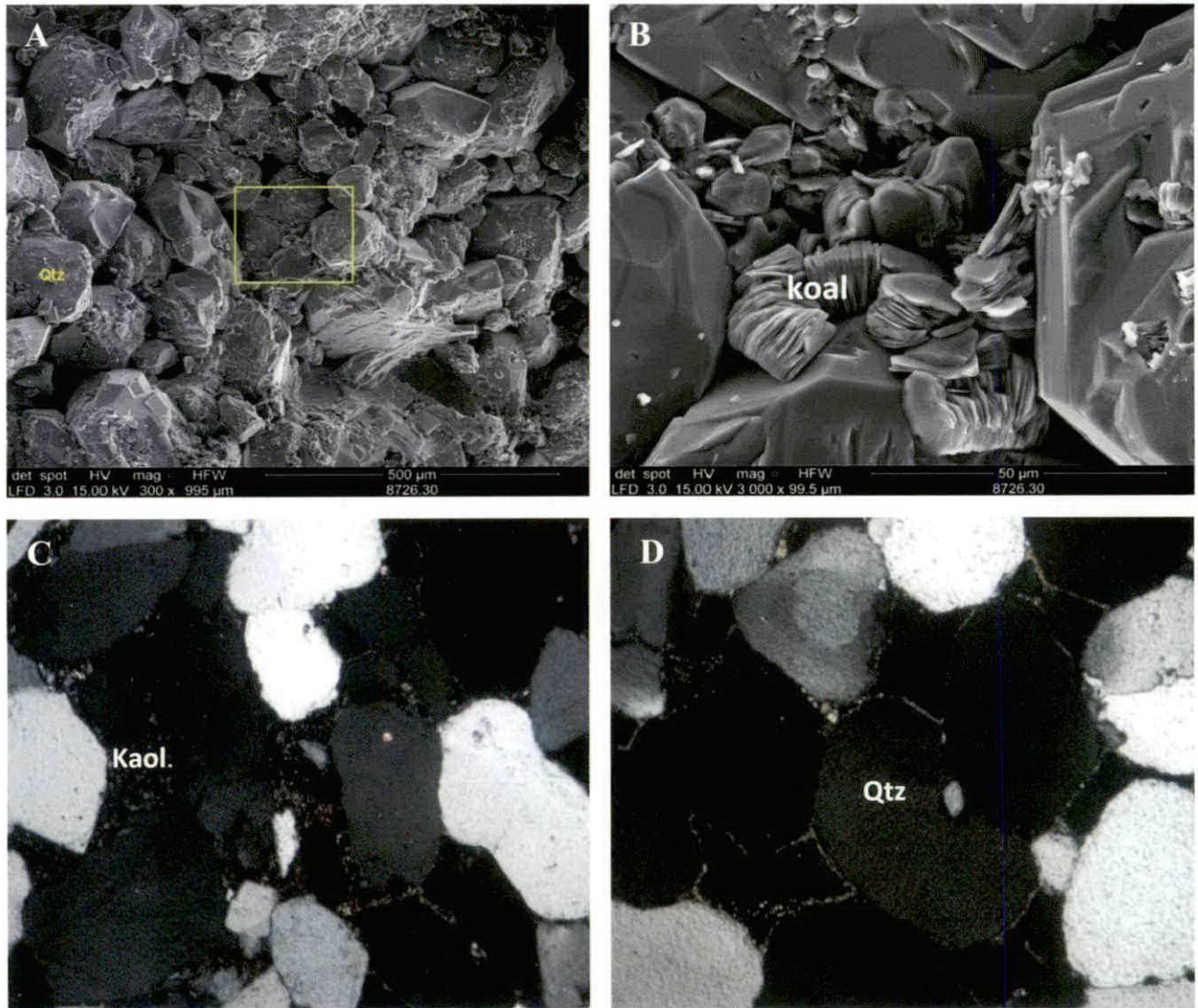


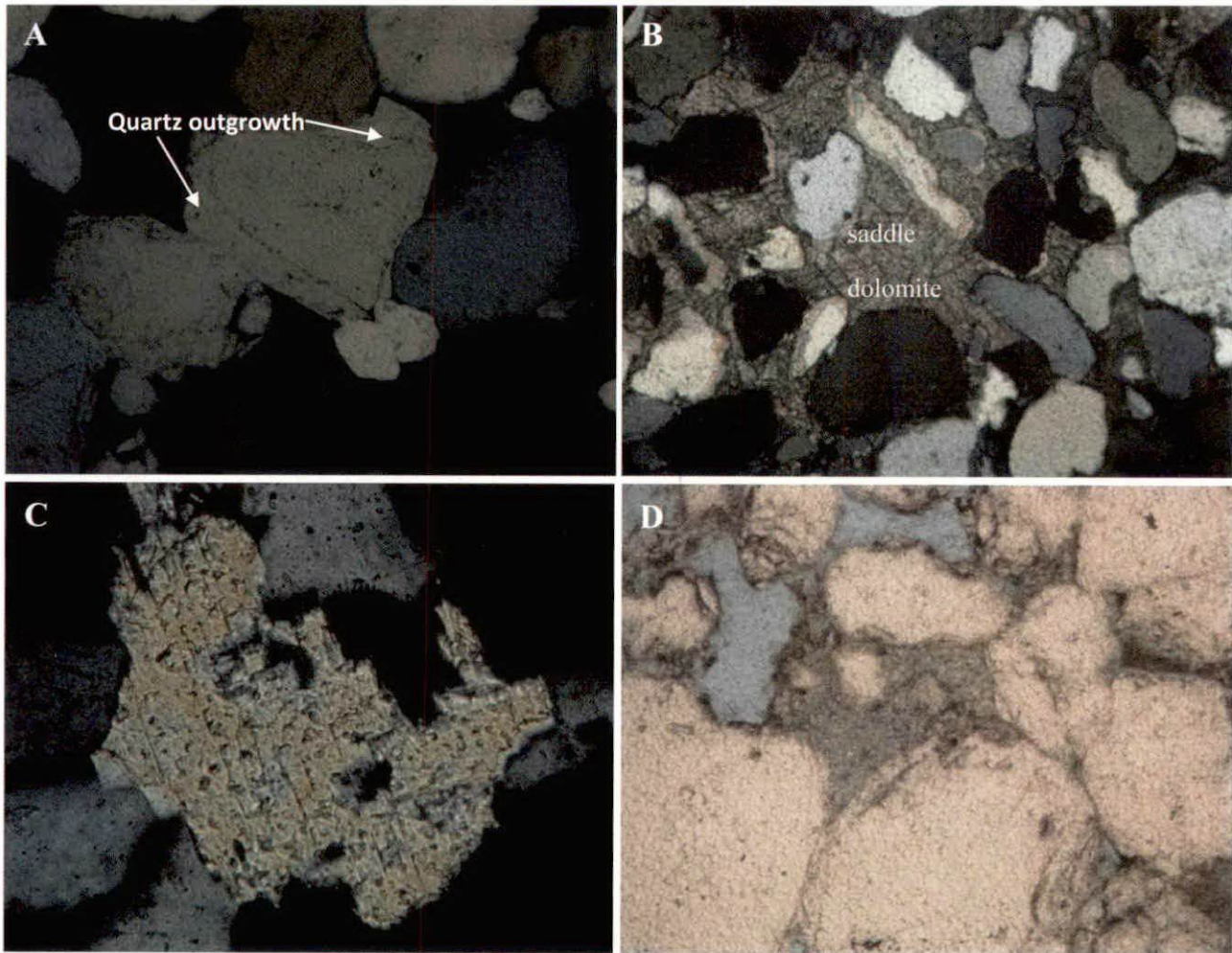
Fig.4 A and B are represent low and high magnification SEM images. In photo (A), the image is centered in the (yellow outline) which is Kaolinite very fine within the pore throat; quartz grains is the main component. (Qtz) identified by EDS (Energy Dispersive Spectroscopy). Photo B is higher-magnification and focuses on an occluded pore at the center Photo A. This pore is filled with kaolinite (Kaol).Kaolinite is vermicular like. (C and D) are polarized microscopic image (C)formation of Kaolinite that replacing mud matrix (kaol);and sandstone is poorly sorting. (D) Photo B depicts a sample that contains mostly quartz dominated and pores are mostly clean (unconcluded pores). Quartz grains (Qtz) and quartz overgrowths are visible and grains appear coated with thin layers of smectite and small platelets of kaolinite.

recovery. Kaolinite reacts with other minerals and condensed steam to form smectite (Hayatdavoudi and Ghalambor, 1998). Transport of kaolinite fines in the reservoir at low temperatures is dependent on both hydrodynamic and colloidal forces. Colloidal forces dominate except near the wellbore where fluid velocities are the highest.

BASIC PROPERTIES AND PERMEABILITY TO OIL AT SWI

Basic rock properties measurements (permeability, porosity, and grain density) were performed on the seven (7) suitable samples at 800 and 3300 psi net

confining stress. The Klinkenberg permeabilities ranged from 1.65 to 501 millidarcies (md) at 3300 psi and the porosities ranged from 10.6 to 18.4 percent. Grain densities for these samples ranged from 2.64 to 2.67 g/cm³. After basic properties measurements, the seven (7) samples were vacuum saturated with 190,000 ppm sodium chloride brine and then spun in a high speed centrifuge to establish initial water saturation (Swi). Permeability to oil at Swi was measured at two flow rates. This permeability is at ambient temperature and pressure and is not representative of the reservoir conditions. The permeabilities to oil (kerosene) ranged from 1.13 to 416 md.



(Fig.5). Photomicrographs in X-polarized light (A) quartz outgrowths, which partly fill intergranular pore; and later-formed discrete quartz crystals completely fill intergranular pore. (B) Grain-replacive saddle dolomite engulfs, and thus post-dating, quartz over growth saddle dolomite is completely replaced mud matrix and partly quartz grains. (C) Example of dolomite completely replace large feldspar grains, dolomite engulfs; and thus postdate quartz overgrowth. (D) Completely grain dissolution (presumably mud-clasts) which has abundant grain dissolution-porosity.

CONCLUSION

Authigenic kaolin which is the main diagenetic mineral developed within the sandstone will depend upon the breakdown of the unstable grains; that mainly replaced mud matrix, and less common feldspars. Permeability changes are mainly attributed to fines kaolinite migration and less impact soiled plugging. Kaolinite is pore-filling and grain-coatings adjacent to the pore throat; kaolinite pore-filling have strong impact on formation damage by pulging pore space. Smaller particles of kaolinite whose morphologies appear to be individual platelets of kaolinite derived from the disaggregation of larger kaolinite booklets is the most impact and casing formation damage when its movement and migrated toward the

pore throat. Lack of porosity and permeability (in local depth) of sandstone is attributed to high amounts of mud matrix and/or to poorly sorting grains these are controlled by depositional facies. As facies controlling solids plugging is another factor of formation damage in poorly argillaceous sandstone; but it is less impact than fines migration kaolinite

ACKNOWLEDGEMENTS

The author thanks the Libyan Petroleum Institute (LPI), Tripoli, Libya for financing this study. I deeply thanks reviewer Dr. Mahmoud Elbakai referee for thorough and constructive comments on a previous version. Thanks to LPI Journal staff for assistance with the presentation.

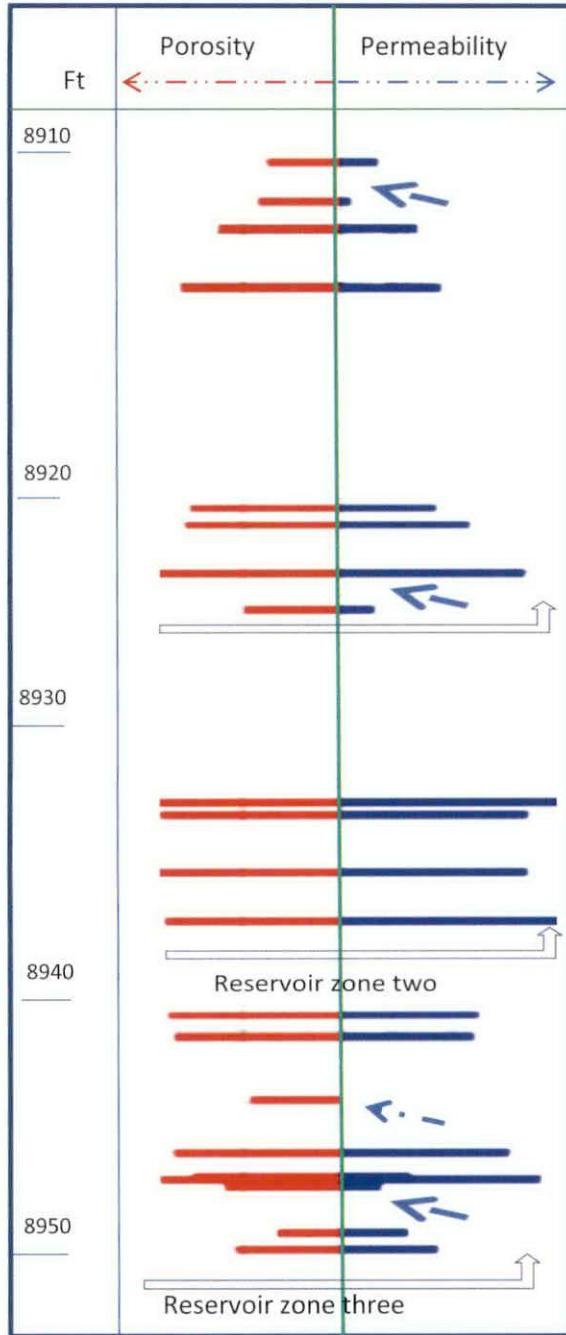


Fig. (6) reservoir quality is strongly controlled by fines migration and less common solids plugging. (zone one) shows porosity values are more higher than permeability values, there is low of permeability values for each porosity (arrows); these are attributed to formation of micro crystals of kaolinite. (Zone three) permeability in certain depth has destroyed note that nil to zero permeability for each porosity value (arrows); both of Solids plugging and fines migration are main controlling.

REFERENCES

El-Ghali, M. A. K., Mansurbeg, H., Morad, S., Al-Aasm, H., and Ramseyer, K. (2006). Distribution of Diagenetic Alterations in Glaciogenic Sandstones within a Depositional Facies and Sequence Stratigraphic Framework: Evidence From The Upper Ordovician of The Murzuq Basin, SW Libya. *Sedimentary Geology*, **V. 190 (1)**: 323–351.

Hayatdavoudi, A. and Ghalambor, A. (1998). A Description of Chemical Precipitation Mechanisms and their Role in Formation Damage During Stimulation by Hydrofluoric Acid. *Journal Of Petroleum Technology*, **V. 34**: 2097-2112.

Morad, S. Mcaulay, G. E., Burley, S. D., Fallick, A. E. and Kusznir, N. J. (1994). Palaeohydrodynamic Fluid Flow Regimes During Diagenesis of the Brent Group in the Hutton-NW Hutton Reservoir, Constraints from Oxygen Isotope Studies of Authigenic Kaolin and Reserves Flexural Modeling. *Clay Minerals*, **V. 29**: 609-629.

Moraes, M. A. S. and De Ros, L. F. (1990). Infiltrated Clays in Fluvial Jurassic Sandstones of Recôncavo Basin, Northeastern Brazil. *Journ. Sedim. Petrol.*, **V. 60**: 809-819.

Pettjohn, F. J. Potter, P. E. and Siever, R. (1981). Sands and Sandstone. Springer, Verlag, New York, 262p.

Radke, B. M. and Mathis, R. L. (1980). On the Formation and Occurrence of Saddle Dolomite. *Journ. Sedim. Petrol.*, **V. 50**, 238, In: Lower Cretaceous Nubian Sandstone Formation, Sirt Basin, Libya: 1149-1168.

Worden, R. H. and Morad, S. (2000). Quartz Cement in Oil Field Sandstones: a Review of the Critical Problems. In: R. H. Worden and S. Morad (Eds), Quartz Cementation in Oil Field Sandstones. *Spec. Publ. Int. Assoc. Sedimentol.*, **V. 29**: 1–20.

REMOTE SENSING TECHNIQUES IN UPDATE GEOLOGIC AND GEOMORPHOLOGIC MAPPING OF SEIF AL UWAYNAT, SOUTHEASTERN LIBYA

Eddawi Ali Elhatmi*

Abstract: Ten colors composite images of Seif Al Uwaynat were obtained by the superimposition of the data of three Landsat Enhanced Thematic Mapper (ETM) bands. After dynamic enhancement processing (Histogram Gaussian Contrast Stretching) facilitate interpretation of the Seif sand dunes and barchans sand dunes information contained in the original Landsat (ETM 7, 4, 2) data. New information is obtained from these ten colors composite images when it is compared with small scale geological data such as the geological map of Seif AL Uwaynat region. The Landsat ETM of this region reveals a textural, moisture content, patterns and color differentiation with the Quaternary deposits which consist of the Seif (longitudinal) sand dunes and clay deposits along their troughs. This differentiation and the results were not observed or mentioned on the geological map of IRC (2007) and Hunting (1974). Another technique has been accomplished to identify terrain features of Seif AL Uwaynat region using band rationing technique. Terrain features of the study area have been identified by this technique from reflectance bands of Landsat ETM image. Twelve band ratios have been created and each ratio has revealed the terrain features. Single color-composite combinations of three ratios have separated subtle differences between different terrain features uniquely. This study has been on the basis of visual interpretation.

Keywords: Landsat Enhanced Thematic Mapper Imagery, Seif Al Uwaynat, Remote Sensing Techniques, Band rationing technique.

INTRODUCTION

The Seif AL Uwaynat area occupies 713 square kilometers and is situated between latitudes 21° 30'N and 21° 45'N and longitudes 24°15'E and 24° 30'E (Figs. 1 and 2). A pronounced feature at the mapped area is the presence of the ends of Seif AL Uwaynat sand dune and extensive sand sheets. The dunes are of longitudinal type oriented as stream lines in northeast-southwest trends. Longitudinal sand dunes in the area of Seif AL Uwaynat area that reaches up to 90km long and usually up to 20m. high. This dune occurs at the western part of the mapped area. There are also dune belts covering a great part of the mapped area and laterally grade into the flat sand sheet forming the plain areas. Most of the undifferentiated Precambrian rocks and the upper member of Carboniferous rocks at the Seif AL Uwaynat area are partially covered by Quaternary deposits (El- Mehdi *et al*, 2004).

Research Objectives

This study has two major objectives: 1-To test the potential and utility of using remote sensing enhancement techniques. 2-To produce update mapping in geologic and geomorphologic studies derived from analysis of Landsat Enhanced Thematic Mapper imagery by using techniques that requires less time and less expenses than more conventional field mapping.

Justification for Choice of Area

1-Seif Al Uwaynat area is a classical region of geological study which is known in considerable details. However, geomorphologic mapping has lagged behind studies of the geology of the province; in particular, remote sensing data have not been used for geological and geomorphological analysis. 2-The region has sufficient complexity, both of terrain and surface cover, to permit an evaluation of the applicability of Landsat Enhanced Thematic Mapper data to study the geomorphology, structure

*Libyan Petroleum Institute Libya -Tripoli eddawi_elhatmi@yahoo.com

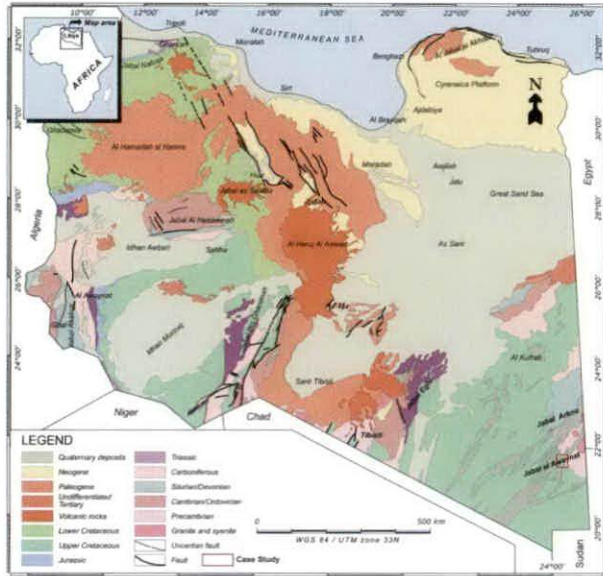


Fig. 1: Location Map of Seif AL Uwaynat Area, geological overview of Libya (modified after Industrial Research Centre, 1977).

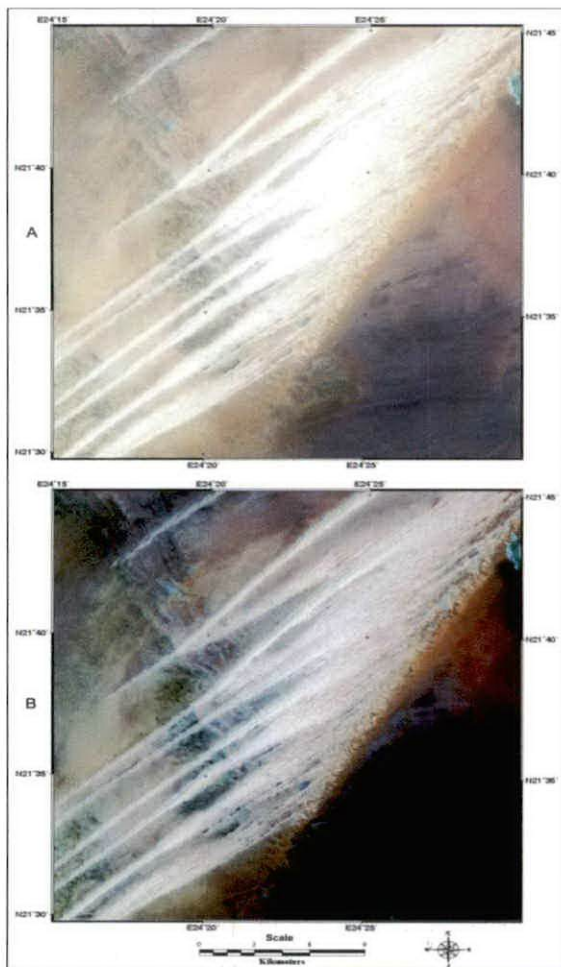


Fig. 2: A – Raw Data of Seif AL Uwaynat Area. B – Landsat Enhanced Thematic Mapper Bands Combination (ETM 7 = Red, ETM 4 = Green and ETM 2 = Blue)

and lithological units in areas of rugged terrain and in flat table area which is difficult to access. 3-The region possess a broad range of surface condition of two types of sand dunes so that results in this area should have and has economic problems typical of those which occur throughout Al Kufrah Basin, so that results in this area should have a wider applicability. 4-Therefore, it is desirable to sum the knowledge of visual satellite image interpretation to produce a series of updating maps such as, geological, tectonic and geomorphologic maps. These will provide more detailed information on the mappable units and highlight the signature and their appearance on satellite images.

The Evaluation of Enhancement Techniques

The major goal of this study is to develop available methodology for producing remote sensing data flow chart for update mapping geologic and geomorphologic study using remote sensing enhancement techniques. The approach adopted in this study has therefore the following steps as illustrated in the flowchart below (Fig. 3, Lillesand & Kiefer, 1999 and Sabins, 1997).

RESULTS AND INTERPRETATION

The principal findings of this research are:
 1-Landsat ETM 7, 4, 2 band imagery synoptic view of the Seif AL Uwaynat provided the basis for update geologic interpretation (Fig. 4). Published map (IRC, 2007) on the lithological mappable units was updated therefore, some discrepancies were found, as follows: This study has corrected the misinterpreted the boundary of the mappable units by IRC, 2007 (Figs. 4 and 5).
 2-To the author’s knowledge, no geomorphologic interpretation previously was available (Fig. 6), and therefore, the present work should greatly highlight the landforms analysis of the district.
 3-It was noticed from Landsat ETM 7, 4, 2 that the Seif sand dunes longitudinal pattern were developed and appeared in a very sharp boundary with white appearance due to the high spectral reflectance of white quartz grains in blue, green and red (i.e., Blue+Green+Red=White). Whereas, the isolated trough between the two crests was developed in clay deposits and appear in blue color because the clay deposits has high spectral reflection in green band (ETM2). In the color composites of ETM 7, 4, 2, has been assigned to a particular color gun of

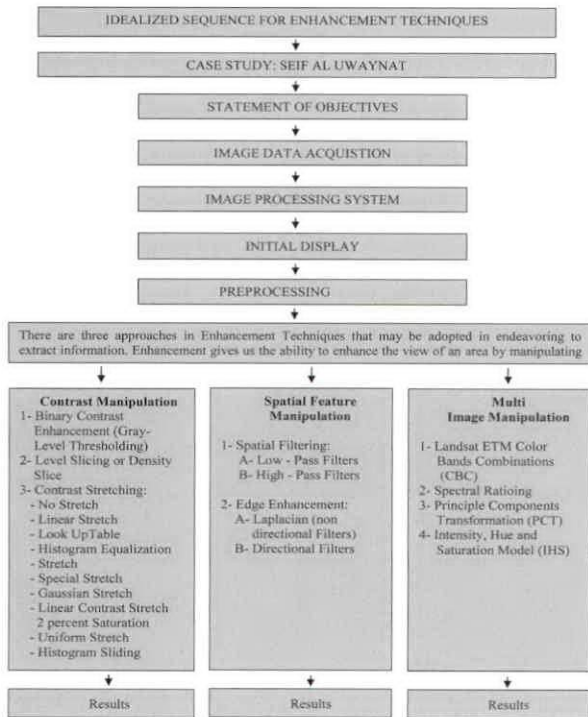


Fig. 3: Flowchart illustrating the methodology adopted in the present study, Lilles and, T.M., and R.W. Kiefer, 1999, and Sabins, F.E., 1997).

RGB composite, that is why the clay trough appears in blue color (Fig. 7).

4-The optimum Landsat ETM channels for lithological and structural discrimination was ETM1, ETM5 and ETM7 (Fig. 8). Histogram Gaussian Contrast Stretch was used to improve image contrast, and was effective in highlighting and enhancement of terrain features in table land terrain as in Seif AL Uwaynat. 5-Color composites of different bands (Figs. 7 and 9) have been selected. Each of the three (ETM) color composites has been assigned to a particular color gun of RGB composites. These twelve color composites of different band allow for the discrimination of terrain features and material classes in a scene. 6-Terrain features can be fairly detected and mapped using color combination of three ratioed images. In this study, twelve band ratios were created. Each ratioed image enhanced at least two or more terrain features (Fig. 10). Three colors composite combinations of three band ratios were classified all terrain features (Fig. 11 and Table 1). 7-Another technique was carried out here with Landsat ETM prepared in the

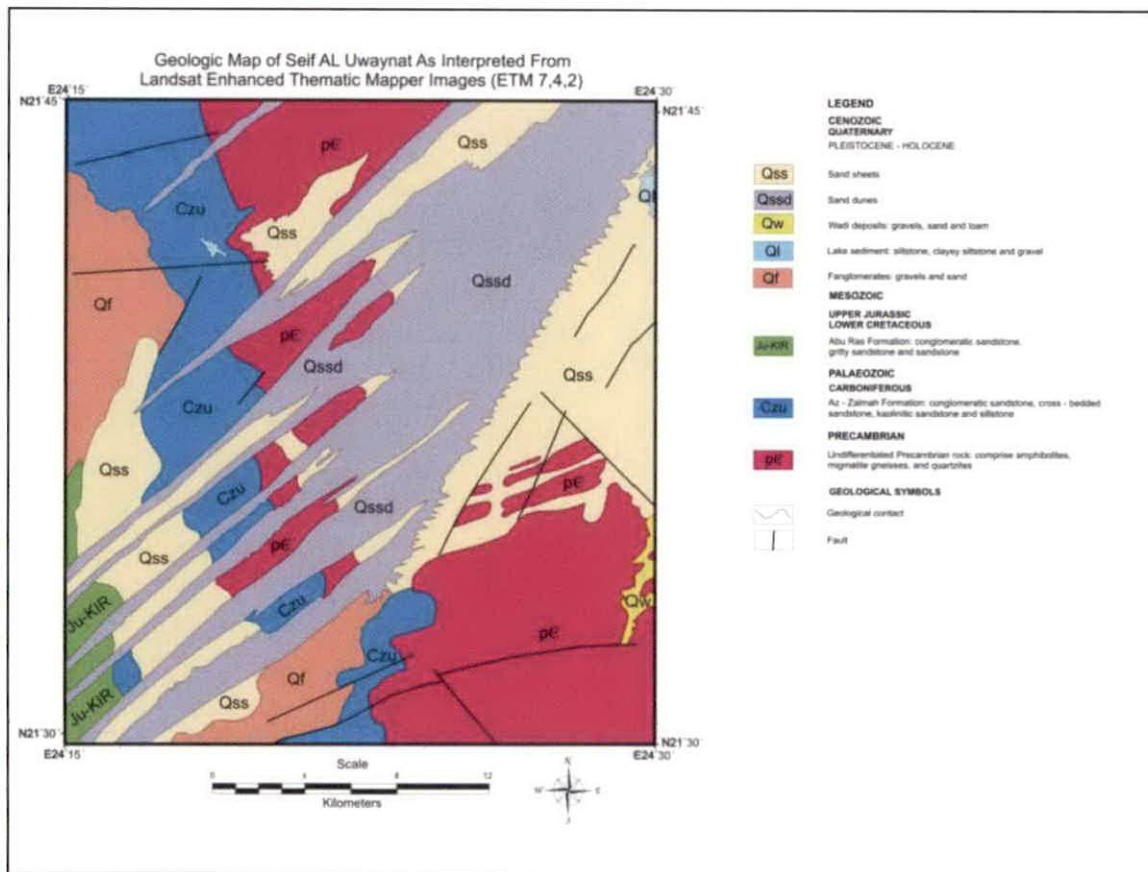


Fig. 4: Geologic Map of Seif AL Uwaynat.

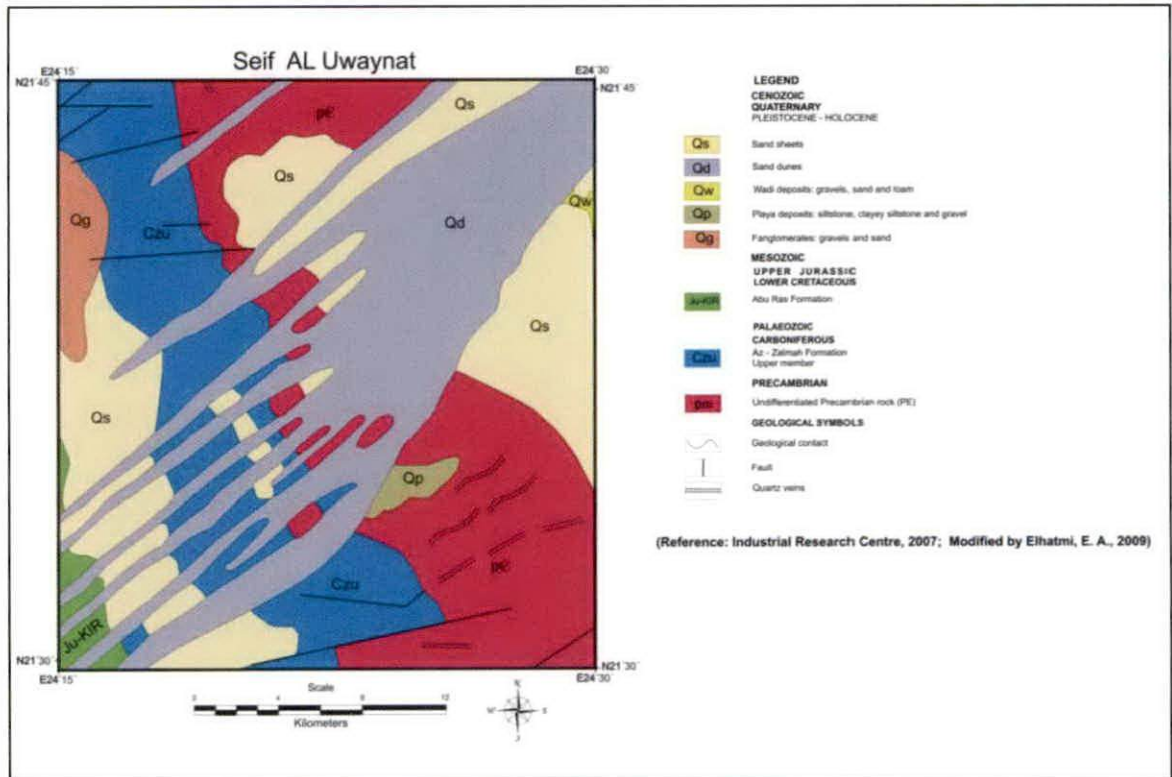


Fig. 5: Geologic Map of Seif AL Uwaynat (IRC, 2007).

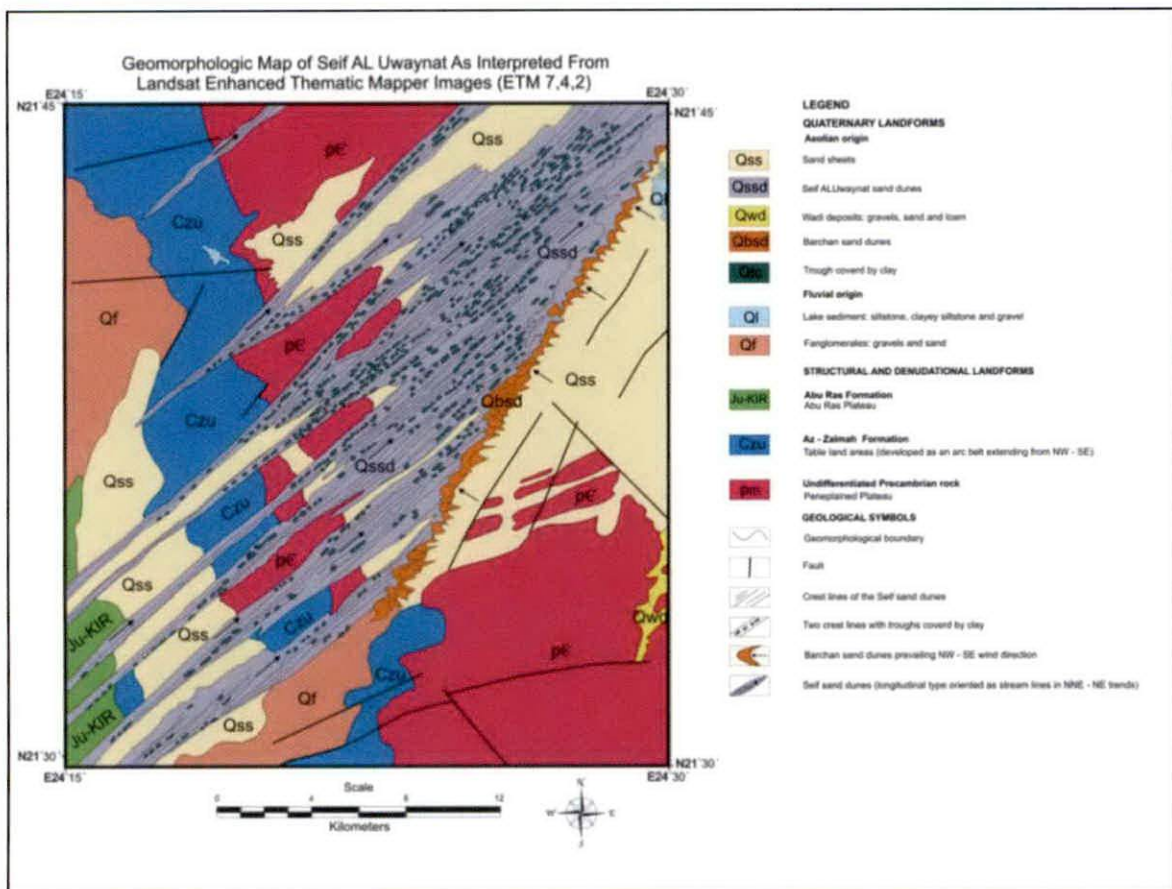


Fig. 6: Geomorphologic Map of Seif AL Uwaynat.

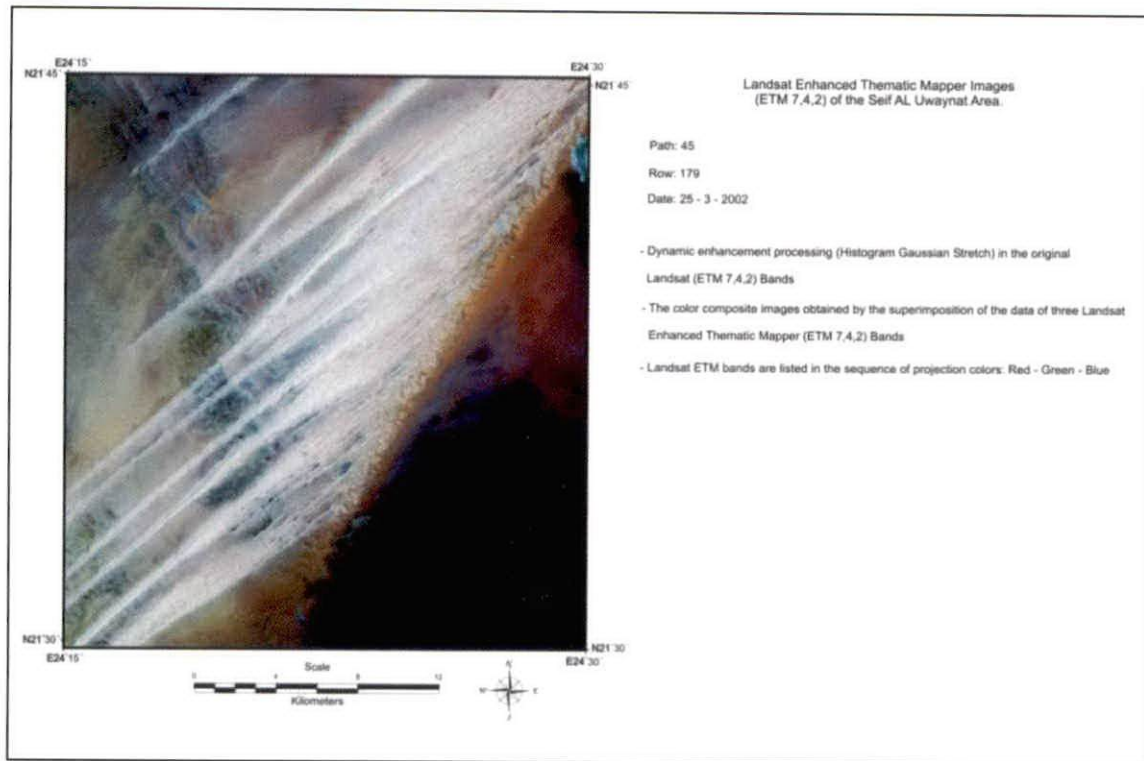


Fig. 7: Landsat Enhanced Thematic Mapper Images (ETM 7,4,2) of the Seif AL Uwaynat.

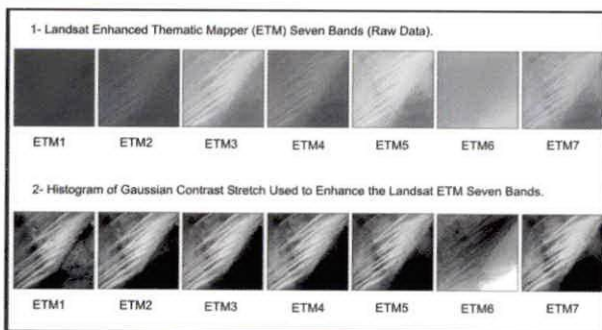


Fig. 8: Original Landsat (ETM) images and the dynamic enhancement contrast Stretch Gaussian applied in Seif AL Uwaynat.

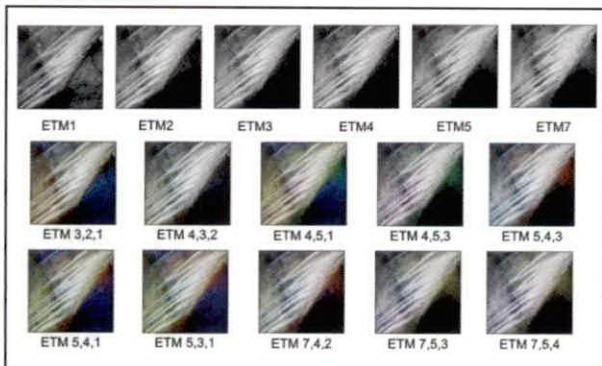


Fig. 9: Landsat (ETM) images resulting from applied of histogram Gaussian contrast stretch and color – composite combinations applied in Seif ALUwaynat.

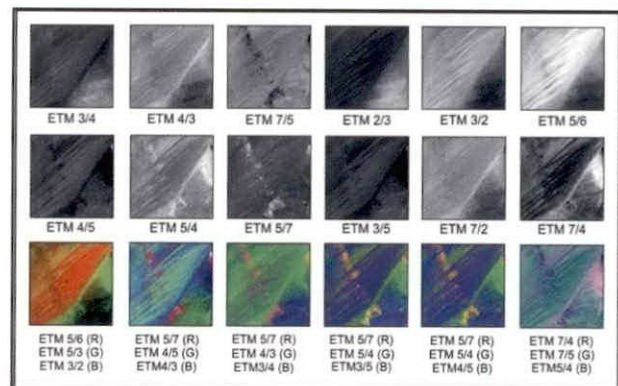


Figure 10: Twelve ratio combinations for Landsat (ETM) applied in Seif AL Uwaynat and six color – composite combinations of band ratios, applied in Seif AL Uwaynat

form of High-Pass and Low-Pass, and the results were suitable the technique was and efficient for Seif AL Uwaynat.(Figs. 12 and 13). 8-Principle Component Transformation and Intensity-Hue-Saturation Color Space Transformation has been identified terrain features, but they are not the best and suitable techniques for discrimination terrain features of the Seif AL Uwaynat.(Fig. 14).

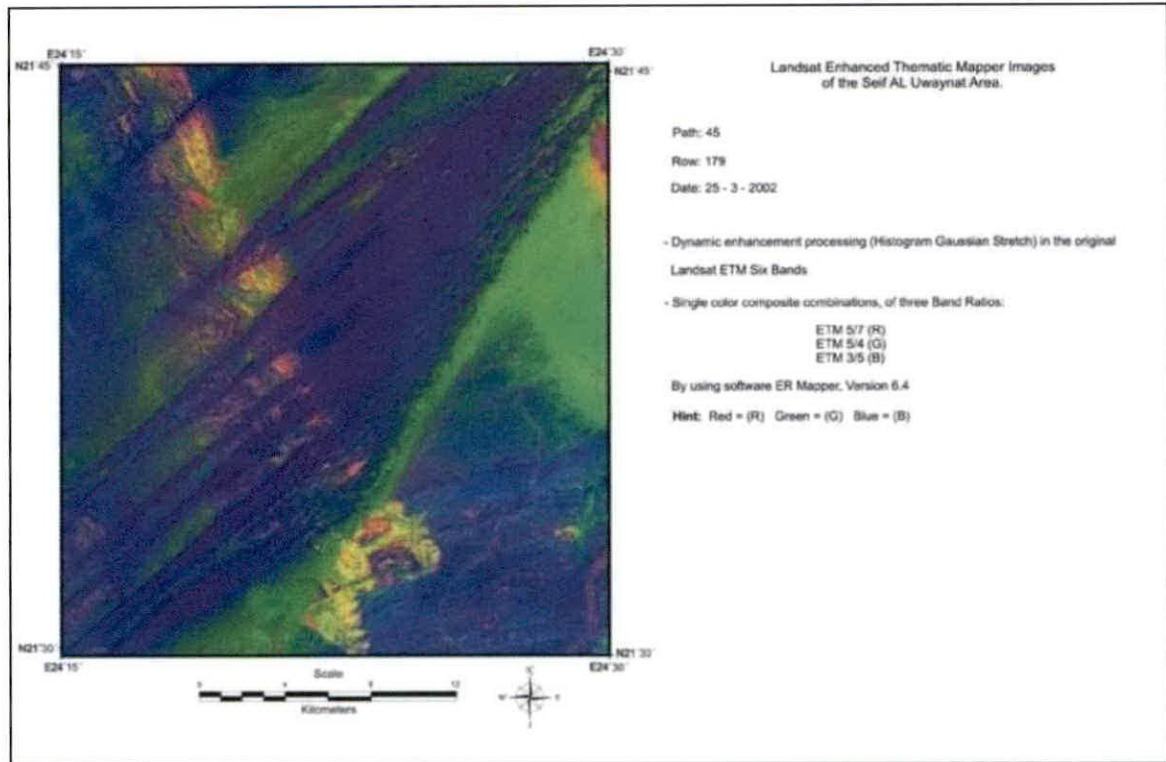


Figure 11: Single color composite combinations, of three Band Ratios ETM 5/7, ETM 5/4 and ETM 3/5.

CONCLUSIONS

The color composites images were obtained the superimposition of the data of three Landsat Enhanced Thematic Mapper (ETM) 7, 4, 2 bands. After dynamic enhancement processing (Histogram Gaussian Contrast Stretching) facilitate interpretation of the Seif sand dunes and Barchan sand dunes information contained in the original Landsat ETM (7,4,2) data. New information is obtained from these images even though it is compared with the small scale geological map of Seif AL Uwaynat area (Figs. 4 and 6). In this regard the map of IRC (2007) and Hunting (1974). The Landsat ETM of this region reveals of textural, pattern and color differentiation with the Quaternary deposits which consist of the Seif (longitudinal) sand dunes and clay deposits along their troughs. As this differentiation was not observed or mentioned on the geological map of IRC (2007) and Hunting (1974).

ACKNOWLEDGEMENTS

Great thanks to Allah, my Lord, Who blessed me to complete this research successfully, and opened the straight paths for me to finalize it in a better form. This research owes much to the

assistance and good will of many people. Birth was not without difficulty, and would not have taken place at all but for Associate Professor Dr. Nabil Subhi AL Daghestani of The Libyan Academy, who has done more than his duty as supervisor, for his support, guidance, friendship and, above all, has been a constant stimulus to effort. Thanks to the management committee of Libyan Petroleum Institute. Thanks go also to the Engineers and Technical working at Libyan Petroleum Institute and all others who in one way or another contributed to the realization of this paper.

Table 1: Three band ratios applied in Seif AL Uwaynat Figure 1: Location Map of Seif AL Uwaynat Area, geological overview of Libya

ETM 5/7	(R)
ETM 5/4	(G)
ETM 3/5	(B)
ETM 7/4	(R)
ETM 7/5	(G)
ETM 5/4	(B)
ETM 5/6	(R)
ETM 5/3	(G)
ETM 3/2	(B)

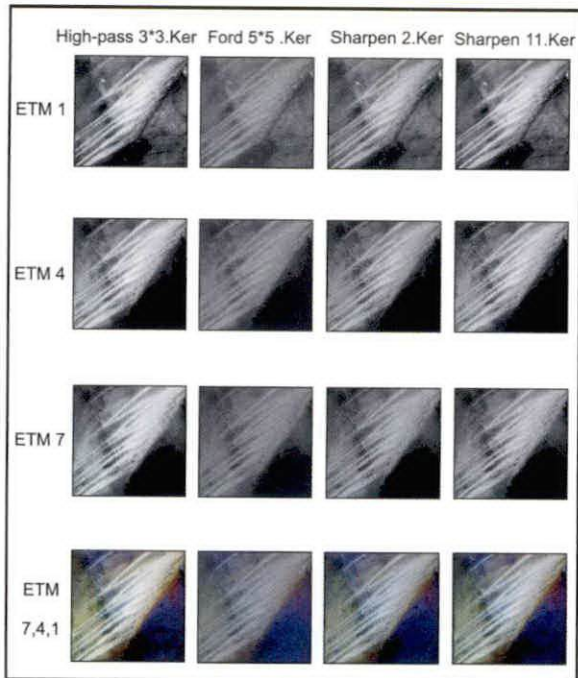


Figure 12: Landsat (ETM 7,4,1) images resulting from application of algorithm spatial filtering High – Pass applied in Seif AL Uwaynat.

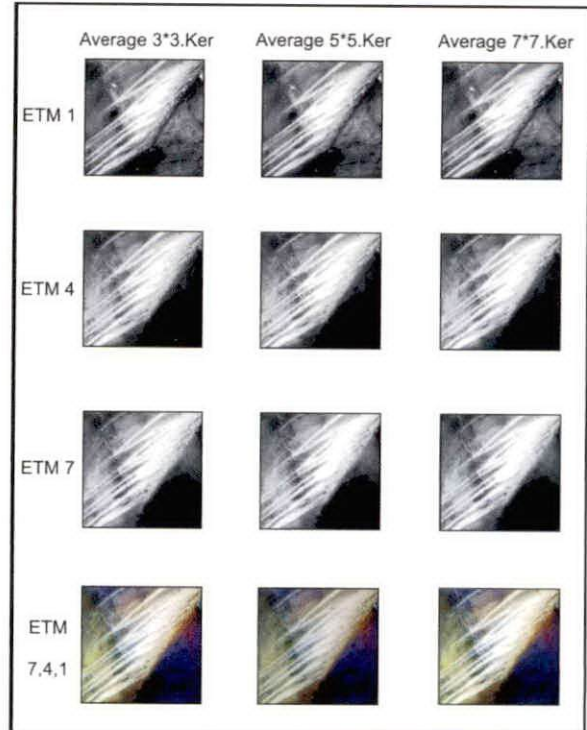


Figure 13: Landsat (ETM 7,4,1) images resulting from application of algorithm spatial filtering Low – Pass applied in Seif AL Uwaynat.

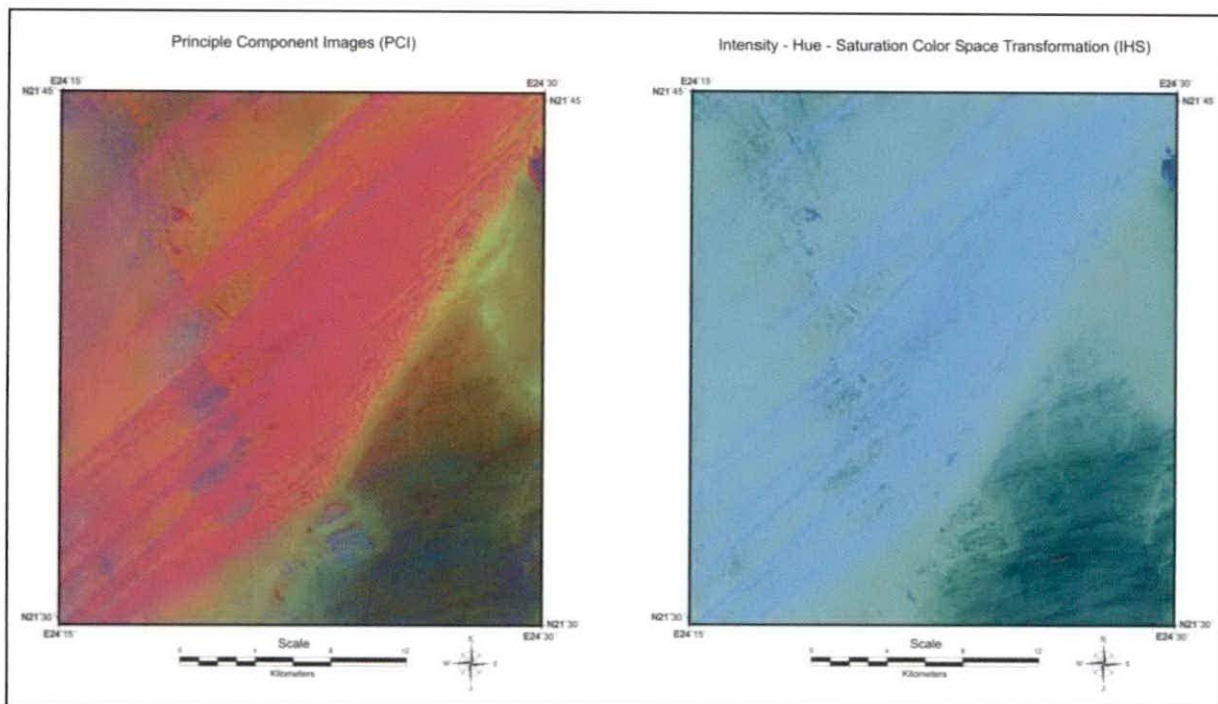


Figure 14: PCI and IHS applied in Seif AL Uwaynat

REFERENCES

- EL-Mehdi, B; Turki, S. M. and Suwesi K. S. (2004). Short Note and Guidebook on the Geology of Al Kufrah Basin AL Uwaynat Area. *IRC*, Tripoli: 67p.
- Hunting Geology and Geophysics Ltd. (1974). Geology of Jabal Al Uwaynat area. Libyan Arab Republic. Unpublished rep. *Ind. Res. Cent.*, Tripoli, Libya; 86p.
- Industrial Research Centre (2007). Joint Geological Mapping Project Sheet, Jabal AL Uwaynat (NF 35-9) Scale 1:250.000, Tripoli, Libya: 99p.
- Lillesand T. and Kiefer, R. W. (1999). Remote Sensing and Image Interpretation. 4th Edition, John Willey and Sons, Inc. New York: 607p.
- Sabins F. E. (1997). Principles and Interpretation. 3rd. Edition. W. H. Freeman and Company, New York: 449p.

THE EFFECT OF WETABILITY ON ARCHIE SATURATION EXPONENT FOR LIBYAN NUBIAN SANDSTONE RESERVOIRS

H. Sbiga*

Abstract: The estimation of oil initially in place is an important issue and since the saturation exponent is the most important factor in determining the hydrocarbon/water saturations from the electrical resistivity measured on core plugs or from wireline logs using the Archie equation, the value of saturation exponent should be determined accurately.

Laboratory measurements methods were undertaken on core samples selected from three different fields (S, T, and U) from the Nubian Sandstone Formation of the central graben reservoir in Libya. The experimental data includes porosity, permeability, and wettability. This includes determining the saturation exponent (n) in the laboratory at two stages. The first stage was before wettability measurements were conducted on the samples, and the second stage was after the wettability measurements in order to find any effect on the saturation exponent.

Changes were also observed in the saturation exponent (n) and water saturation (S_w) before and after wettability measurement. Samples with an oil-wet tendency have higher irreducible brine saturation and higher Archie saturation exponent values than samples with a uniform water-wet surface. A significant change in slope (saturation exponent, n) between resistivity index and water saturation after wettability measurement was observed.

Keywords: Wettability, Saturation, resistivity, Sandstone, permeability, core, reservoir

INTRODUCTION

Reservoir description plays an important role in the petroleum industry. The understanding of reservoir rock properties such as porosity, permeability, water saturation, and resistivity assists engineers to improve the characterisation of the reservoir. In this work the experimental data includes porosity, capillary pressure by using porous plate method, and wettability were obtained. This includes determining the saturation exponent (n) in the laboratory at two stages. The first stage was before wettability measurements were conducted on the samples, and the second stage was after the wettability measurements in order to find any effect on the saturation exponent.

Generally, reservoir rocks are often assumed to be water wet and their saturation exponent (n) is generally assumed to be close to 2. However, it is substantially affected by wettability as well as the pore geometry and often no longer equals 2. Killer (1953) presented evidence that the saturation exponent could be substantially different from 2. He found that Archie's saturation exponent (n) varies from 1.5 to 11.7 for the same rock, depending on how cores were treated. For the same water saturation, the resistivity of an oil reservoir can vary by three orders of magnitude for different wetting conditions. The wettability played a significant role in the fluid distribution within the rock pore space by changing the relative position of the conducting fluid with respect to the rock surface, which affected the electric behaviour of fluid-filled rocks.

Sweeny and Jenning (1960) found that the resistivity of hydrocarbon bearing rocks is strongly affected by the wettability. Their data showed that

* Libyan Petroleum Institute, Tripoli-Libya

the resistivity is greater when the wetting conditions are changed from water-wet to oil-wet. They concluded that the conducting fluid (water) exists in discrete non-connected globules when the rock is oil-wet, which are unable to conduct electric current. Archie's saturation exponent varies from 1.6 to almost 8.0 for water-wet and oil-wet carbonate cores respectively.

Mungan And Moore (1968) pointed out that an Archie's saturation exponent as high as 9.0 can be calculated when the conductive liquid is non-wetting. For strongly water-wet rocks, a unique relationship exists between Archie's saturation exponent and resistivity as described by Archie's law. At lower saturation, Archie's saturation exponent becomes larger and more saturation dependent. They attributed the change of saturation exponent (n) to higher values at lower water saturation to the fact that water is becoming discontinuous and not contributing to the flow of current. For the same core specimen, cleaning may have some impact on the wettability conditions of the rock. Archie's saturation exponent varied from 1.91 to 2.71 for extracted and non-extracted cores respectively.

Location and Geology of the Nubian Sandstone Formation in Sirt Basin

The Sirt Basin is the youngest of the Libyan basins (Fig. 1). It has the largest petroleum reserves in Libya and is ranked the 13th among the world's petroleum basins. The basin's recoverable reserves are about 45 billion barrels of oil and 33 trillion cubic feet of gas. The Sirt Basin contains some sixteen giant oil fields with about 117 billion barrels of proven oil-in-place. The two principal source rocks in the Sirt Province are the Upper Cretaceous Rachmat Shale and the Sirte Shale. Hydrocarbon distribution in the Sirt Basin has been controlled by major tectonic events. This is particularly true of reservoirs related to Cretaceous and Eocene to Miocene rift structures. These reservoirs in the Sirt Basin are composed of 58% clastics, mostly of Mesozoic age and 42% of carbonate rocks mostly of Tertiary age.

The Nubian Formation of the eastern Sirt Basin, Libya, comprises mainly sandstones and shale resting unconformably on a basement of igneous and metamorphic rocks. The Nubian Formation has been subdivided into three members. Member 1 forms the uppermost part of the formation, and comprises mainly sandstones with intercalation of siltstones and shale of variable thickness, and has a maximum known thickness of about 1099ft. Member

2 represents the middle part of the Nubian Formation, and consists of shale and silty shale, with a maximum known thickness of 2362ft. Member 3 is the basal part of the formation, and rests directly on the crystalline basement. It comprises sandstones with subordinate intercalations of siltstones and shale, and exceeds 3002ft in thickness.

The sandstones tend to be fine to coarse grained, quartzitic, tan-grey coloured and are usually poorly sorted with a clay matrix. The finer sandstones are more poorly sorted, but the coarser sandstones have very little in terms of matrix and are thus very porous. The shale tends to be red, maroon, green, micaceous and laminated. There are also conglomerates containing rounded quartz pebbles within a sandstone and claystone matrix, (Barr and Weegar 1972). Much of the Nubian Formation was probably deposited in fluvial depositional systems (Barr and Weegar, 1972).

EXPREMINTAL PROCEDURES

Porosity, Permeability, and Grain Density Measurements

The 65 clean and dry plug samples were subjected to various analyses to determine porosity, permeability and grain density values where possible. The core analysis laboratory of the Libyan Petroleum Institute uses a twin cell helium expansion gas porosimeter for the plug sample grain volume measurement. The porosity and the grain density are then calculated by determining the bulk volume, and the weight of the sample. The positive displacement mercury pump is used to determine the bulk volume of each sample.

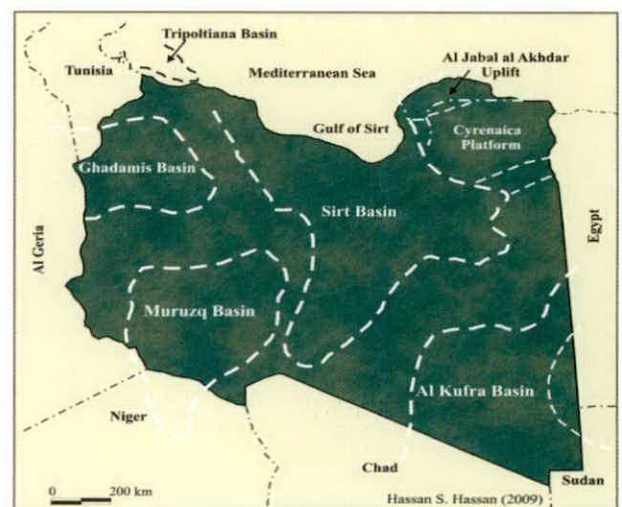


Fig. 1. Location of major sedimentary basins of Libya. (Hassan S.Hassan, 2009)

A clean, dry sample is placed in the Hassler-type core holder and an overburden pressure of 200 psi (industry standard practice to sample) is applied to the cell, compressing the rubber sleeve around the sample. Nitrogen gas pressure is applied to one end face of the sample, whilst the other end face is open to atmospheric pressure, causing the gas to flow through the sample. The flow of gas is measured at the low pressure (downstream) end face of the sample. The flow rate is measured by passing the gas through one of three laminar flow orifices and the differential pressure developed across the orifice is also measured. The length of the sample, upstream and downstream pressures, and flow rate, viscosity of nitrogen, barometric pressure and temperature are entered into Darcy's equation for gas permeability, and the permeability of the sample is calculated.

Resistivity Index (RI) and Wettability Measurements

Twelve samples were selected for resistivity index measurements. These tests were conducted after the formation resistivity factor tests. The fully saturated samples were placed on a semi-permeable porous plate cell in a capillary pressure apparatus, to bring the samples to lower saturation. Air humidified by water was admitted at a controlled pressure to the apparatus and the volume expelled was monitored. When equilibrium saturation had been attained, the samples were removed from the cell, and their weight and electrical resistance were measured. The sample dry weight, the fully saturated weight and the weight after each desaturation step were used to calculate the average saturation of the sample. The resistance was used to calculate the true sample resistivity and the resistivity was divided by the sample resistivity at 100% liquid saturation which yield the resistivity index (RI). In the laboratory it is necessary to firstly determine the resistivity at 100% water saturation (R_o) of the sample. Once this value has been established, the air as the non-conducting fluid is forced into the sample over a range of designated pressures to displace an increasing portion of the brine phase. At each stage, when the saturation is in equilibrium relative to the pressure, the true formation resistivity (R_t) is measured.

The water saturation in hydrocarbon reservoirs is generally estimated from resistivity well logs. The interpretation of these logs is based on two empirical equations by Archie (1942). In clean formations (those containing little or no clay),

Archie (1942) defined the resistivity index as the ratio of the resistivity of the formation (R_t), which is partially saturated to the resistivity of the same formation when it is entirely saturated with water (R_o). Therefore, the resistivity index can be expressed in terms of rock resistivities and water saturation as follows:

$$RI = \frac{R_t}{R_o} = S_w^{-n} \quad (1)$$

Wettability measurements were performed for the same previous samples using the Amott method. This involves a static imbibition phase followed by forced displacement in a flow cell. With a core sample saturated with oil and water at irreducible water saturation, it was placed in an Amott cell under water for 1000 hours. The oil displaced by spontaneous water imbibition is monitored daily until a stable oil measurement was obtained ($V_{w,s}$). The rock sample was then placed in a flow cell and the oil is flushed with water down to residual oil saturation (S_{or}) and the oil displaced dynamically (approximately equal to the volume of water dynamically imbibed) is measured ($V_{w,d}$). Following brine displacement, the rock sample is placed in an Amott cell under oil for 1000 hours. The water displaced by spontaneous imbibition of oil was monitored daily until a stable water measurement was obtained ($V_{o,s}$). The core is then removed and placed in a flow cell and flushed with oil down to irreducible water saturation (S_{wirr}) and the amount of water dynamically displaced (approximately equal to the volume of oil dynamically imbibed) was measured ($V_{o,d}$):

$$I_w = \frac{V_{w,s}}{V_{w,s} + V_{w,d}} \quad (2)$$

$$I_o = \frac{V_{o,s}}{V_{o,s} + V_{o,d}} \quad (3)$$

Where I_w and I_o are the displacement ratios by water and oil ratios respectively. Care should be taken in the interpretation of this data due to the fact that sample wettability may be altered or reversed by a large number of factors (type of coring fluid, exposure to air, temperature, sample handling and plugging, cleaning, drying and preservation). The Amott-Harvey wettability index ($I_{w,AH}$) is a single number that combines the displacement by water and oil ratios:

$$I_{w,AH} = I_w - I_o \quad (4)$$

RESULTS AND DISCUSSION

In this study the porosity and permeability of Nubian sandstone Formation which are determined from the laboratory are highly variable across the whole volume of the reservoir being moderate to good in the some intervals and poor in other intervals.

Core data of porosity and permeability plot as permeability versus porosity of Nubian Sandstone Formation (6 wells, S-01, S-02, S-03, T-01, U-01, and U-02) are shown in Fig. 2 and the values are presented in Table 1. The twelve representative sandstone core samples used had porosities between 8.01% and 17.91% and permeabilities between 4.9 mD and 1146 mD.

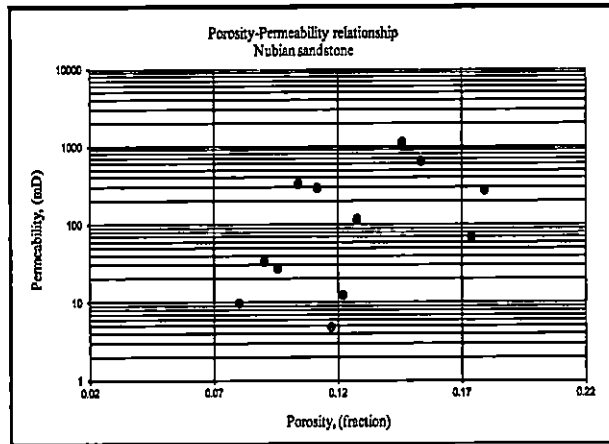


Fig. 2. Porosity Vs. Permeability for the studied area

Table 1. Porosity and permeability values of the selected representative samples

Samples#	Well Name	Ø (%)	K(mD)
1	S1	10.39	337.5
2	S2	9.01	34.11
3	S3	12.17	12.55
3	T1	14.59	1146
5	S3	8.01	9.910
6	U2	17.38	69.86
7	U1	15.34	660.4
8	S3	11.71	4.901
9	U2	17.91	279.7
10	S1	11.16	297.7
11	S2	9.56	27.73
12	S2	12.76	118.1

Saturation exponent (n), capillary pressure(Pc) and resistivity index (RI) before and after wettability measurement

Saturation exponent (n) values are normally determined experimentally in the laboratory on core samples of the actual formation under consideration. Due to the fact that the saturation exponent varies with both lithology and wettability a suite of saturation exponent value measurements is often conducted on samples with a range of porosity, permeability and lithology which may be present in the formation (Bennion *et al*, 1996). Saturation exponent values were determined on the twelve representative core samples from porous plate capillary pressure measurements in the laboratory.

The selected plugs were taken from six wells from the Nubian Sandstone Formation. The samples were cleaned in hot solvents, dried and then mounted into the core holder. All the samples were saturated with the brine (salinity 135,000 ppm). Powder was used between the samples and the porous plate to maintain hydraulic contact during the test. During the measurement, the pressure was increased in steps and the final equilibrium produced volumes of the wetting phase were recorded for each step. In the present work, the output data of capillary pressure for sample #3 before and after wettability measurement is displayed in Table 2 and in Fig. 3 and 4. Because the wettability affects waterflood performance, Amott wettability measurements were made on the same samples.

The saturation exponent for sample # 1 before wettability measurement was 1.39. When the wettability measurement was conducted on the

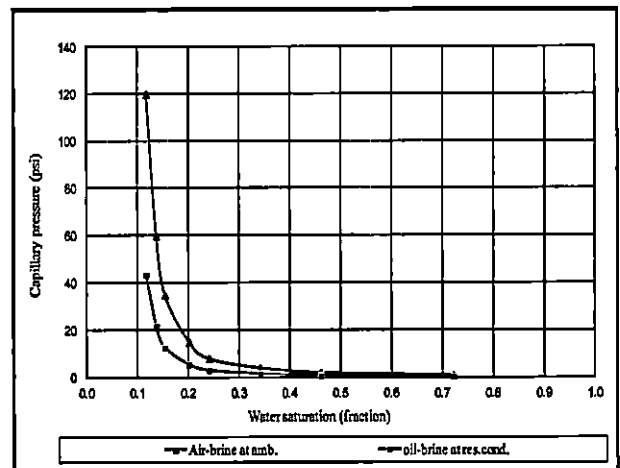


Fig. 3 Capillary pressure curves for sample # 1 before wettability measurement

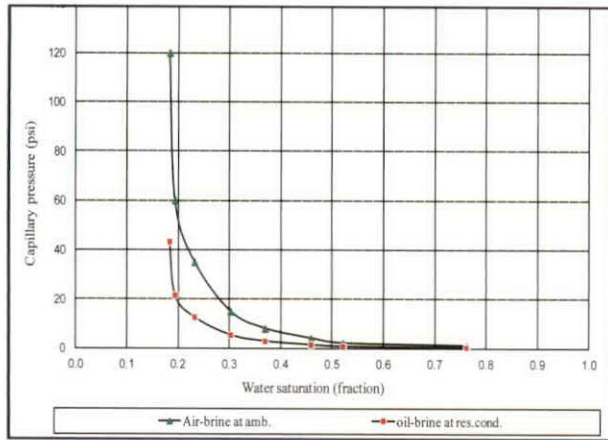


Fig. 4 Capillary pressure curves for sample # 1 after wettability measurement

sample, the sample imbibed oil (tendency to be oil-wet), and the saturation exponent increased to 2.39 as shown in Table 3 and in Fig. 5.

Estimation of hydrocarbon reserves are strongly dependent of electric log data and on the value of saturation exponent (n) used. The saturation exponent is usually either assumed to be 2.0 regardless of reservoir wettability or is derived from laboratory measurement of electrical properties of the cores. It can vary between 1.2 and 2.2 (Serra, 1984) for water-wet rocks and can have a value from 2.2 or higher when the rock wettability changes towards oil-wet (Anderson, 1986). For sample #1 the saturation exponent before wettability measurement was 1.39, and when the wettability test was conducted the sample imbibed oil (tendency to be oil wet), and the saturation exponent increased to 2.39. In water-wet rock, the brine occupies the small pores and forms a continuous film on the rock surface. In an oil-

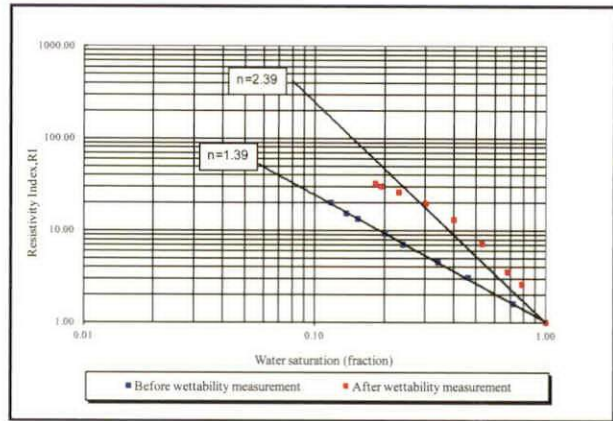


Fig. 5. Resistivity index versus water saturation before and after wettability measurement for sample # 1.

wet rock, the brine is located in the centres of the large pores. This difference in brine distribution caused by the wettability becomes very important as the brine saturation is lowered. Generally, almost all of the brine in the water-wet rock remains continuous, so the resistivity increases because of the decrease in cross-sectional area that can conduct flow. In oil-wet rock, a portion of the brine will lose electrical continuity, so the saturation exponent will increase at a faster rate. In oil-wet rock, a fraction of the non-wetting phase (specially at low brine saturation) which is located in the middle becomes disconnected and surrounded by oil which acts as an insulator to the flow of electric current. The insulation of this portion of brine prevents it from contributing to the flow of electric current and hence leads to higher values of saturation exponent. Finally, in Fig. 6 Archie's saturation exponent increases as the rock becomes more oil wet.

Table 2. Resistivity index and water saturation for sample #1 from porous plate capillary pressure measurement.

Capillary pressure at ambient. (Psi)	Capillary pressure at reservoir (Psi)	Water Saturation Before Wettability Measurement (fraction)	Water Saturation After Wettability Measurement (fraction)	Resistivity Index (RI) Before Wettability Measurement	Resistivity Index (RI) After Wettability Measurement
1	0.36	0.7214	0.7873	1.451	3.997
2	0.72	0.4612	0.6843	1.460	3.327
4	1.44	0.3414	0.5300	1.407	3.099
8	2.89	0.2410	0.4000	1.371	2.799
15	5.42	0.2014	0.3018	1.387	2.475
35	12.6	0.1536	0.2315	1.382	2.223
60	21.7	0.1368	0.1935	1.371	2.072
120	43.3	0.1174	0.1832	1.400	2.047

Table 3. Saturation exponent values before and after wettability measurement.

Sample #	Well Name	Saturation Exponent (n) Before Wettability Measurement	Saturation Exponent (n) After Wettability Measurement
1	S1	1.39	2.39
2	S2	1.75	2.60
3	S3	2.06	2.79
3	T1	1.76	2.65
5	S3	1.93	2.18
6	U2	1.79	2.59
7	U1	1.87	2.50
8	S3	2.18	2.86
9	U2	1.91	2.65
10	S1	1.78	2.43
11	S2	1.97	2.49
12	S2	1.73	2.22

CONCLUSIONS

- Changes were observed in the saturation exponent (n) and water saturation (S_w) before and after wettability measurement. Samples with an oil-wet tendency have higher irreducible brine saturation and higher Archie saturation exponent values than samples with an uniform water-wet surface.
- A linear relationship existed between wettability index and the saturation exponent for the studied wells. Archie's saturation exponent increases with decreasing wettability index because the saturation exponent increases as the rock becomes more oil-wet.

NOMENCLATURES

I_w	=	Displacement by water ratio
I_o	=	Displacement by oil ratio
I_{AH}	=	Amott Harvey Wettability Index
K	=	Permeability, mD
n	=	Archie's saturation exponent, dimensionless
R	=	Resistivity, ohm.m
RI	=	Resistivity Index, dimensionless
R_t	=	True resistivity of the partially saturated rocks, ohm.m
R_o	=	Resistivity of fully saturated rock, ohm.m
R_w	=	Water resistivity, ohm.m

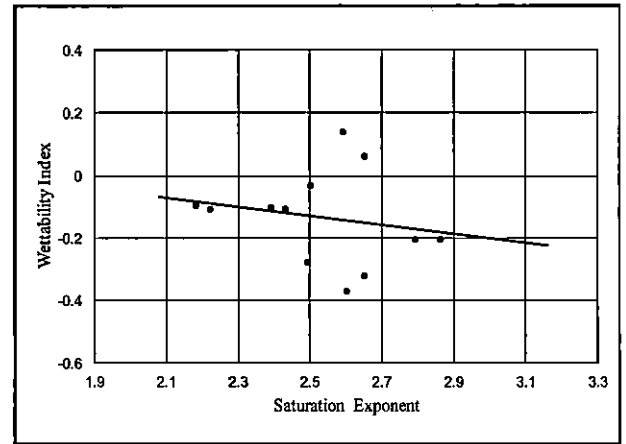


Fig. 6. Saturation exponent as a function of wettability index for the twelve selected representative samples.

S_w	=	Water saturation, fraction
S_{or}	=	Residual Oil Saturation, fraction
$V_{o,s}$	=	Volume of oil Spontaneously imbibed, cc
$V_{o,d}$	=	Volume of oil dynamically imbibed, cc
V_w	=	Water Volume, cc
$V_{w,s}$	=	Volume of water Spontaneously imbibed, cc
$V_{w,d}$	=	Volume of water dynamically imbibed, cc

ACKNOWLEDGEMENTS

I would like to take this opportunity to thank the people that have helped me to this work. The author acknowledges very much to head of reservoir rock section at Libyan Petroleum Institute, LPI, who patiently supervised the evolution of my work. I wish also to express my sincere thanks to Libyan Petroleum Institute for providing the necessary data.

REFERENCES

- Anderson, W. G. (1986). Wettability Literature Survey-Part 3: The Effect of Wettability on Electrical Properties of Porous Media. *JPT*: 1371-1378.
- Archie, G. E. (1942). The Electrical Resistivity Log as an Aid in Determining Some Reservoir Characteristics. *Trans.AIME, V. 146*: 54-62.
- Barr, F. T. and Weegar, A. A. (1972). Stratigraphic Nomenclature of the Sirte Basin, Libya, *Petrol. Explor. Soc. Libya*: 179.
- Bennion, D., B., Thomas, F., B. and Bietz, R., F. (1996). Determination of Initial Fluid Saturations Using Traced Drilling Media. *Hycal Energy Research Laboratory Ltd. 99-8*: 2-11.
- Killer G. V. (1953). Effect of Wettability on Electrical Resistivity of Sand. *Oil and Gas Journal*: 62-65.

Mungan, N. And Moore, E. J. (1968). Certain Wettability Effects on Electrical Resistivity in Porous Media. *The Journal of Canadian Petroleum Technology*: 20-25.

Serra, O. (1984). Fundamentals of Well-Log Interpretation (Vol. 1): The Acquisition of Logging Data. *Dev. Pet. Sci.*, 15A, Amsterdam (Elsevier).

Sweeny, S. A. and Jennings, H. Y. (1960). The Electrical Resistivity of Preferentially Water-Wet and Preferentially Oil-Wet carbonate Rock. *Producers Monthly*, may; 29-32.

EVALUATION OF EMPIRICAL PVT CORRELATIONS AND EOS TUNING TO MODEL LIBYAN CRUDE OIL PROPERTIES USING PVTi SOFTWARE

Wahid R. Shtewi, Msc.*

Abstract: Understanding the PVT properties is very important to many kinds of petroleum determinations such as calculations of reservoir fluid properties, expect the future performance, selection of enhanced oil recovery methods, and production facilities design. Predict forecasting the reservoir fluid properties through imperical models have been increased during the last decade by knowing reservoir pressure and temperature, oil API gravity, and gas gravity. Correlations are used whenever experimentally derived PVT data are not available and data from local regions are expected to give better approximation to estimated PVT values.

In this paper, complete PVT lab experiments were done and then evaluate the most frequently used empirical black oil PVT correlations for application in the Middle East. Empirical PVT Correlations for Middle East crude oil have been compared as a function of commonly available PVT data. Correlations have been compared for: bubble point pressure; solution gas oil ratio, oil formation volume factor, and oil viscosity. After evaluates the Empirical correlations the crude sample was characterized using different EOS to arrive at one EOS model that accurately describes the PVT behavior of crude oil produced. The multi-sample characterization method is used to arrive at one consistent model for crude oil for the whole reservoir. The fluid sample is first analyzed for consistency to make sure that they are representative of oil produced, and then it is used to obtain parameters for EOS model. The tuning procedure for the EOS is done systematically by matching the volumetric and phase behavior results with laboratory results. Results showed some correlations gives good results and can be used with Libyan oil and some gives high percentage of error. For EOS all of them need tuning because mismatching with lab data but after regression a very good match of PVT properties predicted are getting.

Keywords: PVT proerties, Bubble point pressure, Solution gas oil ratio, Oil formation volume factor, Oil viscosity, Emperical correlations, EOS.

INTRODUCTION

The PVT studies or analysis is very important in petroleum engineering, it is considered as the main part for petroleum reservoir studies, the selection of enhanced oil recovery techniques, production equipments design and the evaluation of the recovery efficiency of oil fields. In the lack of PVT data for any reason; correlations are used to get the physical properties of reservoir hydrocarbons (Hemmati and Kharrat, 2007).

A reservoir PVT behavior can be very complicated especially when the composition and PVT properties vary with depth, or when different geological formations produce significantly different fluids from the same field. The PVT behavior cannot be

described properly by a single set of PVT properties, where composition, saturation pressure, API oil gravity, producing GOR and reservoir temperature may vary (Danesh, 1998). As a result the PVT data are considered to be essential and need to be updated continuously. Thus, understanding, handling and using the resulting data from traditional PVT reports is of great importance to the petroleum engineers. It is worth mentioning that PVT data to be feed into the black-oil or compositional simulator can be obtained from empirical correlations, laboratory measurement, and EOS fluid characterization (McCain, 1990).

In reservoir performance estimations the Empirical PVT correlations which are generally used in petroleum engineering are very vital tools. The PVT parameters usually obtained from lab experiments by using representative samples. But, reservoir fluid properties must be calculated when detailed laboratory PVT data are not available. Because the chemical

*Petroleum Engineering, Specialist in Reservoir Fluid section (PVT lab)
Libyan Petroleum Institute Tripoli/Libya Email: w.shtewi@lpilibya.com

composition of crude oil differs from region to region, the geological conditions must be considered for modified or developing correlations.

Equations of State E.O.S are increasingly being used to model fluid properties of crude oil and gas reservoirs. This technique offers the advantage of an improved fluid property prediction over conventional black oil models. Once the crude oil or condensate fluid system has been probably characterized, its PVT behavior under a variety of conditions can easily be studied. This description is then used, within a compositional simulator, to study and choose among different scenarios for EOR schemes, such as miscible gas injection for oil reservoirs or liquid recovery under lean gas injection for condensate reservoirs (PVTI Reference Manual, 2014).

GETTING PVT PROPERTIES TECHNIQUES

Laboratory Experiments

Typical tests are performed on bottom hole or surface samples to characterize the hydrocarbon fluids. They involve differential test, constant mass expansion, constant volume depletion, and flash separation tests and the measurement of the fluid composition, molecular weight, specific gravity, viscosity, compressibility, saturation pressure, formation volume factor, solubility. These tests are designed to simulate to the thermodynamic reservoir processes. Although some assumptions where applied, and some other real factors were not considered (such as the presence of porous media and water phase) testing results are considered to be an important source of data in reservoir engineering calculations (Ahmed, 1989; Bradley, 1987). The three main application areas of the PVT data are:

- To provide data for reservoir calculations.
- To provide physical property data for fluid flow calculations.
- For designing surface production facilities.

Oil System Correlations

The knowledge of physical properties for reservoir fluids are very important to petroleum engineers for both reservoir and production estimations. For reservoir performance studies these properties should be calculated at reservoir temperature and various pressures, and for wellbore hydraulics determinations at conditions of both changing temperature and pressure.

If reservoir fluid samples are available, the fluid properties of interest can be measured with

a pressure-volume-temperature (PVT) analysis. However, these analyses usually are conducted at reservoir temperature only and the variation of the properties with temperature is not available for production system calculations. Also, in many cases a PVT analysis may not be available at the beginning of the reservoir life or may never be available because of economic reasons. To overcome these obstacles, empirical correlations have been developed for predicting various fluid physical properties from limited data. The main purpose of correlations is for estimating properties of reservoir fluids such as:

- Bubble Point Pressure (Al-Marhun, 1988; Khazame, 2016; Dokla and Osman, 1992; Vasquez & Beggs, 1980; Petrosky and Farshad, 1990; Glaso, 1980).
- Oil Formation Volume Factor (Vasquez & Beggs, 1980; Al-Marhun, 1988; Petrosky and Farshad, 1990; Glaso, 1980).
- Gas Oil Ratio. (Vasquez & Beggs, 1980 ; Al-Marhun, 2002; Petrosky and Farshad, 1990; Glaso, 1980).
- Crude Oil Viscosity (Chew and Connally, 1959; Beggs and Robinson, 1975; Glaso, 1980).

Equation of State Simulation

"Equation of State" is defined as an analytic expression relating pressure to temperature and volume.

Because of relatively high cost of performing the experimental PVT tests and the uncertainties in the accuracy of such laboratory measurements, equation of state offer an attractive approach for generating these necessary data.

The major goal of reservoir simulation is to predict future performance of the reservoir and find ways and means of optimizing the recovery of some of the hydrocarbons under various operating conditions.

CONDUCTED WORK & RESULTS

Part One: Evaluation of PVT Correlations

Complete PVT analysis including direct flash, constant composition expansion (flash liberation process), differential liberation process, and oil viscosity tests were conducted for reservoir oil sample from one of Libyan oil fields.

In this part, all the PVT experiments were conducted in the PVT lab of the Libyan Petroleum Institute then the results of experiments were compared with the results from the Empirical correlations. All tests at reservoir temperature 204 °F:

- **Bubble Point Pressure, P_b :**
The Experimental $P_b = 660$ Psia
- **Oil Formation Volume Factor, B_{oi} :**
The Experimental $B_{oi} = 1.0965$ bbl/STB
- **Gas Oil Ratio, R_s :**
The Experimental $R_s = 93$ Scf/STB
- **Oil Viscosity:**
Experimental dead oil viscosity =5.705cp
Experimental bubble point (saturated) oil viscosity = 4.915 cp
Experimental under saturated oil viscosity at reservoir $P=2686$ psia & $T =204$ F° =5.184cp
To evaluate the Empirical correlations for estimating the oil viscosity, the viscosity by correlations in three faces have to be determined at dead oil, saturated oil, and under saturated oil viscosity and compare them with the lab results.

Part Two: Equation of State Model Simulation of PVT lab data by E.O.S (PVTi software)

In this part, the PVTi software was used to simulate the Laboratory PVT data by using the scenario of entered the reservoir component up to C7+(with impurities N_2 , CO_2 , H_2S) and tuning by changing these parameters, binary interaction parameter (BIP), omega a parameter (Ω_a), acentric factor parameter (ω), and Zc for oil viscosity. All results of comparison and model are illustrated in tables 1-8 and figures 1-3

CONCLUSIONS

The followings are the main conclusions that can be withdrawn from this study:

- 1- Complete PVT lab studies have been done for Libyan oil samples to compare the properties with the empirical correlations for Middle East crude oil and the results show that there is a clear difference.
- 2- The results of evaluation show that some of correlations are reliable to use with Libyan crude oil and others give high percentage of error.
- 3- Average absolute relative error is an important indicator of the accuracy of an empirical model; it is used in this study as a comparative criterion for testing the accuracy of correlations.
- 4- The oil formation volume factor correlation provided the best accuracy of the correlations evaluated.
- 5- Characterization the experimental data by PVTi software show that when we use the original Equation of State to predict the previous PVT

properties, we have got unsatisfactory results and all the E.O.S needs tuning.

- 6- After regression we found that:
- There are a good match with lab results.
 - The bubble point pressure is very sensitive to the omega A and Tc.
 - The best EOS are 3parameter Peng_Robinson (PR3) and 3parameter Soave_Redlich_Kwong (SRK3), while Radlich_Kowng (RK) proved to be the worst one.
 - For oil viscosity the ZJ correlation gives high percentage of error so it's not advised to use.
 - The best regression for oil viscosity by change Zc parameter.

Table 1: Experimental and Calculated P_b , Psia.

Correlation	Experimental P_b	Calculated P_b	Abs. Error %
Standing	660	615	6.8
Glaso	660	596	10.7
Vesquez	660	609	7.7
Marhoun	660	746	11.5
Petrosky	660	632	4.4
Dokla	660	539	18.3
Mohsen Khazam	660	797	20.8
Valko & McCain	660	631	4.4
Omar & Todd	660	702	6.3
Al-shammasi	660	667	1.1
Macary & Elbatanoney	660	806	22
Mehran	660	652	1.2

Table 2: Experimental and Calculated B_o , bbl/STB.

Correlation	Experimental B_o	Calculated B_o	Abs. Error %
Standing	1.0965	1.1091	1.15
Glaso	1.0965	1.0802	1.5
Vesquez	1.0965	1.1189	2
Marhon	1.0965	1.1303	3
Petrosky	1.0965	1.0961	0.03
Material Balance	1.0965	1.0190	7
Schmidt	1.0965	1.1273	2.8
Arps	1.0965	1.0965	0

Table 3: Experimental and Calculated Rs, Scf/STB

Correlation	Experimental R_s	Calculated R_s	Abs. Error %
Standing	93	529	469
Glaso	93	442	375
Vesquez	93	471	407
Marhon	93	558	500
Petrosky	93	475	411
Velarde	93	553	495
Hanafy	93	789	748
De Ghetto	93	213	129

RECOMMENDATIONS

From this study, it is recommended that before using the Empirical correlations in reservoir calculations, make sure that they can be used for estimating the same PVT parameters for all types of oil and gas mixture with properties falling within the range of data for each correlation. With Libyan crude oil we advice to modify a new correlations that special for Libyan oil. When we use any simulator we should to choose the right parameter for tuning to get good match model.

Table 4: Experimental and Calculated oil viscosity

Dead Oil Viscosity			
Correlation	Experimental μ_{od}	Calculated μ_{od}	Abs. Error %
Beal's	5.705	3.334	41.5
Beggs	5.705	3.291	42.3
Glaso	5.705	3.793	33.5
Saturated Oil Viscosity			
Correlation	Experimental μ_{ob}	Calculated μ_{ob}	Abs. Error %
Chew	4.915	4.059	17.4
Beggs	4.915	3.129	36.3
Under-Saturated Oil Viscosity			
Correlation	Experimental μ_o	Calculated μ_o	Abs. Error %
Beggs	5.184	6.885	32.8

Table 5: Experimental and simulated Pb

Equation	P_b lab	Pb before tuning	ADD%	Pb After tuning	ADD%
PR3	660	403	39	660	0
SRK3	660	395	40	660.18	0.02
RK	660	267	59.5	478	27.5
ZJ	660	398	39.6	660.3	0.04

Table 6: Experimental and Simulated Bo

Equation	B_o lab	Bo before tuning	ADD%	Bo After tuning	ADD%
PR3	1.0965	1.1151	1.7	1.1112	1.3
SRK3	1.0965	1.1223	2.3	1.0781	1.68
RK	1.0965	1.1791	7.5	1.0965	0
ZJ	1.0965	1.1474	4.6	1.1096	1.2

Table 7: Experimental and Simulated Rs

Equation	R_s lab	Rs before tuning	ADD%	Rs After tuning	ADD%
PR3	93	81.9	12	89.3	4
SRK3	93	84.4	9.2	76	18
RK	93	74.3	20	75.5	19
ZJ	93	85.6	7.9	87.9	5.5

Table 8: Experimental and Simulated oil viscosity

Dead Oil Viscosity					
Equation	μ_{od} lab	Before tuning	ADD%	After tuning	ADD%
PR3	5.705	4.121	27.7	6.764	18.5
SRK3	5.705	3.834	32.7	5.022	11.9
RK	5.705	1.084	80.9	2.458	56.9
ZJ	5.705	3.420	40	13.219	132
Saturated Oil Viscosity					
Equation	μ_{ob} lab	Before tuning	ADD%	After tuning	ADD%
PR3	4.915	3.674	25.3	4.774	2.868
SRK3	4.915	3.463	29.5	4.815	2
RK	4.915	1.072	78.2	2.382	51.5
ZJ	4.915	3.111	36.7	11.893	142
Under-Saturated Viscosity					
Equation	μ_o lab	Before tuning	ADD%	After tuning	ADD%
PR3	5.184	4.583	11.6	5.773	11.3
SRK3	5.184	4.617	10.9	5.742	10.7
RK	5.184	1.326	74.4	2.959	42.9
ZJ	5.184	3.827	26.2	14.289	175

NOMENCLATURES

- PVT pressure-volume-temperature
- B_o oil formation volume factor, bbl/STB
- API stock-tank oil gravity, APIo
- GOR gas oil ratio
- OFVF oil formation volume factor
- P_b bubble point pressure, psia
- R_s solution gas-oil-ratio, SCF/STB
- SCF standard cubic feet
- STB stock tank barrel
- Y_g gas specific gravity (air = 1)
- Y_o oil specific gravity (water = 1)
- T reservoir temperature, °R
- μ_o viscosity of under-saturated oil, cp
- μ_{ob} viscosity of saturated oil, cp
- μ_{od} viscosity of the dead oil as measured at 14.7 psia and reservoir temperature, cp
- EOS equation of state
- SCF standard cubic feet
- STB stock tank barrel
- SW schmidt-wenzel E.O.S
- PR peng-robinson E.O.S
- RK redlick-kwong E.O.S
- SRK soave-redlick-kwong E.O.S

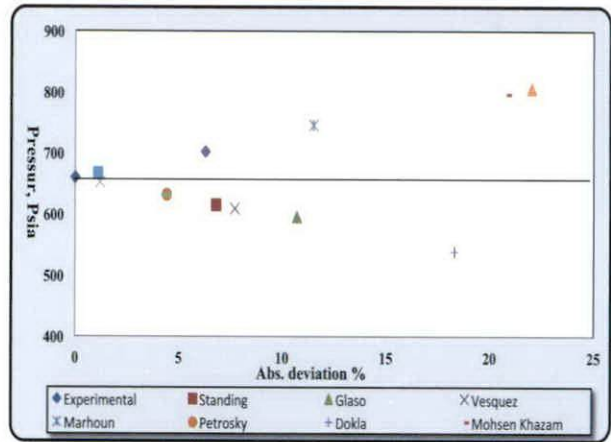


Fig. 1. Experimental and Calculated P_b

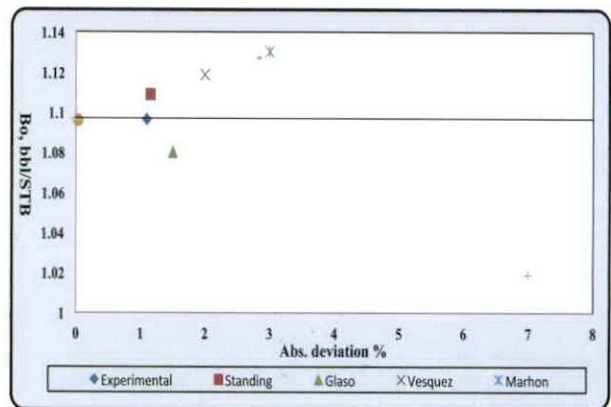


Fig. 2. Experimental and Calculated B_o

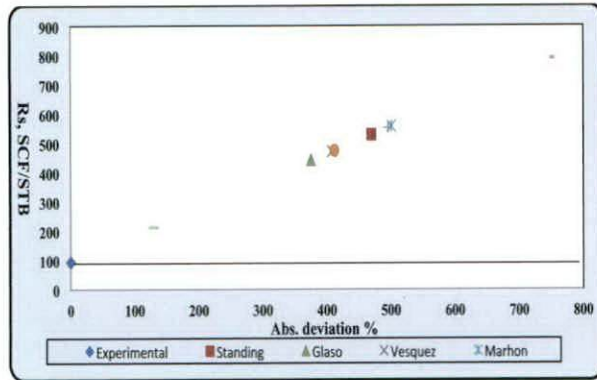


Fig. 3. Experimental and Calculated Rs

REFERENCES

- Ahmed, T. (1989). Hydrocarbon Phase Behavior. *Gulf Publishing Company*, Houston, Texas, *V. 7*: 136-244.
- AL-Marhoun, M. A. (1988). PVT Correlations for Middle East Crude Oils, *JPT*, *V. 40(5)*: 650-666.
- AL-Marhoun, M. A. (2002). Reservoir Fluid Properties—State of the Art and Outlook for Future Development. *Distinguished Lecturer Program SPE*: 2001-2002.
- Beggs, H. D. & Robinson, J. R. (1975). Estimating the Viscosity of Crude Oil Systems. *JPT*, P.P 1140-1141.
- Bradley, H. B. (1987). Petroleum Engineering Handbook, *Third Edition*, USA, *Society of Petroleum Engineers*: 680.
- Chew, J. and Connally, C. A. (1959). A Viscosity Correlation for Gas-Saturated Crude Oils. *Trans. AIME*, *V. 216*: 23-25.
- Danesh, A. (1998). PVT and Phase Behavior of Petroleum Reservoir Fluids, *First Edition*, Amsterdam, Elsevier Science B.V. 403.
- Dokla, M. F. and Osman, M. E. (1992). Correlation of PVT Properties for UAE Cruds. *SPE*: 80-81.
- Glaso, O. (1980). Generalized Pressure-Volume-Temperature Correlations, *JPT*: 785-795.
- Hemmati, M. N. and Kharrat, R. (2007). Evaluation of Empirically Derived PVT Properties for Middle East Crude Oils. *Scientia Iranica*, *V. 14(4)*: 358-368.
- Khazame, M. (2016). New PVT Correlations Based on Libyan Crudes for Predicting Fluid Physical Properties, *Oil and Gas Research*, **2016**:1-9.
- McCain, W. D. (1990). The Properties of Petroleum Fluids, *Second Edition*, Tulsa, OK, USA: Pennwell Books: 584.
- McCain, W. D. (1991). Reservoir-Fluid Property Correlations—State of the Art. *SPE*: 266-272.
- Petrosky, G. E. & Farshad F. F. (1990). Pressure-Volume-Temperature Correlations For Gulf of Mexico Crude Oils, *SPE Paper No.26644*.
- PVTi Software Technical Description file (2014). Schlumberger Reference Manual.
- Vasquez, M. and Beggs, D. (1980). Correlations for Fluid Physical Properties Prediction. *JPT*: 968-970.

THE EFFECTS OF CHANGES IN OVERBURDEN PRESSURE ON KLINKENBERG PERMEABILITY MEASUREMENTS FOR SIRT BASIN

Rashid Toumi, Adel Grera, Ahmed Naami*

Abstract: Klinkenberg permeability (Kl) correction at different overburden pressures and air permeability (Ka) was carried out at the same overburden pressures for one hundred plug samples of 1" and 1.5" diameter from different formations from Sirt Basin of clastic and carbonate reservoirs. The samples were measured using Keyphi instrument, the measurements covered a permeability range of 0.03mD - 600mD. The results showed a strong correlation between the Klinkenberg and air permeabilities for the samples of high permeability values and the effect of slippage is more clear on the low permeability samples (less than 1mD), a composite curve has been established for all the samples in order to investigate the effect of variation in O.B.P on the permeability values.

Keywords: Air permeability, Klinkenberg permeability, Gas slippage, Overburden pressure.

INTRODUCTION

Permeability is a property of the porous medium and is a measure of the capacity of the medium to transmit fluids. Absolute permeability is a very important parameter necessary for any prediction of reservoir production performance. In the measurement of permeability certain precautions must be exercised in order to obtain accurate results when gas is used as a testing fluid. Correction must be made for gas slippage; this correction must also be applied to the change in permeability caused by the reduction in pore size due to the effect of the change in overburden pressure (Estes *et al*, 1956 and Amyx *et al*, 1960;).

Klinkenberg (1941) had reported variations in permeability as determined using gases as the flowing fluid from that obtained when using non reactive liquids at ambient conditions. These variations were attributed to slippage, a phenomenon well known with respect to gas flow in capillary tubes (Klinkenberg, 1941; Jones, 1972). In general, conventional measurement of porosity and permeability are conducted at ambient conditions. However, in the reservoir the rocks are subjected to both pressure and temperature. When cores are

brought up from the well bottom, all the external forces acting on them are eliminated and the rock matrix is allowed to expand in all directions. The shape of the pores for storage of fluids and pore throats for fluid flow are therefore changed.

Expansion of the rock due to overburden pressure/stress relief can produce an increase of 30% or higher in the permeability of the rock. Consequently, a large population of plug samples was subjected to porosity and permeability measurements at varying overburden pressures in order to develop an empirical correlation necessary for correcting the permeability of the rest of the rock samples for the effect of overburden pressure. Groups of samples with low, medium and high permeability were used (Jones, 1988; Abousrafa, 2004).

EXPERIMENTAL WORK

Core data was gathered over a period of years from 18 wells representing all of the formations in Sirt Basin. One hundred plug samples of 1" and 1.5" diameter were used in this petrophysical analysis at LPI laboratories to establish a relationship between air permeability and Klinkenberg permeability at different overburden pressures.

The plug samples used for permeability testing were cleaned using toluene to extract the hydrocarbons, then leached of salt using methanol and

*Libyan Petroleum Institute, Libya

oven dried at 80 °C. The samples were then placed in the Keyphi instrument, which is a fully automated porosimeter and permea-meter which is used to determine porosity and permeability at different overburden pressures, Keyphi utilizes an unsteady state measurement technique. The measurements and the calculations of these petrophysical properties are based on the techniques described by API (Recommended practice 40, 1998).

The plug sample is mounted in a hydrostatic core holder, which is connected by pipe-work and valves to a chamber of known volume in conjunction with a pressure transducer (Fig. 1). The core holder is capable of applying confining pressure of up to 10,000psi. The chamber is charged with helium to a predetermined pressure. When the valve which separates the core holder and the chamber is opened, the gas flows through the sample and exits to atmosphere at the downstream end of the sample (Keyphi User Manual, 2001).

The draw down pressure is then recorded versus time. Analysis of the pressure transient profile makes it possible to calculate Klinkenberg corrected permeability and non-corrected permeability. The permeability of the plug samples were measured at confining pressure values of 800, 1500, 2500, 4000 and 6000psi with a permeability range of 0.03mD to 600mD.

RESULTS AND DISCUSSION

Klinkenberg (Kl) and air (Ka) permeabilities for a range of 0.03-600 mD were measured at different overburden pressures (OBP) and compared graphically. The lithologies of the rock samples included clastic and carbonate rocks are all from formations of the Sirt Basin. Air and Klinkenberg permeabilities at each OBP

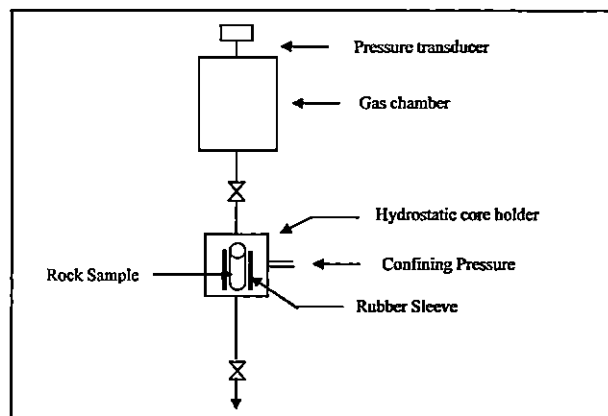


Fig. 1. Schematic of pressure-fall off gas permeameter.

are presented separately in log-log scale along with a composite plot for all the pressures. The two parameters show a strong relationship over the measured range. Klinkenberg Corrected permeabilities at O.B.P are slightly lower than the equivalent air permeabilities as would be expected, but also because of the changes in pore geometries due to the effects of the applied OBP.

Figures 2 through 6 show equivalent data for one hundred sets of specific air and Klinkenberg permeabilities measured at an increasing OBP for both clastic and carbonate formations. The graphs show good correlation between the measured permeabilities at each overburden pressure.

Figure 7 shows a composite plot of all of the overburden data and gives the equation derived from that data. This plot displays a strong correlation over the OBP range, where the correlation coefficient (R2) of this plot is 0.9939 and the standard error is 0.077. There is a tendency for the lower permeability samples (less than 0.1 mD) to deviate from the trend line; this may be due an increased gas slippage in these tight samples

CONCLUSIONS

- 1) The composite graph shows a strong correlation between Klinkenberg permeability and air permeability at varying OBP.
- 2) Based on the data presented, a general equation fits all the tested samples is established. This equation has the form:

$$Kl_{(OBP)} = 0.834 * K_{a(OBP)}^{1.025}$$

- 3) Corrected Klinkenberg permeability obtained from this correlation can be used as a good tool in reservoir characterization for the Sirt Basin.
- 4) The correlation is a cost-effective method for estimating Klinkenberg permeability instead of measuring Kl in the laboratory. This correlation can also be applied to previously measured air permeabilities at different OBP.

RECOMMENDATIONS

- 1) This study should be continued to include more samples and also cover a wider permeability range.
- 2) Implementation of such a correlation tool could be extended to cover all the Libyan basins.

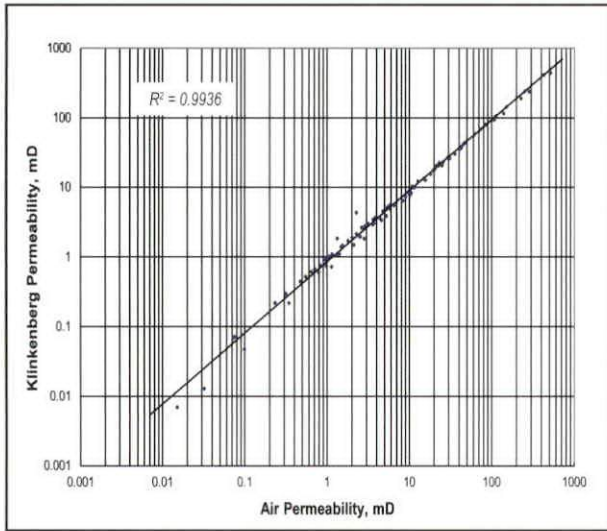


Fig. 2. Klinkenberg Permeability Vs Air Permeability at NOB of 800.

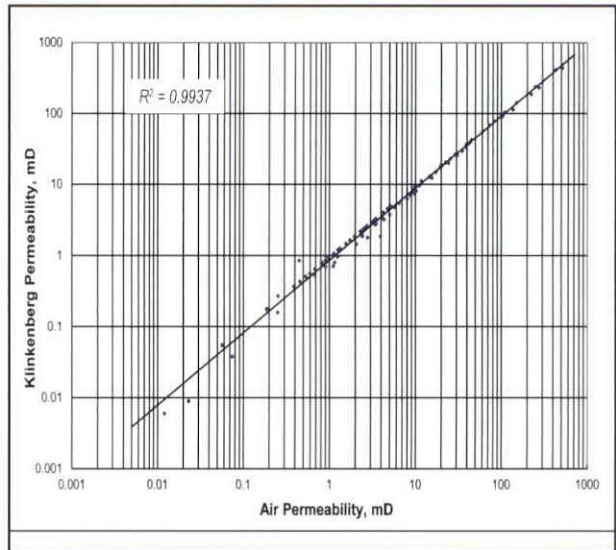


Fig. 3. Klinkenberg Permeability Vs Air Permeability at NOB of 1500.

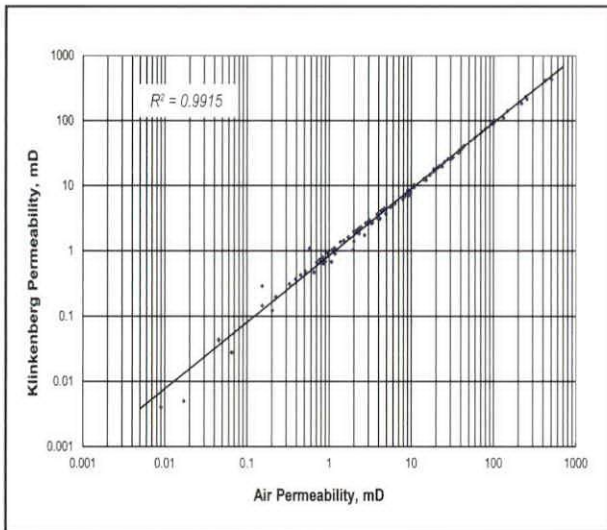


Fig. 4. Klinkenberg Permeability Vs Air Permeability at NOB of 2500.

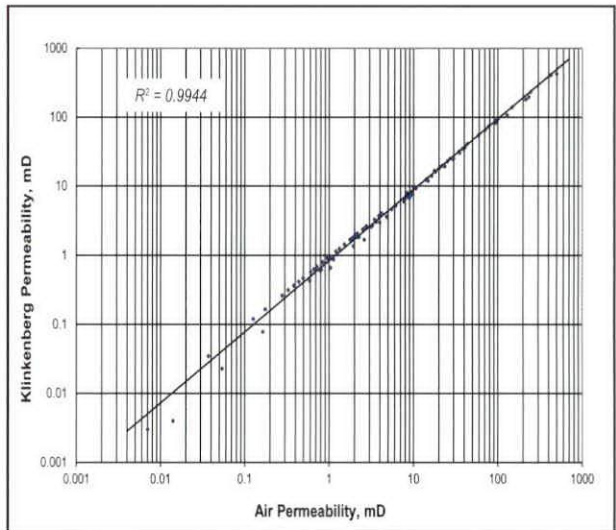


Fig. 5. Klinkenberg Permeability Vs Air Permeability at NOB of 4000.

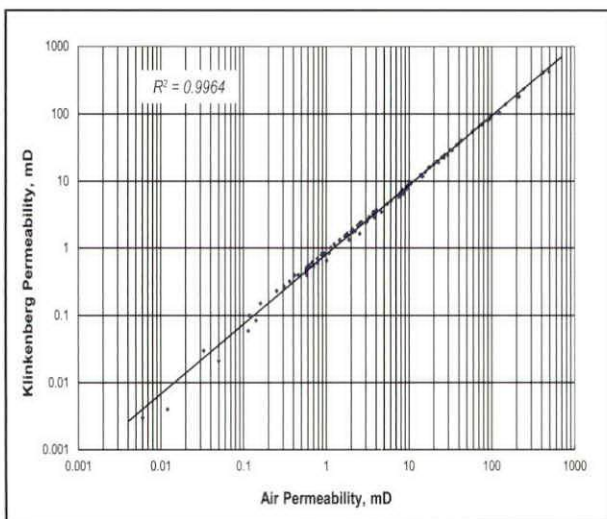


Fig. 6. Klinkenberg Permeability Vs Air Permeability at NOB of 6000.

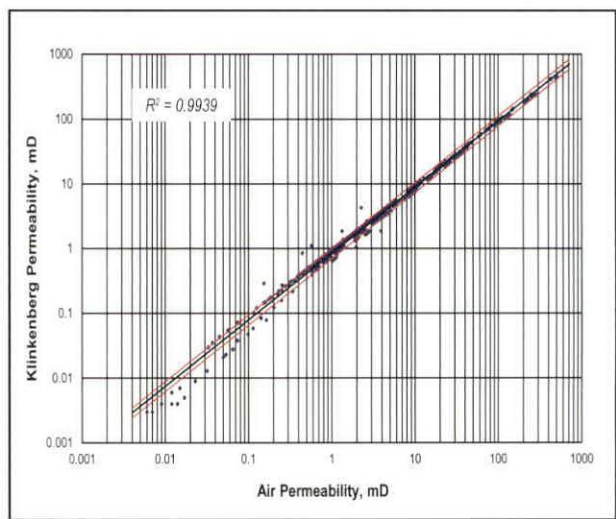


Fig. 7. Composite Graph.

NOMECLATURES

K_a = Air permeability, mD

K_l = Klinkenberg permeability, mD

$K_{a(OBP)}$ = Air permeability at overburden pressure, mD

$K_{l(OBP)}$ = Klinkenberg permeability at overburden pressure, mD

OBD = Overburden pressure, psi

mD = milli Darcy

REFRERNCES

- Abousrafa, E. (2004). Coring and Core Analysis, Training Manual, *Pet. Research Center*, Libya: 252.
- Amyx, J. W., Bass D. M. Jr. and Whiting R. L. (1960). *Petroleum Reservoir Engineering: Physical Properties*. McGraw-Hill Book Co., New York, USA: 610.
- API (1998). Recommended Practice 40, *section 6(4)*: 32-38.
- Estes, R. K. and Fulton, P.F. (1956). Gas Slippage and Permeability Measurements. *JPT. V. 8*: 63-73.
- Jones, S. C. (1972). A Rapid Accurate-Unsteady State Klinkenberg Permeameter. *SPEJ, Trans. AIME, 253*: 383-397.
- Jones, S. C. (1988). Two-Point Determination of Permeability and PV vs. Net Confining Stress. *SPE Formation Evaluation*: 235-241.
- Keyphi User Manual (2001). *VINCI Technologies*, France : 208.
- Klinkenberg, L .J. (1941). The Permeability of Porous Media to Liquid and Gases. *American Petroleum Institute*, Drilling and Production Practice: 200-213.

LIBYAN GAS COMPOSITION ANALYSIS AND PREDICTION

Omar Hussein El Ayadi Esra A. Swedan*

Abstract: Gas process or refrigerate always requires specific gas details i.e. gas composition. Generally, types of gas or differentiating between gases depend on composition. The main aim of this study is to evaluate and predict the Libyan gas composition utilizing the triangle plots. The gas composition data (313 old +60 last) collected for most of Libyan reservoirs. Moreover, getting a relation between gas molecular weight and ($C_1 + C_2$) and hence to find whole other compositions. The average value of every gas component was estimated including the non-hydrocarbon gases. Nevertheless, the isomers and normal structure of C_4 and C_5 were also obtained.

It is concluded that the old collected data matched and very close to the new or last collected data. However, the gas composition can be easily obtained if gas molecular weight (measured or estimated) at different separator pressure of oil and associated gas.

Keywords: Gas composition analysis, refrigerate, PVT.

INTRODUCTION

Petroleum is a mixture of naturally occurring hydrocarbons which may exist in the solid, liquid, or gaseous states, depending upon the condition of pressure and temperature to which it is subjected. All petroleum is produced from the earth in either liquid or gaseous form, and commonly, these materials are referred to either crude oil or natural gas or associated gas with oil. Oil and gas are naturally existing hydrocarbon mixtures quite complex in chemical composition that exist at elevated temperature and pressure of the mixture are reduced. The state of hydrocarbon mixture at the surface conditions depends upon the composition of hydrocarbon fluid.

Crude oil is the material most sought after of these naturally occurring hydrocarbons, but natural gas is commonly produced along with the crude oil in the early years of the petroleum industry. Natural gas was considered to be a nuisance and

was burned at the well site. In years with the advent of transcontinental transmission lines and petrochemical industries, the demand for natural gas as a fuel and a raw product has increased. The value of natural gas to the point where it is no longer a nuisance but a valuable raw material.

Hydrocarbons in reservoir are frequently classified by "base". The earliest such classification system provided three classifications on the basis of composition of hydrocarbon:

- a- Paraffin-base, (alkane C_nH_{2n+2}) or oils containing predominantly paraffin series hydrocarbons.
- b- Asphaltenic-base or oils containing predominantly polyethylene or olefin (alkene C_nH_{2n}).
- c- Mixed-base, or oils containing large quantities of both paraffin and polyethylene series hydrocarbon.

Petroleum consists chemically of approximately 11 to 13 wt. % hydrogen and 84 to 87 wt % carbon. Traces of oxygen, sulfur, nitrogen, and helium may be found as impurities in crude petroleum. Although, all petroleum is constituted primarily of carbon and hydrogen, the molecular constitution of crude oils differs widely. About 18 series of hydrocarbons have been recognized in crude petroleum.

*Petroleum Engineering Dept., Faculty of Engineering, University of Tripoli, Libya. O_elayadi@yahoo.com.

Natural gas is composed predominantly of lower-molecular weight hydrocarbon paraffin hydrocarbon, also called (alkane), any of the saturated hydrocarbons having the general formula C_nH_{2n+2} , (C) being a carbon atom, (H) a hydrogen atom, and n an integer. The paraffins are major constituents of natural gas and petroleum. Paraffins containing less than 5 carbon atoms per molecule are usually gaseous at room temperature. Those having 5 to 15 carbon atoms are usually liquids, and the straight-chain paraffins having more than 15 carbon atoms per molecule are solids.

Gas gravity and molecular weight are widely used to characterize natural gas. Gas gravity is the ratio of the density of a gas at atmospheric pressure and temperature to density of air at the same conditions. The densities of gases are directly proportional to the molecular weight, the gravity is the ratio of the molecular weight of gas to the molecular weight of air. Gas gravities for gases range from 0.6 to 1.1, depending on the relative concentration of the heavier hydrocarbons present in the gas. The main aim of this study is to determine and predict the Libyan gas composition utilizing Tri-angle coordinate plots.

COMPONENTS OF HYDROCARBON

Since hydrocarbon molecules have specific ratios of hydrogen and carbon atoms, hydrocarbon compounds making up petroleum can be grouped chemically into a few series, although each series may have thousands of members. The most common hydrocarbon compounds are those of paraffin/alkenes series which include methane, ethane, propane, butane, etc. They are straight chain or branched configurations of carbon and hydrogen atoms that follow the general formula C_nH_{2n+2} . The alkenes are saturated, that is, the carbon atoms are connected with single bonds. Fig. 1 shows the models used to visualize the structure of these hydrocarbons, and their shorthand formulae.

As longer chains are built, it becomes possible to arrange the carbon atoms in either linear or branched fashion without changing the relative number of carbon and hydrogen atoms. These different arrangements are called isomers and possess different physical properties (Fig. 2). All straight chain alkenes form CH_4 (methane) to $C_{40}H_{82}$ (tetracontane) have been identified in crude oil typically they amount to 15% to 20% of the oil (Fig. 3). The possible isomers for these alkenes range from two for butane to 6.2×10^{13} for tetracontane. The

alkenes are characterized by their chemical inertness, which probably accounts for the stability over long periods of geological times. The first four members of the series (methane, ethane, propane, butane) exist as gases under standard conditions of pressure and temperature. Those from C_5H_{12} (pentane) to about $C_{17}H_{36}$ are liquids and $C_{18}H_{38}$ and higher are wax-like solids. Paraffin is a mixture of these solid members of the series. Saturated hydrocarbons that form closed rings rather than chains belong to a series known as cycloalkanes (also called cycle paraffin or heptanes). These hydrocarbons follow the general formula C_nH_{2n} . Being saturated; they are relatively stable and possess chemical properties similar to those of the alkenes.

Unsaturated hydrocarbons are compounds that contain a carbon-carbon double bond. These compounds can add hydrogen to their structures under appropriate conditions, and are therefore, said to be unsaturated (with hydrogen). One class of hydrocarbons that contains carbon-carbon double bonds is the arene series (also called aromatic because many of them have fragrant odors (Fig. 4). This group is made up of derivatives of benzene, whose formula is C_6H_6 and whose unique structure allows it to be relatively stable and un-reactive. Arene hydrocarbons are either liquids or solids under standard conditions and are common constituents of crude oil.

Other unsaturated compounds include alkenes or cyclo alkenes (also known as olefins) and the acetylene series (triple carbon-carbon bond). Olefin compounds are very uncommon in crude oils and the acetylene series is virtually absent. This is undoubtedly due to their high degree of reactivity and their tendency to become saturated with hydrogen forming alkanes. Of the eighteen different possible hydrocarbon series, therefore, alkanes, cycloalkanes and arenes are the common constituents of most crude oils.

CLASSIFICATION OF HYDROCARBONS

Common oil field classification of oil and natural gas relies on observed producing characteristics and easily measured specific gravity. The gas-oil ratio (GOR), gas gravity and oil gravity are used to categorize reservoir hydrocarbons.

Gas-oil ratio (GOR) in this case refers to the cubic feet of gas produced per barrel of liquid (or cubic meters per cubic meter), with both volumes measured at standard conditions of temperature and pressure.

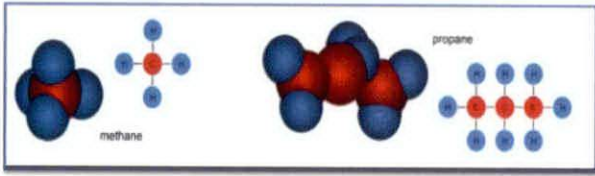


Fig. 1. models for methane and propane, showing the tetrahedral nature of the carbon-hydrogen configuration (Shlumberger, Introduction to welltesting)

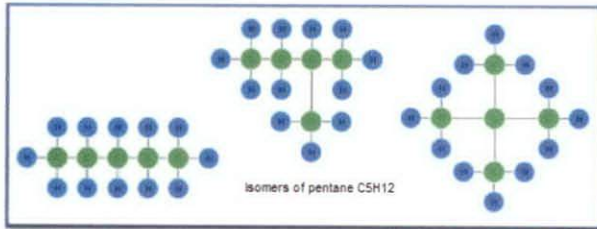


Fig. 2. shows Isomers of pentane (C₅-H₁₂).

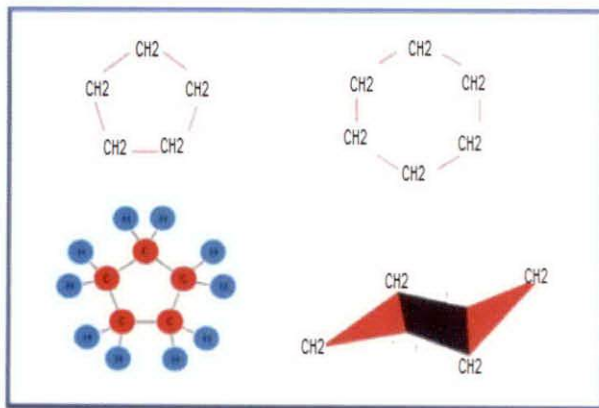


Fig. 3. Structure of two members of the cyclo alkane series of hydrocarbons. Cyclo hexane has an actual three dimensional Geometry that is slightly puckered, not planar as the formula suggests.

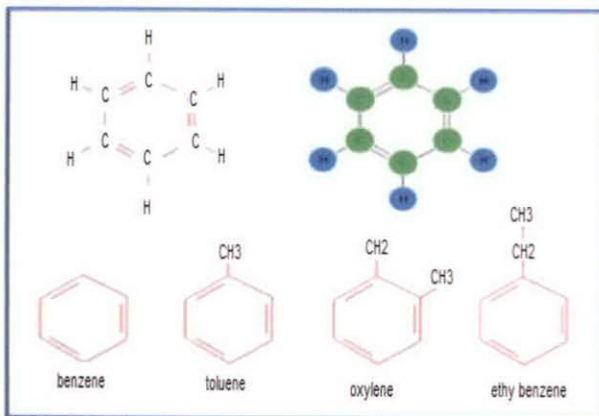


Fig. 4. Structure of several members of the arene, or aromatic, series.

Specific gravity is the ratio of the density of a substance to the density of some reference substance. For gases, the standard reference are dry air at the same temperature and pressure as the gas in question. For liquids, the reference are pure water at 60°F and one atmosphere (14.7 Pisa). For hydrocarbon liquids, the API gravity scale are most commonly used in the oil industry. It expands and inverts the range of numerical values for oil specific gravity. Water has an API gravity of 10.0 and the relationship between API and specific gravity is given as:

$$^{\circ}\text{API} = [141.5 / (\text{SP.gr}) - 131.5] \dots 1$$

Table (1) shows the classifications of reservoir fluids based on GOR and fluid gravities. In general, low GOR; low API oils have lesser amounts of the light paraffinic hydrocarbons, while dry gases are composed almost entirely of these compounds. Sampling and analyzing the behavior of dry gas or black oil systems are relatively straight forward procedures. Condensate and volatile oil systems, on the other hand, can be much more complex in terms of their physical chemistry.

PROPERTIES OF NATURAL GASES

Petroleum engineers are usually interested in the behavior of mixtures and rarely deal with pure component gases. Because natural gas is a mixture of hydrocarbon components, the overall physical and chemical properties can be determined from the physical properties of the individual components in the mixture by using appropriate mixing rules. Knowledge of Pressure-Volume-Temperature (PVT) relationships (Labedi, 1980; Katz & Hachmuth, 1937; Glaso, 1979); Standing, 1970;

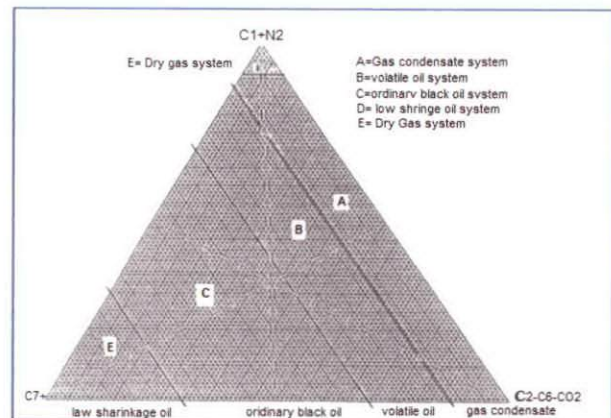


Fig. 5. Compositions of various reservoir fluid types.

Table 1 General categories of reservoir hydrocarbons.

Reservoir fluid	Surface appearance	GOR range	Gas specific gravity	API gravity	C1	C2	C3	C4	C5	C6+
Dry Gas	Colorless gas	Essentially no liquids	0.60-0.65		96	2.7	0.3	0.5	0.1	0.4
Wet gas	Colorless gas with small amount of clear or straw colored liquid	Greater than 100 MSCF/bbl (18000 m ³ /m ³)	0.65-0.85	60						
Condensate	Colorless gas with significant amounts of light-colored liquid	3 to 100 MSCF/bbl (550-18000 m ³ /m ³)	0.65-0.85	50-70	87	4.4	2.3	1.7	0.8	3.8
"Volatile" or high shrinkage oil	Brown liquid with various yellow, red or green hues	About 3000 SCF/bbl (550 m ³ /m ³)	0.65-0.85	40-50	64	7.5	4.7	4.1	3.0	16.7
"Black" or low shrinkage oil	Dark brown to black viscous liquid	100-2500 SCF/bbl (20-450 m ³ /m ³)	0.65-0.85	30-40	49	2.8	1.9	1.6	1.2	43.5
Heavy oil	Black, very viscous liquid	Essentially no gas in solution		10.25	20	3.0	2.0	2.0	2.0	71
Tar	Black substance	Viscosity > 10000 cp		<10						

Hoffman *et al*, 1953 and Alani & Kennedy, 1960). Other physical and chemical properties of gases is essential for solving problems in natural gas reservoir engineering. These properties include:

- Apparent molecular weight, M_a
- Specific gravity, γ_g
- Compressibility factor, z
- Density, ρ_g
- Specific volume, v
- Isothermal gas compressibility coefficient, C_g
- Gas formation volume factor, β_g
- Gas expansion factor, E_g
- Viscosity, μ_g

The above gas properties may be obtained from direct laboratory measurements or by prediction from generalized mathematical expressions.

This section reviews laws that describe the volumetric behavior of gases in terms of pressure and temperature and also documents the mathematical correlations that are widely used in determining the physical properties of natural gases.

CLASSIFICATION OF RESERVOIR AND RESERVOIR FLUIDS

Petroleum reservoirs are broadly classified as oil or gas reservoirs (Fig. 5). These broad classifications are further subdivided depending on:

- The composition of the reservoir hydrocarbon mixture

- Initial reservoir pressure and temperature
- Pressure and temperature of the surface production

The state of hydrocarbon mixture at the surface condition depended upon the composition of hydrocarbon fluid as produced from the well and upon the pressure and temperature. The fluid remaining in the reservoir at any stage of reservoir at any stage of depletion undergoes physical change as the pressure is reduced by producing quantities of oil or gas from that reservoir. Physical properties of engineer ordinarily are defined in terms of the pressure and temperature at which hydrocarbon exists. Fluids in general are classified as gases, vapor, or liquids, it should be pointed out that particular words convey ideas only when conditions of pressure and temperature are specified.

The conditions under which these phases exist are a matter of considerable Practical importance. The experimental or the mathematical determinations of these conditions are conveniently expressed in different types of diagrams commonly called phase diagrams. One such diagram is called the pressure-temperature diagram or phase behavior or phase envelope.

Gas Reservoirs

A gas is defined as a homogeneous fluid of low viscosity and density that has no definite volume but expands to completely fill the vessel in which it is placed. Generally, the natural gas is a mixture

of hydrocarbon and non hydrocarbon gases. The hydrocarbon gases that are normally found in a natural gas are methane's, ethane's, propane's, butanes, pentanes, and small amounts of hexanes and heavier. The non hydrocarbon gases (i.e., impurities) include carbon dioxide, hydrogen sulfide, and nitrogen.

However, if the reservoir temperature is above the critical temperature of the hydrocarbon system, the reservoir is classified as a natural gas reservoir (Ahmed, 2001 & 2007 and Ahmed & McKinny, 2005). On the basis of their phase diagrams and the prevailing reservoir conditions, natural gases can be classified into four categories:

- Retrograde gas-condensate.
- Near-critical gas-condensate.
- Wet gas.
- Dry gas.

Estimating and Measuring Associate Gas Molecular Weight

Molecular weight can be calculated from gas gravity which is predicted from some correlation is available in literature in terms of production data. Vasquez correlate gas gravity maybe estimated from:

$$\gamma_g = gp [1+5.912*[10]^{(-5)}(API)(Ts)\text{Log}(P_1/114.7)] \quad 2$$

It may be estimated from Katz's correlations (Katz and Hachmuth 1937) that relate total gas gravity to total gas oil ratio and the oil gravity.

Gas gravity may be also calculated gas gravity using which is developed by Labedi (1980).

$$\gamma_g = \frac{0.07547 [(API)]^{0.6021} [(T_s/R_{P_1})]^{(0.06593)}}{(1.19379)/(10\sqrt{P_1})} \quad 3$$

Where:

P_1 = First stage separator pressure (Onat, 1975), psia

T_s = First stage separator temperature °F.

γ_{gp} = Gravity (air= 1.0) of the gas produced at P_1 and T_s .

°API = Stock tank oil gravity,

R_{P_1} = G.O.R. from production at P_1 and T_s , SCF/STB

Gas gravity γ_g may also be determined using balance method which is the most commonly used method for the field. This instrument compares the density of the gas being tested with the density of air. The calculation of specific gravity is based on

the principle that the densities of two gases at base pressure are an inverse ratio to the pressure that provides equal buoyant forces for the two gases. This method of specific gravity determination is used at locations involving both small and large volume sales and purchases of gas. The recommended equipment for use in obtaining gas gravities by the balance method is as follows:

1. The Acme senior gas gravity balance, for use by measurement specialists and all locations where large volumes of gas are tested detailed description in (Fig. 6).
2. The Acme junior gas gravity balance, for use by measurement specialists working with small volumes of casing-head gas. (See Fig. 7).

Recording gravimeters may be used when a continuous record is desirable or required. The types most frequently used are those working use of weighing methods (Fig. 8).

RESULTS AND DISCUSSION

Illustration of how to estimate the molecular weight of the gas as a function of composition in percentage of methane and ethane (C_1+C_2) is shown in Fig. (9) which proves a good trend between the molecular weight and the percentage of (C_1+C_2) with difference separator pressure.

The relation between the compositions in percent of the gases associated it selves were also developed; the composition may be estimated from Figs. 11 to 20.

However, utilizing (Fig. 9), it was found that the molecular weight of Libyan gas ranges from 17 to 50. Moreover, the Libyan separator pressure used in the Libyan field ranged from zero to 600 psi. It is appearing from the figure that the molecular weight of gas decreases with increases of (C_1+C_2). Nevertheless, the molecular weights decrease with increase separator pressure. Generally, the straight line relationship between molecular weight and composition can be presented in Table (2).

On the anther hand, Figure (10) can also be used to find gas composition of (C_1+C_2). Any increase in separator pressure will decrease in molecular weight. This effect is major in low (C_1+C_2) gas composition, it may be considered minor in high (C_1+C_2). Figs. 11 to 20 present triangle coordinate utilized for estimation two unknown gas composition if the other third composition is known for old and last data collated from liberating.

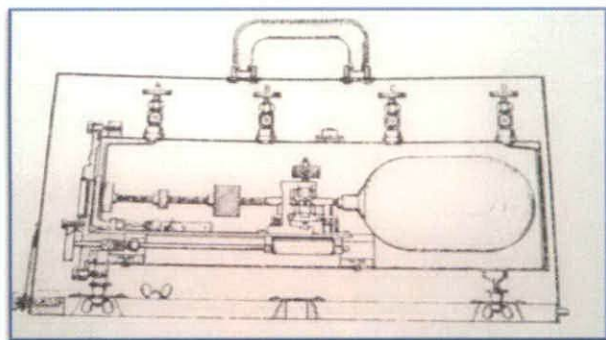


Fig. 6. acme senior gas gravity balance.



Fig. 7. Proptional Torque Differential indicator for measuring the specific gravity gas.

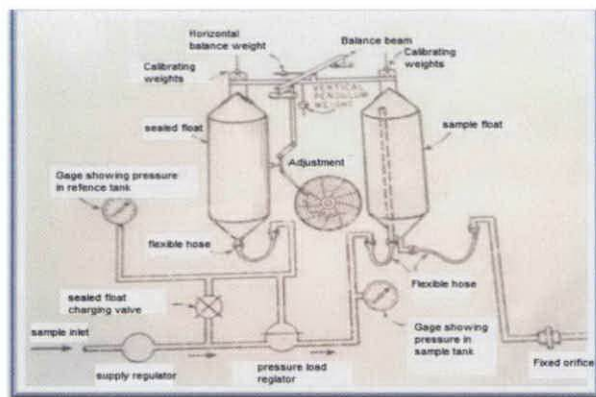


Fig. 8. schematic diagram of a recording gravitometer having gas filled drums suspend from a balance

Table 2 gas molecular weight verses (C₁+C₂) gas composition.

Separator pressure	Equation
Zero	Mwt= 54.54- 0.335* (C ₁ +C ₂).....(4)
50	Mwt=45.61 – 0.263* (C ₁ +C ₂).....(5)
100	Mwt= 41.36-0.227* (C ₁ +C ₂).....(6)
300	Mwt= 34.34-0.168* (C ₁ +C ₂).....(7)
400	Mwt= 32.85-0.156* (C ₁ +C ₂).....(8)
600	Mwt= 26.69-0.095* (C ₁ +C ₂).....(9)

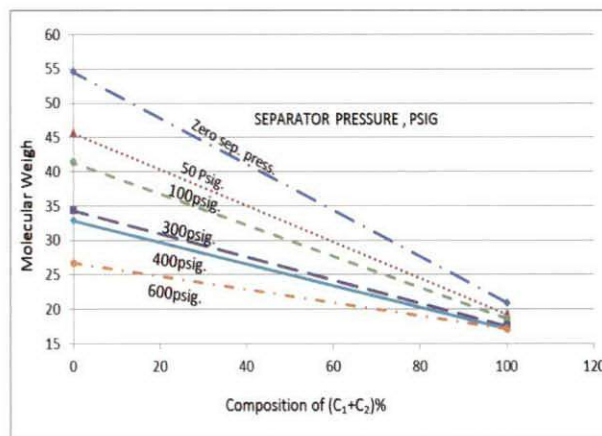


Fig. 9. Molecular weight verses gas composition to different separator pressure.

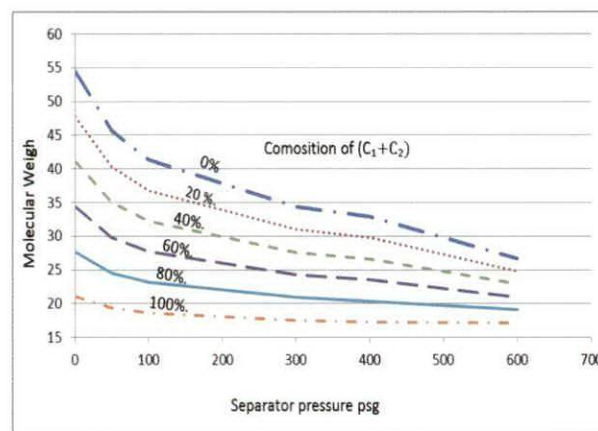


Fig. 10. Molecular weight as function composition

Fig. 11 illustrating relationship between (C₁+C₂) C₃ and (C₄⁺ + N.H.C). However, most of (C₁+C₂) a accumulated between 50 to 95 %.

The fitted line equation that maybe used to find C₃ is

$$(C_1+C_2) = e^{(0.092 * C_3\#)} \tag{10}$$

Where:

$$C_3\# = C_3 + (C_1+C_2)/2.0$$

Fig. (12) shows (C₁+C₂) as a function of (C₃+C₄) and (C₅⁺ + N.C.H). Most of the data contain low values of (C₅⁺ + N.H.C) that is about 10%.

The equation that can be used for estimation C₄%, from Fig. (12) is:

$$(C_1+C_2) = 209.7 - 2.470 (C_3+C_4)\# \tag{11}$$

Where:

$$(C_3+C_4)\# = (C_3+C_4) + (C_1+C_2)/2.0$$

C_1 and C_2 separately can be estimated from Fig. (13) or from equation:

$$C_1 = 0.019 * C_2^{2.112} \quad (12)$$

Where:

$$C_2\# = C_2 + \frac{C_1}{2.0}$$

The average values of C_2 range from 8 to 18.

C_5 also can be estimated from Fig. (14). Moreover, C_5 can be calculated from the following equation:

$$C_1 = 173.3 - 1.780 * (C_2-C_5)\# \quad (13)$$

Where:

$$(C_2 - C_5)\# = (C_2-C_5) + C_1/2.0$$

It is appearing that the values of $(C_6^+ + N.H.C)$ low averaged value of about 7%.

Fig. (15) can be used to estimate C_6 with an equivalent value calculated from the following equation:

$$C_1 = 1.88 - 1.942 * (C_2+C_6)\# \quad (14)$$

Where:

$$(C_2 + C_6)\# = (C_2 + C_6) + C_1/2.0$$

The average value of $(C_7^+ + N.H.C)$ is approximately 6%. C_7^+ and Non Hydrocarbon (N.H.C) dividedly can be estimated from Fig. (16). It can be also calculated by the help of using the following equation:

$$N.H.C = 191.1 - 1.916 * (C_1-C_6)\# \quad (15)$$

Where:

$$(C_1-C_6)\# = (C_1-C_6) + N.H.C./2.0$$

$$\text{And } C_7^+ = 100 - N.H.C - (C_2-C_6)$$

The average value of C_7^+ is less than 1.0

Most of the Libyan N_2 composition range up 5%. Only, one or few reservoirs may contain higher values. As shown in (Fig. 17) never, it can be calculated from the following equation:

$$N_2 = 0.575 - 2E^{-6(CO_2-H_2S)\#5} + (CO_2 - H_2S)^4\# - 0.006(CO_2-H_2S)\#^3 + .070(CO_2 - H_2S)\#^2 + 0.207(CO_2-H_2S)\# \quad (16)$$

Where:

$$(CO_2-H_2S)\# = (CO_2 - H_2S) + N_2/2.0$$

H_2S composition can be obtained after estimating or calculated CO_2 from Figure (18) and calculated from the following equation:

$$CO_2 = 1.167 + 1E^{-05(N_2-H_2S)^{4\#}} E^{-05(N_2-H_2S)^{4\#}} - 0.001(N_2 - H_2S)^3\# S^3\# + 0.066(N_2-H_2S)\#H_2S\# - 0.008(N_2-H_2S)\# \quad (17)$$

Where:

$$(N_2-H_2S)\# = (N_2-H_2) + CO_2/2.0$$

Average value of CO_2 is about 5%, other values can be higher (30%) in few reservoirs.

To demonstrate other gas composition relationships, Figs. (19) and (20) illustrate this relation.

Fig. (19) shows that even numbers $(C_2+C_4+C_6)$ has low value composite to odd numbers, however, the value of odd numbers ranged between 50% to 100%, whereas the even numbers ranged from 0% to 50%. The equation which can be used to find the exact value are:

$$C_7+(N.H.C) = 0.680 + 0.206 (C_2+C_4+C_6) \quad (18)$$

Where:

$$(C_2+C_4+C_6)\# = (C_2+C_4+C_6) + \frac{C_7+N.H.C}{2}$$

$$\text{And } (C_1+C_3+C_5) = 100 - (C_2+C_4+C_6) - (C_7^++N.H.C)$$

Fig. (20) shows addition way to recognize (C_1+C_3) from $(C_2+C_4+C_5+C_6)$. The equation that can be used is:

$$(C_1+C_3) = 175 - 1.751 (C_2+C_4+C_5+C_6)\# \quad (19)$$

Where:

$$(C_2+C_4+C_5+C_6)\# = (C_2+C_4+C_5+C_6) + \frac{(C_1+C_3)}{2}$$

Generally, the value of C_7^+ has low or negligible value in gas phase composition. This true criteria is considered when fitted line was made. Other important point also was considered in case of total gas composition exceed 100% or less than that.

In all previous plots, the isomers or normal values of C_4 and C_5 were not individually estimated.

Figs. (21) and (22) show the relationship between normal C_4 and Iso C_4 . Fig. (21) shows a direct simple straight line relationship and Fig. (22) present Log-Log plot.

The equation that can be used to estimate $i.C_4$ and $n.C_4$ are from Fig. (21) is:

$$i-C_4 = 0.103 + 0.501 (n-C_4) \quad (20)$$

Or from Figure (22)

$$i-C_4 = 0.103 + 0.501 (n-C_4) \quad (21)$$

It is known that

$$C_4 = i-C_4 + n-C_4 \quad (22)$$

Solving two equations with two unknown, equation (22) can be become

$$n-C_4 = C_4 - i-C_4 \quad (23)$$

Substituting (23) into (20)

$$\begin{aligned} i-C_4 &= 0.103 + 0.501 (C_4 - i-C_4) \\ \therefore i-C_4 &= 0.103 + 0.501 C_4 - 0.501 (i-C_4) \\ 1.501 i-C_4 &= 0.103 + 0.501 C_4 \\ i-C_4 &= 0.068621 + 0.333777 C_4 \quad (24) \end{aligned}$$

$$\begin{aligned} \therefore 0.333777 C_4 &= i-C_4 - 0.068621 \\ n-C_4 &= 100 - n-C_4 \\ n-C_4 &= 100 - (0.068621 + 0.333777 C_4) \\ n-C_4 &= 100 - 0.068621 - 0.333777 C_4 \\ n-C_4 &= 99.931 - 0.333777 C_4 \quad (25) \end{aligned}$$

To find Isomers and normal gas composing of C_5 (Figs. 23 & 24) can be used with normal and Log-Log plot.

The normal plot (Fig. 23) equation is:

$$i-C_5 = 0.034 + 1.069 n-C_5 \quad (26)$$

Also, from Figure (24), the same equation can be obtained.

$$\therefore C_5 = i-C_5 + n-C_5$$

Following the same steps as with C_4 the following equations repress the relation between Iso and

normal C_5 with C_5 obtained from the previous triangle coordinate.

$$i-C_5 = 0.0164 + 0.516 C_5 \quad (27)$$

$$n-C_5 = 99.98 - 0.516 C_5 \quad (28)$$

CONCLUSIONS

The conclusions from this study can be presented as following:

- 1- Utilize Excel Microsoft Office to draw triangle coordinate instead of rectangle plots.
- 2- The triangle coordinate fitted data points also obtained, there converted to traditional fitted equations of rectangular.
- 3- The Libyan gas compositions can be easily obtained from this study, if the molecular weight measured directly by the specific instrument.
- 4- The average of Libyan gas composition may be demonstrated or tabulated in Table 3.
- 5- The normal and Isomers of C_4 and C_5 range (Table 4).
- 6- The old (more than 25 years) Libyan gas composition collected data are much closed to the last or recent collected data.

Table 3 the average of Libyan gas composition (El-Ayadi, 1997).

Libyan Gas composition	Range value %	Average value %
C_1	40 - 85	65
C_2	8 - 18	14
C_3	10 - 15	11
C_4	4 - 6	5
C_5	1 - 5	3
C_6	0 - 2	1
C_7^+	Less than 1	0.5
N_2	0 - 4	3
CO_2	0 - 5	4
H_2S	0 - 0.5	0.4

Table 4 the normal and Isomers of C_4 and C_5 range.

Component	Average value %		Average value %
	Maximum	Minimum	
$i-C_4$	Up to 8	0 - 3.5	2.3
$n-C_4$	Up to 18	0 - 5	3.5
$i-C_5$	Up to 5	0 - 2.5	1.4
$n-C_5$	Up to 5	0 - 2.5	1.2

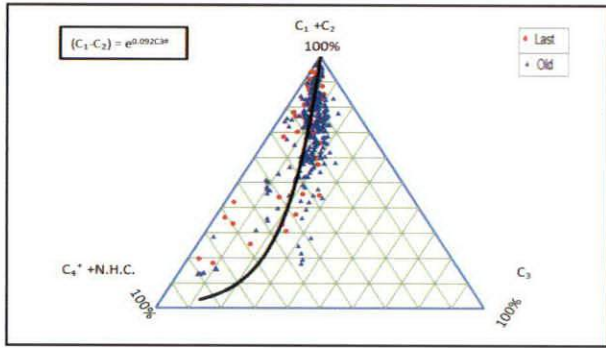


Fig. 11. (C_1+C_2) as function of C_3 and $C_4^+ + N.H.C.$

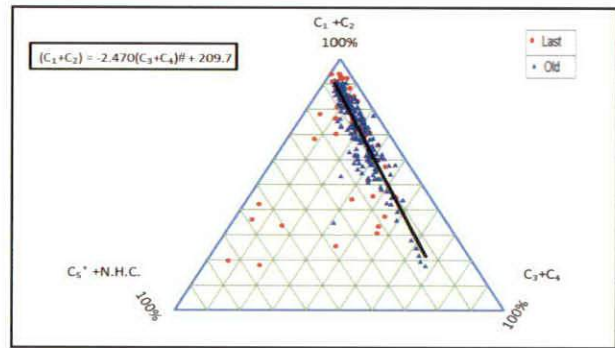


Fig. 12. (C_1+C_2) as function of $(C_3$ and $C_4)$ and $C_5^+ + N.H.C.$

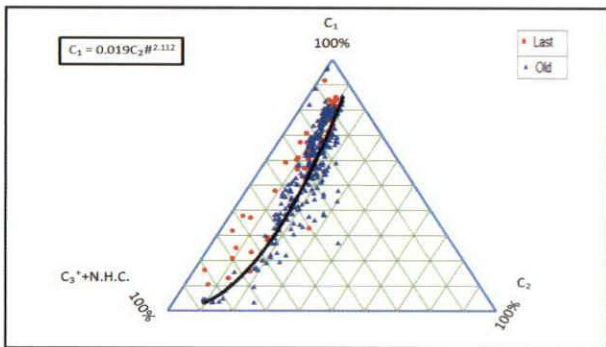


Fig. 13. C_1 as function of C_2 and $C_3^+ + N.H.C.$

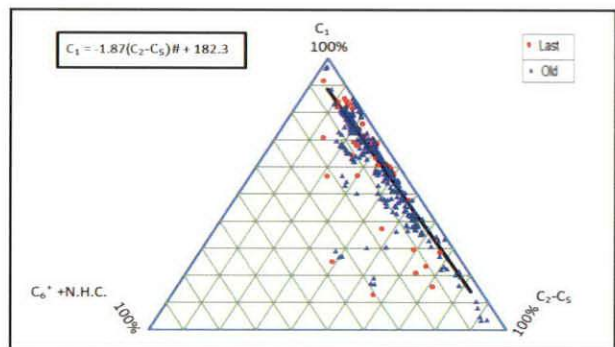


Fig. 14. C_1 as function of (C_2-C_5) and $C_6^+ + N.H.C.$

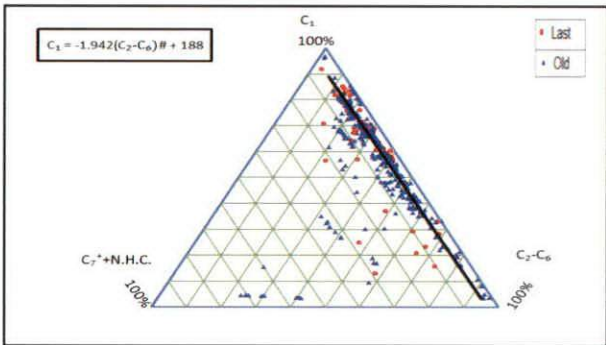


Fig. 15. C_1 as function of (C_2-C_6) and $C_7^+ + N.H.C.$

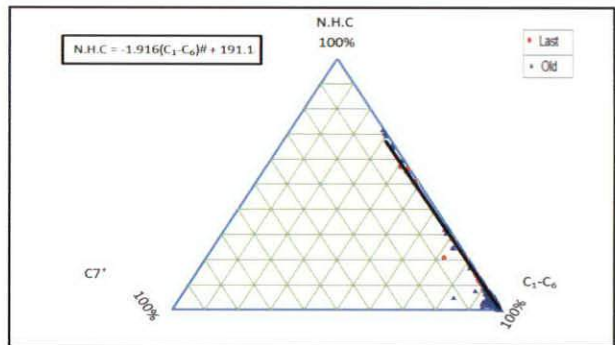


Fig. 16. N.H.C as function of (C_1-C_6) and $C_7^+ + N.H.C.$

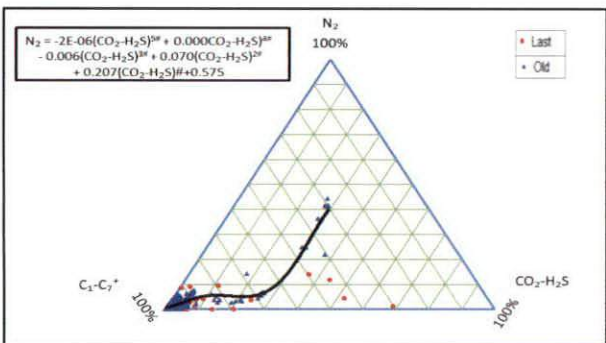


Fig. 17. CO_2 as function of (N_2-H_2S) and $C_1-C_7^+$

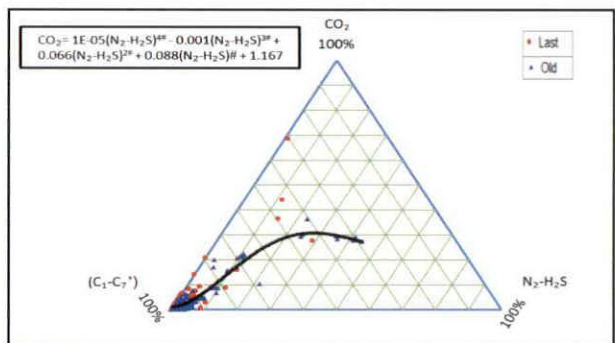
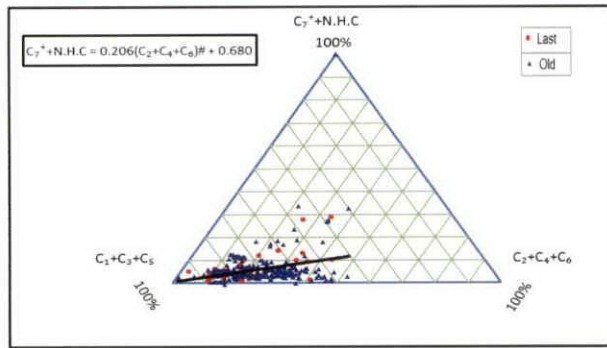
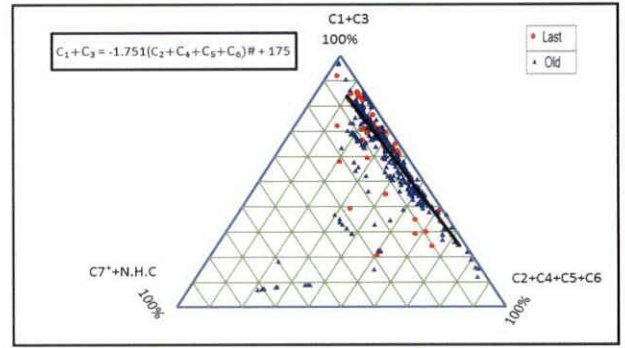
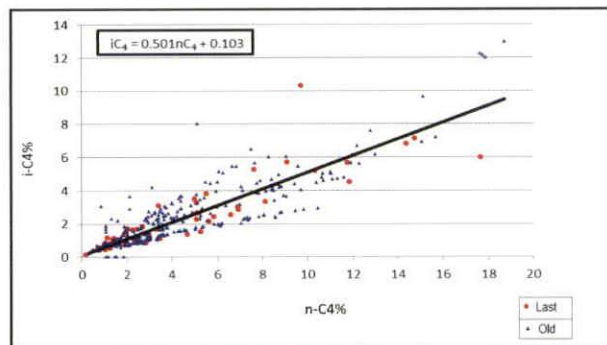
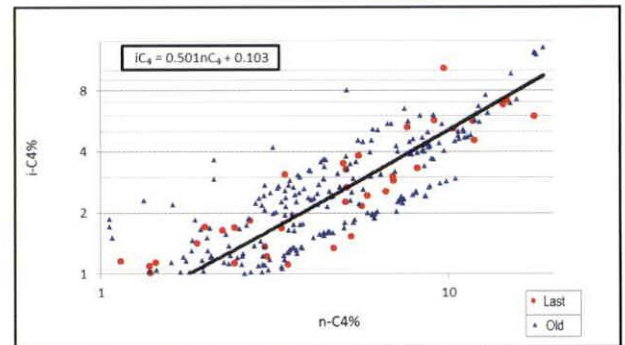
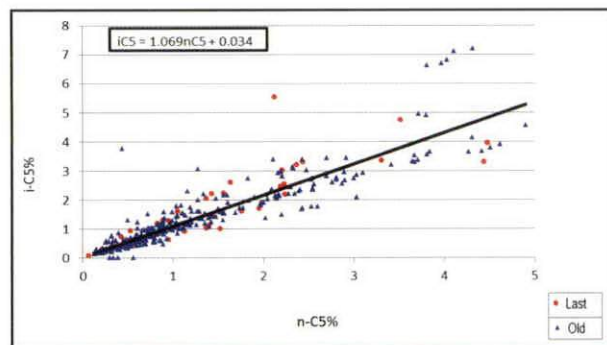
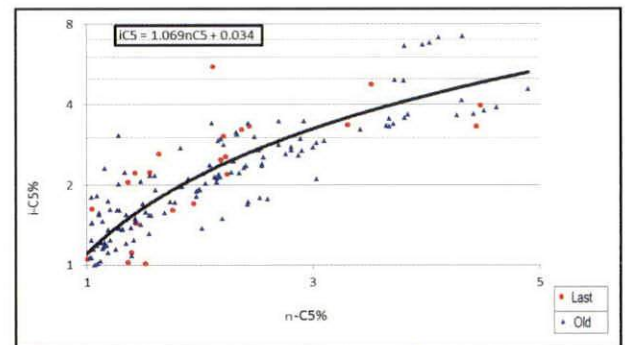


Fig. 18. CO_2 as function of (N_2-H_2S) and $(C_1-C_7^+)$

Fig. 19. $C_7^+ + N.H.C$ as function of $(C_2 + C_4 + C_6)$ and $C_1 + C_3 + C_5$ Fig. 20. $(C_1 + C_3)$ as function of $(C_2 + C_4 + C_5 + C_6)$ and $C_7^+ + N.H.C$ Fig. 21. iC_4 as function of nC_4 liner plotFig. 22. iC_4 as function of nC_4 Log-Log plotFig. 23. iC_5 as function of nC_5 liner plotFig. 24. iC_5 as function of nC_5 Log-Log plot

- 7- The relationship between associated gas molecular weight and $(C_1 + C_2)$ composition is approximated as straight line at different separator pressure.
- 8- An average molecular weight of Libyan associated gas range between 17 to 50.

RECOMMENDATIONS

- 1- Further investigation needed or required to obtained other physical gas properties that can be

correlated with composition i.e. pseudo critical properties. Moreover, correlation according to composition instead of weigh density is probably more appropriate.

- 2- Screen the data and the fields that contain high gas composition i.e. N_2 and CO_2 or H_2S .
- 3- Utilize the obtained composition for EOR process.
- 4- Use of the discovered Tri-angle plots or coordinates to find any other properties summated by 100 i.e. Clay-Sandstone-Dolomite.

REFERENCES

- Ahmed, T. (2001). Reservoir Engineering Handbook. *Gulf publishing company Houston, Texas*: 1-187.
- Ahmed, T. (2007). Equations of State and PVT Analysis. *Gulf publishing company Houston, Texas*: 1-453.
- Ahmed, T. and McKinny, P. D. (2005). Advanced Reservoir Engineering: 3-147.
- Alani, G. H. and Kennedy, T. H. (1960). Volumes of Liquid Hydro Carbons at High Temperatures and Pressures. *Transactions AIME* **219**: 28- 29.
- Glaser, O. (1979). Generalized Pressure Volume-Temperature Correlations. *SPE, Paper* 8016.
- Hoffman, A. E.; Crump, J. S. and Hocott, C. R. (1953). Equilibrium Constants for a Gas-Condensate System. *Transaction of AIME* **198**: 1-10.
- Katz, D. L and Hachmuth, D. H. (1937). Vaporization Equilibrium Constants in a Crude Oil-Natural Gas System. *Ind. Eng. chem.* **29**: 1072 -1077.
- Labedi, R. M. (1980). PVT correlations the African Crudes.
- Onat, N. I. (1975). An Investigation of Sequential Field Separation System Optimization. Petro. Eng. Dep.
- Standing, M. B. (1970). Volumetric Phase Behavior of Oil Field Hydrocarbon System. *sixth Edition, chevron research company*: 43.56.

BACTERIAL CORROSION INDUCED BY AEROBIC AND ANAEROBIC MICROORGANISMS

I.El Musrati and B.Gammudi*

Abstract: The biocide is a chemical substance capable to killing different forms of microorganisms which is widely used in oilfields to control microbial problems. In this study, the efficacy of biocide (Quaternary-ammonium compounds 'QACs' blended with Glutaraldehyde) that is commonly used in Libyan oilfields was investigated against natural micro-flora isolated from open re-circulating cooling water system. The effects of those chemicals were studied on bacterial isolates used to build up biofilms on stainless steel coupons (AISI 304 and AISI 316). Two bacterial strains have been selected to be carried out in this study and identified as *Pseudomonas aeruginosa* and Sulfate-reducing bacteria (*Desulfobulbus sp.*).

The strains were grown with increasing concentrations of the Quaternary-ammonium compounds blended with glutaraldehyde. Atomic Force Microscope (AFM) was used to visualize the topographic of biofilms developed on metal surfaces. The efficiency of the biocide was determined by acridine orange (AO) staining. In addition, electrochemical technique (linear Polarization Resistance) gave information on corrosion rate associated with the microbial activity and the biocide effects. The results show that microbial strains have different responses against biocide. While *Pseudomonas aeruginosa* shows ability to grow at high concentrations of biocide, *Desulfobulbus sp.* has no resistance-where 25ppm was enough to cause a shock for the growth of microbes-not only the microbial growth but their adhesion and the biofilm formation decrease dramatically.

Keywords: Disinfectants, biocide, Quaternary-ammonium compounds, Glutaraldehyde, biofilm

INTRODUCTION

Biofilms (Microorganisms attaching to the surfaces) are involved in many industrial fouling, corrosion, and hygiene problems. The main strategy of biofilm control to use chemicals (called biocide) to that are kill the attached microorganisms and/or remove them from the surface. Unfortunately, bacteria in biofilms are usually found to be many times more difficult to eradicate than their planktonic counterparts. Actually, over 80% of microorganisms have shown ability of associating to surfaces. (Dinty *et al*, 2006; Wingender and Flemming, 1999). The relative resistance of biofilm microorganisms has tremendous economic and environmental ramifications in applications as diverse as cooling water, medical implants,

drinking-water distribution, metalworking, and products quality (Keresztes *et al*, 2001; Zarnea, 1994; Flemming, 1996 and Beech, 2004).

Inside the biofilm, living cells belonging to various groups of microorganisms live together in a slimy matrix made of extracellular polymeric substances (EPS). That is produced by one or several species that includes organic and inorganic substances captured from the environment. This structure constitutes a protected mode of growth that allows survival in aggressive environment (Bandoni and Koske, 1974; Busscher and Weerkamp, 1987). There are four stages through the development of a mature biofilm: initial attachment, irreversible attachment with the production of extracellular polymeric substances (EPS), early development, and maturation of biofilm architecture (Stoodley *et al*, 2002; Kimberly, 2004). They differ from their planktonic form in their growth rate, composition and increased resistance to biocide. This makes

* Libyan Petroleum Institute, i.elmusrati@lpilibya.com

them highly difficult to eliminate with treatment regime of antimicrobial agents. Many studies have stated that the bacteria enclosed within the biofilm are extremely resistance for antimicrobial treatments (Russell, 1995; Heinzl, 1998; McBain, and Gilbert, 2001; Chapman, 2003). One of the most important bacteria in oilfields is Sulphate Reducing Bacteria (SRB). Those bacteria involved in many problems in petroleum industries such as Microbial Influenced Corrosion (MIC) by cathodic depolarization of metal surfaces resulting in formation of localized pitting. Hydrogen sulphide as a metabolic by-product can result in the formation of iron sulphide deposits which depolarizes the anode and increases the corrosion rate. And slime forming bacteria that has potential to produce large volumes of exopolymers which is ideal for biofilm formation. Slime production can result in fouling and blocking of filter. Establishment of oxygen concentration cells, which can lead to under deposit corrosion and promote an ideal environment for SRB.

For that, a wide range of biocides (active chemical agents) has been used to control biofilms (microbial). These are including oxidizing and non-oxidizing biocides such as chlorine, hypochlorite, glutaraldehyde, and quaternary ammonium salts (Hector, 2002 and Russell, 2003). Glutaraldehyde and QACs have intensively studied. Currently, the largest application of glutaraldehyde is in the industries, whereas, it is employed, to a lesser degree, for oil drilling applications and gas pipelines to reduce populations of sulfate bacteria. Where, Glutaraldehyde characterized as strong antimicrobial (biocidal) properties. Like other compounds in the aldehyde family, glutaraldehyde possesses carbonyl groups that react readily with nucleic acids and proteins by alkylating sulfhydryl, hydroxyl, carboxyl, and amino groups (Chambon *et al*, 1992; Rutala, 1990). But glutaraldehyde cannot cross the cell's lipid membrane. Thus, it can only act outside these micro-organisms and has consequently a rather slow action. On the other hand, QAC's are cationic tensio-active agents. At low concentrations, they have cidal properties on a wide range of microorganisms. Their major site of action is the cell membrane, where they create dissolution of phospholipids and cause changes in permeability that allow the escape of cell constituents and cause cell disorientation (Russel, 2003). These changes in permeability also allow glutaraldehyde to penetrate inside the biofilms.

However, the additive biocide with QAC's show effective results but it needs high concentrations to control microbial activities. Several references showed that many types of gram-negative organisms such as *P. aeruginosa* have high levels tolerance to QACs. (Guerin-Mechin *et al*, 2000; Sundheim *et al*, 1998).

The present study was investigated the antimicrobial efficacy of Quaternary-Ammonium Compounds (QACs) blended with Glutaraldehyde against natural micro-flora from open re-circulating cooling water system in Libyan oil field.

MATERIAL AND METHODS

Bacterial strains and growth conditions:

The consortium used in this work was isolated from deposit fouling samples from open re-circulating cooling water system in Libyan oil field. *Pseudomonas* species was chosen for this study, because it is known to be responsible for the microbial fouling on various surfaces. These bacteria are the most widely recognized in resistant of antimicrobial agent (Sundheim *et al*, 1998). Sulphate reducing bacteria (SRB) was also chosen because of their role to accelerate the corrosion process for metal surfaces. *Pseudomonas* sp cultured on R2A medium consisting of: yeast extract 0.5g, proteose peptone 0.5g, casamino acids 0.5g, glucose 0.5g, soluble starch 0.5g, sodium-pyruvate 0.3g, dipotassium hydrogen orthophosphate (K_2HPO_4) 0.3g, magnesium sulfate ($MgSO_4 \cdot 7H_2O$) 0.05g, distilled water 1,000mL (final pH 7.2). SRB cultured on Postage Medium B-Lactate Base consisting: Potassium Phosphate, monobasic (KH_2PO_4) 0.5g, Ammonium chloride (NH_4Cl) 1.0g, Calcium sulfate ($CaSO_4$) 1.0g, Magnesium sulfate ($MgSO_4 \cdot 7H_2O$) 2.0g, Sodium lactate ($C_3H_5NaO_3$) 3.5ml, Yeast extract 1.0g, Sodium chloride (NaCl) 1g, Ascorbic acid ($C_6H_8O_6$) 0.1g, Thioglycolic acid ($C_2H_4O_2S$) 0.3g, Ferrous sulfate ($FeSO_4 \cdot 7H_2O$) 0.5g, distilled water 1,000ml (final pH 7.6) All experiments were incubated at 25°C.

Biocide: The chemical treatment that used in this study was Quaternary-Ammonium Compounds (QACs) blended with Glutaraldehyde (GA).

Metal sample preparation: AISI 304 and AISI 316 stainless steel samples (10mm x 10mm x 2mm) were used. Table 1 presents the chemical composition of the steel. All samples have been polished firstly with emery paper grades 600, 800, 1000 and 2000 grit,

Table 1. Chemical composition of the AISI 304 and AISI 316 austenitic stainless steel

Composition (%) type	C	Si	Mn	Ni	Cr	Mo	N	S	P	Cu
AISI 304	0.052	0.510	0.900	8.05	18.050	0.1900	0.0057	0.0025	0.023	0.180
AISI 316	0.08	0.75	2.0	14.0	18.0	3.0	0.1	0.03	0.045	-

then with diamond paste of 6, 3, 1 and 0.25 μ m, degreased with acetone, and dried on air.

Biofilm formation: These experiments were performed in R2A and postgate medium B at 25°C in the presence of *pseudomonas* species and sulphate reducing bacteria (SRB). R2A agar was used to monitor the growth of bacteria and to check for contamination for *Pseudomonas* species and postgate medium E for SRB. The short term submersion of AISI 304 and AISI 316 coupons with pure cultures of isolated bacteria was carried out in 250 ml Erlenmeyer flasks containing 100 ml of medium. The coupons were exposed for 5 days up to three weeks for sulphate reducing bacteria (SRB) with/without adding biocide at different concentrations (25,100 and 500 ppm).

Characterization of Bacterial Stains: The Preliminary characterization of bacterial strains was achieved according to standards for microbial identification in Bergy's manual of systematic bacteriology, on the basis of colony morphology, biochemical tests and microscopic examination.

Fluorescent microscope: Coupons from inoculated media with/without biocide were removed after 5 days of incubation, and then rinsed with distilled water to remove any unattached bacteria. Then the following staining procedures were used. Coupons were bathed in a 0.01% aqueous (w-v) solution of Acridine Orange (AO) (SCP LTD., UK) for 3 min before being rinsed twice in non-flowing distilled water (Ladd and Costerton,1990), and air dried.

The coupons were examined by a Fluorescent Microscope (ZEISS, AXIO, and Imager A1 with digital camera under 100x magnification).The images were taken at different places on the surface.

AFM operation for measurement of bacterial biofilm: Atomic force microscope (AFM) (Nanoscope IIIA contact mode, Digital Instruments) was used to obtain topographic images of sample

surfaces on air. Treated and untreated coupons were examined after removing from medium and left to air-dry. Images were taken close to the middle of the samples, at least on three different places.

Electrochemical technique (Polarization Resistance technique): A potentiodynamic method was used to obtain the potential-current (E-I) ratio, with respect to the free corrosion potential, E_{corr} Steel rod electrodes were placed in 300-ml Erlenmeyer flasks filled with 250 ml of described medium with and without inoculums and biocides. The flasks were inoculated with bacterial isolates as following: control with inoculated medium without adding biocide, and adding biocide at 25ppm, 100ppm, and 500ppm. At the same time, the blank was non-inoculated medium. The steel rods screwed to the samples holder, connected to the potential measuring instrument, were polarized by 50mV and the corrosion rate calculated automatically from the E values and was presented digitally on the screen. Measurements were made daily and at extended time periods depending on potential changes.

RESULTS AND DISCUSSION

Characterization and identification of the isolate: The characteristic of *pseudomonas* species was aerobic, gram-negative, and motile, rod shaped, producing green pigments and biochemical tests were Catalase and Oxidasepositive. According to Bergy's manual, it clearly seems to be *pseudomonas aeruginosa*. The characteristic of sulphate reducing bacteria (SRB) was anaerobic, gram negative, lactate oxidation, not utilize the acetate and motile, the deslfvoirdin was negative, it might be *Desulfobulbussp*.

Fluorescent micrographs: The most widely used stain is the Acridine Orange (AO). It is a nucleic acid selective stain. AO interacts with DNA and RNA by intercalation or electrostatic attraction respectively. Cells may appear red-orange or green. It may be distinguished based on

color as live vs. dead cells; live cells contain more RNA and appear orange/red, dead cells lack RNA but may contain DNA and appear green.

In experiments of this study, the stained coupons showed that fluorescent colors were changed, depending on adding biocide. (Fig. 1) illustrates a typical image of *Pseudomonas aeruginosa* settlement on stainless steel coupons AISI 304 after immersion in R2A medium with different concentration of biocide for 5 days of incubation. Attached bacteria have shown ability to grow under stress condition (increasing concentrations of biocide), which indicate the acclimation, while 25 and 100ppm have shown slighter effect on embedded bacteria, 500ppm showed effective result, but takes longer time for proper effectiveness.

Figure (2) illustrates image of *Desulfobulbus* settlement on stainless steel coupons AISI 316 after immersion in postgated medium B with different concentrations of biocide for 5 days to three weeks. The results show that 25ppm of biocide concentration is enough to prevent the bacterial attachments. In order to confirm previous results, the electrochemical technique (LPR) was used.

Electrochemical results and biocide assessment: The use of electrochemical techniques for the evaluation of microbial corrosion, as well as the biocide selection and evaluation, has been recently studied by Mansfeld, 2003.

The polarization resistance (PR) is the most common electrochemical technique used to evaluate corrosion rates on metals surface. This evaluation technique allows measuring instantaneous corrosion rates, and its monitoring can be continuous. Therefore, the technique is useful when the corrosion rate changes. A simplification of the Polarization resistance technique is the linear polarization techniques which assumed that the relationship between the potential (E) and current density (i) is linear. The results of *Pseudomonas aeruginosa* have shown a different trend as can be seen in (Fig. 3) the result confirm that, the corrosion rate of the inoculated medium without any biocide was dramatically increased and reached after 3 days for maximum value. Regarding the biocide action, 25 and 100ppm concentration of biocide has showed lower effect on the corrosion rate, while 500ppm concentration of biocides decreased significantly the corrosion rate. The corrosion rate was steady

after 9 days, this due to the adhering bacteria and their polymeric material. At the same time, when the microorganisms were inhibited due to the biocide action, there is a reduction on the corrosion rate values. In Fig.4 the corrosion rate was increasing with inoculated medium (corrosion rate is reflection to bacterial activities) but at 100 and 500ppm concentrations of biocide no bacterial activities has been shown. This is an indicator for biocide efficiency against bacterial attachment.

These results confirm that presence of 500 ppm significantly reduce the corrosion rate and has most effect against *Pseudomonas aeruginosa*. But in case of SRB the 25ppm is enough to prevent attached bacteria.

The effect and action of antimicrobial compounds: Atomic force microscopy (AFM) has been used in several studies for the investigation of the effect and mode of action of antimicrobial agents upon bacterial cells. These studies including the action of Penicillin on *Bacillus subtilis* (Kasas *et al*, 1994), the effect of pretreatment of steel with glutaraldehyde on aerobic marine biofilms formed upon stainless steels (Tapper *et al*, 1998; Li-Chong *et al*, 2002, Beech *et al*, 2002; Beech and 2004), as well as the microorganisms embedded into biofilm were visualized by AFM: this technique is good for the visualization of shape and size of microbes embedded into biofilms and for determination of thin layer thickness.

This research have used the AFM to study the adhesion of cells and the formation of biofilms on AISI 304 and 316 AISI stainless steel surfaces in the absence and present of the biocide and on other way, to investigate the action of biocide on pure bacterial cells. Fig.5 illustrates a typical image of *Pseudomonas aeruginosa* cells attached to the stainless steel surface after immersion in R2A medium for 2 days. The dimensions of the cell were 3.406 x 0.281 μm (length x width). The shape of the bacteria is clearly visible. Fig.6 illustrates aggregates growth of sulphate reducing bacteria on surface after immersion in postgate medium B for 5 days and the mature biofilms on surface where the attached bacteria surrounded by by-products (polymeric materials "EPS" and sulphied, Fig.7). However, the obtained results in present work confirmed that, *Pseudomonas aeruginosa* has tolerance to increasing biocide, and optimum efficacy of biocide at 500ppm. But in case of SRB, 25ppm is enough to control bacterial activities

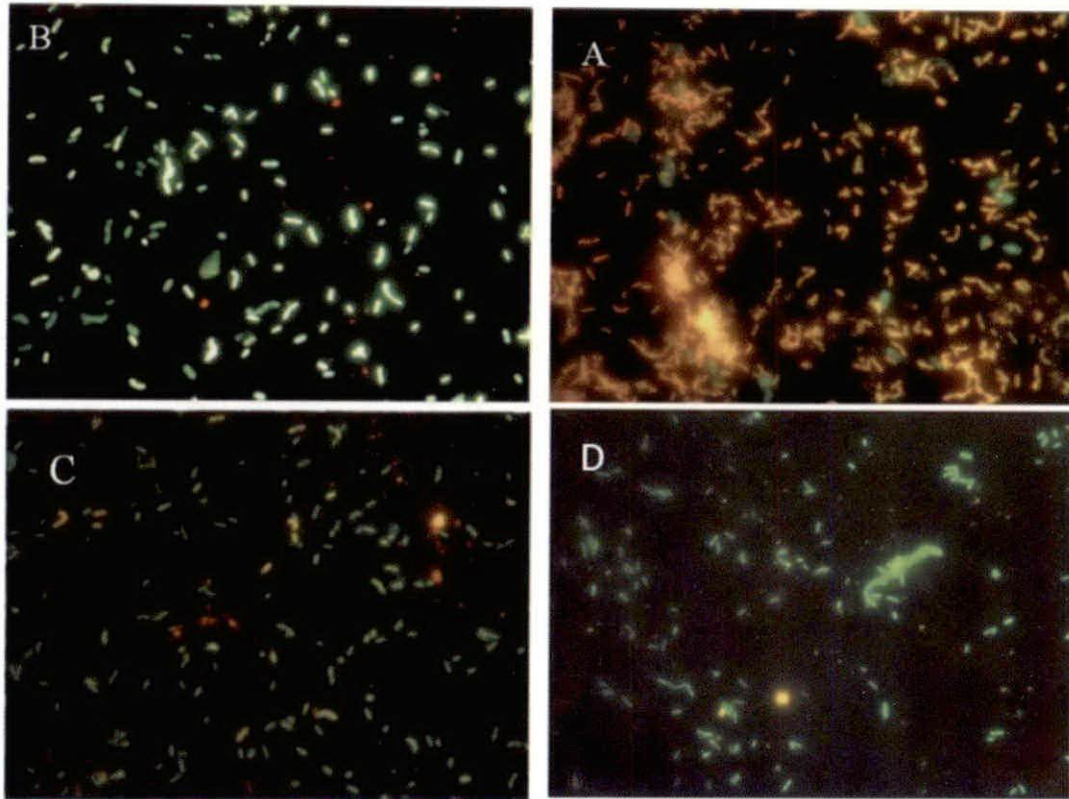


Fig. 1 The fluorescent images of *Pseudomonas aeruginosa* on AISI 304 after 5 days with different concentrations of biocide stained with AO (A) without biocide (B) with 25ppm (C) with 100ppm (D) with 500ppm – green could be indication for dead cells and red-orange for live cells .

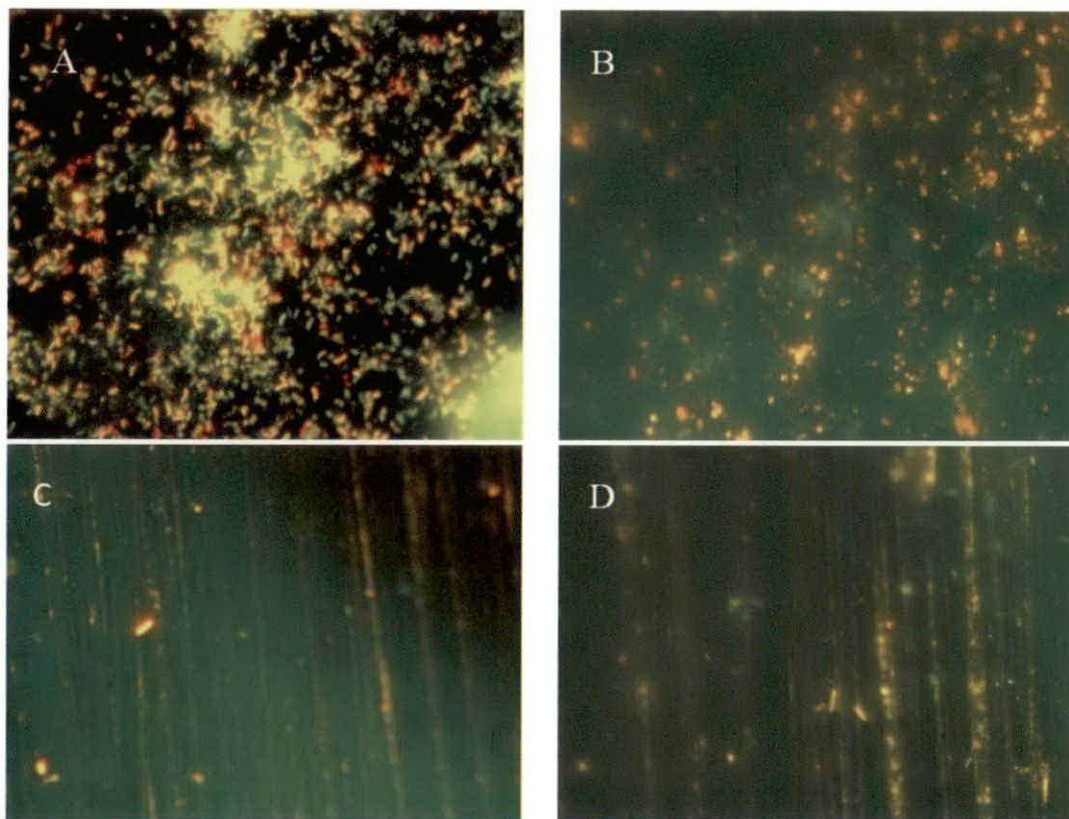


Fig. 2 The fluorescent images of *Desulfobulbus* sp on AISI 316 after 21 days with different concentrations of biocide stained with AO (A) without biocide (B) with 25ppm (C) with 100ppm (D) with 500ppm.

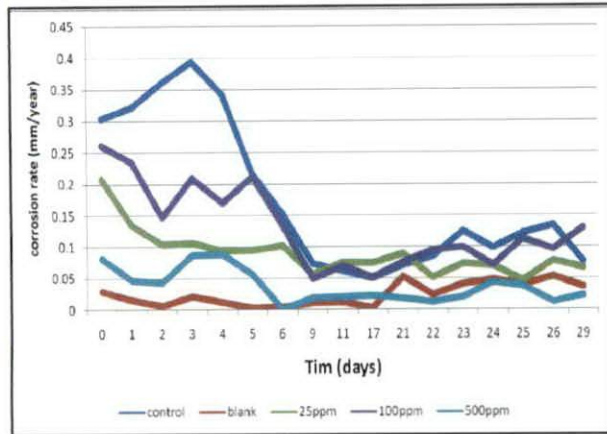


Fig. 3 Effect of *Pseudomonas aeruginosa* with and without biocide (at different concentrations; 25ppm, 100ppm and 500ppm) on the corrosion rate.

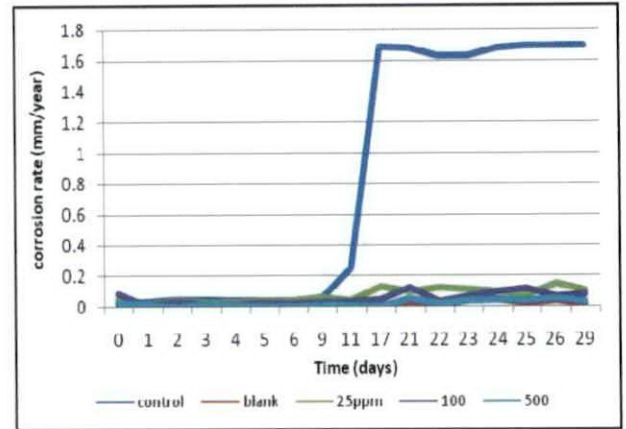


Fig. 4 Effect of *Desulfobulbus* sp with and without biocide (at different concentrations; 25ppm, 100ppm and 500ppm) on the corrosion rate.

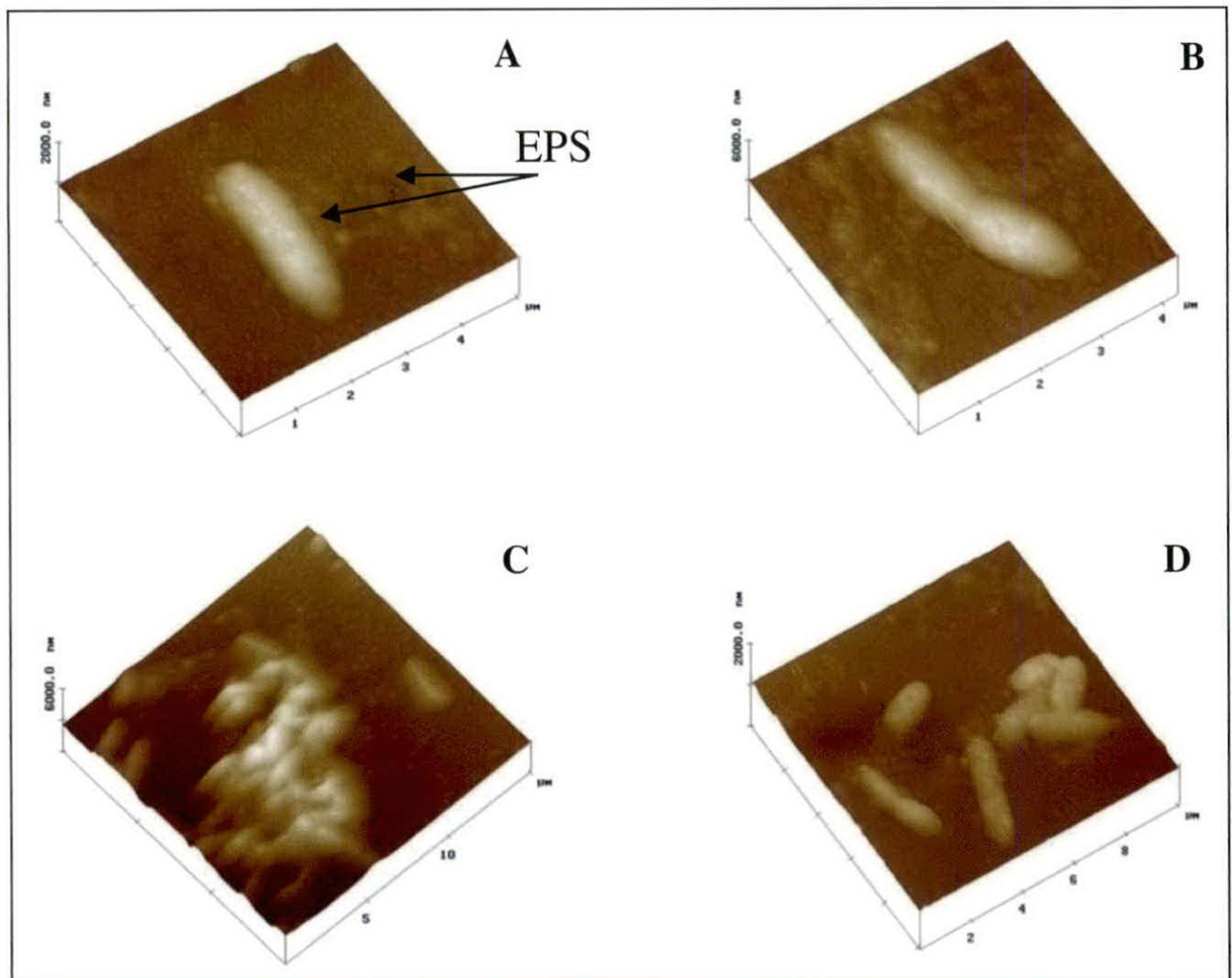


Fig. 5 The typical shaped of *pseudomonas aerugnoa* cells attached to AISI 304 stainless steel surfaces (A) single cell on the metal surface (B) multiplying cells on the metal surface and EPS produces are all over the surface (C) several microbes pre-treated (D) biofilm covering the stainless steel 304 surface.

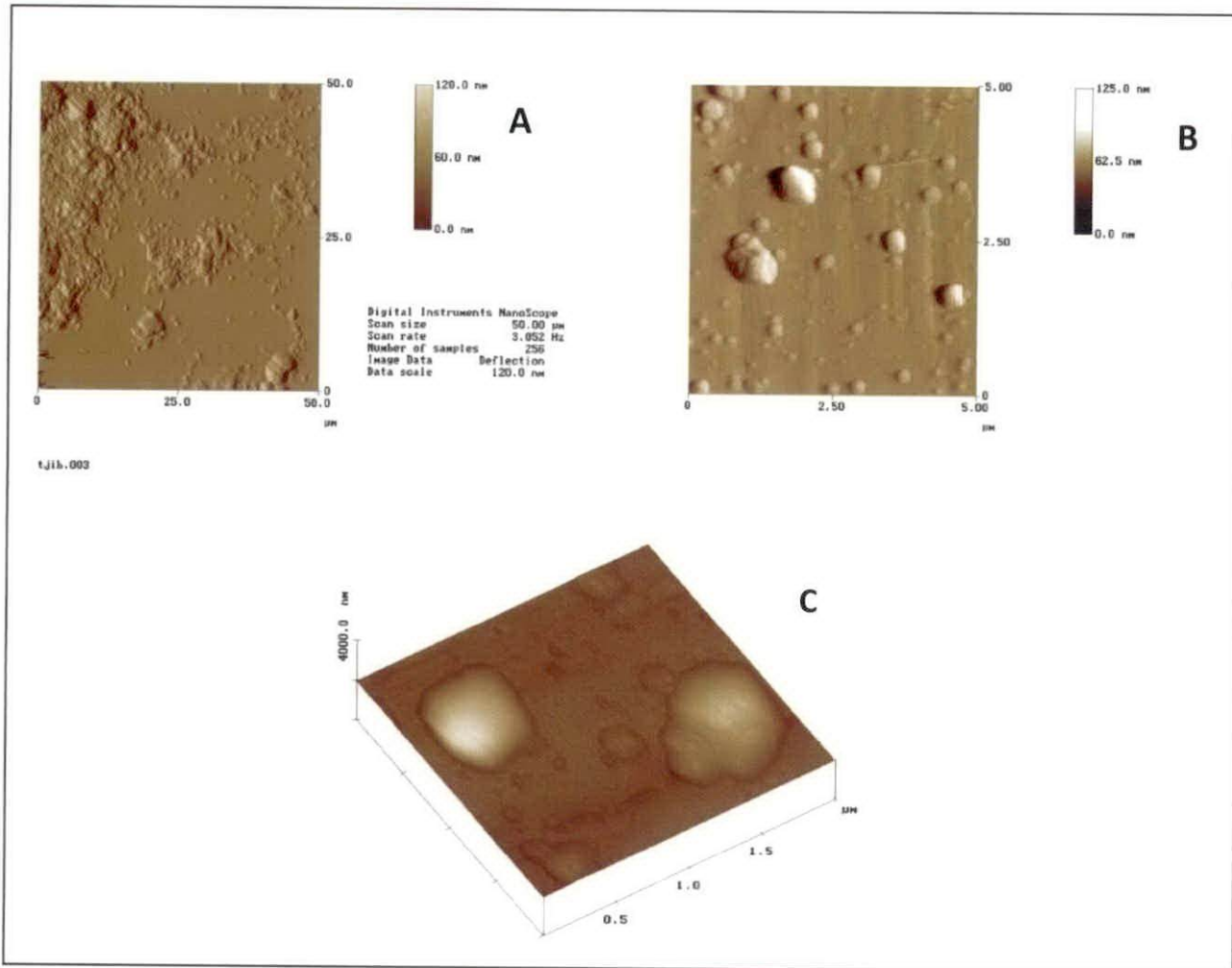


Fig.6 The *Desulfobulbus* sp cells attached to AISI 316 stainless steel surfaces (A) aggregates growth on the metal surface (B) several microbes pre-treated (C) biofilm covering the stainless steel 316 surface

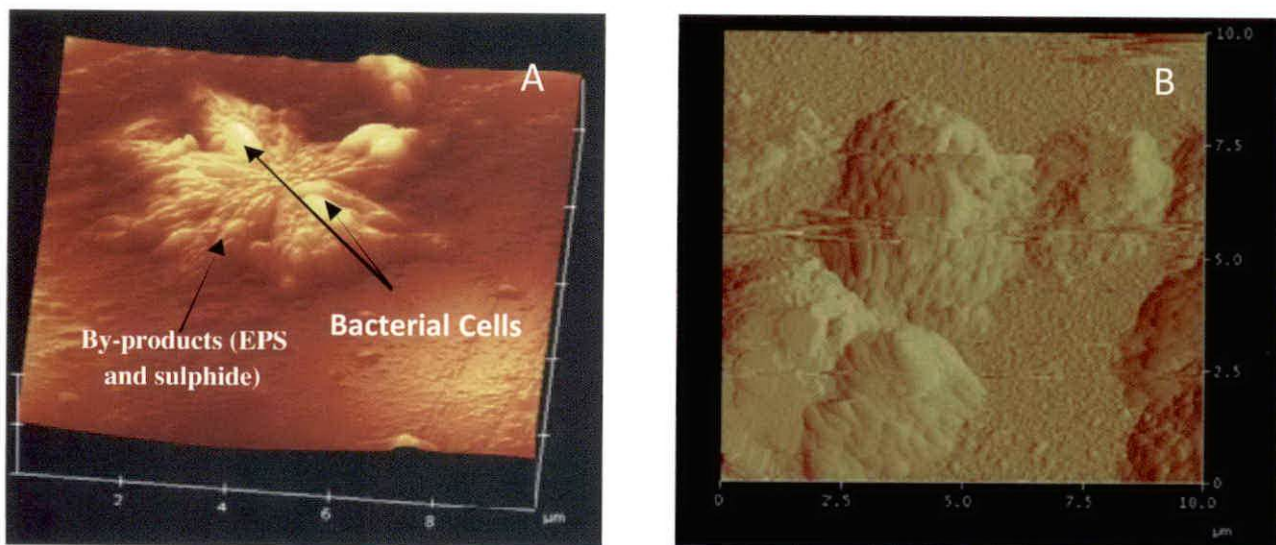


Fig. 7 The mature biofilms of *Desulfobulbus* sp cells attached to AISI 316 stainless steel surfaces after three weeks (A) multiplying cells on the metal surface surrounded by EPS and some sulfides (B) biofilm covering the stainless steel 316 surface.

CONCLUSION

Results showed that *Pseudomonas aeruginosa* has the ability to grow at high concentration of QACs and GA biocide and has tolerance up to 500ppm. The fluorescent images showed that bacteria were attached on surface even at high concentration, and the response to biocide, however showed low efficiency versus time. But, in case of SRB, 25ppm is sufficient to prevent attached bacteria.

The electrochemical results showed that *Pseudomonas aeruginosa* has effect on the corrosion rate where the corrosion rate of control without any biocide was dramatically increased. While the concentrations of 500ppm has showed decreases of the corrosion rate significantly for *Pseudomonas aeruginosa*. But for *Desulfobulbus* sp, all concentrations showed the same efficiency on the corrosion rate.

AFM showed the visualizing bacteria on stainless steel surface. The maturation of biofilms is difficult to visualize because of microbial by-products.

More investigations need to be carried out to study the effect of the blending biocides on mixed culture. Also simulation of continuous culture by using biofilms reactor should be considered.

REFERENCES

- Bandoni, J. R., and Koske, R. E., (1974). Monolayers and Microbial Dispersal, *Science (SUA)*, **183**: 1079-1080.
- Beech, I. B.; Smith, J. R.; Steele, A. A.; Penegar, I., and Campbell, S., (2002). The Use of Atomic Force Microscopy for Studying Interactions of Bacterial Biofilms with Surfaces. *Colloids and Surfaces B. Biointerfaces*, **23**: 231-247
- Beech, I. B. (2004). Corrosion of Technical Materials in the Presence of Biofilms—Current Understanding and State-of-the Art Methods of Study. *International Biodeterioration & Biodegradation*, **53**: 177 – 183.
- Bergey's Manual of Determinative Bacteriology (7th ed) (1964). American Journal of Public Health and the Nation's Health, **54(3)**: 544.
- Busscher, H. J. and Weerkamp, A. H., (1987). Specific and Nonspecific Interactions in Bacterial Adhesion to Solid Substrata, *FEMS Microbiol. Rev.*, **46**: 165-173.
- Chambon, M.; Bailly, J.-L., and Peigue-Lafeuille, H. (1992). Activity of Glutaraldehyde at Low Concentrations Against Capsid Proteins of Polio-Virus Type 1 and Echoirus Type 25. *Appl. Environ. Microbiol.* **58**: 3517–3521.
- Chapman S. J., (2003) . Disinfectant Resistance Mechanisms, Cross-Resistance, and Co-Resistance. *International Biodeterioration & Biodegradation*, **51**: 271 – 276.
- Dinty, J., Musk, J. and Hergenrother, P. J. (2006). Chemical Countermeasures for the Control of Bacterial Biofilms: Effective Compounds and Promising Targets. *Current Medicinal Chemistry*, **13**: 2163-2177.
- Flemming, H. C. (1996). Biofouling and Microbiologically Influenced Corrosion (MIC)—an Economical and Technical Overview. In: E. Heitz, W. Sand and H.-C. Flemming (eds.) *Microbial Deterioration of Materials*, Springer, Heidelberg: 5-14.
- Guerin-Mechin, L.; Dubois-Brissonnet, F.; Heyd, B. and Leveau, J. Y. (2000). Quaternary Ammonium Compound Stresses Induce Specific Variations in Fatty Acid Composition of *Pseudomonas aeruginosa*. *International Journal of Food Microbiology*, **55**: 157–159.
- Hector, A. V., (2002). Prevention and Control of Biocorrosion. *International Biodeterioration & Biodegradation*, **49**: 259 – 270.
- Heinzel, M. (1998). Phenomena of Biocide Resistance in Microorganisms. *International Biodeterioration & Biodegradation*. **41**: 225-234.
- Kasas, S.; Fellay, B. and Cargnello, R. (1994). Surf. Interface Anal., **21**: 400– 401.
- Keresztes, Z.; Felhosi, I. and Kalman, E. (2001). Role of Redox Properties of Biofilms in Corrosion Processes. *Electrochimica Acta*, **46**: 3841–3849.
- Kimberly, K. J. (2004). What Drives Bacteria to Produce a Biofilm?. *FEMS Microbiology Letters*, **236**: 163–173.
- Lado, Ti. and J. W. Costerton (1990). Methods for Studying Biofilm Bacteria. *Methods in Microbiology*, **22**: 385-307.
- Li-Chong Xua; Kwong, Yu. and Herbert, H. P. (2002). Application of Atomic Force Microscopy in the Study of Microbiologically Influenced Corrosion. *Materials Characterization*, **48**: 195– 203.
- Mansfeld, F. (2003). The use of Electrochemical Techniques for the Investigation and Monitoring of Microbiologically Influenced Corrosion and its Inhibition—a review. *Materials and Corrosion*, **54**: 489–502.

- McBain, A. J., and Gilbert, P., (2001). Biocide Tolerance and the Harbingers of Doom. *International Biodeterioration & Biodegradation*, **47**: 55–61.
- McBain, A. J., Ruth G. L., Louise E. M., Carl E. C. and Gilbert, P., (2004). Effects of Quaternary-Ammonium-Based Formulations on Bacterial Community Dynamics and Antimicrobial Susceptibility. *Appl. Environ. Microbiol.*: 3449–3456.
- Russell, A. D. (1995). Mechanisms of Bacterial Resistance to Biocides. *International Biodeterioration & Biodegradation*: 247-265.
- Russell, A. D. (2003). Similarities and Differences in the Responses of Microorganisms to Biocides. *Journal of Antimicrobial Chemotherapy*, **52**: 750– 763.
- Rutala, W. A. (1990). APIC Guideline for Selection and use of Disinfectants. *Am. J. Infect. Control*, **18**: 99–117.
- Stoodley, P.; Sauer, K.; Davies, D.G. and Costerton, J. W. (2002). Biofilms as Complex Differentiated Communities. *Annu Rev Microbiol*, **56**:187-209.
- Sundheim, G.; Langsrud, S.; Heir, E. and Holck, A. L. (1998). Bacterial Resistance to Disinfectants Containing Quaternary Ammonium Compounds. *International Biodeterioration & Biodegradation*, **41**: 235-239.
- Tapper, R. C.; Smith, J. R.; Cocking, C. and Beech, I. B. (1998). *Biofilm J. 3 (BF98004), Paper 4*: Online Journal.
- Wingender, J.; Neu, T. and Flemming, H. C. (1999). What are Bacterial Extracellular Polymer Substances? Springer, Heidelberg, Berlin, 1-19.
- Zarnea, G., (1994). *Tratat de Microbiologie Generală, V,159-160*: 971-976.

OPTIMISATION OF BIOSTIMULATION BY USING DIFFERENT NUTRIENT RATIOS TO IMPROVE BIOREMEDIATION OF PETROLEUM CONTAMINATED SOIL

Althalb Hakima*

Abstract: Petroleum contamination of sandy soils is a severe environmental problem in Libya, but relatively little work has been carried out to optimize the bioremediation of such heavily contaminated soil, particularly at a pilot scale.

This study assessed the effect of varying nutrient (NPK) levels and types (urea) on bioremediation of diesel contaminated soil by a combination of chemical and toxicological analyses. Varying nutrient C:N:P ratios were used 100:10:10, 100:10:1, 100:1:1 and 100:1:0.1 that contained both NPK fertilizer and urea as an extra source of nitrogen, the optimum C:N:P ratio found was 100:10:1 (and urea was found to be a good nutrient source). In this study (achieved approximately 69% TPH removal). The amounts of petroleum removed as revealed by chemical analysis appeared to correspond well to bacterial counts and the residual toxicity of soil as estimated by the Microtox assay. The highest amounts of nutrients used (C:N:P ratio of 100:10:10) did slightly reduce bioremediation effectiveness. GC analysis revealed that hydrocarbons of chain length C9-C20 were most effectively removed and that the higher chain length petroleum compounds (>C20) remained in the soil. Overall the work demonstrated the clear potential of nutrient stimulation to reduce levels of hydrocarbons present and to reduce the soil toxicity.

Keywords: Nutrient, NPK, toxicity, bioremediation, biostimulation

INTRODUCTION

The comparison of PH transformation levels between bioaugmentation and biostimulation as carried out in the previous studies (data not shown) revealed that biostimulation was the best potential treatment method for the bioremediation of the Zawia Oil Refinery soils. However, only one nutrient level was used and bioremediation could be enhanced further if nutrient levels were optimized. In petroleum-contaminated soils, the availability of nitrogen and phosphorus are often limited due to the excessive carbon input from the hydrocarbons (Jin and Fallgren, 2007). The importance of obtaining the correct nutrient level for bioremediation is emphasized in several previous studies. For example Sarkar *et al* (2005) showed that the microbial population was decreased in the fertilizer-amended soils, suggesting NH₃ overdosing and/or the toxic effect of the used fertilizer. Chaillan *et al* (2006)

reported that the addition of urea appeared to be toxic. In addition, several authors have reported the negative effect of high nitrogen, phosphorus and potassium concentrations on the biodegradation of hydrocarbons. For instance, Eke and Scholz (2008) concluded that biodegradation activity can be inhibited by the addition of excessive nutrient concentrations. It has been demonstrated that microbial activity and petroleum degradation in contaminated soils can be depressed as result of excess nitrogen due to osmotic soil water potential depression (Walworth *et al*, 2007). Thus, in order to avoid any inhibition excessively high nutrient levels were not used in this study. Overall, it appears that both the level and type of nutrients added can either improve or decrease the level of bioremediation achieved.

There are no specific methods for determining the exact nutrient sources and ratios to utilize at a site and indeed nutrient optimization for bioremediation appears to have received relatively little attention despite its' clear importance. Therefore, the optimal C:N:P ratio frequently recommended for

* Industrial and Production Chemistry Department,
Libyan Petroleum Institute, Tripoli, Libya, althalb798@yahoo.com

bioremediation is 100:10:1 as used in this work (Liebeg and Cutright, 1999). Other work has reported that the optimal C:N:P ratio is 100:15:3 (33:5:1) for hydrocarbon biodegradation (Sarkar *et al*, 2005).

The principle aim of the work in this study was to determine the best nutrient level to reduce PH in the soils to a safe level. The determination of the success of bioremediation (i.e. reduction of risk from the contamination) is an interesting area and most studies only chemically analyse soil for compounds present. However, there is a need to also determine soil toxicity as toxic transformation intermediates may be produced during bioremediation. This is indicated by several previous studies e.g. pentachlorophenol transformation in soil and microbial transformation of diesel oil (Mariano *et al* (2007). The presence of toxic intermediates produced during biodegradation of crude oil caused luminescence inhibition (Plaza *et al*, 2008). There are a number of methods that can be used for determining soil toxicity e.g. bacterial bioluminescence, plant growth, earthworm etc. Dorn and Salanitro (2000) assessed bioremediation using different ecotoxicity methods, the earthworm (*Eiseniafetida*) 14-d lethality assay, the modified Microbics Microtox Solid-Phase assay, and the 14-d plant seed germination and growth assays.

In this research, a microbiological luminescence-based bacterial kit was applied to assess the toxicity of petroleum hydrocarbon contaminated soil during and after nutrient assisted bioremediation. Specifically, this involved the use of *Vibrio fischeri* inhibition assay (Microtox TM). This toxicity test has been used previously in several soil toxicity studies and has the advantages of being rapid and economical to carry out. Light-emitting bacteria can be a suitable tool for environmental studies. In vivo luminescence is a sensitive indicator of xenobiotic toxicity to microorganisms and reflects the metabolic status of the cell as result of being directly coupled to respiration via the electron transport chain (Girotti *et al*, 2008).

The use of a combination of both chemical and toxicological analysis was considered to be the best method to determine the optimum nutrient level for bioremediation of the PH contaminated the Zawia Refinery soils.

Aims and Objectives

The aim of this study was to optimise bioremediation of PH contaminated the Western

Refinery soils by altering nutrient levels. A secondary aim was to assess the success of bioremediation by a combination of chemical and toxicological methods.

Objectives

To optimize nutrient levels for bioremediation, by using different types and ratios of nutrient amendments (Nitrogen based fertilizer and urea).

To assess the use of a bacterial biosensor-based tool kit to monitor hydrocarbon bioremediation.

To compare the bacterial based toxicity of treated soil with more traditional chemical analysis of PH e.g. does a decrease in soil toxicity (as measured by Microtox) correlate with a lower level of petroleum compounds as determined by chemical analysis?

To choose the optimum nutrient type and ratio for use in subsequent pilot scale bioremediation studies.

MATERIALS AND METHODS

Site Description and soil collection

Target soil samples were obtained from the Zawia Oil Refinery. A total of twenty four fresh soil samples were collected at 20-30 cm depth from a contaminated diesel-refuelling area, from the spill around pipelines which carry the refined products to the shipping points situated at the studied site the Zawia Refinery, Libya. The soil contained a total petroleum hydrocarbon (TPH) level of 35000 mg/kg (see results section below). Samples were placed in plastic bags and cooled for transport (see details analyses below).

Overview of experiments on nutrient optimization for bioremediation

The initial nutrient levels (available C, N and P) in the soil samples were measured in order to evaluate the amount of nutrient addition needed to achieve the optimal C:N:P ratio. The amount of nutrient required for microbes are approximately the same as their cell composition. Though, carbon is needed at higher quantities by cells, this can be supplied by the contaminant present (Liebeg and Cutright, 1999). Degradation tests were set up in small-scale microcosms simulating soil conditions, to examine the response of the indigenous hydrocarbon degraders to different nutrient supplements in soil by manipulating the C/N/P ratio. The initial nutrient levels in the soil samples were measured (see nutrient analysis's section) and results indicated that nitrogen and phosphorus levels were very low.

Gas chromatography analysis showed that the contaminants consist of an average carbon chain length of approximately between C₂₃- C₂₇. This indicates that the contaminant was mainly diesel fuel and/or crude oil. Based on this result the required amount of nitrogen and phosphorus were calculated accordingly. The required amount of nitrogen and phosphorus was based on the typical C:N:Pratio of 100:10:1.

Soil Analysis

Soil texture: Particle size was determined using a Master Sizer 2000 (Malvern International) at a chemical analysis laboratory of the Libyan Petroleum Institute (LPI). Libyan soils are essentially of the texture of "sandy loam". They are typically poor in essential nutrients (N, P) and have low microbial counts. Loamy sand soils tend to be dry and need to be humidified continuously during biological treatment. They do, however, have good permeation properties and thus facilitate aeration and gas exchange during bioremediation. The petroleum products that contaminated the soil samples were extracted using a Soxhlet Extraction System (SES) (see petroleum analysis of contaminated soil samples below). Dichloromethane was used for the extraction.

Soil pH

Soil pH was determined using a pH meter (Jenway 3020) on soil suspensions in water in triplicates as described by ISO 10390 (1994). Twenty five grams of soil was stirred continuously with 50ml of deionised water d.d.H₂O for 15 minutes and allowed to equilibrate for another 15 minutes. The pH meter was immersed in the supernatant and was rotated gently. Then a pH reading was recorded, with the pH value being expressed in terms of $\text{pH} = \log_{10}\{\text{H}^+\}$, where $\{\text{H}^+\}$ = hydrogen ion concentration.

Moisture Content and Water Holding Capacity (WHC)

Moisture content was determined by drying 10g of the soil sample in an oven at 105°C. In triplicate, 10g of soil was added on filter papers (Whatman No. 42) and fitted into Buchner funnels. Deionised water was added slowly (at a rate of 1cm hr⁻¹) until the water level was just above the soil surface and the soil was saturated and dripping into the flask below. The funnel was then removed and left to drain overnight until no further drainage occurred. The soil was left for 24 hours, rewetted to saturation and the whole apparatus was reweighed. The percentage

of moisture content of the soil in triplicate was then determined. The 100% water holding capacity could then be calculated as follows:

$$100\% \text{ WHC} = \frac{\text{mean total water (g) taken up by the soil samples}}{\text{Average amount of oven dried soil (ODS) in the funnel}}$$

Nutrient Analyses

The soils were dried, sieved (2mm) and analysed for available K, N, and P. Available potassium was measured by exchangeable cation extraction with NH₄NO₃ at 1:5 w/v (Anon, 1986). The extractable potassium in the soil was measured using flame photometric determination. Available nitrogen was determined after extraction with 50ml 2M KCL (potassium chloride), (Keeney and Bemner, 1966). Available phosphorus was measured as Olsen-P (Olsen *et al.*, 1954), extracted by sodium bicarbonate at a pH of 8.5 for 30min.

Soil Microcosms

Nine different nutrient treatments were carried out with varied C:N:P ratios and the use of urea as an additional nutrient source.

Microcosm experiments were prepared. All experiments were run in triplicate. For each set of experiments, 100g of soil (dry wt) were placed in a 250ml dark jars, the control soil was left un-amended (no nutrients added) whilst the amended soils were mixed with different types and levels of nutrients to give varying C:N:P ratios 100:10:10, 100:10:1, 100:1:1, and 100:1:0.1, respectively.

Another set of nutrient amended microcosms containing varying nutrient ratios was also set up that contained both NPK fertilizer and urea as an extra source of nitrogen. 0.76g urea was added to 100g soil. This gives 100gC:10g N, and the rest of N and P were made to the required C:N:P ratio by adding the commercial NPK fertilizer. The following C:N:P ratios were used 100:10:10, 100:10:1, 100:1:1 and 100:1:0.1.

For all treatments, moisture was adjusted (added water to 60% WHC) and kept constant throughout the duration of the experiment. Soils were incubated for 130 days at 30°C.

Chemical and microbiological assessment of contaminated soil samples were carried out as described below.

Microbial Enumeration

The estimation of total bacterial viable counts in the bioremediation soil samples was carried out using a dilution plate count technique.

Soil (1g) was suspended in 9 ml of ¼ strength ringers solution, shaken for 10min (with a vortex mixer) to achieve a homogenized suspension. Following suspension, the supernatant containing bacterial cells was serially diluted with Ringers solution. A series of dilutions was then carried out up to 10^{-6} , which was used for the bacterial counts. A sample (0.1ml) of the appropriate dilution was then inoculated onto sterile, 20-ml petri dishes containing Nutrient Agar (DIFCO). Bacterial viable counts were estimated on days 0, 15, 31, 65, 130.

Petroleum Hydrocarbons Assays

Petroleum analysis of contaminated soil samples

Soil samples (triplicates) were analysed for petroleum hydrocarbons at the start and end of the experimental incubation.

10g of petroleum contaminated soil were weighed, dried, and extracted for 8 hours using soxhlet extraction apparatus (VELP Scientific, Model SER 148 Solvent Extractor) with 450 ml DCM (dichloromethane, 93%, 1:10). To absorb the moisture from the samples, extracts were decanted and concentrated to 40ml using a rotary evaporator. The dichloromethane was concentrated to 1.5-2mL, and the extracts were transferred into 2 ml gas chromatography (GC) vial for subsequent analysis. The organic phase of the extract was removed with a volumetric pipette and put in a sealed flask for further examination.

- 1) TPH fractions were analysed using a Varian CP-3800 Gas Chromatograph, with flame ionization detection (FID). The determination of hydrocarbon concentrations is usually by capillary gas chromatography and a flame ionization detector (GC/FID). The effects of the bioremediation process have been followed by evaluating the changes in hydrocarbons content by gas chromatography and TPH analyser.
- 2 -An infra-red spectrophotometric method based on USA EPA method 418.1 (Spectrophotometric, Infrared): InfraCal TPH/TOG/ Model CVH. Statistical analysis of the results was performed using SPSS version 14 STATISTICA for Windows release 5.1.

Gas Chromatograph Analysis

Analyses of n-alkanes and total petroleum hydrocarbons were performed at the beginning and end (130 days) of the chemostat incubation using a Chrompack Model 439 capillary gas chromatograph flame ionization detector (FID).

The gas chromatographic analyses were conducted with a 300°C detector, 300°C injector, split ratio on 100:1 and samples of 0.1µl injections. A column temperature of 40°C was held for 2min and then ramped at a rate of 5°C/min to a final temperature of 300°C and held for 30min.

Degradation in the microcosms was estimated as the difference between the initial and final concentrations of total hydrocarbons (Rahman *et al*, 2002).

Bioluminescence bioassay for toxicity

Inhibition Assay

The assay is based on the analysis of light emission reduction of luminescent bacteria *Vibrio fischeri* (NRRL B-11177) when exposed to a contaminated environmental sample. In this work soil extract was exposed to *V. fischeri*: on days 0, 15, 31, 65, 130 of the bioremediation experiment.

Soil ethanol extract method: 2 g dry wt soil sample was placed in 10ml polypropylene centrifuge tubes and 2ml of 95% ethanol was added (in triplicate). They were mixed for 30 minutes in order to extract all the toxic components and then centrifuged at 6000rpm for 5 minutes. The supernatant was removed and the extract mixed with 3% sterile solution of NaCl (3% ethanol in 2% NaCl) following standard extraction procedure described by Girotti *et al*, (2008).

Freeze dried, bioluminescent cells of *V. fischeri* (as supplied by the manufacturer: SDIX Europe Ltd) were resuscitated by adding 1ml 0.1M sterile KCl and shaking at 25°C, 200rpm for 1 hour. In general assays were performed as described in Paton *et al*. (2006). After resuscitation, *V. fischeri* was used immediately. 100µl aliquot of this suspension was added to 900µl of extracted soil ethanol solution and mixed at 15-s intervals. The luminescence of the samples was measured after 15 min. exposure using the Microtox acute toxicity test Microtox Model 500 Analyzer (SDIX Europe Ltd.), as per the manufacturer's instructions. Microtox reagents and test solutions were also supplied by Strategic Diagnostics Inc. Three independent replicates of each assay were performed for each soil extract and the luminescence inhibition after 15 min exposure to each sample was taken as endpoint and recorded as relative light units (RLU).

Light emission was measured as RLU and calculated from the mean of the three replicates for each sample as % bioluminescence relative to control

samples (ethanol blank) for each assay (Girottiet al., 2008). Bioassays were carried out at room temperature which varied from 18 to 20°C.

The toxicity effect of different concentrations of nutrient amendments calculated by the following

$$\% \text{INH} = \frac{Be - Se}{Be} \times 100 \quad \text{Or}$$

$$\text{INH} (\%) = (1 - (Se/Be)) \times 100$$

Where *Be* is the emission of the blank and *Se* that of the sample at the different times. The INH (Inhibition efficiency) values are the averages of at least three measurements, EC50 values are calculated corresponding to INH (%) = 50. If the inhibition caused by the extracted sample is below 20 %, the amount of toxicants is less than the detection limit. If the inhibition is between 20 - 50 %, the sample contains low amounts of toxicants and if over 50 % inhibition is observed, the sample contains high amount of toxicants (LaFarré et al., 2001; Girotti et al., 2008).

RESULTS

Soil chemical and physical analysis

Although the soil samples used in the previous work and current experiments originated from the same site, namely the Western Refinery, Libya, the initial contamination level was not the same. The source of the soil used in this experiment was a diesel-refuelling area, and soil was contaminated by a mixture of crude oil and diesel oil. In order to obtain an indication of potential pollutants, samples were taken from oil-containing soil samples. A suite of chemical analyses and biological assessments carried out (Table 1) showed that soil texture was sandy and of a low nutrient level (N and P). Soil pH was neutral to slightly alkaline. The soil samples

Table 1: Site Information and general properties of diesel contaminated soil studies

Contaminated soil property	
Sampling location	Western Refinery
Texture	Sand
pH	7.6
Water holding capacity (%)	1.29
Moisture (%) @105°C	3.16
Available C (ppm)	8.69 ppm
Available N (ppm)	0.051 ppm
NH ₄ -N	
Available P (ppm)	19.76 ppm
Total Petroleum Hydrocarbon (ppm)	35000 ppm
CFU	2.4 × 10 ⁷ CFU g ⁻¹

taken were mixed for homogenization to decrease the localized aggregates of contaminant levels. Total Petroleum Hydrocarbon (TPH) content was 35,000ppm, pH 7.6, 0.051ppm nitrogen, 19.76ppm phosphorus, and 1.29% moisture.

Change in microbial population during microcosm incubation

Generally there was a significant increase ($p < 0.05$) in viable counts over the first 31 days of the bioremediation in all soil microcosms including the non-amended control (Figs.1 & 2). Counts decreased after this time in all microcosms to levels that were determined initially.

In soil microcosms treated with NPK the nutrient ratios of 100:10:10; 100:10:1 and 100:1:1 gave significantly higher ($p < 0.02$) bacterial counts than the control soils after 31 days incubation. For example, the cell count with C:N:P ratio of 100:10:1 was 7.33×10^{10} cfu/g soil after 31 days compared to the control which gave 4.2×10^{10} cfu/g soil.

In soil microcosms treated with urea and NPK fertiliser, bacterial counts achieved during the middle stages of incubation were significantly higher ($p < 0.003$) than those observed with NPK fertiliser alone. Increases in bacterial counts to 4.1×10^{11} cfu/g soil and 3.6×10^{11} cfu/g soil during week 15 in amended microcosms by urea mixed C:N:P ratios (100:10:1 and 100:1:1 respectively) were observed interestingly. The highest ratio of urea mixed with NPK (100:10:10) appeared to restrict microbial counts to levels similar to those found in control soils after 2 weeks of incubation but the counts increased significantly after a further incubation period. The lowest level of urea plus NPK fertilizer did not increase bacterial counts relative to the control.

Effect of different nutrients ratios on bioremediation

The chemical analysis of the soil samples confirmed that the five soils had the same level of TPH contamination at the start of the experiment. The total content, before and after 4 months treatment, is reported in (Figs. 3 and 4).

During the bioremediation process it was possible to observe that the impact of NPK treated microcosms and urea mixed with NPK treated microcosms was clearly different to that of the control in relation to petroleum transformation. All treated microcosms with NPK alone, and urea mixed with NPK ratios after 4 months treatment gave a

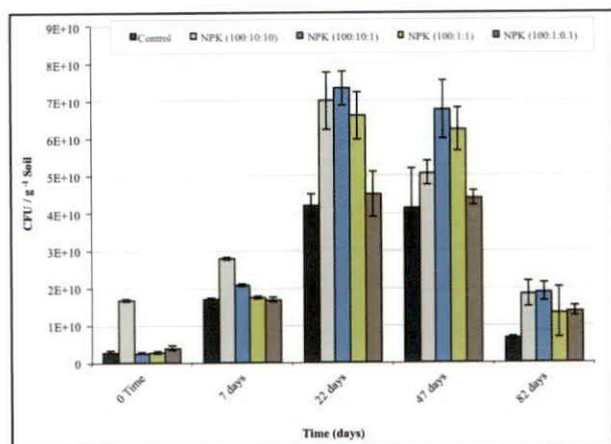


Fig. 1 Changes in heterotrophic bacteria counts (CFU g⁻¹ soil) in treated soil microcosms with different ratios of NPK treatment.

significant decrease in total petroleum hydrocarbon content, with the only exception of lowest ratios 100:1:0.1.

NPK fertilizer microcosms: Soil microcosms treated with NPK only in the ratio 100:10:10 resulted in the highest TPH removal which was 46% by day 65 and 66% after four months treatment. 100:10:1 ratio gave significantly higher ($p < 0.017$) transformation rate than the control and the other NPK ratio (100:10:10 and 100:1:0.1) after 130 days incubation.

C:N:P ratios 100:10:1 & 100:1:1 showed similar results of 40% and 34% removal by day 65 of incubation and the transformation level increased to reach 52.5% and 49.5% by four months treatment respectively. The lowest petroleum hydrocarbon transformation was obtained with C:N:P ratio (100:1:0.1) treatment and control untreated soils. The former exhibited 27.6% removal by 65 days, then the removal increased to 31.7% by the end of experiment, whereas 17% TPH removal was obtained with control untreated soils by middle of the treatment time and 29% removal by the end of the experiment.

Urea plus NPK fertilizer microcosms: Urea mixed with NPK treatments appeared to be more effective in TPH transformation than NPK treatment alone. However, the degree of TPH removal using urea mixed with C 100: N 10: P 1 ratio was significantly higher (69%) than other treatments urea mixed with C:N:P ratios (100:1:1) resulted in 67% TPH removal after 17 weeks treatment. Treatment with urea mixed with C:N:

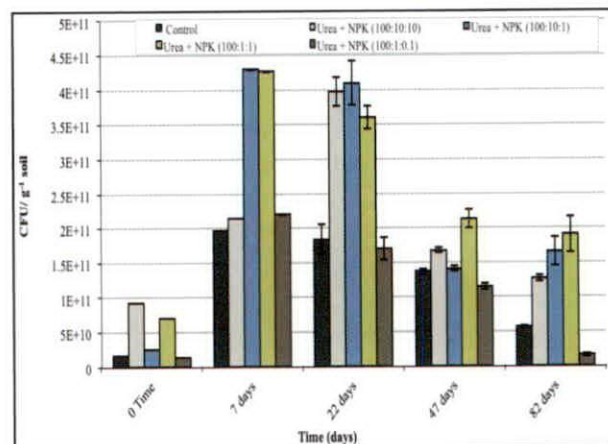


Fig. 2 Changes in heterotrophic bacteria counts (CFU g⁻¹ soil) in treated soil microcosms with different ratios of Urea/NPK treatments.

Pratio (100:10:10) and (100:1:0.1) reached 45.7%, and 49% by the end of incubation time respectively. The lowest TPH transformation was obtained again with control untreated soils which was 25.7%. The standard deviation for each analysis is presented in (Figs.3 and 4).

Gas Chromatograph analysis of the effective nutrient regime (Urea mixed with NPK)

A comparison study was made between the hydrocarbon composition of contaminant in the soil at the beginning of the study and after 130 days incubation in all soil microcosms. The gas chromatographic mass spectrophotometry analysis detected aliphatic compounds with carbon number between C14 and C27. Fig.5 shows the typical change (the urea plus NPK fertilizer treatments used as an example) in the distribution profile of n-alkanes during bioremediation in which a decrease in the middle chain carbon lengths (C14-C19) was observed. Fig. 5 was developed using GC/MS chromatograms showing individual peaks of each petroleum compound. The higher molecular weight carbon compounds (C20 and upwards) were generally not reduced in level during bioremediation.

The addition of nutrients and increasing the nitrogen sources in the form of urea enhanced the removal of the short - and middle chain aliphatic compounds. The highest petroleum reduction was with middle chain C14-C19 when soil was amended with urea mixed with NPK ratios (100:10:1 & 100:1:1).

The C17/Pr and C18/ Ph ratios were calculated using the chromatograms of extracted soil samples from the treated soil microcosms to determine if

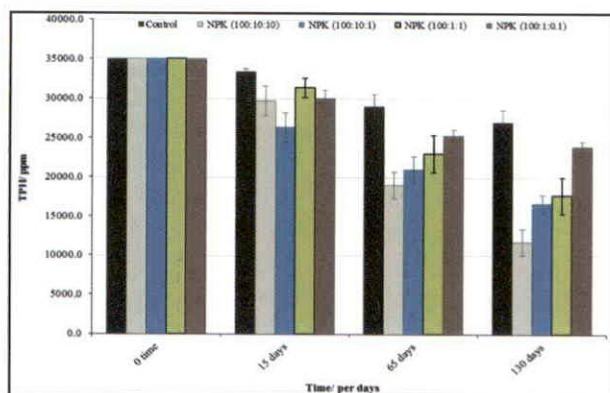


Fig. 3 Changes in TPH content in treated soil microcosms with different ratio of NPK treatments determined by TPH analyzer before and after treatment. Error bars represent standard deviation of the mean from triplicate soil microcosms.

significant bioremediation was occurring. At the end of the 130 days study, results showed that urea mixed with C:N:P ratios (100:10:1 & 100:1:1) had removed pristane and phytane of their original values. The changes of C17/pristane from 13.4 to 10.5, and C18/phytane from 7.8 to 4.8, and changes of C17/pristane from 13.4 to 8.1, and C18/phytane ratios from 7.8 to 5.0, with both nutrient ratios respectively. Overall the results demonstrate that TPH removal was more extensive with short and middle chain aliphatic compounds compared to the longer chain hydrocarbons (C20-C27 chain length).

The effect of the different bioremediation treatments on PH contamination was estimated by gas chromatography and a TPH analyser (infra red spectrophotometry). Both methods gave good agreement in PH levels. The total PH content at the start of the experiment and after 130 days treatment for both nutrient treated soils, is reported in Figs. 3 and 4 (TPH analyser results) and (Fig. 5, GC results).

Measurements of Residual Toxicity during Petroleum Hydrocarbon transformation

The changes in toxicity as a function of petroleum transformation activity were also determined over 130 days. The results of the toxicity tests all given as averages for three replicates, are summarized in (Figs. 6 & 7). The biotoxicity analyses of the soil microcosms treated with NPK ratios of 100:10:10 & 100:10:1 and urea mixed with NPK ratios 100:10:1 & 100:1:1 performed during the treatment period initially showed little change. However, toxicity decreased markedly after three months treatment compared to control (non-treated soils). The greatest

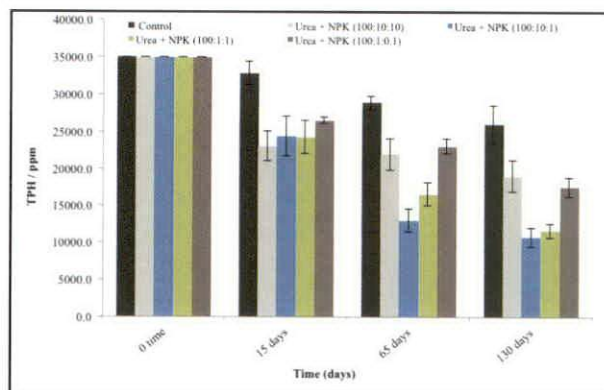


Fig. 4 Changes in TPH content in treated soil microcosms with different ratio of Urea/NPK treatments determined by TPH analyzer before and after treatment. Error bars represent standard deviation of the mean from triplicate soil microcosms.

reduction in toxicity was observed with soil treated with urea mixed with NPK ratio (100:10:1), where toxicity was reduced to 75%, and 56.5% with urea mixed with NPK ratio (100:1:1).

DISCUSSION

The effect of nutrient treatment on bacterial counts

In this study, the effect of nutrient level (C:N:P ratio) over time on TPH transformation and microbial counts were investigated. Margesin *et al* (2007) found that hydrocarbon concentration and incubation time are important factors during bioremediation of diesel-contaminated soil. The higher the initial contamination, the more marked was the effect of fertilizer supplements.

Initial results from this study also indicated that simple nutrient addition was the most effective and economical potential bioremediation method for the Libyan soils studied. Given that the soils used in this work are low in nutrients (and the indigenous microbial population present potentially susceptible to nutrient shock). It was decided to investigate if different nutrient levels and different nitrogen sources (commercial NPK fertilizer and urea) had varied effects on microbial populations and bioremediation. Previous authors reported a range of different nutrient ratios to be optimum for different soils adding further reasons to optimize nutrient ratios in the soils studied here. Bacterial counts at eight different nutrient concentrations (C:N:P, ranging from 100:10:10, 100:10:1, 100:1:1, 100:1:0.1) were monitored over 130 days incubation at 30°C.

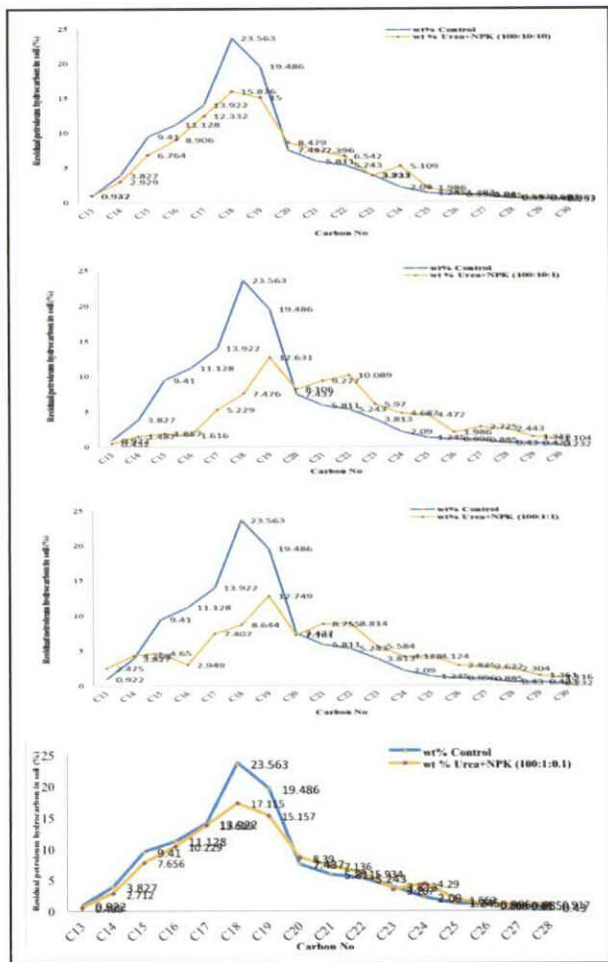


Fig. 5 Representative GC Chromatograms of TPH extracted from diesel-contaminated soil treated with urea mixed with NPK after 17 weeks incubation. The values in brackets represent the nutrient ratios.

Significant increases over time in microbial populations in oil contaminated soil were recorded and results found in this work were generally similar to previous studies i.e. increases in counts were observed during the initial to middle stages of incubation followed by a decreases in counts. For example Margesin *et al* (2000) reported increased the number of hydrocarbon degraders in both nutrient stimulated samples and soil without nutrient amendments. Some authors have reported a decrease in counts with nutrient addition. Urea in particular has been known to cause a decreases in microbial counts, and the released of ammonia killed the fungal population and the hydrocarbon degraders (Chaillan *et al*, 2006; Peltola *et al*, 2006; Jin and Fallgren, 2007), but in this work, urea actually stimulated bacterial populations to the greatest extent.

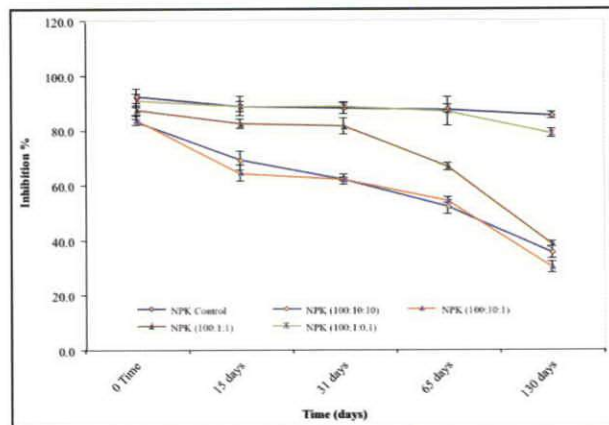


Fig. 6 Biotoxicity values during bioremediation treatment determined by *V. fischeri* bacteria. Error bars represent standard deviation of the mean from triplicate soil microcosms.

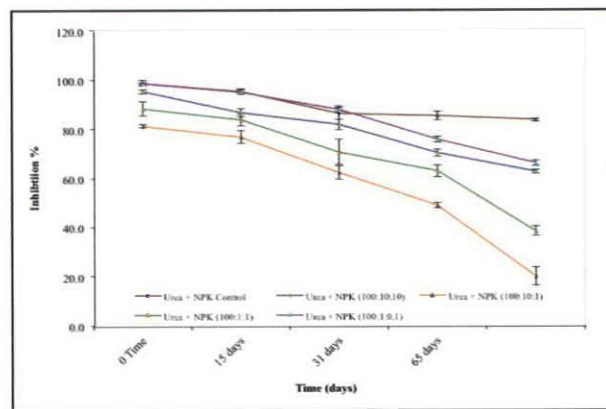


Fig. 7 Biotoxicity values during bioremediation treatment determined by *V. fischeri* bacteria. Error bars represent standard deviation of the mean from triplicate soil microcosms.

Overall, the higher additions of nutrients used stimulated bacterial counts to the highest extent suggesting that the indigenous bacterial population was not susceptible to nutrient shock (apart from the highest level of urea plus NPK fertilizer used where counts were not as high). A viable count does not indicate any effects on bacterial diversity and it is possible that hydrocarbon transforming bacterial populations may have been affected detrimentally. If this was the case then petroleum analysis of the soil with nutrient amendment should indicate that nutrient addition decreased petroleum transformation; results actually showed that nutrient addition served to stimulate petroleum removal. It must be noted that as NPK fertilizer was used in this work then K levels in soil would also increases in nutrient amended soils. It is possible that added K

acted (in synergy with N and P) to boost microbial populations but it is assumed that K would have less effect on microbial growth than N and P as it is required in much less quantity by microbes.

The overall effect of nutrient treatment on TPH transformation

In this study a range of petroleum transformation levels were obtained as a result of using different nutrient levels emphasizing the importance of optimizing nutrient levels added for bioremediation. Liebeg and Cutright (1999) suggested that the optimal recommended C:N:P ratio for bioremediation is 100:10:1, and other authors have suggested similar and/or different nutrient ratios; e.g. Embar *et al.*, (2006) obtained maximal reduction of TPH (91%) after 90 days in contaminated sandy soil supplemented with nitrogen and phosphorus at C:N:P ratio of 100:10:1, and the soil containing high concentration of crude oil 163,800ppm.

Atagana *et al.* (2003) used different C:N ratios 5: 1, 10 : 1, 15 : 1, 20 : 1 and 25 : 1 and only 33% hydrocarbon removal was achieved using the highest nutrient supplementation (C : N 5 : 1), thus they concluded that the highest ratio was the least effective in supporting growth of microorganisms. This may be due to the high concentration of nutrient used being toxic to the microbial population.

Several authors have reported the negative effect of high nitrogen, phosphorus and potassium concentrations on the biodegradation. Walworth *et al.* (2007) amended petroleum contaminated sandy soil with ammonium chloride (NH₄Cl) to levels 0, 125, 250, 375, 500, and 625 mg N / kg soil. They discovered that addition of greater levels of N (375, 500, or 675 mg N kg⁻¹ soil) significantly depressed oxygen consumption to levels equivalent to that of the untreated control (no nitrogen). Also changes of residual petroleum levels in the nutrient amended soils were not significantly different from the untreated control soil. Other studies have showed that relatively high total nutrient addition had no inhibitory effects if the nutrients were added gradually and not in a single dose. Ferguson *et al.* (2003) reported that the addition of nutrients in small dose kept nutrients concentration in the range required for microbial mineralisation of petroleum hydrocarbons. Nikolopoulou and Kalogerakis (2008) suggested using urea as a nitrogen source for bioremediation of petroleum compounds in open systems and our work would also support the use of urea as a nutrient source. It may have been possible

that the indigenous microflora utilized the carbon in urea in preference to the pollutant carbon but in this case these levels of urea used appeared to have been stimulatory to petroleum removal.

Interestingly, the best petroleum removal rates observed in this study appeared to correlate with the highest increases in bacterial viable counts, which indicating that the less sophisticated but rapid and cheap bacterial count method is a good indicator of overall functionality of the population. In this case functionality refers to the ability of the bacterial population to reduce petroleum levels in soil. Clearly, the level and type of nutrient addition required for bioremediation is an area worthy of detailed investigation and it would appear that different soils have different nutrient requirements i.e. nutrient levels should be optimized for different soils. In this work nutrient levels of 100:10:1 (C:N:P) appeared to be the most suitable and urea was an effective nutrient source but this may not be the case for all soils.

Jin and Fallgren (2007) indicated that urea wasn't a good source of nutrient for bioremediation of petroleum contaminants and found to inhibit the enzyme responsible for petroleum degradation in contaminated sandy soil collected from an Egyptian site, and thus it was suggested that the application of urea in stimulating the petroleum degradation may be site-specific.

Effect of nutrient addition on transformation of individual petroleum hydrocarbons

As well as examining the effect of nutrients on the reduction of total petroleum hydrocarbon levels it was also considered important to examine the removal of individual petroleum compounds, to see if microbial transformation was restricted to any particular type. Or if the different nutrient levels caused a change in the types of petroleum compounds removed. The results showed that the aliphatic compounds were optimally reduced as result of addition of urea mixed with C:N:P ratios 100:10:, and 100:1:1 after 130 days treatment. This might due to the balance between nitrogen supply and the carbon supply during the oil degradation.

Significant reduction in hydrocarbon content (C9-C27) was observed in the soil samples amended ratios (100:10:1 and 100:1:1). It has been demonstrated that the intermediate length n-alkane chains (C10-C20) are the substrates most degradable by soil microorganisms (Balba *et al.*, 1998). The long chains of n-alkanes (C20-C40) tend

to be recalcitrant due to their poor water solubility and lower bioavailability (Venosa and Zhu, 2003) and similar observations were made in this work.

The most readily degradable petroleum fractions are n-alkanes of intermediate length (C10-C20), whereas, shorter chain compounds are rather more toxic. Longer chain alkanes known as waxes (C20-C40) are hydrophobic and difficult to degrade. Results showed that urea mixed with NPK ratios (100:10:1 & 100:1:1) had further biodegraded C17/pristane from 13.4 to 8.3, and C18/phytane from 7.8 to 4.8, and C17/pristane from 13.4 to 8.1, and C18/phytane ratios from 7.8 to 5.0, of their original values respectively. Whereas, amended sludge contaminated soil with urea mixed with C:N:P ratios (100:10:10) only removed from C17/pristane from 13.4 to 10.5 and C18/phytane from 7.8 to 6.5. A similar change in pristane/phytane ratios has been observed previously in sludge contaminated soil treated with nutrients, and evidence for biodegradation and changes in C17/Pr and C18/Ph ratios were determined using the GC-FID analysis. This confirms that nutrients are key parameters for promoting biodegradation (Hejazi and Husain, 2004).

Pristane has been reported to be a recalcitrant compound for attack by biodegrading microorganisms so any reduction in this compound (as observed in this work with urea plus NPK fertilizer) is an interesting result. It could be possible that more time is required for the microbial populations to degrade this branched-alkane to below detection levels.

The best petroleum (pristane and phytane) transformation rates in this work were obtained with urea and NPK fertilizer addition in a C:N:P ratio of 100:10:1. High levels of removal (approx 66%) were also seen with NPK fertilizer alone in a C:N:P ratio of 100:10:1. Addition of extra nutrients (C:N:P ratio of 100:10:10) reduced petroleum transformation slightly in comparison to 100:10:1 C:N:P ratios indicating a potential toxic effect of higher nutrient levels.

Ecotoxicity assessment

It has been demonstrated that ecotoxicity bioassays can be effectively used as supplementary tools for monitoring the effectiveness of remediating petroleum contaminated soils (Girotti *et al*, 2008). In this work a bacterial based luminescence bioassay was used to monitor the toxicity of soil samples taken during bioremediation. In all

samples, toxicity levels were high at the beginning of bioremediation (100% inhibition was observed) indicating the high toxicity associated with the contaminated soil. The toxicity of the control soil samples remained high throughout the experiment and this was correlated with a small reduction in the petroleum hydrocarbons present. In contrast, nutrient amended microcosms showed a steady decrease in toxicity and the soils showing the highest reduction in hydrocarbons also gave the highest reduction in toxicity. The reduction in the smaller carbon compounds (C9-C20) clearly removed most of the associated soil toxicity and it appears the larger petroleum compounds not removed during bioremediation were less inhibitory. This may be due to the fact that the larger compounds are less soluble and therefore, are not removed during the ethanol extraction. Other workers have also shown that bioremediation using nutrient addition leads to a reduction in toxicity (Philp and Atlas, 2005). Generally, an increase in toxicity during the early stages of bioremediation is observed as pollutants are incompletely transformed into more toxic intermediates, but as bioremediation progresses the toxic intermediates are further transformed and toxicity reduces as a result. Girotti *et al* (2008) noticed that the toxicity of contaminant increased after short time of the treatment as result of existence of long chain hydrocarbons during the bioremediation of hydrocarbon contaminated soil, which decreased after long period of bioremediation. In this work as 100% toxicity of soil samples was observed initially it was impossible to see this initial toxicity increase. The percentage of light inhibition obtained by this assay was in good correlation with the reduction in total petroleum hydrocarbon determined, probably because both nutrient levels used representing the right level of amendment needed. However, it is important to realize the limitations of the toxicity methods used in this work ;the method only gives an indication of the short term toxicity of samples. For example, over a longer incubation period toxic residues may be released into soil due to changes in soil structure caused by rewetting/drying or freeze/thaw cycles or microbial mineralization of that releases pollutants bound to organic materials in soil (e.g. humic matter). Also, it is important to test toxicity to other trophic levels such as plants and other eukaryotes (Salanitro *et al*, 1997). Millioli *et al*, (2009) used lettuce seeds of the *Lactucasativa species* to assess the soil toxicity of the addition

of rhamnolipid in a crude oil contaminated soil. However, the microbial toxicity test used here is quick and economical and does appear to reflect the level of hydrocarbons present as estimated by chemical analysis.

SUMMARY AND CONCLUSIONS

This study assessed the effect of varying nutrient (NPK) levels and types (urea) on bioremediation of diesel contaminated soil by a combination of chemical and toxicological analyses. In general, the optimum C:N:P ratio found was 100:10:1 (and urea was found to be a good nutrient source). Urea is a source of N and easily utilised carbon and appeared to stimulate bioremediation effectively. In this study (achieved approximately 69% TPH removal) despite previous studies finding it to cause inhibition of the microbial population present. The amounts of petroleum removed as revealed by chemical analysis appeared to correspond well to bacterial counts and the residual toxicity of soil as estimated by the Microtox assay. The highest amounts of nutrients used (C:N:P ratio of 100:10:10) did slightly reduce bioremediation effectiveness. GC analysis revealed that hydrocarbons of chain length C9-C20 were most effectively removed and that the higher chain length petroleum compounds (>C20) remained in the soil. Overall, the work demonstrated the clear potential of nutrient stimulation to reduce levels of hydrocarbons present and to reduce the soil toxicity. These promising results were used as the basis for subsequent scale-up studies: a pilot scale bioremediation experiment to treat a larger amount of contaminated soil.

REFERENCES

- Atagana, H. I.; Haynes, R. J. and Wallis, F. M. (2003). Optimization of Soil Physical and Chemical Conditions for the Bioremediation of Creosote-Contaminated Soil. *Biodegradation*, **14**: 297-307.
- Anon. (1986). The analysis of agricultural material-ministry of agriculture fisheries and food. Reference Book **427**. Stationary office. London.
- Balba, M. T.; Al-Awadhi, N. and Al-Daher, R. (1998). Bioremediation of Oil Contaminated Soil: *microbiological methods for feasibility assessment and field evaluation microbiological methods*, **32**: 155-164.
- Chaillan, F.; Charneau, C. H.; Point, V.; Saliot, A. and Oudot, J. (2006). Factors Inhibiting Bioremediation of Soil Contaminated with Weathered Oils and Drill Cuttings. *Environmental Pollution*, **144**: 255-265.
- Dorn, P. B. and Salanitro, J. P. (2000). Temporal Ecological Assessment of Oil Contaminated Soils before and after Bioremediation. *Chemosphere*, **40**: 419-426.
- Eke, P. E. and Scholz, M. (2008). Benzene Removal with Vertical-Flow Constructed Treatment Wetlands. *J. Chem. Tech. & Biotech.*, **83**: 55-63.
- Embar, K.; Forgace, C. and Sivan, A. (2006). The Role of Indigenous Bacterial and Fungal Soil Populations in the Biodegradation of Crude Oil in a Desert Soil. *Biodegradation*, **17**: 369-377.
- Ferguson, S. H.; Franzmann, P. D.; Revill, A. T.; Snape, I. and Rayner, J. L. (2003). The Effects of Nitrogen and Water on Mineralisation of Hydrocarbons in Diesel-Contaminated Terrestrial Antarctic Soils. *Cold Regions Science and Technology*, **37**: 197-212.
- Girotti, S.; Maiolini, E.; Boleele, L.; Ferri, E.; Pompei, A.; Matteuzzi, D.; Medvedeva, S. and Fonti P. (2008). Bioremediation of Contaminated Soils by Hydrocarbons Degrading Bacteria and Decontamination Control. In: *Soil Chemical Pollution, Risk Assessment, Remediation and Security* (ed. by: Simeonov, L., Sargsyan, V.): 369-383.
- Hejazi, R. and Husain, T. (2004). Landfarm Performance Under Arid Conditions 2. Evaluation of Parameters. *Environmental Science Technology*, **38**: 2457-2469.
- Jin, S. and Fallgren, P. H. (2007). Site-Specific Limitation of Using Urea as a Nitrogen Source in Biodegradation of Petroleum Wastes in Soil. *Soil and Sediment Contamination*, **16**: 497-505.
- Keeney, D. R., and Bremner, J. M. (1966). Determination and isotope-ratio analysis of different forms of nitrogen in soils. 4. Exchangeable ammonium, nitrate, and nitrite by direct distillation methods. *Soil Science Society of America Proceedings*, **30**: 583-587.
- ISO 10390. (1994). Soil Quality-Determination of pH. International Organization for Standardization. Geneva, Switzerland. 5 p. (available at www.iso.ch)
- LaFarré, M.; García, M. J.; Tirapu, L. and Ginebreda, A. (2001). Wastewater Toxicity Screening of Non-Ionic Surfactants by Toxalert® and Microtox® Bioluminescence Inhibition Assays. *Analytica Chimica Acta*, **427**: 181-189.

- Liebeg, E. W. and Cutright, T. J. (1999). The Investigation of Enhanced Bioremediation Through the Addition of Macro and Micro Nutrients in a PAH Contaminated Soil. *International Biodeterioration and Biodegradation*, **44**: 55-64.
- Mariano, A. P.; Kataoka, A. P.; Angelis, D. F. and Bonotto, D. M. (2007). Laboratory Study on the Bioremediation of Diesel Oil Contaminated Soil from A Petrol Station. *Brazilian Journal of Microbiology*, **38**: 346-353.
- Margesin, R.; Zimmerbauer, A. and Schinner, F. (2000). Monitoring of Bioremediation by Soil Biological Activities. *Chemosphere*, **40**: 339-346.
- Margesin, R.; Ha'hammerle, M. and Tschерko, D. (2007). Microbial Activity and Community Composition During Bioremediation of Diesel-Oil-Contaminated Soil: Effects of Hydrocarbon Concentration, Fertilizers, and Incubation Time. *Microbial Ecology*. **53**: 259-269.
- Millioli, V. S.; Servulo, E. L. C.; Sobral, L. G. S. and Carvalho, D. D. (2009). Bioremediation of Crude Oil-Bearing Soil: Evaluation the Effect of Rhamnolipid Addition to Soil Toxicity and to Crude Oil Biodegradation Efficiency. *Global Network for Environmental Science and Technology J.*, **11**: 181-188.
- Nikolopoulou, M. and Kalogerakis, N. (2008). Enhanced Bioremediation of Crude Oil Utilizing Lipophilic Fertilizers Combined with Biosurfactants and Molasses. *Marine Pollution Bulletin*, **56**: 1855-1861.
- Olsen, S. R. V., Cole, V. C., Watanabe, F. S., Dean, L. A. (1954). Estimation of Available Phosphorus in Soils by Extraction with Sodium Bicarbonate. *Department of Agriculture Circular*, U.S.
- Paton, G. I., Viventsova, E., Kumpene, J., Wilson, M. J., Weitz, H. J, Dawson, J. J. (2006). An ecotoxicity assessment of contaminated forest soils from the Kola Peninsula. *Sci. Total Environ.*; **355**:106-117.
- Plaza, G. A.; Lukasik, K.; Wypych, J.; Nalecz-Jawecki, G.; Berry, C. and Brigmon, R. L. (2008). Biodegradation of Crude Oil and Distillation Products by Biosurfactant-Producing Bacteria. *Polish Journal of Environmental Studies*, **17**: 87-94.
- Peltola, R.; Salkinoja-Salonen, M.; Pulkkinen, J.; Koivunen, M.; Turpeinen, A.-R.; Aarnio, T. and Romantschuk, M. (2006). Nitrification in Polluted Soil Fertilized with Fast- and Slow-Releasing Nitrogen: A Case Study at a Refinery Landfarming Site. *Environmental Pollution*, **143**: 247-253.
- Philp, J. C. and Atlas, R. M. (2005). Bioremediation of Contaminated Soils and Aquifers. In: Atlas R.M., Philp, J., (eds.), *Applied Microbial Solution for Real-World Environmental Cleanup*. ASM press, *American society for microbiology*, Washington DC, USA
- Rahman, K. S.; Banat, I. M.; Thahira, J.; Thayumanavan, T. and Lakshmanaperumalsamy, P. (2002). Bioremediation of Gasoline Contaminated Soil by a Bacterial Consortium Amended with Poultry Litter, Coir Pith and Rhamnolipid Biosurfactant. *Bioresour Technol*, **81**: 25-32.
- Salanitro, J. P.; Dorn, P. B.; Huesemann, M.; Oore, K. O. M.; Rhodes, I. A.; Ricejackson, L. M.; Vipond, T. E.; Western, M. M. and Wisniewski, H. L. (1997). Crude Oil Hydrocarbon Bioremediation and Soil Ecotoxicity Assessment. *Environmental Science and Technology*, **31**: 1769-1776.
- Sarkar, D.; Ferguson, M.; Datta, R. and Birnbaum, S. (2005). Bioremediation of Petroleum Hydrocarbons in Contaminated Soils: Comparison of Biosolids Addition, Carbon Supplementation, and Monitored Natural Attenuation. *Environmental Pollution*, **136**: 187-195.
- Venosa, A. D. and Zhu, X. (2003). Biodegradation of Crude Oil Contaminating Marine Shorelines and Freshwater Wetlands: *review paper*. *Spill Science and Technology Bulletin*, **8**: 163-178.
- Walworth, J.; Pond, A.; Snape, I.; Rayner, J.; Ferguson, S. and Harvey, P. (2007). Nitrogen Requirements for Maximizing Petroleum Bioremediation in a Sub-Antarctic Soil. *Cold Regions Science and Technology*, **48**: 84-91.

AN ELECTROCHEMICAL BEHAVIOR OF CO₂ CORROSION OF STATIC CARBON STEEL ELECTRODE IN PRESENCE OF ACETIC ACID, ACETATE AND METAL INHIBITOR (Zn²⁺, Ca²⁺) USING AC AND DC ELECTROCHEMICAL TECHNIQUES

H. A. Mahfud*

Abstract: AC and DC electrochemical techniques: electrochemical impedance spectroscopy (EIS), and (Potentio-dynamic), electrochemical corrosion measurements are conducted on static carbon steel electrode at room temperature in 3.5 % NaCl Solution, bubbled with 1 atm CO₂, or 1 atm. N₂ or air exposed test solution. Different chemicals; e.g. (acetate, sodium acetate, acetic acid, sodium sulphate, calcium chloride and zinc chloride) were added to test solution. The results of polarisation curves are compared with impedance measurements results to understand the mechanism of the corrosion process. And take the benefits of the comparison to understand more the physical meaning of AC corrosion data. The results of polarisation curves suggest that CO₂ makes a large contribution in the corrosivity of all solutions. However, in the presence of acetic acid the solutions were found to be corrosive even in the absence of CO₂, and this can strongly attributed to the pH. The impedance results confirm the mentioned findings; also there was a good agreement between AC (Impedance) and DC (Polarisation curves) results. Zinc and Calcium considered as metal ions inhibitors, DC and AC results suggest that, Ca²⁺ in aerated solution may tends to forming (CaOH₂) that gives more isolation for cathodic species (i.e. hinders the diffusion links leads to fresh metal surface). Regarding zinc ions the polarisation curves indicate that electrochemical behaviour of zinc in terms passivity, depends strongly on the electrode potential.

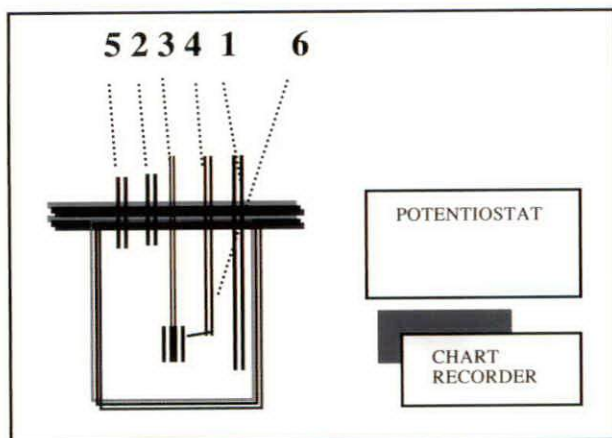
Keywords: Electrochemistry, CO₂ corrosion mechanism, and steel surface inhibition

INTRODUCTION

In CO₂ corrosion there are many studies on the effect of fluid characteristic (e.g pH, CO₂ pressure and temperature, (Nesic *et al*, 1996). This is based on the fact that CO₂ corrosion is by far the most common form of attack encountered in upstream operations (Kermani and Morshed, 2003). Basically, an empirical parameter models have been developed; these models have been used as major tool for prediction and selection of material performance in sweet environments. Unfortunately, these models are not accurate for many working conditions, as there are some factors that are not taken into account. Furthermore, relatively new factors, such as acetate, which are observed to affect on CO₂ corrosion rate, are not

fully understood (Crolet & Nicolas 1999, and Guo *et al*, 2005). Electrochemical techniques; polarisation curves and electrochemical impedance spectroscopy (EIS) shall be used to study CO₂ corrosion of steel. Some workers found that corrosion in the CO₂ environment was higher than in the aerated solutions (Aagotnes *et al*, 1999). Polarisation curves are used to study the electrochemical behaviour of carbon steel in CO₂ saturated solutions and compared with deaerated and aerated solutions. The investigation will drive us to understand the electrochemical behaviour of carbon steel in the presence metal ions (e.g. Ca²⁺, Zn²⁺) as well as acetic acid and acetate species. Previous work has been carried out about the effect of acetate in CO₂ saturated solution but most of them done only in static conditions. In the current research (Part. I, Part II will follow in the next issue of this Journal), all corrosion tests are conducted using static electrode and

* Libyan Petroleum Institute LPI, KM 7 Gergarsh Road, PO Box 6431 Tripoli – Libya
Email: h.mahfud@lpilibya.com or hishammahfud@gmail.com



Sketch. 1 shows schematic drawing of corrosion cell utilized in corrosion measurements [Sketch. 1 shows schematic drawing of corrosion cell that was used to conduct lab corrosion measurements: (1) gas inlet; (2) gas outlet; (3) carbon steel working electrode; (4) Saturated calomel electrode with capillary salt bridge (SCE); (5) platinum auxiliary electrode; (6) salt bridge].



Picture 1 shows the iron oxide film formed as result of anodic polarization



Picture. 2 Nice view of zinc hydroxide on steel Surface.

future work (Part II) expected to be published in next Petroleum Research Journal versions. This future work (Part II) is aimed to focus on carbon steel electrochemical respond by AC and DC techniques in a dynamic CO_2 saturated medium and the emphasis will be on the flow effect in presence of Acetates and calcium chloride, using rotating electrode.

EXPERIMENTAL WORK

Equipment

All experimental work was done at atmospheric pressure and room temperature in enclosed cells similar to that shown in Sketch 1. In this experiment carbon dioxide [CO_2] and nitrogen [N_2] gases were bubbled inside the cell continuously before the experiment (to remove dissolved oxygen gas from the solution) and during the experiment (to exclude oxygen). The electrochemistry of the carbon steel for corrosion evaluation was studied using AC and DC electrochemical techniques. Three conditions were used for the static (unstirred) solution. They are; aerated, de-aerated using N_2 bubbling and CO_2 saturated solution. Solutions were bubbled for 10 minutes before starting the test. The three electrodes were placed in the cell, where a platinum electrode (used to collect the current) was used as a counter electrode (CE). A saturated calomel reference electrode (RE) was connected to the cell externally using a Luggin Capillary Salt Bridge. A digital pH-meter was used to measure the pH of the solution before and after the experiment finished.

The electrochemical polarization curves were developed using ACM potentiostat with sweep rate generator connected to an X-Y recorder, and the correction for IR-drop was made manually after the experiment. Impedance measurements were developed using a Solartron Frequency Response Analyser (FRA) and potentiostat connected with personal computer.

Material

A low carbon steel rod, of 1 cm diameter was used. Specimen of chemical composition is given in Table 1. The steel specimen was connected to a copper current lead wire using a spot welding machine and then some wax was used to isolate the upper and lower end of the cylindrical specimen, leaving an exposed area of 6.28 cm^2 (see Picture 1).

Table 1 A low carbon steel rod, of 1 cm diameter was used. Specimen chemical composition

Chemical Element	C	Si	Mn	P	S	Cr	Mo	Ni	Al
%Mass/Mass	0.18	0.16	0.8	0.005	0.034	<0.02	0.03	0.1	<0.005
Chemical Element	Co	Cu	Sn	Ti	V	W	-	-	-
%Mass/ Mass	0.007	0.18	0.02	<0.005	<0.02	<0.02	-	-	-

Solutions

All the solutions used in this experiment were in three conditions: aerated, de-aerated by N₂ gas and saturated by CO₂ gas at room temperature and atmospheric pressure.

The solutions used in the static electrode tests were:

- 1- 3.5% NaCl in distilled water (15Ω cm²)
- 2- 3.5% NaCl + the following chemical additive is added individually,
 - 0.1M acetic acid
 - 0.1M sodium acetate
 - 0.1M CaCl₂
 - 0.1M ZnCl₂

Work Procedure

All the electrochemical measurements were applied with 1 litre of fresh solution for each experiment and all of them at room temperature. Solutions that were de-aerated were initially rapidly bubbled with nitrogen for 10-15 minutes then the gas flow reduced. For solution saturated in carbon dioxide, nitrogen bubbling was carried out first, then CO₂ bubbling was performed for 10 minutes. The pH of the solution was measured after the experiment to know the situation of solution species equilibrium. The steel-working electrode was prepared by grinding with 400 grit using SiC grinding papers and rinsed using distilled water and ethanol to remove any greases or wax. The clean specimen was fixed immediately in the glass cell electrolyte. The open circuit potential (E_{corr}) was observed using a digital voltmeter. The experiments were starting after E_{corr} had stabilised.

Potentiodynamic Measurements

Potentiodynamic polarization was applied to produce polarization curves of mild steel area of 6.28cm². The experimental work was carried out at room temperature in three different solution conditions (i.e aerated, N₂ and CO₂ bubbled) at one atmosphere pressure. The electrochemical experiment was carried out in a suitable cell with gas inlet and outlet gas connections. It is connected with a saturated calomel electrode

(SCE) as reference electrode by a using salt bridge to minimize IR-drop. The working electrode was cylindrical in shape. An ACM potentiostat with sweep rate generator controlled the scan rate potential at 30mV/min. The current was measured using the voltage drop across a resistor and recorded on an X-Y recorder; the potential was monitored via a sensitive voltmeter. The electrochemical test was undertaken by applying a full polarization on fresh/clean specimen in new solution. The potential was swept from -1200mV (SCE) up to 0 mV (SCE). Any IR-drop correction that was required was estimated from Ohmic behavior at high current and corrected manually.

Impedance measurements

AC Impedance measurement were carried out by applying a corresponding potential to of ± 10mV (SCE) around the open circuit potential to the working electrode. This is equivalent to a AC voltage of 7mV rms. The frequency range used in the measurements was (30000 Hz-0.03Hz). All impedance measurements were performed at open circuit potential using a Saturated Calomel Electrode (SCE) as reference electrode. The aeration conditions and test condition and sample geometry which were used in the impedance measurements are the same as those were used in the potentiodynamic technique. (Princeton Applied Research AC-1 note).

RESULTS AND DISCUSSION

Potentiodynamic polarization experiments were performed in order to understand the electrochemical behavior of steel in aerated, and nitrogen and carbon dioxide bubbled solution. Therefore, the curves obtained shall be compared in order to determine the electrochemical behavior of the salt solutions, containing acetic acid and acetate, in the presence and absence of CO₂, also to know how the degree of aggressiveness of acetic acid. More explanations and details discussion relates to the effect of metal ion inhibitors in the presence and absence of CO₂ are mentioned below. More explanations and details are discussed below.

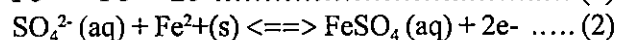
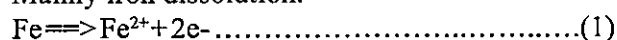
Electrochemical test procedure

Full polarization was applied on freshly prepared and abraded specimens and for each new solution the potential was swept from -1200mV (SCE) up to near zero mV (SCE). Where it is necessary, IR-drop correction was estimated from the high-current portion of the polarization curve.

Basic Reactions in this Experiment

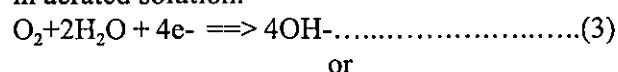
Anodic Reaction

Mainly iron dissolution:

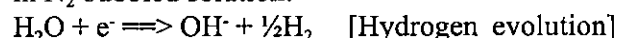


Cathodic Reaction

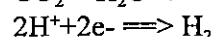
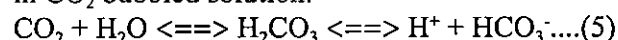
in aerated solution:



in N₂ bubbled solution:



in CO₂ bubbled solution:



Effect of acetate (in acetic acid or as the acetate anion)

3.5% NaCl Solution and without acetate

In aerated solution the polarization curves revealed that hydrogen evolution and oxygen reduction were the cathodic reactions and iron dissolution was the anodic reaction. According to the polarization curves, the increases in dissolution rate is not strongly changed with increasing the potential this may be due to the known property of steel in aerated near natural solutions, which usually featured by greater stability of formed oxide layers over acid solutions (Newman, RA. 2002). but in N₂ bubbled solution the anodic kinetics depends on the potential changing since E_{corr} decreased to more a negative value (-880mV).

In CO₂ bubbled solution, the corrosion increased because the presence of carbonic acid lower the pH and makes the solution more corrosive. This is because it represents an additional source of H⁺ and, hence, cathodic reactant. At room Temperature it is reported that the CO₂ corrosion rate is controlled by charge transfer processes (Tourgoose 2004). During corrosion, iron oxide forms on the metal surface (see picture 1). As well as due to the presence of carbonate (from

the dissolved carbonic acid) in the solution, it is thermodynamically possible for a black/thin iron carbonate layer to form. A cathodic limiting current in CO₂ bubbled solution was found to start at a potential different from the aerated solution. The maximum limiting current was about 0.09mA/cm in CO₂ bubbled solution (Figs.1, 2 and 3).

3.5% NaCl + 0.1M Sodium Acetate solution

The results suggest that higher corrosion rate in CO₂ containing solution is controlled by carbonic acid diffusion but in N₂ bubbled and in aerated solution the corrosion rate is mass transport controlled as well. The polarization curves show that the corrosion rate is about 10 times lower in these solutions than that observed in CO₂ containing solution. This can be explained from fact that CO₂ makes the solution more aggressive and lowers the pH (Figs. 1 and 4). In addition, as for the polarization curves, iron oxide formation is more favoured by the higher pH value ≈ 10.5 (Fig. 5) and pH ≈ 11.5 (Fig. 6) and may be some passivation is occurring.

3.5% NaCl +0.1 Acetic Acid solution

In this solution all three polarization curves show the corrosion rate quite close to each other. In other words, because acetic acid is considered aggressive and keeps the pH values in range of (3-4) for all solutions, thus the resulting corrosion rate is approximately five times greater than for the other two solutions. In N₂ bubbled solution the corrosion process appeared mainly under activation control. This indicates that acetic acid is aggressive since formation of an oxide/corrosion product film is clearly hindered. Eventually, an un-filmed steel surface is exposed

Table. 2 show corrosion test condition

Material	Carbon steel & mild steel
Test solution	Mainly 3.5% NaCl + others additives
Temperature	RT
Pressure	1bar
pH	Dependence on the solution
Test duration	Dependence on the technique
Sweep rate	0.5mV/s
AC impedance	±10 mV .VS. E _{corr} 30000Hz up to 0.3Hz
Potentiodynamic sweep range	-1200 to 0 mV (SCE). VS.E _{corr}

to the solution most of the time and this activates the electrochemical process and stimulates the iron dissolution reaction.

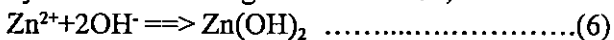
Effect of metal ion inhibitors

3.5%NaCl + 0.1M CaCl₂ solution

The presence of calcium chloride in the three solution conditions causes a reduction in the corrosion rate (Figs. 7, 8 and 9). The lowest corrosion rate was in aerated solution and this can be attributed to the formation of a calcareous protective layer (CaOH₂) that gives more isolation for cathodic species to reach the fresh iron surface (i.e. hinders the diffusion processes). Since the presence of the oxygen encourages the formation of Fe₂O₃, by shifting the E_{corr} to more positive value, (E-pH diagram for iron water system; Module Notes - Aqueous Corrosion UMIST, 2003), the pH of solution (near neutral) will favour formation of Ca(OH)₂ and Fe₂O₃. However, in the absence of oxygen, i.e. with Picture 1 shows the iron oxide film N₂ bubbling, the current density (I_{corr}) increases about five times, formed as result of anodic polarization. Obviously, in CO₂ containing solution, the pH is further lowered to 5 or below and the current density might be higher. Also, the measured corrosion rate is still low since in this case formation of protective calcium carbonate occurs because of the dissolved CO₂.

3.5%NaCl+ 0.1ZnCl₂ solution

Zinc ions are considered as good cathodic inhibitors in solution and should work well to protect steel in near neutral solutions in a similar way (but more effective than) calcium ions. In this experiment zinc chloride was considered as a source of zinc metal ions that will suppress the cathodic reaction by precipitation of zinc hydroxide according to this reaction;



Eventually the iron surface will be covered with a layer of zinc hydroxide. The polarization curves in Fig.10, 11 and 12 show an active state at lower potential values -1000 to -900mV (SCE). In CO₂ containing solution, the passivity range is small but in aerated solution the passivity range was greater (-1000 to -580mV (SCE) but the CO₂ passivation current < N₂ passivation current < O₂ passivation current; i.e. the presence of oxygen has no synergetic effect with zinc in CO₂. On the other hand, in aerated solution (pH=6.2), it is

expected to find a beneficial affect of oxygen, since oxygen causes an extension of the passivity range (Newman, 2002a & b). This can be understood from the E-pH diagram of the iron/water system. In the presented polarization curves the observed active state may result from instability of the zinc hydroxide protective layers in this solution.

The electrochemical behaviour of mild steel in 3.5% NaCl + 0.1MNaSO₄ solution

In aerated solution, in presence of NaSO₄, oxygen reduction and hydrogen evolution happen at lower potential than in 3.5% NaCl solution alone. Some authors suggest that the most probable anodic reaction in such sulphate concentration in natural solution is iron sulphate formation. There is region of passivity and formation of iron sulphate layers that provide protection against further corrosion. At a potential of approximately 660mV SCE, the formed protective film is destroyed and the anodic dissolution re-activates again to higher values than before. In aerated solution the potential where the limiting current observed is lower than -880mV SCE (Fig .4).

In N₂ bubbled solution the E-logI curve shows a clear cathodic Tafel region and this implies that the corrosion process strongly dependent on the H₂ evolution as cathodic reaction. In CO₂ bubbled solution there is similarity with the NaCl solution in the shape of polarization curve and E_{corr} values, but in NaCl solution the limiting current shall be less than that observed in Na₂SO₄ contained solution (Figs. 2 and 5). (Arzola, 2003).

Impedance (EIS) results

The impedance measurements have been performed in order to measure the electrolyte resistance , and the polarization resistance and if there is any change in corrosion mechanisms (Table 2). The results from all impedance plots have agreement that the worst corrosion resistance (i.e. faster corrosion) is in the presence of CO₂ (Kinsella *et al*1998).

Effect of acetate

3.5% NaCl + 0.1M sodium acetate solution

Fig. 19 shows the impedance response in the presence of sodium acetate. This result suggests that there is a higher corrosion resistance in N₂ bubbled solution. Also, from the plot (Fig. 19), lower R_s values were observed. In the presence of CO₂, a

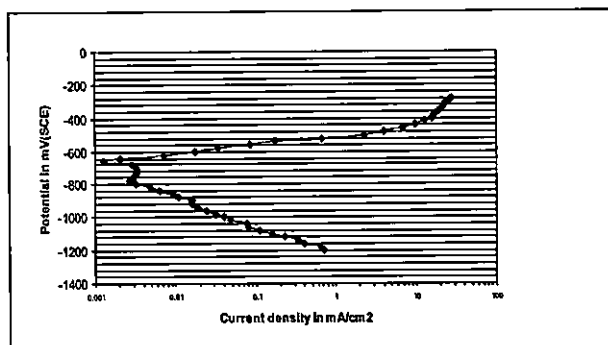


Fig. 1: Polarization curve of mild steel in 3.5% NaCl aerated solution.

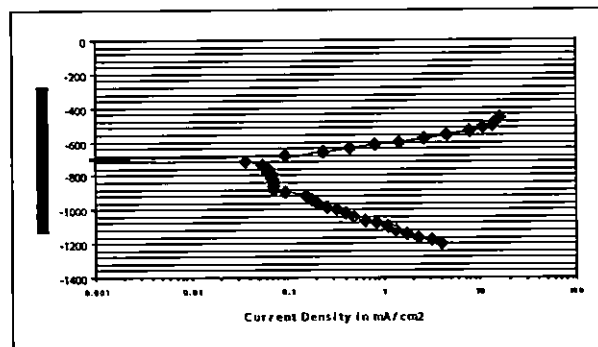


Fig. 2: Polarization curve of mild steel in 3.5% NaCl CO₂ bubbled solution.

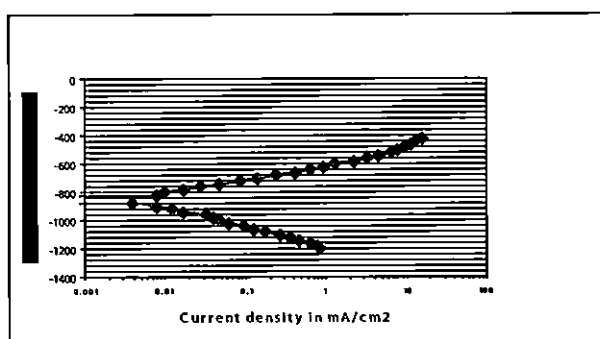


Fig. 3: Polarization curve of mild steel in 3.5% NaCl N₂ bubbled solution.

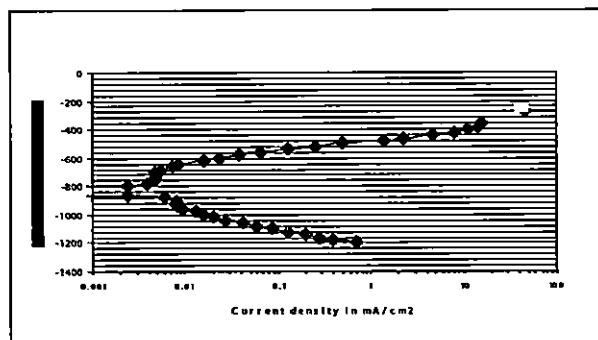


Fig. 4: Polarisation curve of mild steel in 3.5% Na₂SO₄ aerated solution.

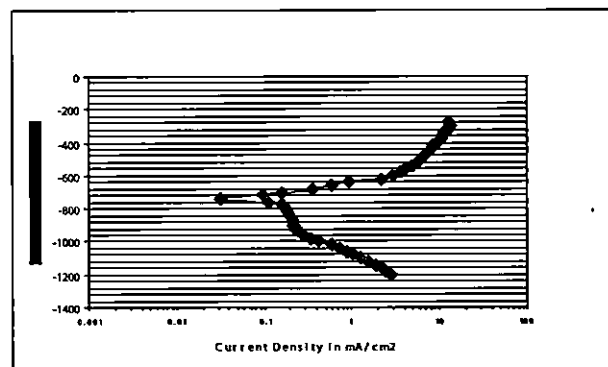


Fig. 5: Polarisation curve of mild steel in 0.6M Na₂SO₄ CO₂ bubbled solution.

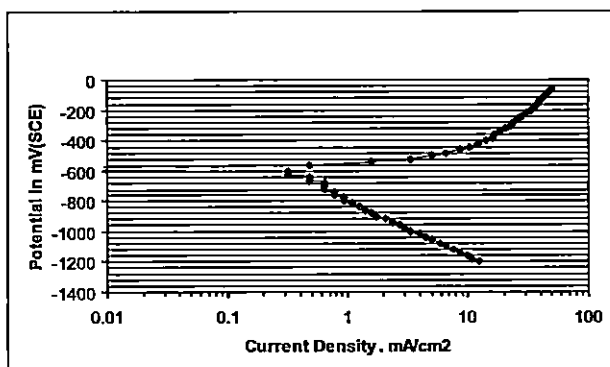


Fig. 6: Polarisation curve of mild steel in 0.6M Na₂SO₄ N₂ bubbled solution.

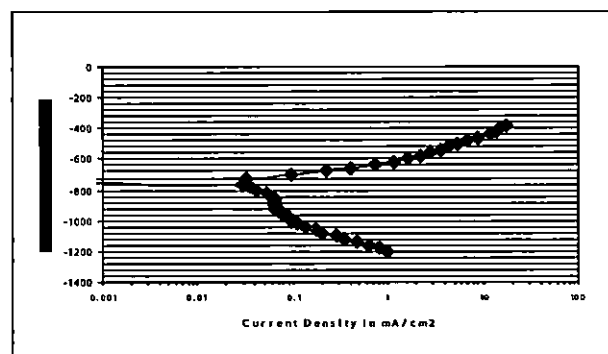


Fig. 7: Polarisation curve of mild steel in 3.5% NaCl + 0.1M acetic acid aerated solution, pH=3.5.

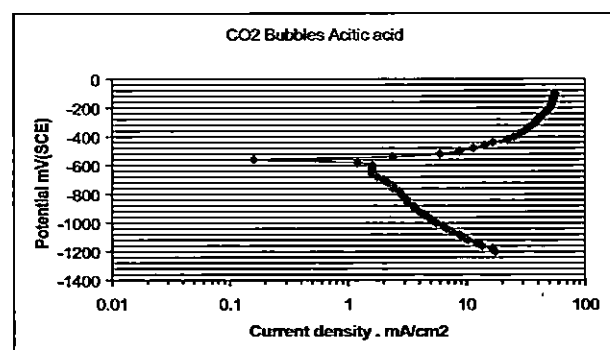


Fig. 8: Polarisation curve of mild steel in 3.5% NaCl + 0.1M acetic acid, pH=3.75.

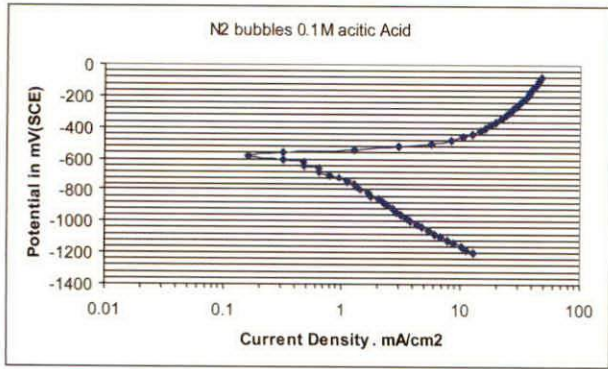


Fig.9: Polarisation curve of mild steel in 3.5% NaCl+ 0.1M acetic acid, pH=3.4.

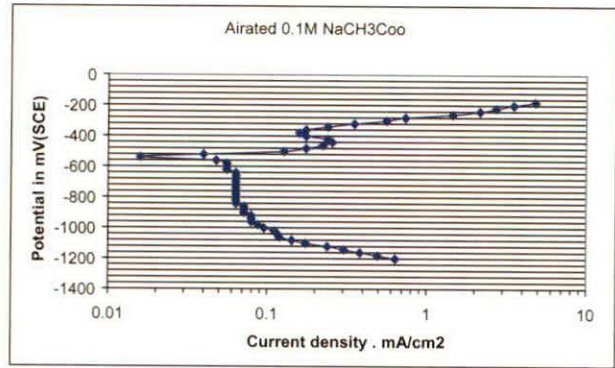


Fig.10: Polarization curve of mild steel in 3.5% NaCl + 0.1M sodium acetate, pH= 11.5.

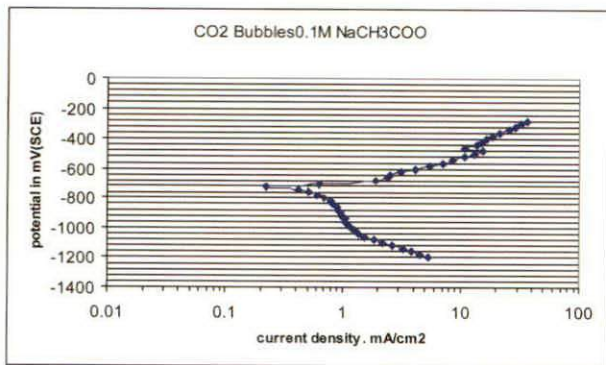


Fig.11: Polarisation curve of mild steel in 3.5% NaCl + 0.1M sodium acetate, pH=4.5.

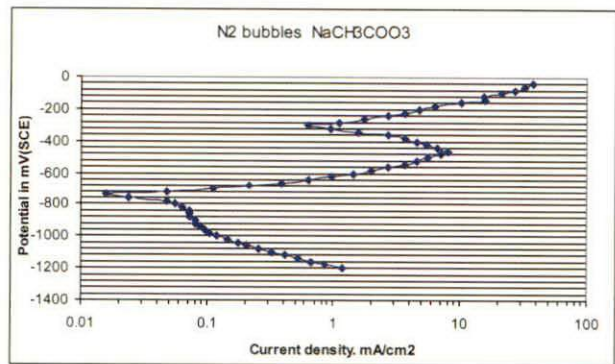


Fig.12: Polarisation curve of mild steel in 3.5% NaCl + 0.1M sodium acetate, pH=10.5.

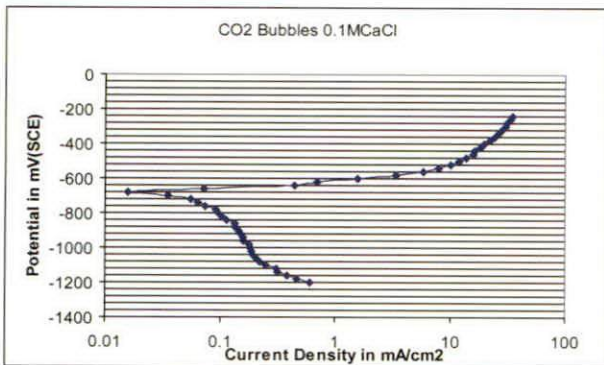


Fig.13: Polarisation curve of mild steel in 3.5% NaCl + 0.1M calcium carbonate, pH= 5.7.

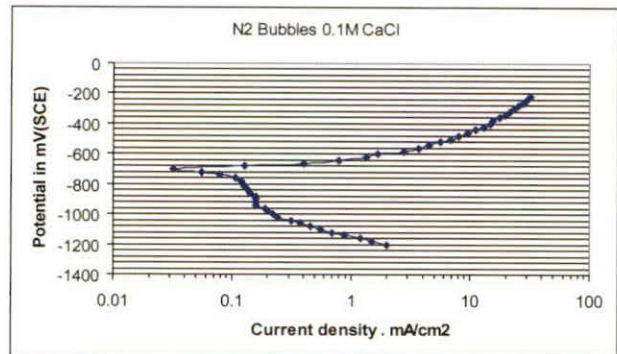


Fig.14: Polarisation curve of mild steel in 3.5% NaCl+0.1M calcium carbonate, pH= 8-9.

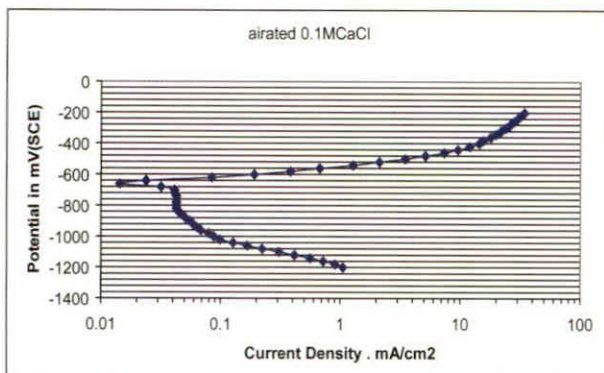


Fig.15: Polarisation curve of mild steel in 3.5% NaCl + 0.1M calcium carbonate, pH= 7.

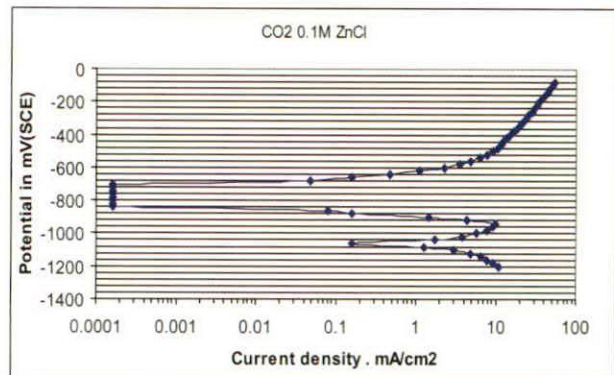


Fig.16: Polarisation curve of mild steel in 3.5% NaCl + 0.1M ZnCl₂, pH= 4.5.

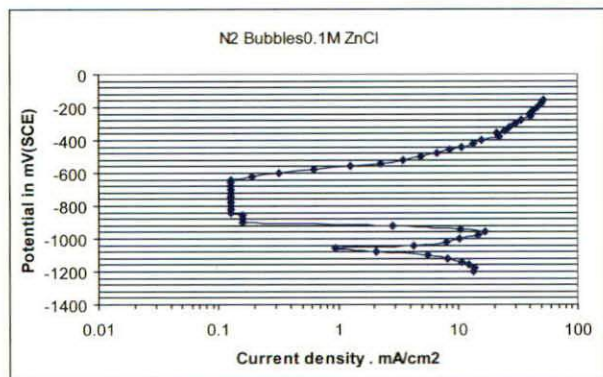


Fig.17: Polarisation curve of mild steel in 3.5% NaCl + 0.1M ZnCl₂; pH= 6.5.

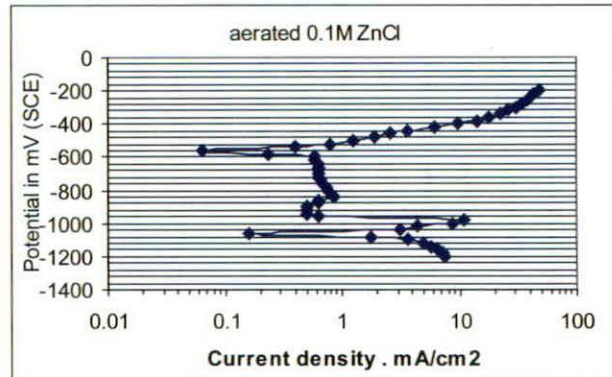


Fig.18: Polarisation curve of mild steel in 3.5% NaCl + 0.1M ZnCl₂; pH= 6.4.

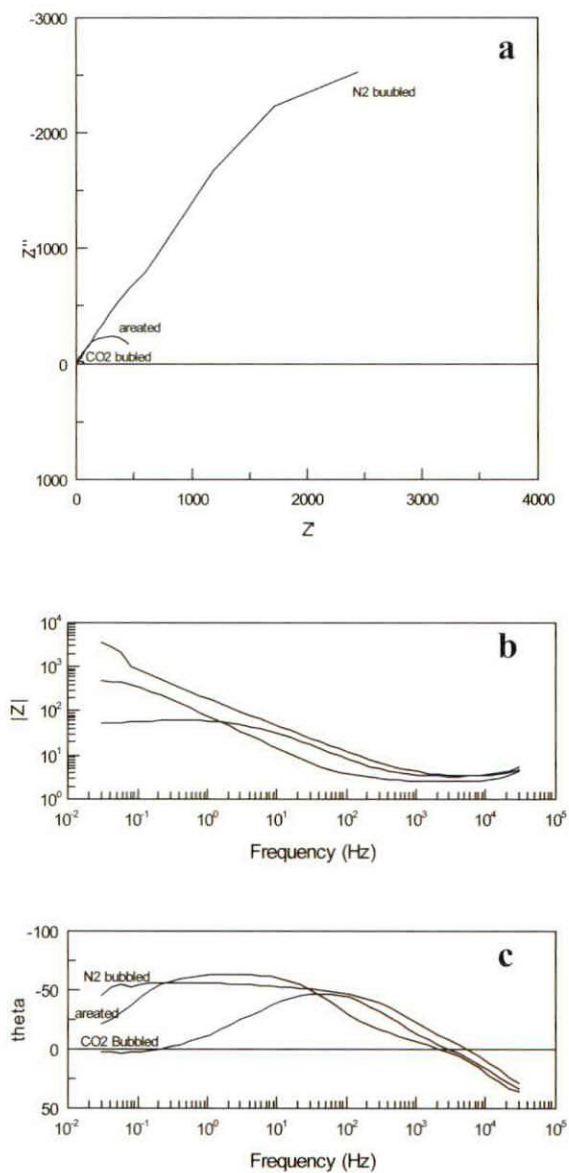


Fig. 19: 0.6 M NaCl 0.1M sodium acetate , a) Nyquist, b) bode plot – modulus, C) Bode plot – phase angle.

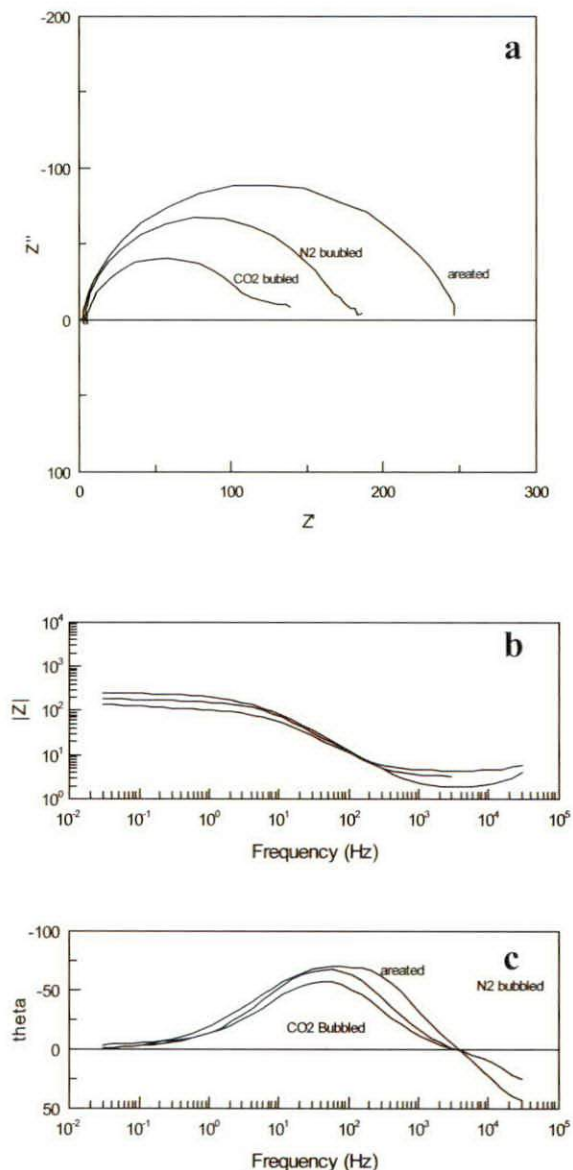


Fig. 20: 0.6 M NaCl 0.1M acetic acid, a) Nyquist, b) bode plot – modulus, C) Bode plot – phase angle.

small corrosion resistance observed $R_{ct} \approx 100 \Omega \cdot \text{cm}^{-2}$ and this implies the most rapid corrosion.

3.5% NaCl + 0.1M acetic Acid solution

Fig. 20 shows the corrosion behaviour of mild steel in the presence of acetic acid. The common feature taken from this plot is that the corrosion rate values are higher than for the other solution condition. It can be observed that corrosion processes are in agreement with the trends apparent in the polarization data (Figs.7, 8 and 9).

Effect of metal ion inhibitors

3.5% NaCl + 0.1M CaCl₂ solution

Fig. 21 shows the impedance response in the presence of calcium chloride. Here there is little improvement in the CO₂ corrosion resistance ($R_{ct} \approx 200-100 \Omega \cdot \text{cm}^{-2}$). There has occurred a significant decrease in the aerated corrosion rate that can be attributed to precipitation of a calcium hydroxide film which increases the charge transfer resistance of the formed protective film.

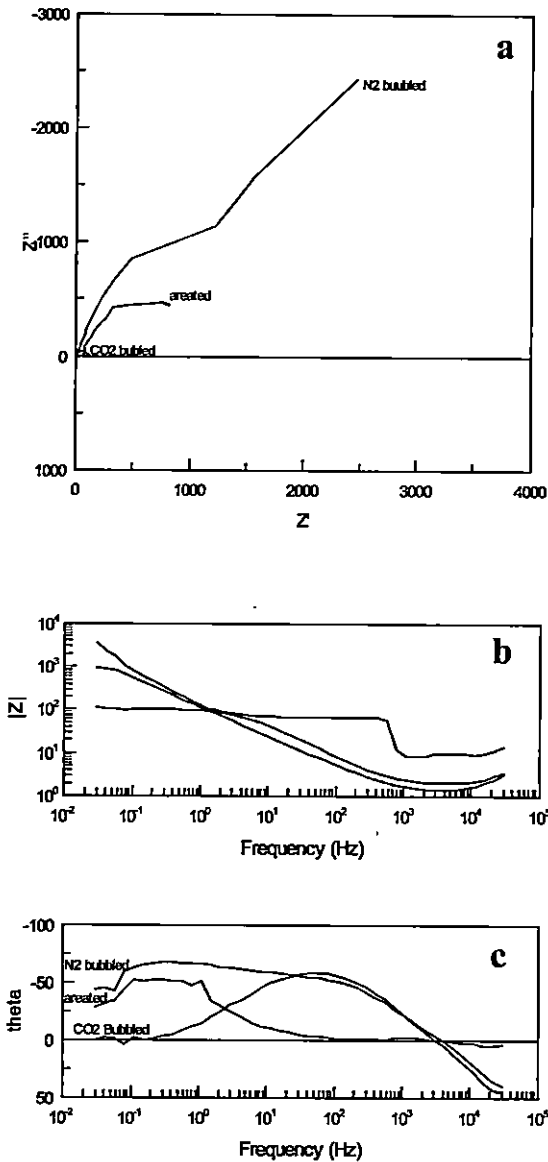


Fig. 21: 0.6 M NaCl 0.1M calcium chloride, a) Nyquist, b) bode plot – modulus, C) Bode plot – phase angle

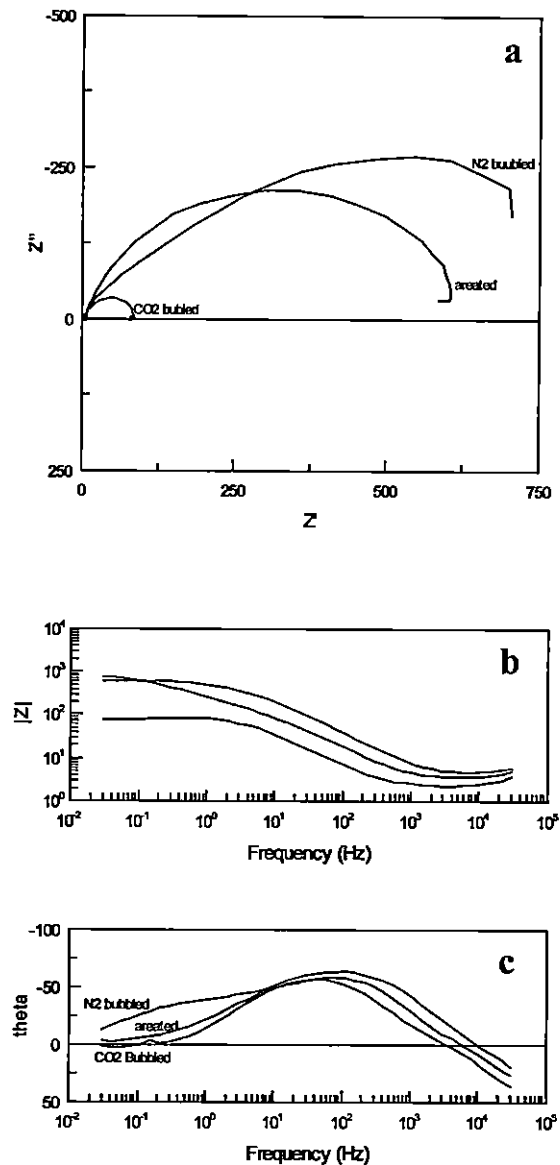


Fig. 22: 0.6 M NaCl 0.1M ZnCl₂, a) Nyquist, b) bode plot – modulus, C) Bode plot – phase angle.

3.5% NaCl + 0.1M ZnCl₂ solution

Fig. 22 shows impedance response in the presence of zinc chloride. Generally, the corrosion resistance is similar to that in calcium chloride solution, but there is some passivation behaviour, shown by the polarisation curves (Figs. 16, 17 and 18), that is difficult to observe on the impedance plots in (Fig. 22). The reason for that is that passivation behaviour strongly depends on the potential and by scientific principle the impedance as a technique was carried out at the open circuit value for potential.

CONCLUSIONS

- 1- Mild steel, in the presence of CO₂, the highest corrosion rates recorded compared with aerated and N₂ bubbled solutions.
- 2- Acetate enhances the mild steel corrosion rate and this confirms that the presence of acetate add some aggressiveness to the solution.
- 3- Mostly, There is good agreement between D.C polarization curves results and A.C impedance results accept in case of zinc chloride corrosion measurements; the AC does not help to know clear info about the mechanism happened on the surface.
- 4- For all solution conditions, the presence of acetic acid gives higher corrosion rate values over solutions containing sodium acetate.

REFERENCES

- Aagotnes, N. O.; Hemmingsen, T.; Haarseth, C. and Midttveit, I. (1999). Comparison of Corrosion Measurements by Use of AC-Impedance, LPR and Polarization Methods on Carbon Steel in CO₂ Purged NaCl Electrolytes. *NACE International Conference, ID NACE 99027 Corrosion: 25(3)*.
- Arzola, S.; Palomar-Pardave, M. E. and Jenesca. (2003). Effect of Resistivity on the Corrosion Mechanism of Mild Steel in Sodium Sulphate Solution. *Journal of Applied Electrochemistry: 33(12): 1233-1237*.
- Crolet, J. and Nicolas, A. D. (1999). Role of Free Acetic Acid on the CO₂ Corrosion of Steels. *NACE International, Corrosion: 25-30*.
- Guo, X. P.; Chen, Z. Y.; Liu, D.; Bando, K. and Tomoe, Y. (2005). The Effect of Acetic Acid and Acetate On CO₂ Corrosion of Carbon steel. *Corrosion; No. 05306: 9p*.
- Kermani, B. M. and Morshed, A. (2003). Corrosion and Gas Production-A Compendium. *Corrosion, 59(8): 659-683*.
- Kinsella, B.; Tan, Y. J. and Bailey, S. (1998). Electrochemical Impedance Spectroscopy and Surface Characterization Techniques to Study Carbon Dioxide Corrosion Products Scales. *Corrosion, 54(10): 835-842*.
- Module Notes-Aqueous Corrosion. (2003). *UMIST: 13p*.
- Nesic, S.; Postlethwaite, J. and Olsen, S. (1996). An Electrochemical Model for Prediction of Corrosion of Mild Steel in Aqueous Carbon Dioxide Solution. *Corrosion, 52(4): 280-294*.
- Newman, R. A. (2002a). Course Note, Corrosion of Metals in Acids, Corrosion and Protection Centre, *UMIST: 26p*.
- Newman, R. A. (2002b). Course Note, Corrosion of Metals in Near Natural Aqueous Solutions, Corrosion and Protection Centre, *UMIST: 5p*.
- Princeton Applied Research Technical Application Note AC-1, Basic Electrochemical Impedance spectroscopy: 13p.
- Princeton Applied Research Technical Application Note AC-1. *Basic electrochemical Impedance Spectroscopy 13p*.
- Tourgoose, S. (2004). Course Note CO₂ Corrosion in Water and CO₂ Corrosion and Effect of Flow on Corrosion. *CAPCIS: 9p*.

ACCURATE AGE RANGE PREDICTION SYSTEM OF INDIVIDUALS FROM FACIAL IMAGES

Tariq Khalifa¹, Kamal Solaiman², Tarik Idbeaa³ and Samar Husain⁴

Abstract: Age prediction is an active study field that can substantially affect on many computer vision problems like object recognition. In this paper, an accurate system with extensive experiments is proposed in order to provide an efficient and accurate approach for age range prediction of people from their facial images. Histogram Equalization technique used to reduce the illumination effects on all facial images taken from FG-NET and UTD aging databases, and image resizing used to unify all image's size. Moreover, Histogram of Oriented Gradient (HOG) and Local Binary Pattern (LBP) are used to extract the features of these images. Then, Support Vector Machine (SVM) and k-Nearest Neighbor (k-NN) are used for the classification processes. To evaluate the performance of proposed system, both Leave-One-Out (LOO) and Confusion Matrix (CM) are used. The extensive and intensified experiments improved the age range predicting performance up to 98.6%.

Keywords: Facial Images, Local Binary Pattern (LBP), Histogram of Oriented Gradient (HOG), SVM, kNN.

INTRODUCTION

Human faces are rich in details, such as age, gender, ethnic, emotions, skin color, etc. Whereas, these abilities that human being have aren't available in machines. Therefore, researchers have been trying to design and develop accurate systems to make the machine meet these challenging tasks. The age prediction of people is one of these tasks; and it is an interesting field of research and has been given increased attention in recent years.

Predicting a person's age from his/her face image isn't easy because of the large variation of face appearances, like variety of human race, poses, and facial expressions. However, age prediction has been recognized as an important module for many computer vision applications such as demographic profiling, forensic art, age-specific human-computer interfaces, security control, age-oriented advertisement systems, and electronic customer relationship management (ECRM).

In general, age prediction approaches are divided into two different groups that are: Age Group Classification and Actual Age Estimation (cumulative years lived). In Age Group Classification, the age range is divided into classes, each class has a range of years (e.g., from 10 to 20 years). On the other hand, in the Actual Age Estimation, we need to determine the specific and correct age of the people, which is usually based on regression methods or a hybrid of classifications and regressions to give an exact number of the age. This study focuses on Age Group Classification approach by dividing the age ranges into 11 classes.

RELATED WORKS

There are many applications and studies trying to predict the age of individuals from facial images. A study related to age prediction based on the use of Anthropometric Models (AM) for age classification was introduced in 1994 by Kwon and Lobo (Ramanathan *et al*, 2009). It is aimed to find the primary features of the face such as eyes, mouth, nose, and chin. Furthermore, an Appearance Model (APM) (Hayashi *et al*, 2002) is also used to

* Department of Computer Science – Faculty of Science – University of Al-Jabal Al-Gharbi
1 tariq.khalifa@jgu.edu.ly, 2 kamal.m.solaiman@gmail.com,
3 tidbeaa@siswa.ukm.edu.my, 4 samar.husain@jgu.edu.ly

determine the density of wrinkles in each face using the snake-lets (Kass *et al*, 1988). They create a facial database for their study, which contains 47 faces, and then divided the images into three age groups; babies, young adults, and senior adults. As a result, 77% successes are obtained. (Lanitis *et al*, 2004) used the Active Appearance Model (AAM) (Cootes *et al*, 2001) for age prediction. They extracted facial features of 500 images from 0 to 35 years old people by using PCA. To estimate the age, they adopted the Neural Network for classification of data, and reported 94.42% age prediction performance. (Guo *et al*, 2008) similarly used the AAM to estimate the age of 500 facial images from FG-NET (Panis *et al*, 2016) database between 0 to 69 years old people. Images features have been extracted by using a Locally Adjusted Robust Regresses (LARR). Then, SVM and Support Vector Regression (SVR) methods are investigated to classify the age. The results of their experiments showed 94.93% success estimation rate. (Kanno *et al*, 2001) used an APM to determine the density of wrinkles and extract the information of the faces. Consequently, accuracy of 80% has been achieved when Artificial Neural Networks (ANN) has been employed to classify four age groups of 110 facial images that were selected from FG-NET aging database. (Bauckhage *et al*, 2010) offered an accurate and efficient approach for age prediction from facial images. They combined HOG and Compute histograms of range filter. They trained their system on UTD database and the FG-Net database. As a result, in a first experiment, they verified whether the algorithm correctly ordered the two images and they measured an accuracy of 77%. In a second experiment, they fixed the candidate images to strictly frontal pose of faces. As a result, the classification accuracy has been improved up to 85%.

(Iga *et al*, 2003) used graph matching with Gabor Wavelet Transformation (GWT) to extract image's information such as, skin color, moustache, hair, etc. All these information were classified by applying SVM on 300 facial images divided into 6 age groups from 15 to 64 years old and taken from Softopia Japan HOIP database. Consequently, they achieved to 67.4% age estimation rate. Yang and Ai (2007) employed LBP feature extractor to know the Chi square distance between the extracted LBPH and a reference histogram. Moreover, real Adaboost algorithm was used as a strong classifier, which learns a sequence of best local features. By using 696 images from PIE (Sim *et al*, 2002) database, accuracy of 92.12% age prediction has been achieved. Shirkey

and Gupta (2013) developed an age recognition algorithm based on rectangle features method that are used to describe sub-regions of a human face, and hence component wise data can be transformed from pixel-wise data. A ratio of 85% for age classification was achieved. Fazl-Ersi *et al* (2014) compared three methods, that are LBP, Color Histogram (CH) and Scale-Invariant Feature Transform (SIFT) to predict the age range. Moreover, they used SVM classifier to classify the features that are extracted from images obtained from Gallagher facial images database (Gallagher & Chen, 2009). As a result, they obtained the best accuracy by combining LBP, CH, and SIFT features, which is reported 63.01% age estimation. Eidingner *et al*, (2014) used LBP and the related Four Patch LBP codes (FPLBP) to learn and extract the most important properties of images features. These images have been selected from Gallagher database. By combining LBP and FPLBP features and SVM, they achieved an accuracy of 80.7% of age estimation.

MATERIALS AND METHODS

The core and methodology of the proposed system mainly rely on four phases: pre-processing phase; feature extraction phase, classification phase, and evaluation phase (Fig. 1).

Pre-processing Phase

Solving age prediction problem requires overcoming some main difficulties, such as differing image dimensions and qualities, varying levels of luminosity, choosing appropriate database for each problem, and employing sufficient number of images in each experiment. Therefore, FG-NET and University of Texas at Dallas (UTD) Database have been employed, and Histogram Equalization (HE) technique and dimensions alignment (image re-sizing) have been used to help solving age prediction problem.

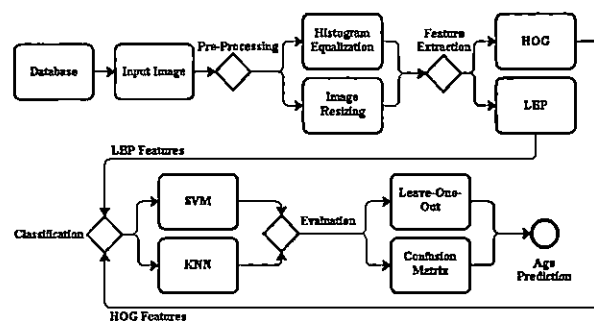


Fig. 1. General Methodology of Age Prediction System

Databases

Two aging databases that are FG-NET database (Panis *et al*, 2016) and UTD Database were used. A non-commercial FG-NET aging database (Fig. 2) was released in 2004 for understanding the changes in facial appearance caused by the age and other disciplines such as age progression, age estimation, age-invariant face recognition, or any other academic research-related activities. The FG-NET database contains 1,002 facial images from 82 different individuals that age ranging from 0 to 69 years old. Another database named UTD (Fig. 3) were provided for age prediction. It contains 580 facial images of people from 18 to 99 years old, where 352 of these images are female and 228 images are male. Furthermore, UTD can be used also for emotional recognition because all images in the database are detailed with face expressions such as happy, angry, annoyed, disgusted, grumpy, sad, and surprised.

However, in this study we combined both FG-NET (1,002 images) and UTD (580 images) databases to obtain huge database, including 1,582 facial images. All images distributed on 11 main classes; each class has a period of ages between 0 and 99 (Table 1).

Illumination Normalization

To normalize the illumination of the facial images, Histogram Equalization (HE) technique was applied. HE helps to reduce the effect of light and unify luminosity of all images in the databases, and this positively affects the accuracy and performance of the system.

Histogram Equalization (HE) (Dey *et al*, 2013) is a fast, simple and effective image illumination

enhancing technique, which can effectively confirms the details of the density in any region.

Dimensions Alignment (Image Re-sizing)

Each image within selected databases has a different resolution dimensions (more than 400×400). Therefore, image re-sizing was applied to decrease the size of images, and make all image's size equal (all images = 192×128 size). This has advantages of helping the feature extractor algorithm to extract same number of features from all images. Moreover, it helps to decrease the processing time, and hence increases the system performance.

Feature Extraction Phase

Two different feature extraction algorithms are used. The details of these algorithms are given below.

Histograms of Oriented Gradients (HOG)

HOG was introduced by Dalal and Triggs (2005), which became later one of the excellent local feature descriptors that has largely been used in computer vision and image processing. It has given promising performance in variety of computer vision problems related to object detection and recognition as an appearance based feature extraction method. In addition, HOG has many advantages such as the easy to use with discriminate classifiers. Due to its ability to capture shape of an object from edges (gradients), HOG gives good results to identify object from cluttered background without using any segmentation algorithm.

HOG algorithm follows some substantial steps to describe objects in the images; first, it divides

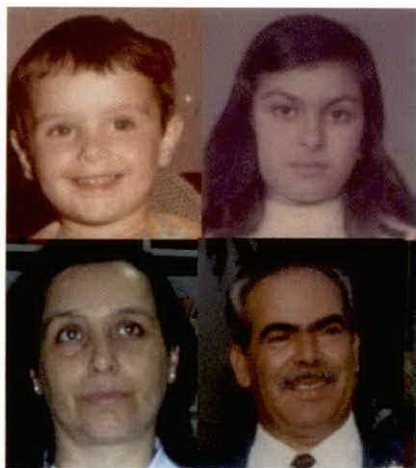


Fig. 2. Examples from FG-NET Database



Fig. 3. Examples from UTD Database

Table 1. The Number of Images in Aging Database (FG-NET & UTD)

Databases	The Age Classes											Total
	0 to 15	16 to 20	21 to 25	26 to 30	31 to 35	36 to 40	41 to 45	46 to 50	51 to 55	56 to 60	+60	
FG-NET	575	155	81	61	39	31	26	13	12	1	8	1,002
UTD	0	53	132	42	23	19	19	16	16	8	252	580
Total	575	208	213	103	62	50	45	29	28	9	260	1,582

the input image into blocks, and divides each block into smaller connected cells. Then it computes a histogram of gradient directions for all the pixels within the cell. According to these gradient orientations, each pixel reshaped into angular bins and then participated gradient to its parallel bin. Then it normalizes the group of cells (block) histograms, which represent a one-dimensional array of histograms called the descriptor (Mary *et al*, 2013).

LBP Features

The LBP, which was presented by Ojala *et al* (2002), is an efficient and powerful texture descriptor that is widely used in image processing and computer vision areas as a feature and histogram representation. LBP algorithm has the ability to capture the shape of body in the image by looking to each pixel's neighbors. The main LBP mechanism is that the input image is divided into local regions composed of a '3×3' neighborhood of pixels. Then, type of binary pattern assigned a label to each pixel according to its intensity value, where the distribution of these binary patterns in each block represents the results with an 8-bits integer, where the calculation of these patterns are represented as a one-dimensional array of patterns used as a feature representation (Ojala *et al*, 1996).

Classification Phase

k-Nearest Neighbour (k-NN) and Support Vector Machine (SVM) are used in the presented work as a classifiers. The details of the classifiers are given below.

k-NN

k-NN is one of the simplest classifiers for predicting the class of a test sample used in machine learning, which is based on training samples that are very close to each other in the features scope (Wu *et al*, 2008). The main idea of the k-NN classifier mechanism is based on calculating and computing

the distances between all training objects to test object, then finding and gathering a collection of k objects in the training set that are nearest to the test object, and finally calculating the average of them (see Fig. 4). Although the k-NN classifier performance is highly sensitive to the number of k value and the results are affected by any changes in it, k-NN classifier is widely used and very easy to implement in many classification problems. However, determining k value is very complex step because it is affected by the parameters like the type of feature extractor algorithm, and number of samples that is available in training set (Sudha & Bhavani, 2012).

Fig. 4 shows the mechanism of k-NN classifier. It is based on the value of k, which is used to compute the distances between training objects (circular shapes) and test object (star shape). For instance, in case of considering k value = 3, k-NN classify the closest 3 training objects to the test object, and then calculates the average of them. In this case, the star as purple-circle. Similarly, in case of considering k value = 6, k-NN classify the closest 6 training objects to the test object, and then calculates the average of them. In this case, the star classified as yellow circle.

SVM

SVM was developed by Cortes and Vapnik (1995) and has extensively been used as a powerful classification algorithm for pattern recognition applications. In addition, it gives promising and excellent performance on the range of machine learning by applying it to different classification problems, data separation, regression, and density estimation (Begg *et al*, 2005).

SVM classifier has many advantages, which make it one of the accurate and robust algorithms, such as:

- Gives promising performance even with small number of images in training set.
- Not sensitive to the number of dimensions,

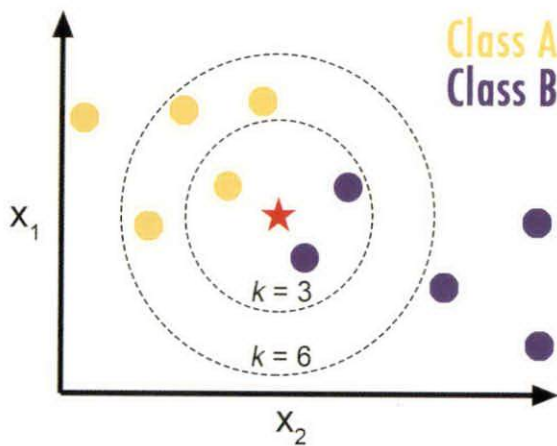


Fig. 4. Basic Concept of k-NN

which gives it promising performance with any images size.

- Ability to minimize empirical and structural risk, which leads to better generalization for data classification.

The main task of SVM is based on searching for the OSH “Optimal Separating Hyper-plane”, which is the closest point between two classes (positive and negative samples) of data in the training set. By increasing the margin between these classes, SVM can modify the input data into a high-dimensional feature space where a hyper-plane may be found. Furthermore, it can reduce the structural risk; hence reducing the number of predictable errors (Sudha & Bhavani, 2012). However, the nearest OSH data to the border of each class are called the “Support Vectors” (Fig. 5).

Fig. 5 shows how SVM classifier can distinguish between two classes, where the Class 1 (star shapes) contains the positive features; and Class 2 (circular shapes) contains the negative features. SVM starts increasing the margin between the two classes bit by bit to find the OSH, which are the closest points between these classes. The OSH features in each class (orange color) are known as “Support Vectors” and used by SVM in classification process.

Evaluation Phase

Leave-One-Out Cross-Validation (LOO) technique

Leave-One-Out Cross-Validation (LOO) mechanism is simple; the dataset is split into N subsets, where N is the number of samples in the dataset. Then, the classification process is repeated N times, in each time, $N-1$ of subsets are used to train the classifier, and only one subset is selected for evaluation. In this study, Leave-One-Out technique

have been applied on FG-NET and UTD databases in order to evaluate the performance of SVM and k-NN classifiers.

Confusion Matrix

The confusion matrix, which is also called an error matrix or a contingency table, provides a simple detail and visualization about predicted and actual classes that are accomplished by a classifier. The systems performance is generally evaluated by using the details mentioned in this matrix. Fig. 6 shows the confusion matrix layout of a two classification classes.

Each column in the above table shows the number of actual and correct class samples, whereas each row shows the number of predicted class samples. In more details, “True Positive” is the number of true or correct predictions that an example is positive. “False Negative” is the number of false or incorrect predictions that an example is negative. “False Positive” is the number of false or incorrect predictions that an example is positive. “True Negative” is the number of true or correct predictions that an example is negative.

EXPERIMENTAL CLASSIFICATION RESULTS AND ANALYSIS

As mentioned previously, FG-NET aging database contains 1,002 facial images, whereas UTD database contains 580 facial images. Therefore, both databases are combined in one bigger database containing 1,582 facial images, and then separated these images into 11 classes depending on their ages. We review all experiments done in order to predict the age range of people in the following subsections.

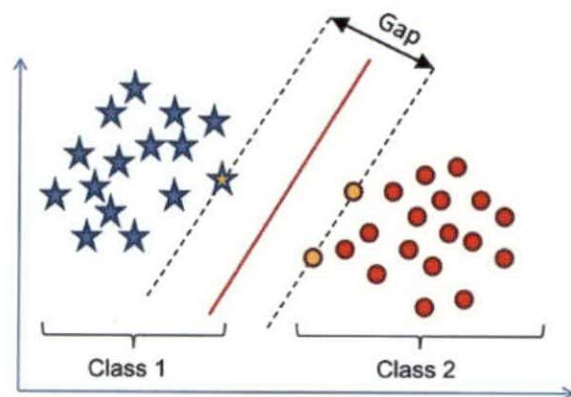


Fig. 5. Basic Concept of SVM

		Actual (as confirmed by experiment)	
		positives	negatives
Predicted (predicted by the test)	positives	TP True Positive	FP False Positive
	negatives	FN False Negative	TN True Negative

Fig. 6. Confusion Matrix

SVM Based Classification

The SVM classifier has been trained on 1,582 images from FG-NET and UTD databases by using Leave-One-Out technique. Consequently, when the HOG features are used with SVM, age prediction accuracy was 98.60%, whereas, when LBP features are used with SVM, the accuracy was 98.29%. Table 2 shows the performance of the proposed methods. In addition, the classifiers are evaluated by using Confusion Matrix (CM), which provides details and visualization about predicted and actual classes that are accomplished by the SVM classifier with HOG and LBP features, as shown in Tables 3 and 4.

As can be seen from the tables, the errors occur on the neighbour classes. For example, the error on the 56-60 age-range class is on (up to 60) class. This shows that the person on the age range of 56-60 is predicted to be in up to 60 age range.

k-NN Based Classification

The k-NN classifier was applied on 1,582 images from FG-Net and UTD databases by using Leave-One-Out technique. k-NN classifier performance is highly sensitive to the number of k value and the results are affected by any changes in it. Moreover, determining k value is not easy, because it is effected by the parameters like number of samples that obtained in training set, and the type of used feature extractor algorithm. Therefore, in this study, many extensive experimentations have been done in order to determine the best optimal k value that can give high performance (Fig. 7).

As can be seen from the Fig. 7, changing k value from 1 to 30 is leading to attain different performance. In addition, it is observed that the best performance can be achieved when k value is equal to 12 and 19 in case of using HOG and LBP features, respectively. Consequently, when the HOG features

are used with k-NN, age prediction accuracy were 98.23%. Similarly, when LBP features are used with k-NN, the accuracy were 88.05%, in case of considering k value = 19. Table 5 shows the summary of the performance of the proposed method. In addition, the evaluation of classifiers is performed by using Confusion Matrix (CM), which provides simple details and visualization about predicted and actual classes that accomplished by the k-NN classifier with HOG and LBP features, as shown in Tables 6 and 7.

DISCUSSION AND CONCLUSION

In order to predict the age range of any person from his/her face image, many extensive experimentations were carried out to make the classifiers obtain high accuracy and performance. In this paper, an efficient and accurate approach was proposed by processing extracted HOG and LBP features from images, while SVM and k-NN are used for classification. Moreover, dimensions alignment that used to reduce the computation cost, and Histogram Equalization technique that used to minimize the illumination effects in different images, had been applied successfully on all images to obtained promising and accurate results. Furthermore, the extensive experiments confirm that using proposed method with correct k value-when using k-NN classifier-lead to achieve excellent performance.

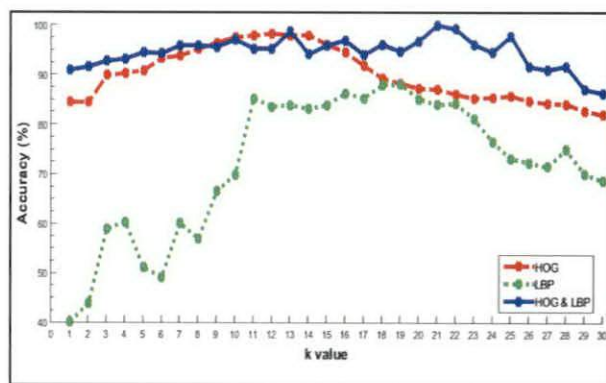


Fig. 7. The Performance of k-NN Based Classification According to 'k' Value

Table 2. SVM Based Age-Classification of FG-NET and UTD Databases

Method	Dataset	Accuracy
HOG + SVM	FG-NET + UTD	98.60%
LBP + SVM	FG-NET + UTD	98.29%

Table 3. Confusion Matrix Evaluation of HOG + SVM

Predicted Classes	Actual Classes										
	0-15	16-20	21-25	26-30	31-35	36-40	41-45	46-50	51-55	56-60	Up 60
0-15	574	1	0	0	0	0	0	0	0	0	0
16-20	1	206	1	0	0	0	0	0	0	0	0
21-25	0	1	211	0	0	0	0	0	0	0	0
26-30	0	0	0	0	102	0	0	0	0	0	0
31-35	0	0	0	0	0	60	0	0	0	0	0
36-40	0	0	0	0	0	1	47	1	0	0	0
41-45	0	0	0	0	0	0	1	43	0	0	0
46-50	0	0	0	0	0	0	0	0	26	0	0
51-55	0	0	0	0	0	0	0	0	0	24	0
56-60	0	0	0	0	0	0	0	0	0	0	7
Up 60	0	0	0	1	1	1	2	1	3	4	2
Total	575	208	213	103	62	50	45	29	28	9	260

Table 4. Confusion Matrix Evaluation of LBP + SVM

Predicted Classes	Actual Classes										
	0-15	16-20	21-25	26-30	31-35	36-40	41-45	46-50	51-55	56-60	Up 60
0-15	575	1	0	0	0	0	0	0	0	0	0
16-20	0	205	0	0	0	0	0	0	0	0	0
21-25	0	0	211	0	0	0	0	0	0	0	0
26-30	0	0	0	0	101	0	0	0	0	0	0
31-35	0	0	0	0	0	60	0	0	0	0	0
36-40	0	0	0	0	0	0	48	0	0	0	0
41-45	0	0	0	0	0	0	0	43	0	0	0
46-50	0	0	0	0	0	0	0	0	27	0	0
51-55	0	0	0	0	0	0	0	0	0	25	0
56-60	0	0	0	0	0	0	0	0	0	0	0
Up 60	0	2	2	2	2	2	2	2	2	3	9
Total	575	208	213	103	62	50	45	29	28	9	260

Table 5. k-NN Based Age-Classification of FG-NET and UTD Databases

Predicted Classes	Actual Classes										
	0-15	16-20	21-25	26-30	31-35	36-40	41-45	46-50	51-55	56-60	Up 60
0-15	575	5	0	0	0	0	0	0	0	0	0
16-20	0	202	0	0	0	0	0	0	0	0	0
21-25	0	1	212	1	0	0	0	0	0	0	0
26-30	0	0	1	102	0	0	0	0	0	0	0
31-35	0	0	0	0	62	0	0	0	0	0	0
36-40	0	0	0	0	0	50	0	0	0	0	0
41-45	0	0	0	0	0	0	45	8	0	0	0
46-50	0	0	0	0	0	0	0	20	2	0	0
51-55	0	0	0	0	0	0	0	1	26	1	0
56-60	0	0	0	0	0	0	0	0	0	0	0
Up 60	0	0	0	0	0	0	0	0	0	8	8
Total	575	208	213	103	62	50	45	29	28	9	260

Table 6. Confusion Matrix Evaluation of HOG + k-NN

		Actual Classes										
		16-20	21-25	26-30	31-35	36-40	41-45	46-50	51-55	56-60	Up 60	
Predicted Classes	0-15	575	127	2	0	0	0	0	0	0	0	0
	16-20	0	76	6	0	0	0	0	0	0	0	0
	21-25	0	5	204	4	0	2	0	0	0	0	0
	26-30	0	0	0	99	0	0	0	0	1	0	0
	31-35	0	0	0	0	49	0	0	0	0	0	0
	36-40	0	0	0	0	0	30	0	0	0	0	0
	41-45	0	0	0	0	0	0	43	0	0	0	0
	46-50	0	0	0	0	0	0	0	26	0	0	0
	51-55	0	0	0	0	1	0	0	0	25	0	0
	56-60	0	0	0	0	0	0	0	0	0	6	0
	Up 60	0	0	1	0	12	18	2	3	2	3	260
Total	575	208	213	103	62	50	45	29	28	9	260	

Table 7. Confusion Matrix Evaluation of LBP + k-NN

Method	Dataset	Accuracy
HOG + k-NN (k = 12)	FG-NET + UTD	98.23%
LBP + k-NN (k = 19)	FG-NET + UTD	88.05%

Consequently, the experimental results show that when SVM is used the performance is on the range of 98% for each feature extractor (HOG and LBP). However, comparing with other similar studies like (Guo et al, 2008 and Bauckhage et al, 2010) that are discussed previously, our results are promising and significant, where the best result achieved by (Guo et al, 2008) was 94.93% success age estimation by applying LARR + SVM on 500 images from FG-Net database. Similarly, the best accuracy that achieved by (Bauckhage et al, 2010) was 85% by applying HOG + Random-forests on UTD and FG-Net databases. Whereas, the age prediction accuracy of all 1,582 experimental images has been achieved upto 98% when using our proposed methods.

However, LOO technique has a disadvantage that it may consumes longer-processing time when applying it on large amount of data, because it evaluates all images we have in the dataset one by one. Another disadvantage is that we directly used facial images to test the performance of the proposed methods, so detecting faces in the images is out of scope to this work.

RECOMMENDATION

In future work, it would be much better results if the researcher plan to focus on predicting the exact age of the people instead of age-range.

REFERENCES

- Bauckhage, C., Jahanbekam, A., and Thurau, C. (2010). Age Recognition in the Wild. In Pattern Recognition (ICPR), *20th International Conference*: 392-395.
- Begg, R. K., Palaniswami, M., and Owen, B. (2005). Support Vector Machines for Automated Gait Classification. *Biomedical Engineering, IEEE Transactions, V.52(5)*: 828-838.
- Cootes, T. F., Edwards, G. J., and Taylor, C. J. (2001). Active Appearance Models. *IEEE Transactions on Pattern Analysis & Machine Intelligence, V. 6*: 681-685.
- Cortes, C., and Vapnik, V. (1995). Support-Vector Networks. *Machine learning, V. 20(3)*: 273-297.
- Dalal, N., and Triggs, B. (2005). Histograms of Oriented Gradients for Human Detection. *Computer Vision and Pattern Recognition, IEEE Computer Society Conference, V. 1*: 886-893.
- Dey, E. K., Khan, M., and Ali, M. H. (2013). Computer Vision-Based Gender Detection from Facial Image. *International Journal of Advanced Computer Science, V. 3(8)*: 428-433.

- Eidinger, E., Enbar, R., and Hassner, T. (2014). Age and Gender Estimation of Unfiltered Faces. *Information Forensics and Security, IEEE Transactions on*, *9(12)*: 2170-2179.
- Fazl-Ersi, E., Mousa-Pasandi, M. E., Laganieri, R., and Awad, M. (2014). Age and Gender Recognition Using Informative Features of Various Types. *Image Processing (ICIP), International Conference*: 5891-5895.
- Gallagher, A., and Chen, T. (2009). Understanding Images of Groups of People. *Computer Vision and Pattern Recognition, Conference*: 256-263.
- Guo, G., Fu, Y., Huang, T. S., and Dyer, C. R. (2008). Locally Adjusted Robust Regression for Human Age Estimation. *IEEE Workshop on Applications of Computer Vision, Copper Mountain Co*: 1-6.
- Hayashi, J., Yasumoto, M., Ito, H., Niwa, Y. and Koshimizu, H. (2002). Age and Gender Estimation from Facial Image Processing. *Proceedings of the 41st SICE Annual Conference, V. I*: 13-18.
- Iga, R., Izumi, K., Hayashi, H., Fukano, G., and Ohtani, T. (2003). A Gender and Age Estimation System from Face Images. *Age*: 25, 34.
- Kanno, T., Akiba, M., Teramachi, Y., Nagahashi, H., and Takeshi, A. G. U. I. (2001). Classification of Age Group Based on Facial Images of Young Males by Using Neural Networks. *IEICE Transactions on Information and Systems, V. 84(8)*: 1094-1101.
- Kass, M., Witkin, A., and Terzopoulos, D. (1988). Snakes: Active Contour Models. *International Journal of Computer Vision, V. 1(4)*: 321-331.
- Kwon, Y. H., & Lobo, N. D. V. (1994). Age Classification from Facial Images. In *Computer Vision and Pattern Recognition, Proceedings CVPR'94, Computer Society Conference*: 762-767.
- Lanitis, A., Draganova, C., and Christodoulou, C. (2004). Comparing Different Classifiers for Automatic Age Estimation. *Systems, Man, and Cybernetics, Part B: Cybernetics, IEEE Transactions, V. 34(1)*: 621-628.
- Mary, P. F. G., Paul, P. S. K., and Dheebea, J. (2013). Human Identification Using Periocular Biometrics. *International Journal of Science, Engineering and Technology Research, V. 2*: 1047-1053.
- Ojala, T., Pietikäinen, M., and Harwood, D. (1996). A Comparative Study of Texture Measures with Classification Based on Featured Distributions. *Pattern recognition, V. 29(1)*: 51-59.
- Ojala, T., Pietikäinen, M., and Mäenpää, T. (2002). Multiresolution Gray-Scale and Rotation Invariant Texture Classification with Local Binary Patterns. *Pattern Analysis and Machine Intelligence, IEEE Transactions, V. 24(7)*: 971-987.
- Panis, G., Lanitis, A., Tsapatsoulis, N., and Cootes, T. F. (2016). Overview of Research on Facial Ageing Using the FG-NET Ageing Database. *IET Biometrics, V. 5(2)*: 37-46.
- Ramanathan, N., Chellappa, R., & Biswas, S. (2009). Computational Methods for Modeling Facial Aging: A Survey. *Journal of Visual Languages & Computing, 20(3)*: 131-144.
- Shirkey, D. M., and Gupta, S. R. (2013). An Image Mining System for Gender Classification & Age Prediction Based on Facial Features. *International Journal of Science and Modern Engineering (IJISME), V. 1(6)*: 8-12.
- Sim, T., Baker, S., and Bsat, M. (2002). The CMU Pose, Illumination, and Expression (PIE) Database. In *Automatic Face and Gesture Recognition, Proceedings Fifth IEEE International Conference*: 46-51.
- Sudha, L. R., and Bhavani, R. (2012). Gait Based Gender Identification Using Statistical Pattern Classifiers. *International Journal of Computer Applications, V. 40(8)*: 30-35.
- Wu, X., Kumar, V., Quinlan, J. R., Ghosh, J., Yang, Q., Motoda, H. and Steinberg, D. (2008). Top 10 Algorithms in Data Mining. *Knowledge and Information Systems, V. 14(1)*: 1-37.
- Yang, Z. and Ai, H. (2007). Demographic Classification with Local Binary Patterns. *Int. Conf. on Biometrics*: 464-473.

OXIDATION OF SODIUM SULFIDE IN INDUSTRIAL WASTEWATER AND SPENT CAUSTIC BY HYPOCHLORITE ION SOLUTION

Youssef Ahmed Al Mestiri*

Abstract: Oxidation of sulfide ion found in Ras Lanuf Oil and Gas Co (RasCo) industrial wastewater and spent caustic to soluble sulphate ion by hypochlorite ion. The method is based on industrial wastewater and spent caustic treatment with free dichromate ion hypochlorite ion solution for a short period of time sufficient to oxidize sulfide ion to sulphate ion. The method is practical and prompt to oxidize sulfide ion to sulphate ion.

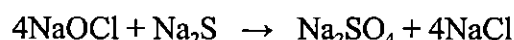
Keywords: Industrial, Waste Water, Spent Caustic, Sulfide Ion, Oxidation, Hypochlorite Ion, Sulphate Ion Solution

INTRODUCTION

The extremely harmful sulfide found in industrial wastewater and spent caustic must be regulated to less than 1 mg S-2/L (Sulfide Treatment, 2010). The sources of sulfide are effluents of some petrochemical, refineries, chemical and tannery industries. Sulfides in industrial wastewater and spent caustic cause environment pollution as well air pollution via the formation and releasing of hydrogen sulfide (Saikat & Naveed, 2010; Saikat *et al*, 2010 and Ueno *et al*, 1979). In industrial wastewater and spent caustic sulfide, is converted by oxidation to thiosulfate, sulfite or sulfate, or it is removed from water by precipitation; in excess oxidants like hydrogen peroxide, chlorine, sodium hypochlorite and potassium permanganate sulfide ion is converted to sulfate ion (Allison *et al*, 2010; Kubicek, 2010 and Wanner *et al*, 2010). Sulfide is catalytically oxidized in spent caustic by air or hydrogen peroxide to thiosulfate or sulfate depends on the amount of oxidants (UOP, 2010). The aim of this work is to regulate the extremely nocuous sulfide ions in both RasCo's industrial wastewater and spent caustic to less than 1 mg S-2/L by oxidizing the nocuous sulfide ions to the innocuous sulfate ions in a short period of time by use dichromate free sodium hypochlorite solution.

EXPERIMENTAL

Free dichromate alkaline sodium hypochlorite solutions having different hypochlorite ion content are tested to oxidize in a short period of time at room temperature. The harmful sulfide ion to the harmless sulfate ion in synthetic sulfide ion standard solutions and in seven spent caustic and industrial wastewater samples S1–S7. Sodium hypochlorite reacts with sodium sulfide according to the following chemical equation:



Four synthetic standard alkaline sodium sulfide solutions containing 276, 250, 137 and 68 mg S-2/L are used. Standard alkaline sulfide ion solutions are prepared by weighing and dissolving sodium sulfide in distilled water to which a 2-3 mL 1M NaOH is added, followed by iodometric determination of the sulfide ion content in the synthetic alkaline standard solutions (Standard Methods for the Examination of Water and Wastewater 1985). The alkaline sodium sulfide solution pH is 12.80. Free dichromate sodium hypochlorite solution brought from RasCo's chlorination plant storage tank where it was produced from sea water electrolysis, it is used as received; sodium hypochlorite solution pH is 9.00. Hypochlorite ion concentration in the free dichromate sodium hypochlorite solution is determined iodometrically (Vogel 1972).

* Ras Lanuf Oil & Gas Processing Co Quality Control Laboratory
P. O. Box 1971, Benghazi – Libya
yaalmisteri@gmail.com, Mobile phone: 0924552998

Experiment I

A 10.50 mL 1050 mg OCI^{-1}/L alkaline sodium hypochlorite solution was added to a 50 mL 68 mg S^{-2}/L alkaline sodium sulfide solution in an open 500 mL conical flask, the mixture was shaken manually at room temperature for about 2 minutes followed by iodometric determination of the excess non reacted sulfide ion in the same conical flask (Standard Methods for the Examination of Water and Wastewater, 1985).

Experiment II

In this experiment the sulfide ion concentration and volume as well the hypochlorite ion concentration are the same as in experiment I, but a 21 mL hypochlorite ion solution instead of 10.50 mL was added. The non reacted hypochlorite ion was determined iodometrically (Vogel, 1972). In both experiments I and II formation of sulfate ion was detected (Standard Methods for the Examination of Water and Wastewater, 1985).

Experiments I and II were repeated 13 times using different hypochlorite and sulfide ion concentrations, and applied to oxidize the sulfide

ion in seven industrial wastewater and spent caustic samples S1 - S7 having sulfide ion concentrations 49, 53, 64, 62, 427, 450 and 464 mg S^{-2}/L ., samples pH is 10.60-13.60. The seven samples brought from RasCo's industrial wastewater treatment plant and ethylene plant. Table 1 tabulates concentrations and volumes of hypochlorite and sulfide ions mixed ratio in each experiment as well milligram hypochlorite ion added to each synthetic alkaline sulfide standard solution, industrial wastewater and spent caustic samples.

RESULTS AND DISCUSSION

To observe and reveal the oxidation capability and potent immediate action of free dichromate hypochlorite ion upon sulfide ion; in experiments 1-6 the milligrams hypochlorite ion added to the synthetic alkaline sulfide ion standard solutions is less than the quantity needed to oxidize entirely the sulfide ion to sulfate ion. Furthermore, in experiments 7-15 the synthetic alkaline sulfide ion standard solutions, the industrial wastewater and spent caustic samples S1-S7 are treated with an appreciable amount of hypochlorite ion. That was to ensure the entire oxidation of the sulfide ion to sulfate ion as indicated by the iodometric methods results (Standard Methods for the Examination of Water and Wastewater, 1985 and Vogel, 1972). Table 2 tabulates milligrams reacted and milligrams non reacted of both hypochlorite and sulfide ions in each experiment and in industrial wastewater and spent caustic samples.

Table 1 hypochlorite and sulfide ions mixed ratio.

Experiment No.	mL S^{-2}	mg S^{-2}	mg S^{-2}/L	ml OCI^{-1}	mg OCI^{-1}	mg OCI^{-1}/L
1	50	3.40	68	10.50	11.03	1050
2	15	2.06	137	4	4.34	1084
3	20	2.74	137	6	6.50	1084
4	10	2.50	250	2	0.76	381
5	10	2.50	250	3	1.14	381
6	10	2.76	276	7	4.96	708
7	50	3.40	68	21	22.05	1050
8	15	2.06	137	10	10.84	1084
9	20	2.74	137	25	27.10	1084
10	40	5.48	137	25	27.10	1084
11	10	2.76	276	25	17.70	708
12	8	2.20	276	25	17.70	708
13	5	1.38	276	25	17.70	708
14	8	2.00	250	25	9.53	381
15	5	1.25	250	25	9.53	381
S1	150	7.35	49	25	23.15	926
S2	100	5.30	53	15	13.89	926
S3	20	1.28	64	10	9.26	926
S4	20	1.24	62	10	9.26	926
S5	10	4.27	427	25	23.15	926
S6	10	4.50	450	25	23.15	926
S7	10	4.64	464	25	23.15	926

CONCLUSION

Free dichromate hypochlorite ion solution regulates the concentration of sulfide ion to less than 1 mg S^{-2}/L in both RasCo's industrial wastewater and spent caustic by oxidize at room temperature the extremely toxic sulfide ion to the nontoxic sulfate ion in a short period of time i.e. 2 minutes.

RECOMMENDATION

Ras Lanuf Oil & Gas Processing Co, petrochemical, chemical, refineries and tannery industries are recommended to use free dichromate alkaline sodium hypochlorite solution to oxidize the harmful sulfide ion in industrial wastewater and spent caustic to harmless sulfate ion.